Electrical Characterization of Mobile Ions in Perovskite Solar Cells

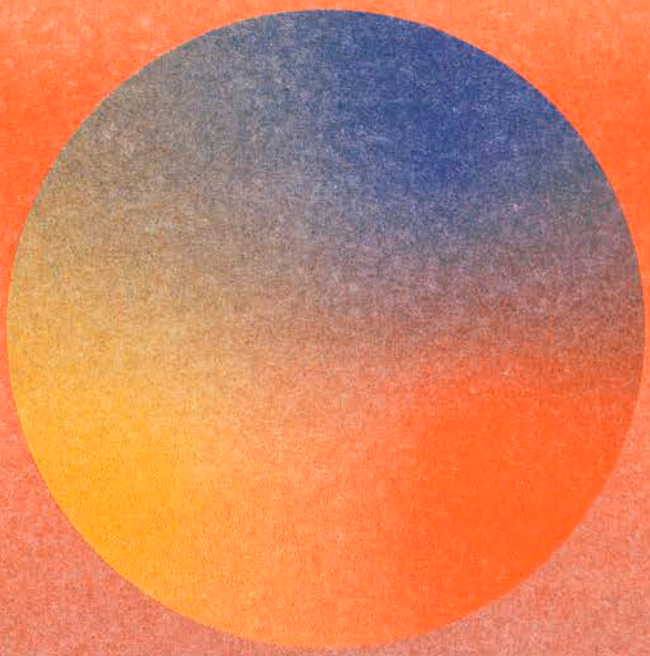

Moritz C. Schmidt

Electrical Characterization of Mobile Ions in Perovskite Solar Cells

university of groningen / faculty of science and engineering / zernike institute for advanced materials

AMOLF physics of functional complex matter

European Research Council

Electrical Characterization of Mobile Ions in Perovskite Solar Cells
Ph.D. Thesis, University of Groningen, October 2025
Moritz Christian Schmidt

ISBN: 978-94-92323-83-5
Thesis number: 2025-46, ISSN 1570-1530

Cover designed together with Annika Rieke Schmidt and printed by Herr & Frau Rio.
Thesis printed by Ridderprint.

Ph.D. Examining Committee:
Prof. T. Kirchartz
Dr. C.P. Aranda Alonso
Prof. S. Tao
Prof. L.J.A. Koster
Prof. M.A. Loi

The work described in this thesis was performed between February 2021 and April 2025 at AMOLF, Science Park 104, 1098 XG Amsterdam, The Netherlands, and financed by the European Research Council (Grant Agreement No. 947221).

A digital version of this thesis can be downloaded at:
https://www.lmpv.nl/theses/

university of groningen

Electrical Characterization of Mobile Ions in Perovskite Solar Cells

PhD thesis

to obtain the degree of PhD of the
University of Groningen
on the authority of the
Rector Magnificus Prof. J.M.A. Scherpen
and in accordance with
the decision by the College of Deans.

This thesis will be defended in public on

31 October 2025 at 11:00 hours

by

Moritz Christian Schmidt

born on 9 April 1995
in Bielefeld, Germany

Supervisor
Prof. B. Ehrler
Prof. E.C. Garnett

Assessment Committee
Prof. T. Kirchartz
Prof. L.J.A. Koster
Prof. M.A. Loi

Contents

1 Introduction

1.1 The Role of Solar Energy in the Energy Transition

A drastic increase in renewable energy production is necessary to keep the global temperature increase below 2 °C. At the United Nations Climate Change Conference 2023, nearly 200 countries pledged to triple global renewable energy capacity by 2030 [1]. One of the core technologies already playing a significant role in transforming the global energy system to electrical energy is solar energy. Within only ten years, the total installed capacity of solar energy has increased almost 10-fold from around 180 GW in 2014 to 1.4 TW in 2024 [2, 3]. In 2024, solar energy made up 18 % of the total electricity production in the Netherlands [4]. On a global scale, solar energy made up 5.4 % of the total electricity demands and is expected to increase to 16 % in 2030 [5].

Next to increasing the number of solar modules, increasing their efficiency is a promising way to increase solar energy capacity. However, the efficiency of silicon solar cells has increased only slowly, improving from 25 % to 27.8 % in the last 25 years [6, 7]. This is mainly because single junction silicon solar cells are already approaching their practical limit of around 29 % (the detailed balance limit is 33.7 % [8], but accounting for Auger recombination, the practical limit is around 29 % [9, 10]). However, within the last 16 years, a new research field has been developing, focusing on metal halide perovskite solar cells. First utilized by Kojima et al. in 2009 [11], the efficiency of metal halide perovskite solar cells has increased from 3.8 % in 2009 to 26.7 % in 2024 [11, 12]. This is only 1.1 percentage points below the most efficient silicon solar cells [12]. Additionally, in perovskite-silicon tandem solar cells, the efficiency has reached 34.6 % in 2024, which is already 0.9 percentage points above the detailed

1

balance limit of single junction solar cells (33.7 %). This rapid increase in efficiency illustrates that perovskite solar cells can be a key technology to increase the global solar energy capacity. However, compared to silicon solar cells, which are stable for more than 20 years, perovskite solar cells already lose significant parts of their efficiency after thousands of hours [13, 14].

1.2 Perovskite Solar Cells

The first report of solar cells based on metal halide perovskites was released in 2009 by Kojima et al. [11]. The typical device stack of a perovskite solar cell is shown in Figure 1.1(a). It consists of the perovskite absorber layer, the hole and electron transport layers, and the anode and cathode.

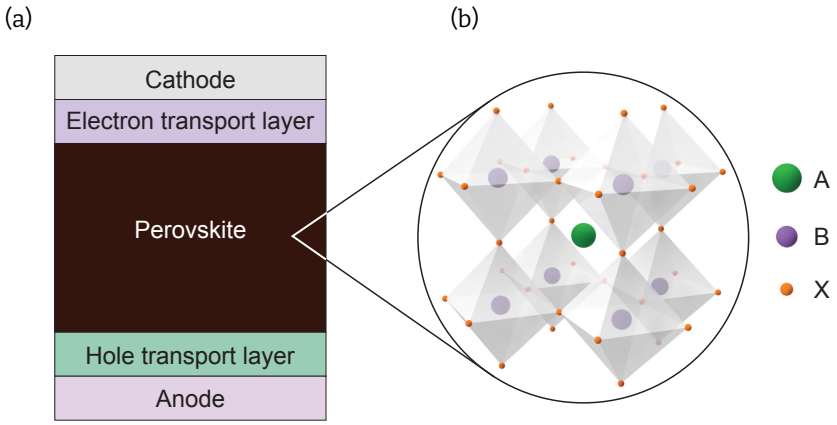

Figure 1.1: (a) Illustration of the device stack of a typical perovskite solar cell. (b) Perovskite ABX_3 crystal structure.

The term *perovskite* generally describes a crystal structure of the form ABX_3, shown in Figure 1.1(b). In metal halide perovskites, the A site is occupied by organic or inorganic cations like methylammonium (MA), formamidinium (FA), or cesium (Cs), the B site is occupied by metal cations like lead (Pb) or tin (Sn), and the X site is occupied by halides like iodide (I), bromide (Br), or chloride (Cl). By combining different A-site cations and halides, the structural properties of metal-halide perovskites can be altered. It has, for example, been shown that alloying MA with FA stabilizes the photoactive phase of the otherwise unstable $FAPbI_3$, leading to a higher short-circuit current density because of the more ideal bandgap of $FAPbI_3$ compared to $MAPbI_3$ [15]. Changing the X-site halide ion has a large effect on the absorption and stability of the perovskite. For example, $MAPb(X_nY_{1-n})_3$ has been shown to cover a bandgap range of 1.61 eV from 3.17 eV

for $MAPbCl_3$ through 2.23 eV for $MAPbBr_3$ to 1.56 eV for $MAPbI_3$ [16, 17]. Substituting Pb with Sn can further lower the bandgap, resulting in a bandgap of 1.36 eV, close to the optimal bandgap for single junction solar cells (1.34 eV) [18]. Next to the compositional freedom, metal halide perovskites have some properties that make them ideal candidates for absorber layers in solar cells. Metal halide perovskites show strong optical absorption near the band edge [19]. Furthermore, diffusion lengths of electronic carriers of hundreds of nanometers to micrometers in thin films and hundreds of micrometers in single crystals have been reported [20–22]. These long diffusion coefficients can be explained by high electronic mobilities [23], and long charge carrier lifetimes [24–26]. To facilitate an efficient and selective extraction of photogenerated charge carriers from the perovskite absorber, charge transport layers are utilized in perovskite solar cells, as shown in Figure 1.1(a). Some popular hole transport layers (HTLs) include thin organic molecules like PTAA or self-assembling monolayers like 2PACz or MeO-2PACz due to low observed losses at the perovskite/HTL interface [27, 28]. For the electron transport layers, fullerene derivatives like C_{60} or PCBM are common choices due to good energetic alignment with the perovskites and efficient charge extraction [29].

1.3 Mobile Ions in Metal Halide Perovskites

1.3.1 Ionic Defects

The bond nature in metal halide perovskites is partially ionic [30, 31]. Compared to covalent bonds, present in semiconductors like silicon or GaAs, ionic crystals are softer and, therefore, more deformable. Ionic bonds can easily break, and ions can leave their position in the crystal to form point defects like vacancies, interstitials, or anti-sites [32]. A defect pair consisting of a vacancy and an interstitial, e.g., a halide vacancy V_X^+ and a halide interstitial X_I^-, is also called a Frenkel defect (see Figure 1.2(b)). In contrast, Schottky defects describe paired defects of a cation vacancy and an anion vacancy, e.g., a A-site cation vacancy V_A^- and a halide vacancy V_X^+ (see Figure 1.2(c)) [33, 34]. In metal halide perovskites, various point defects can form due to their relatively low formation energies. For example, formation energies of below 0.1 eV have been calculated for the formation of both Frenkel and Schottky-type defects in $MAPbI_3$ [35, 36]. It has further been shown that most of the point defects in $MAPbI_3$ are shallow [37], which is consistent with experimentally observed shallow traps [26, 38].

After creating ionic defects, these ions can undergo temperature-activated migration through the perovskite lattice. The migration occurs via hopping of the ionic defects from one lattice site to another. The ionic conductivity σ_{ion} is dependent on the ionic

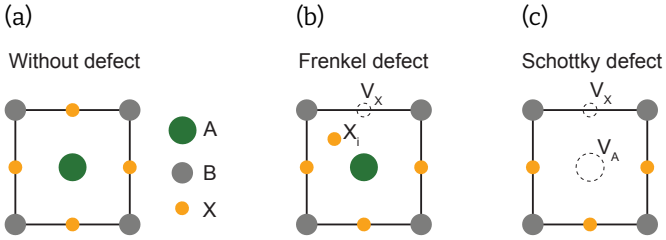

Figure 1.2: Illustration of a crystal lattice (a) without a defect, (b) with a Frenkel defect, and (c) with a Schottky defect.

mobility μ_{ion} and the density of mobile ions N_{ion}:

$$\sigma_{\text{ion}} = q\mu_{\text{ion}}N_{\text{ion}} \tag{1.1}$$

with the charge q. The ionic mobility μ_{ion} can be expressed in terms of the diffusion coefficient D_{ion} via the Nernst-Einstein relation:

$$\mu_{\text{ion}} = \frac{qD_{\text{ion}}}{k_{\text{B}}T} \tag{1.2}$$

with the Boltzmann constant k_{B}, and the temperature T. The diffusion coefficient follows a temperature-activated Arrhenius relationship with activation energy E_{a}, and a prefactor D_0 according to [36, 39, 40]:

$$D = \frac{v_0 d^2}{6} e^{-\frac{\Delta G}{k_{\text{B}}T}} = D_0 e^{-\frac{E_{\text{a}}}{k_{\text{B}}T}} \tag{1.3}$$

where v_0 is the attempt-to-escape frequency, d is the jump distance, and ΔG is the change in Gibbs' free energy [36].

In metal halide perovskites, ion migration can occur through either vacancies or interstitials. In vacancy-mediated migration, ions move through the perovskite via neighboring vacancies, as illustrated in Figure 1.3(a)-(c) for the A, B, and X-site ions [40]. Interstitials of, for example, halides, move through the crystal by hopping and form Pb-halide-Pb bridges [36], shown in Figure 1.3(d).

A body of work exists focusing on determining the dominant migrating species. Eames et al. computationally predicted via first-principles calculations that vacancy-mediated iodide migration V_I^+ has the lowest activation energy of 0.58 eV in $MAPbI_3$, followed by the migration of methylammonium vacancies V_{MA}^- (0.84 eV) and lead vacancies V_{Pb}^{2+} (2.31 eV) [41]. Other studies have also predicted that vacancy-mediated halide migration has the lowest activation energy, followed by migration of the A-site cation and Pb [42, 43]. Therefore, when modeling mobile ions in this thesis,

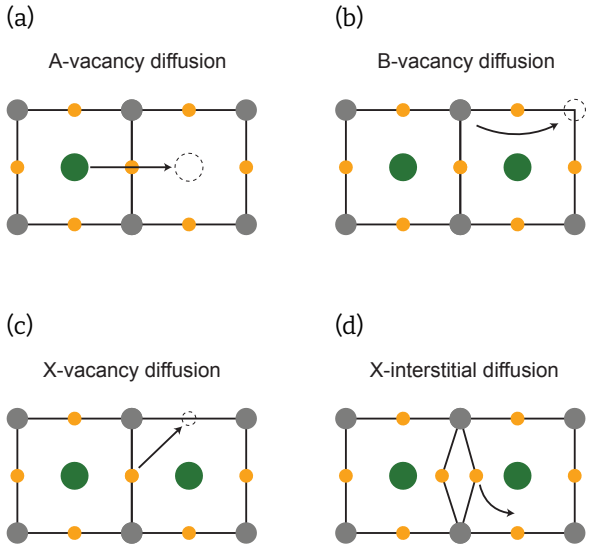

Figure 1.3: Migration paths of (a) A-site vacancies, (b) B-site vacancies, (c) X-site vacancies, and (d) X-interstitials.

we assume that halide vacancies dominate ion migration in the perovskite layer, as similarly done in other studies [44–46].

In a more macroscopic view, it has been found that ion migration along grain boundaries is preferred compared to migration through the perovskite grains [47, 48]. It has also been shown that light can increase the ionic conductivity [49, 50]. Additionally, Hoke et al. reported the formation of bromide and iodide-rich regions in mixed-halide perovskites after constantly illuminating the perovskite [51]. This light-induced phase segregation leads to an effective reduction of the band gap of the perovskite, resulting in a plateauing V_{oc} for higher-band gap perovskites [52]. Understanding and minimizing phase segregation has been a strong topic of interest in the perovskite field [53–55]. Next to light, electric fields applied to perovskite solar cells lead to the redistribution of mobile ions within the perovskite.

1.3.2 Ionic Field Screening

The current understanding in the perovskite field is that well-performing lead-based perovskites have low electronic carrier densities below $10^{12}\,\mathrm{cm}^{-3}$ [56]. This entails that, when sufficient mobile ions are present in the perovskite, these ions can alter the potential distribution and, consequently, the energy band diagram of the perovskite solar cell. Figure 1.4 illustrates this effect utilizing drift-diffusion simulations of a perovskite solar cell for two applied voltages of 0 V and the built-in voltage

1

V_{bi} in the first and second column, respectively. The rows correspond to different ion densities of 10^{15} cm^{-3} (few ions), $3 \cdot 10^{16}$ cm^{-3}, and 10^{18} cm^{-3} (many ions). At 0 V, mobile ions accumulate at the perovskite/CTL interfaces due to the built-in potential of the perovskite solar cell. This is, for example, illustrated in Figure 1.4(a) for low ion densities. Even though ions accumulate at the interfaces, their charge density is not high enough to alter the potential of the perovskite solar cell. Therefore, the conduction and valence band energy decreases linearly in the perovskite, as would be the case for a device without ions. When applying a forward bias to the device, mobile ions no longer accumulate at the interface, as illustrated in Figure 1.4(b). Because the ionic carriers are of opposite charge, they cancel out and do not impact the potential.

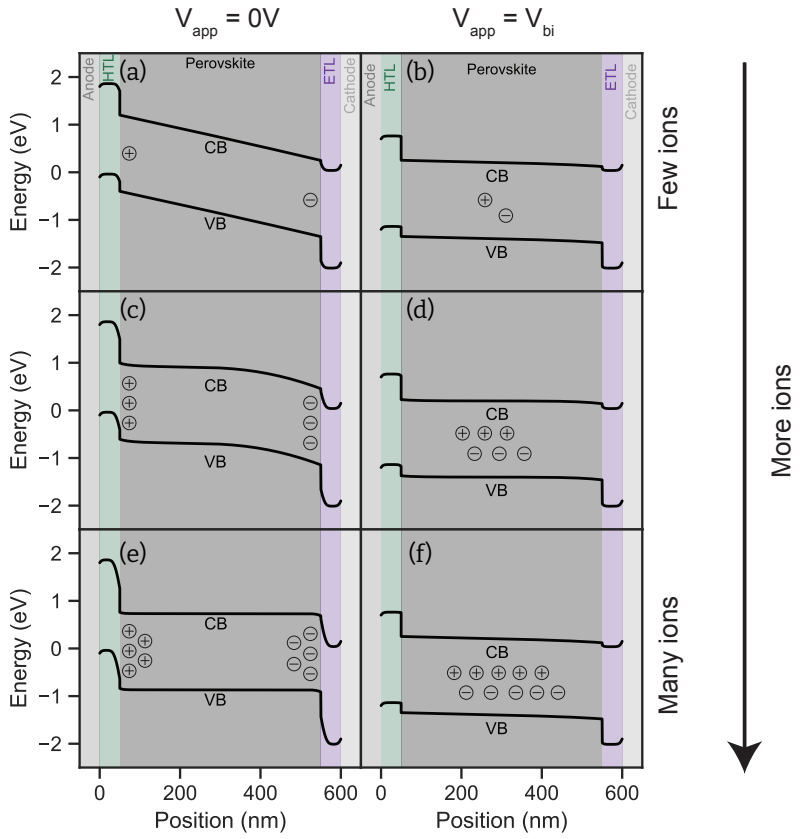

Figure 1.4: Simulated impact of mobile ions on the conduction band (CB) and valence band (VB) of a perovskite solar cell for three different ion densities and two different applied voltages. (a) and (b) low ion density, (c) and (d) medium ion density, (e) and (f) high ion density. The applied voltage is 0 V in the first column and V_{bi} in the second column. The circles indicate positively and negatively charged ions.

For a medium ion concentration in Figure 1.4(c) at 0 V, the ions start to impact the energetics of the conduction and valence band. Ions that accumulate at the perovskite/charge transport layer (CTL) interfaces introduce a significant potential drop. This potential drop occurs because 1) the potential drops in the ionic accumulation layers and 2) ions lead to a depletion of electronic carriers in the CTLs, increasing the potential drop in the depletion layers in the CTLs. The effect of mobile ions accumulating at the perovskite/CTL has been the focus of many studies and is known as ionic field screening [57, 58]. When V_{bi} is applied to the perovskite solar cell (see Figure 1.4(d)), the ions alter the energy band diagram less significantly, because not as many ions are accumulated at the perovskite/CTL interface. The energetics in this case are very similar to those in the case with few ions.

For a high ion density, the effects of ionic field screening become much more pronounced, as shown in Figure 1.4(e). At 0 V, most potential drops at the interface, leading to largely flat bands in the perovskite bulk. When V_{bi} is applied to the device and fewer ions are accumulated at the perovskite/CTL interfaces, the impact of ions is not significant, illustrated by similar energetics compared to the cases with fewer ions. This demonstrates that the impact of ions at 0 V on the potential and energetic distribution in perovskite solar cells is more pronounced than when forward bias is applied.

Ionic field screening can have a significant impact on the device performance in perovskite solar cells. A study by Thiesbrummel et al. showed that losses due to ionic-field screening can significantly reduce the J_{sc} and, consequently, the PCE of perovskite solar cells [57]. By carrying out JV measurement with different sweep speeds [57] while aging a device, they could attribute most efficiency losses to mobile ions, as shown in Figure 1.5(a). At slow scan speeds, mobile ions can accumulate the perovskite/CTL interface, reducing the efficiency of charge extraction by screening the electric field (similar to the high ion density case in Figure 1.4(d)) and reducing the J_{sc} in Figure 1.5(b). At high sweep speeds, the ions can not follow the potential change. Therefore, the bulk electric field is significantly higher (similar to the low ion density case in Figure 1.4(a)), facilitating efficient charge extraction. This effect has also been observed in other studies [58, 59].

Next to the impact on the J_{sc}, mobile ions have also been assigned to losses in the open-circuit voltage V_{oc}. Hart et al. showed that the distribution of mobile ions can significantly impact the surface recombination currents, resulting in differences of tens to hundreds of millivolts in V_{oc} [60]. They further suggested that ions can even be beneficial for the V_{oc} and efficiency because they decrease the sensitivity to band-misalignment in perovskite solar cells.

These different results illustrate that the impact of mobile ions on the device per-

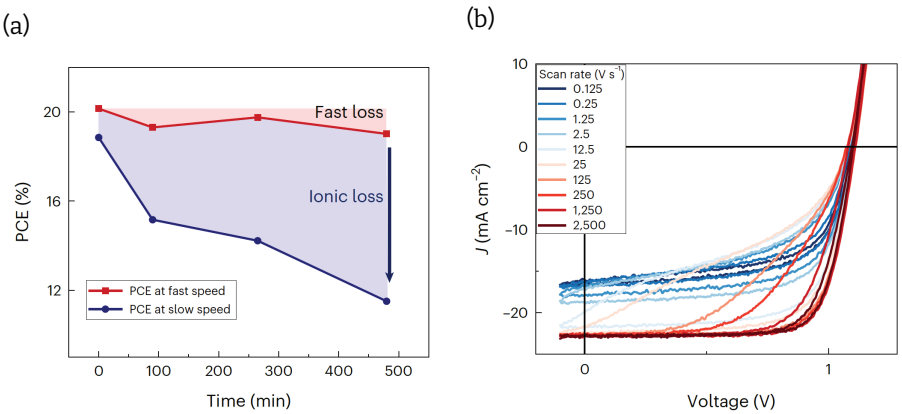

Figure 1.5: (a) PCE of a perovskite solar cell during aging, measured with fast and slow sweep speeds. (b) JV-measurements at different sweep speeds of an aged device. Reproduced from [57].

formance cannot be linked to a single loss process. Instead, how and to what extent mobile ions impact the efficiency is strongly dependent on other inherent device properties like the non-radiative recombination velocities, charge extraction efficiencies, energetic alignment between perovskite and CTLs, and mobilities in the perovskite and CTLs. These properties can significantly vary between devices with different perovskites and CTLs, resulting in various loss processes assigned to mobile ions.

1.4 Characterization of Mobile Ions

1.4.1 Qualitative Characterization

The characterization of mobile ions has been the focus of many studies, and various techniques have been applied to characterize them. Some techniques focus on the qualitative characterization of ions. Prominent examples include Kelvin-probe force microscopy (KPFM), Time-of-Flight secondary-ion mass spectroscopy (ToF-SIMS), and lateral photoluminescence (PL) measurements. For example, Weber et al. measured the redistribution of ions upon the application of voltage or light by conducting later KPFM measurements [47]. In ToF-SIMS, the position-dependent chemical composition of the perovskite can be studied by gradually sputtering ions off the surface. This technique has been applied to study the impact of degradation on the composition [61]. However, ToF-SIMS is prone to measurement artifacts due to its destructive nature [62].

Lateral PL measurements have been used to visualize the migration of mobile ions. This measurement is usually carried out on a device with lateral contacts. When a bias is applied to the lateral contacts, mobile ions redistribute within the perovskite. This can result in a change of the PL measurement, given that ions impact the recombination dynamics in the perovskite. One prominent work by Li et al. [63] is shown in Figure 1.6. They observed quenching of the PL starting at the positive electrode in Figure 1.6(a). Then, after tens of seconds, the quenching extended over most of the channel, as illustrated in Figure 1.6(b) and (c). They explain the quenched PL with an initial doping due to iodine interstitials in the high PL sections of the perovskite. Then, when applying the potential, iodine vacancies start drifting into this region, compensating the doping, which lowers the electronic carrier density and, consequently, the PL. Lateral PL measurements have shown quenching of the PL [63, 64], but also photo-brightening [65], which has both been attributed to the redistribution of mobile ions.

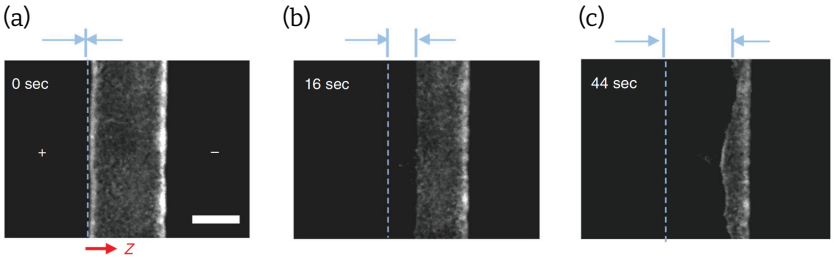

Figure 1.6: Spatially resolved photoluminescence measurement of a perovskite thin film (a) 0 s, (b) 16 s, and (c) 44 s after turning on a voltage. With increasing time, the photoluminescence gets quenched, resulting in a darker appearing channel in Figure (b) and (c). Reproduced from [63].

1.4.2 Electrical Measurements

Electrical measurement techniques build the foundation when characterizing complete perovskite solar cells, with the most important one being JV measurements to evaluate the efficiency. In 2014, Snaith et al. observed anomalous hysteresis in perovskite solar cells, where the efficiency was significantly dependent on the direction and speed of the voltage sweep, as shown in Figure 1.7 [66]. They and others proposed different mechanisms as possible explanations, among others, filling and emptying of traps at the interfaces during the sweeps, ferroelectric polarization impacting charge collection, and mobile ions [66, 67]. Since then, many studies have focused on explaining hysteresis in perovskite solar cells, with the most prominent explanation being mobile ions that impact recombination at the perovskite/CTL interfaces [68–70].

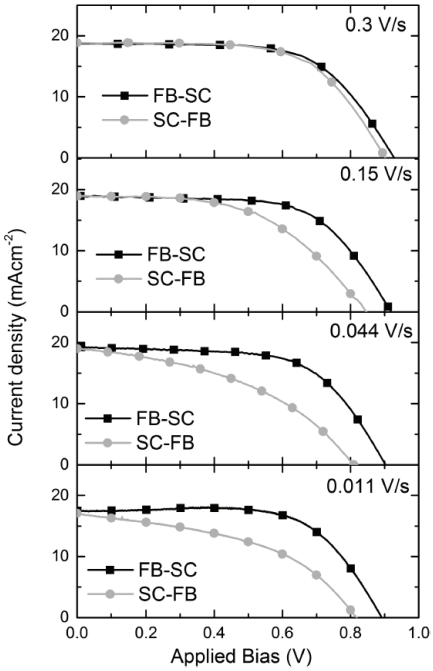

Figure 1.7: Current density vs. voltage measurements of a perovskite solar cell with different sweep speeds from short circuit (SC) to forward bias (FB) and back. The hysteresis is more pronounced for slow sweep speeds. Reprinted with permission from [66]. Copyright 2025 American Chemical Society.

Another popular subsection of electrical characterization is impedance spectroscopy. Impedance spectroscopy is a powerful technique that is based on exciting and probing different processes in the perovskite solar cell based on their characteristic times. The basics of impedance spectroscopy are shown in Figure 1.8. A small perturbation voltage is applied to the perovskite solar cell around a DC operating point, as illustrated in Figure 1.8(a). The voltage amplitude must be low enough to ensure a linear current response by the probed device. The voltage can be expressed in terms of the DC voltage V_{DC}, AC amplitude V_{AC}, and frequency $\omega = 2\pi f$:

$$V(t) = V_{\mathrm{DC}} + V_{\mathrm{AC}} e^{i\omega t} \tag{1.4}$$

where i is the imaginary unit. The current is measured, which also consists of a DC part I_{DC}, an AC amplitude I_{AC}, and has the same frequency ω. Additionally, the current can be phase-shifted by Φ compared to the voltage, as illustrated in Figure 1.8(a). In total, the current is then:

$$I(t) = I_{\mathrm{DC}} + I_{\mathrm{AC}} e^{i\Phi} e^{i\omega t} \tag{1.5}$$

With the applied voltage and the current response, the impedance can be calculated from the AC amplitudes:

$$Z = \frac{V_{\mathrm{AC}}}{I_{\mathrm{AC}}} e^{-i\Phi} = |Z| e^{-i\Phi} \tag{1.6}$$

The impedance can also be expressed in terms of its real and imaginary parts:

$$Z = \mathrm{Real}(Z) + i\,\mathrm{Imag}(Z) \tag{1.7}$$

which is illustrated in the complex plane in Figure 1.8(b). The amplitude and phase of the impedance depend on the response of the excited process. By varying the frequency of the perturbed voltage, different processes in perovskite solar cells can be excited. Then, the impedance is determined for each frequency, resulting in the Nyquist diagram, plotting the imaginary against the real part of the impedance for each frequency. Under illumination or bias, the Nyquist diagram consists of characteristic semicircles, which are illustrated in Figure 1.8(c).

A common analysis technique to extract information from impedance measurements is to fit equivalent circuit models to the semicircles. However, choosing the correct equivalent circuit is a difficult process. Over the years, many different equivalent circuits have been proposed to extract information from perovskite solar cells [71]. Alvarez et al. showed that multiple equivalent circuits can fit the same impedance spectrum. Only by combining impedance measurements with additional small-signal techniques were they able to ensure the correct choice of the equivalent circuit [72]. Another issue when using equivalent circuits is that there is no general connection between the components in the equivalent circuit and the physical process in the device. Often, the low-frequency response is connected to mobile ions. However, when carrying out impedance spectroscopy under illumination and/or bias, a convolution of ionic, electronic, and recombination processes is measured [73].

One way to probe mainly the ionic response of a perovskite solar cell is to measure in

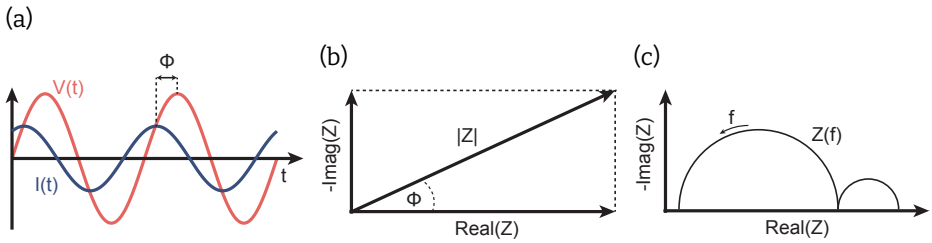

Figure 1.8: (a) Illustration of the time-dependent perturbed voltage and current response during an impedance measurement. (b) Complex plane representation of the impedance. (c) Nyquist plot of a frequency-dependent impedance measurement.

1

the dark and at 0 V DC bias. Then, it is helpful to express the impedance in terms of the conductance and capacitance:

$$\frac{1}{Z} = Y = G + i\omega C \tag{1.8}$$

where Y is the complex admittance, G is the conductance, and C is the capacitance. G is dependent on the in-phase processes of the perovskite, like recombination or electronic charge transport. Because the electronic carrier density in the dark at 0 V is low, G does not contain much information. We, therefore, focus mainly on the capacitance of the device, which can be calculated from the impedance:

$$C = \frac{1}{\omega}\mathrm{Imag}\left(\frac{1}{Z}\right) \tag{1.9}$$

In perovskite solar cells, capacitance frequency measurements have been applied to characterize mobile ions [73–75]. The advantage of capacitance frequency measurements in the dark at 0 V compared to measurements under bias and light is that we do not have a strong convolution of different processes. Figure 1.9(a) shows a sketch of a capacitance frequency spectrum. In perovskite solar cells, we generally observe a high-frequency plateau and an increase in the capacitance at lower frequencies. At lower frequencies, mobile ions can follow the perturbed electric field, leading to ionic polarization at the perovskite/CTL interface, as illustrated in Figure 1.9(b). This ultimately leads to the capacitance C_{ion} in Figure 1.9(a). At higher frequencies, mobile ions cannot follow the perturbed electric field. Therefore, the capacitance at higher frequencies, often called the geometrical capacitance C_{geo}, is just the series connection of the geometrical capacitances and/or depletion layers of the individual layers, as illustrated in Figure 1.9(c).

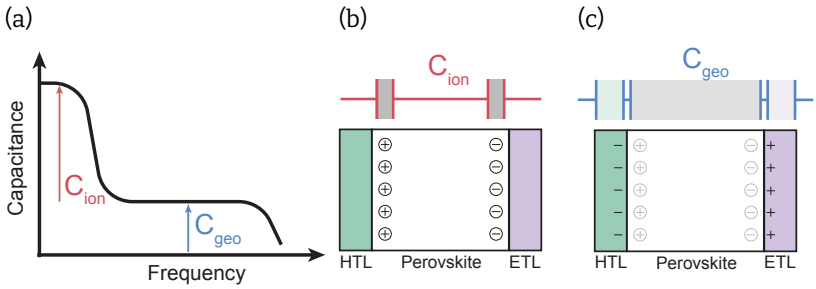

Figure 1.9: (a) Illustration of a capacitance frequency measurement. (b) shows the origin of the low-frequency capacitance C_{ion} due to ionic polarization. (c) illustrates the origin of the high-frequency geometrical capacitance C_{geo} in a perovskite device. The ions in the perovskite are transparent because they do not directly contribute to the capacitance.

Another method to study mobile ions is based on deep-level transient spectroscopy (DLTS), which was first introduced by Lang et al. to study traps in silicon semiconductors [76]. DLTS is based on filling traps in the semiconductor during a voltage pulse. Then, after removing the voltage pulse, electrons and holes are emitted back to the conduction and valence bands. This re-emission of electronic carriers alters the depletion layer capacitance in doped semiconductors. Therefore, measuring the change of the capacitance as a function of time and temperature contains information about the density of traps, whether the trap levels are close to the conduction or valence band, their capture cross section, and their activation energy [76]. To quantify mobile ions, Futscher et al. applied DLTS, also called transient ion drift (TID), to perovskite solar cells [77]. However, mobile ions cannot be treated in the same way as traps, and the device properties of perovskite solar cells significantly differ compared to p-n junctions in silicon semiconductors. Therefore, the interpretation of capacitance transients differs from the originally proposed one, as we will show in Chapter 2.

Our current understanding of capacitance transients is sketched in Figure 1.10. Figure 1.10(a) illustrates a capacitance transient after a voltage pulse is removed. For simplicity, we assume highly doped transport layers. During the voltage pulse, mobile ions diffuse away from the perovskite/CTL interfaces into the bulk, resulting in a homogeneous distribution of ions as illustrated in Figure 1.10(b). The capacitance is probed at high frequencies. The initial capacitance can then be approximated with the geometrical capacitance of the perovskite. Then, because of the built-in field E, mobile ions start to drift and accumulate at the perovskite/CTL interfaces. The accumulation results in a depletion of electronic carriers in the CTLs, as shown in Figure 1.10(c). This depletion of electronic carriers from the CTLs results in a decrease in the high-frequency capacitance, which is measured in Figure 1.10(a).

Another electrical measurement technique used numerous times to characterize

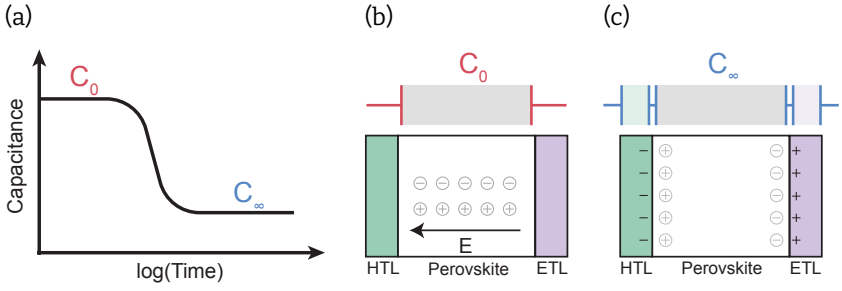

Figure 1.10: (a) Illustration of a capacitance transient measurement. (b) illustrates the origin of the initial capacitance C_0, when the ions are homogeneously distributed in the bulk. The ions in the perovskite are transparent because they do not directly contribute to the capacitance. (c) shows the origin of the capacitance C_∞ due to depletion of electronic carriers from the CTLs, caused by the accumulation of ions.

1

mobile ions in perovskite solar cells is current transient measurements [57, 78–80], also known as bias-assisted charge extraction. An illustration and a basic principle are shown in Figure 1.11. Similar to capacitance transient measurements, a voltage pulse is applied to the device, during which ions diffuse into the perovskite bulk. Then, the voltage pulse is removed. The built-in potential of the device leads to an electric field that drives mobile ions to the perovskite/CTL interface, leading to an initial current J_0, as shown in Figure 1.11(a) and (b). This current is dependent on the ionic current and the displacement current in the device. When no more ions remain in the bulk or enough ions are accumulated to screen the built-in potential (see Figure 1.11(c)), the current decreases, as illustrated in Figure 1.11(a).

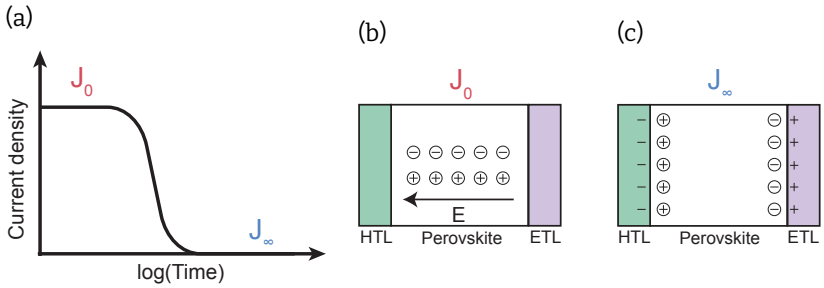

Figure 1.11: (a) Illustration of a current transient measurement. (b) illustrates the origin of the initial current J_0, when the ions are homogeneously distributed in the bulk. The built-in field E leads to an ionic current that drives mobile ions to the perovskite/CTL interfaces. Ultimately, the field is screened, as shown in (c), leading to a reduction of the current.

A variation of current transient measurements is the thermally activated ion current measurements (TAIC), which we will introduce in Chapter 6. In the TAIC technique, the device is cooled down during the applied voltage pulse, freezing mobile ions. Then, when slowly heating the device, ions drift to the perovskite/CTL interface, leading to a current. The advantage of TAIC is that the measurement allows for the extraction of the activation energy and distinguishes between different ionic species.

Generally, measurements in the time domain, like capacitance transients, current transients, and TAIC measurements, are well suited to characterize slow ionic migration processes that last seconds to hours. Resolving these processes in capacitance frequency measurements would require long measurement times because of the necessity of measuring and averaging multiple periods of the perturbed current response. In contrast, capacitance frequency measurements are well suited to measure faster ionic processes with characteristic times of milliseconds or lower, which can be challenging to capture with common source measure units, especially in the case of low currents.

1.5 Drift-Diffusion Simulations

Drift-diffusion simulations are an essential and powerful tool that has become increasingly important in the perovskite field. They allow the simulation of interactions between mobile electronic and ionic charge carriers, recombination processes, and the potential of perovskite solar cells. Drift-diffusion simulations have been used to study numerous electrical measurements like JV measurements with hysteresis [44, 81], space-charge limited current measurements [82], fast-hysteresis measurements [83], and impedance spectroscopy [73].
Drift-diffusion simulations are based on numerically solving the current continuity and Poisson equations. The Poisson equation describes the potential introduced by charges. In one dimension, it is defined as:

$$\frac{d^2\Phi}{dx^2} = -\frac{e}{\epsilon}(p - n + G) \tag{1.10}$$

where Φ is the potential, e is the elementary charge, p is the hole density, n is the electron density, and G are other charges, e.g., dopands or ions. The current continuity equation for electrons and holes in one dimension is defined as:

$$\frac{dn}{dt} = +\frac{1}{e}\frac{dj_\mathrm{n}}{dx} + g_\mathrm{n} - r_\mathrm{n} \tag{1.11}$$

$$\frac{dp}{dt} = -\frac{1}{e}\frac{dj_\mathrm{p}}{dx} + g_\mathrm{p} - r_p \tag{1.12}$$

where j_n and j_p are the electron and hole current densities, g_n and g_p are the electron and hole generation rates, and r_n and r_p are the recombination rates of electrons and holes. The current densities can be expressed in terms of drift and diffusion currents:

$$j_\mathrm{n} = en\mu_\mathrm{n}E + eD_\mathrm{n}\frac{dn}{dx} \tag{1.13}$$

$$j_\mathrm{p} = ep\mu_\mathrm{p}E - eD_\mathrm{p}\frac{dp}{dx} \tag{1.14}$$

where μ_n and μ_p are the electron and hole mobilities, E is the electric field, and D_n and D_p are the electron and hole diffusion coefficients. The diffusion coefficients relate to the mobility via the Einstein relation:

$$D_\mathrm{n,p} = \frac{\mu_\mathrm{n,p}k_\mathrm{B}T}{e} \tag{1.15}$$

where k_B is the Boltzmann constant and T is the temperature.

1.5.1 Generation and Recombination

1

The current continuity equations in Equations 1.11 and 1.12 depend on the generation and recombination terms g and r. The generation term accounts for the creation of electronic carriers by photo-absorption. The recombination term accounts for different recombination processes, which can be separated into radiative and non-radiative recombination processes:

$$r = r_{\mathrm{rad}} + r_{\mathrm{non-rad}} \tag{1.16}$$

where r_{rad} is the radiative recombination rate, and $r_{\mathrm{non-rad}}$ is the non-radiative recombination rate. The radiative recombination depends on both the electron and hole density as:

$$r_{\mathrm{rad}} = B\, n\, p \tag{1.17}$$

where B is the radiative recombination coefficient. The non-radiative recombination rate $r_{\mathrm{non-rad}}$ in perovskites is dominated by Shockley-Read-Hall recombination. Auger recombination can be neglected in cases of non-concentrated solar illumination [84]. The non-radiative recombination can then be expressed as [8]:

$$r_{\mathrm{non-rad}} = r_{\mathrm{SRH}} = \frac{np - n_{\mathrm{i}}^2}{\tau_{\mathrm{p}}(n + n_1) + \tau_{\mathrm{n}}(p + p_1)} \tag{1.18}$$

where n_{i} is the intrinsic carrier density, τ_{n} and τ_{p} are the electron and hole carrier lifetimes and n_1 and p_1 account for thermal emission from traps and are defined as:

$$n_1 = N_{0,\mathrm{CB}} e^{\frac{E_{\mathrm{t}} - E_{\mathrm{CB}}}{k_{\mathrm{B}} T}} \tag{1.19}$$

$$p_1 = N_{0,\mathrm{VB}} e^{\frac{E_{\mathrm{VB}} - E_{\mathrm{t}}}{k_{\mathrm{B}} T}} \tag{1.20}$$

where $N_{0,\mathrm{CB}}$ and $N_{0,\mathrm{VB}}$ are the effective density of states in the conduction and valence band, E_{CB} and E_{VB} are the conduction and valence band energies, and E_{t} is the energy level of the trap. For shallow traps, which have been shown to be dominant in perovskite solar cells [26], the trap level is close to either the conduction or valence band. Then, trapped electronic carriers from the conduction or valence band are likely to be emitted back into that band. This results in a lower non-radiative recombination rate compared to when the trap energy is in the center of the band gap, i.e., deep traps.

1.5.2 Mobile Ions in Drift-Diffusion Simulations

To account for mobile ions in drift-diffusion simulations, the Poisson and current continuity equations need to be adapted. In the Poisson equation, the constant G can be

adapted to also account for ions. G then becomes:

$$G = c - a \tag{1.21}$$

where c is the cation density and a is the anion density. In addition to electronic charges, the ions also need to be accounted for in a current continuity equation:

$$\frac{da}{dt} = +\frac{1}{e}\frac{dj_{\mathrm{a}}}{dx} \tag{1.22}$$

$$\frac{dc}{dt} = -\frac{1}{e}\frac{dj_{\mathrm{c}}}{dx} \tag{1.23}$$

Generally, the generation and recombination of mobile ions are omitted in drift-diffusion simulations. The ionic current depends on a drift and a diffusion term:

$$j_{\mathrm{a}} = en\mu_{\mathrm{a}}E + eD_{\mathrm{a}}\frac{da}{dx} \tag{1.24}$$

$$j_{\mathrm{c}} = ec\mu_{\mathrm{c}}E - eD_{\mathrm{c}}\frac{dc}{dx} \tag{1.25}$$

1.5.3 Solving the Semiconductor Equations

The semiconductor equations are coupled, meaning that the potential in the Poisson equation in Equation 1.10 depends on the charge densities, and the charge densities, in turn, depend on the potential via the current continuity equations in Equations 1.11, 1.12, 1.22, and 1.23. Therefore, the equations can only be solved numerically by iteratively solving the Poisson and continuity equations.
Multiple drift-diffusion solvers exist to simulate perovskite solar cells. These include SIMsalabim [85], IonMonger [86, 87], Driftfusion [88], and Setfos [89]. In this thesis, we will use Setfos because we require demanding simulation settings (e.g., voltage steps and simultaneous impedance calculation, large ranges of ion densities), and only Setfos could reliably solve the semiconductor equations under these conditions.

1.6 Outline of This Thesis

This thesis focuses on how electrical measurements can be utilized to characterize mobile ions in perovskite solar cells. In **Chapter 2**, we evaluate the established theory behind capacitance transient measurements. By combining drift-diffusion simulations and intensity-dependent capacitance transient measurements, we show that the polarity of mobile ions cannot be extracted from these measurements. We further propose that the direction of capacitance transients depends on which capacitance

is modulated by mobile ions. In **Chapter 3**, we then apply capacitance frequency, capacitance transient, and current transient measurements in combination with simulations to characterize mobile ions of a simple $MAPbI_3$ perovskite device without transport layers. In **Chapter 4** we illustrate that ionic field screening limits the density of mobile ions that can be determined with various electrical measurements. **Chapter 5** focuses on the derivation and application of a drift-diffusion approximation that allows the extraction of ionic properties from capacitance frequency, capacitance transient, and current transient measurements. Finally, in **Chapter 6**, we introduce the thermally activated ion current (TAIC) technique. A powerful measurement to characterize activation energy, diffusion coefficient, and, under certain conditions, the mobile ion density.

Bibliography

[1] International Energy Agency, *COP28 Tripling Renewable Capacity Pledge*, https://www.iea.org/reports/cop28-tripling-renewable-capacity-pledge, Accessed: 2025-04-17.

[2] International Renewable Energy Agency, *Renewable Capacity Statistics 2024*, https://www.irena.org/Publications/2024/Mar/Renewable-capacity-statistics-2024, Accessed: 2025-04-15.

[3] International Renewable Energy Agency, *Renewable Capacity Statistics 2025*, https://www.irena.org/Publications/2025/Mar/Renewable-capacity-statistics-2025, Accessed: 2025-04-15.

[4] Centraal Bureau voor de Statistiek, *Nearly Half the Electricity Produced in the Netherlands is Now Renewable*, https://www.cbs.nl/en-gb/news/2024/10/nearly-half-the-electricity-produced-in-the-netherlands-is-now-renewable, Accessed: 2025-04-15.

[5] International Energy Agency, *Renewables 2024 - Analysis and Forecasts to 2030*, https://www.iea.org/reports/renewables-2024, Accessed: 2025-04-15.

[6] National Renewable Energy Laboratory, *Best Research-Cell Efficiency Chart*, https://www2.nrel.gov/pv/cell-efficiency, Accessed: 2025-04-15.

[7] PV Magazine, *Longi Claims World's Highest Efficiency for Silicon Solar Cells*, https://www.pv-magazine.com/2025/04/14/longi-claims-worlds-highest-efficiency-for-silicon-solar-cells/, Accessed: 2025-05-14.

[8] W. Shockley and W. T. Read, "Statistics of the Recombinations of Holes and Electrons", *Physical Review*, vol. 87, no. 5, pp. 835–842, 1952.

[9] R. Swanson, "Approaching the 29% Limit Efficiency of Silicon Solar Cells", in *Conference Record of the Thirty-first IEEE Photovoltaic Specialists Conference, 2005.*, Lake buena Vista, FL, USA: IEEE, 2005, pp. 889–894.

[10] M. Kerr, P. Campbell, and A. Cuevas, "Lifetime and Efficiency Limits of Crystalline Silicon Solar Cells", in *Conference Record of the Twenty-Ninth IEEE Photovoltaic Specialists Conference, 2002.*, New Orleans, LA, USA: IEEE, 2002, pp. 438–441.

[11] A. Kojima, K. Teshima, Y. Shirai, and T. Miyasaka, "Organometal Halide Perovskites as Visible-Light Sensitizers for Photovoltaic Cells", *Journal of the American Chemical Society*, vol. 131, no. 17, pp. 6050–6051, 2009.

[12] M. A. Green *et al.*, "Solar Cell Efficiency Tables (Version 64)", *Progress in Photovoltaics: Research and Applications*, vol. 32, no. 7, pp. 425–441, 2024.

[13] Z. Shen *et al.*, "Efficient and Stable Perovskite Solar Cells with Regulated Depletion Region", *Nature Photonics*, vol. 18, no. 5, pp. 450–457, 2024.

[14] Y. Yang *et al.*, "Amidination of Ligands for Chemical and Field-Effect Passivation Stabilizes Perovskite Solar Cells", *Science*, vol. 386, no. 6724, pp. 898–902, 2024.

[15] C. Wang *et al.*, "Compositional and Morphological Engineering of Mixed Cation Perovskite Films for Highly Efficient Planar and Flexible Solar Cells With Reduced Hysteresis", *Nano Energy*, vol. 35, pp. 223–232, 2017.

[16] B. R. Sutherland and E. H. Sargent, "Perovskite Photonic Sources", *Nature Photonics*, vol. 10, no. 5, pp. 295–302, 2016.

[17] S. A. Kulkarni, T. Baikie, P. P. Boix, N. Yantara, N. Mathews, and S. Mhaisalkar, "Band-Gap Tuning of Lead Halide Perovskites Using a Sequential Deposition Process", *J. Mater. Chem. A*, vol. 2, no. 24, pp. 9221–9225, 2014.

[18] A. Filippetti *et al.*, "Fundamentals of Tin Iodide Perovskites: a Promising Route to Highly Efficient, Lead-Free Solar Cells", *Journal of Materials Chemistry A*, vol. 9, no. 19, pp. 11 812–11 826, 2021.

[19] J. S. Manser, J. A. Christians, and P. V. Kamat, "Intriguing Optoelectronic Properties of Metal Halide Perovskites", *Chemical Reviews*, vol. 116, no. 21, pp. 12 956–13 008, 2016.

[20] S. D. Stranks *et al.*, "Electron-Hole Diffusion Lengths Exceeding 1 Micrometer in an Organometal Trihalide Perovskite Absorber", *Science*, vol. 342, no. 6156, pp. 341–344, 2013.

[21] G. Xing *et al.*, "Long-Range Balanced Electron- and Hole-Transport Lengths in Organic-Inorganic CH_3 NH_3 PbI_3", *Science*, vol. 342, no. 6156, pp. 344–347, 2013.

[22] Q. Dong *et al.*, "Electron-Hole Diffusion Lengths > 175 μm in Solution-Grown CH_3 NH_3 PbI_3 Single Crystals", *Science*, vol. 347, no. 6225, pp. 967–970, 2015.

[23] L. M. Herz, "Charge-Carrier Mobilities in Metal Halide Perovskites: Fundamental Mechanisms and Limits", *ACS Energy Letters*, vol. 2, no. 7, pp. 1539–1548, 2017.

[24] F. Staub *et al.*, "Beyond Bulk Lifetimes: Insights into Lead Halide Perovskite Films from Time-Resolved Photoluminescence", *Physical Review Applied*, vol. 6, no. 4, p. 044 017, 2016.

[25] Y. Bi, E. M. Hutter, Y. Fang, Q. Dong, J. Huang, and T. J. Savenije, "Charge Carrier Lifetimes Exceeding 15 μs in Methylammonium Lead Iodide Single Crystals", *The Journal of Physical Chemistry Letters*, vol. 7, no. 5, pp. 923–928, 2016.

[26] Y. Yuan *et al.*, "Shallow Defects and Variable Photoluminescence Decay Times up to 280 μs in Triple-Cation Perovskites", *Nature Materials*, vol. 23, no. 3, pp. 391–397, 2024.

[27] M. Stolterfoht *et al.*, "The Impact of Energy Alignment and Interfacial Recombination on the Internal and External Open-Circuit Voltage of Perovskite Solar Cells", *Energy & Environmental Science*, vol. 12, no. 9, pp. 2778–2788, 2019.

[28] A. Al-Ashouri *et al.*, "Conformal Monolayer Contacts With Lossless Interfaces for Perovskite Single Junction and Monolithic Tandem Solar Cells", *Energy & Environmental Science*, vol. 12, no. 11, pp. 3356–3369, 2019.

[29] A. A. Said, J. Xie, and Q. Zhang, "Recent Progress in Organic Electron Transport Materials in Inverted Perovskite Solar Cells", *Small*, vol. 15, no. 27, p. 1 900 854, 2019.

[30] M. Wuttig *et al.*, "Halide Perovskites: Advanced Photovoltaic Materials Empowered by a Unique Bonding Mechanism", *Advanced Functional Materials*, vol. 32, no. 2, p. 2 110 166, 2022.

[31] A. Walsh, "Principles of Chemical Bonding and Band Gap Engineering in Hybrid Organic–Inorganic Halide Perovskites", *The Journal of Physical Chemistry C*, vol. 119, no. 11, pp. 5755–5760, 2015.

[32] N. Li, Y. Jia, Y. Guo, and N. Zhao, "Ion Migration in Perovskite Light-Emitting Diodes: Mechanism, Characterizations, and Material and Device Engineering", *Advanced Materials*, vol. 34, no. 19, p. 2 108 102, 2022.

[33] D. Moia and J. Maier, "Ion Transport, Defect Chemistry, and the Device Physics of Hybrid Perovskite Solar Cells", *ACS Energy Letters*, vol. 6, no. 4, pp. 1566–1576, 2021.

[34] L. Zuo, Z. Li, and H. Chen, "Ion Migration and Accumulation in Halide Perovskite Solar Cells †", *Chinese Journal of Chemistry*, vol. 41, no. 7, pp. 861–876, 2023.

[35] A. Walsh, D. O. Scanlon, S. Chen, X. G. Gong, and S.-H. Wei, "Self-Regulation Mechanism for Charged Point Defects in Hybrid Halide Perovskites", *Angewandte Chemie International Edition*, vol. 54, no. 6, pp. 1791–1794, 2015.

[36] D. Meggiolaro, E. Mosconi, and F. De Angelis, "Formation of Surface Defects Dominates Ion Migration in Lead-Halide Perovskites", *ACS Energy Letters*, vol. 4, no. 3, pp. 779–785, 2019.

[37] W.-J. Yin, T. Shi, and Y. Yan, "Unusual Defect Physics in $CH_3NH_3PbI_3$ Perovskite Solar Cell Absorber", *Applied Physics Letters*, vol. 104, no. 6, p. 063 903, 2014.

[38] L. Krückemeier, B. Krogmeier, Z. Liu, U. Rau, and T. Kirchartz, "Understanding Transient Photoluminescence in Halide Perovskite Layer Stacks and Solar Cells", *Advanced Energy Materials*, vol. 11, no. 19, p. 2 003 489, 2021.

[39] M. H. Futscher and J. V. Milić, "Mixed Conductivity of Hybrid Halide Perovskites: Emerging Opportunities and Challenges", *Frontiers in Energy Research*, vol. 9, p. 629 074, 2021.

[40] A. Walsh and S. D. Stranks, "Taking Control of Ion Transport in Halide Perovskite Solar Cells", *ACS Energy Letters*, vol. 3, no. 8, pp. 1983–1990, 2018.

[41] C. Eames, J. M. Frost, P. R. F. Barnes, B. C. O'Regan, A. Walsh, and M. S. Islam, "Ionic Transport in Hybrid Lead Iodide Perovskite Solar Cells", *Nature Communications*, vol. 6, no. 1, p. 7497, 2015.

[42] J. M. Azpiroz, E. Mosconi, J. Bisquert, and F. De Angelis, "Defect Migration in Methylammonium Lead Iodide and Its Role in Perovskite Solar Cell Operation", *Energy & Environmental Science*, vol. 8, no. 7, pp. 2118–2127, 2015.

[43] J. Haruyama, K. Sodeyama, L. Han, and Y. Tateyama, "First-Principles Study of Ion Diffusion in Perovskite Solar Cell Sensitizers", *Journal of the American Chemical Society*, vol. 137, no. 32, pp. 10 048–10 051, 2015.

[44] G. Richardson *et al.*, "Can Slow-Moving Ions Explain Hysteresis in the Current–Voltage Curves of Perovskite Solar Cells?", *Energy & Environmental Science*, vol. 9, no. 4, pp. 1476–1485, 2016.

[45] J. Diekmann *et al.*, "Determination of Mobile Ion Densities in Halide Perovskites via Low-Frequency Capacitance and Charge Extraction Techniques", *The Journal of Physical Chemistry Letters*, vol. 14, no. 18, pp. 4200–4210, 2023.

[46] L. Bertoluzzi *et al.*, "Mobile Ion Concentration Measurement and Open-Access Band Diagram Simulation Platform for Halide Perovskite Solar Cells", *Joule*, vol. 4, no. 1, pp. 109–127, 2020.

[47] S. A. L. Weber *et al.*, "How the Formation of Interfacial Charge Causes Hysteresis in Perovskite Solar Cells", *Energy & Environmental Science*, vol. 11, no. 9, pp. 2404–2413, 2018.

[48] L. McGovern, I. Koschany, G. Grimaldi, L. A. Muscarella, and B. Ehrler, "Grain Size Influences Activation Energy and Migration Pathways in $MAPbBr_3$ Perovskite Solar Cells", *The Journal of Physical Chemistry Letters*, vol. 12, no. 9, pp. 2423–2428, 2021.

[49] J. Xing, Q. Wang, Q. Dong, Y. Yuan, Y. Fang, and J. Huang, "Ultrafast Ion Migration in Hybrid Perovskite Polycrystalline Thin Films under Light and Suppression in Single Crystals", *Physical Chemistry Chemical Physics*, vol. 18, no. 44, pp. 30 484–30 490, 2016.

[50] T.-Y. Yang, G. Gregori, N. Pellet, M. Grätzel, and J. Maier, "The Significance of Ion Conduction in a Hybrid Organic–Inorganic Lead-Iodide-Based Perovskite Photosensitizer", *Angewandte Chemie International Edition*, vol. 54, no. 27, pp. 7905–7910, 2015.

[51] E. T. Hoke, D. J. Slotcavage, E. R. Dohner, A. R. Bowring, H. I. Karunadasa, and M. D. McGehee, "Reversible Photo-Induced Trap Formation in Mixed-Halide Hybrid Perovskites for Photovoltaics", *Chemical Science*, vol. 6, no. 1, pp. 613–617, 2015.

[52] Y. Guo, X. Yin, J. Liu, and W. Que, "Focusing on Mixed-Halide Br-Rich Perovskite Solar Cells: An Inevitable Open-Circuit Voltage Deficit Derived From Photoinduced Halide Segregation?", *Matter*, vol. 5, no. 7, pp. 2015–2030, 2022.

[53] S. J. Yoon, M. Kuno, and P. V. Kamat, "*Shift Happens* . How Halide Ion Defects Influence Photoinduced Segregation in Mixed Halide Perovskites", *ACS Energy Letters*, vol. 2, no. 7, pp. 1507–1514, 2017.

[54] K. Datta *et al.*, "Effect of Light-Induced Halide Segregation on the Performance of Mixed-Halide Perovskite Solar Cells", *ACS Applied Energy Materials*, vol. 4, no. 7, pp. 6650–6658, 2021.

[55] A. J. Knight, J. B. Patel, H. J. Snaith, M. B. Johnston, and L. M. Herz, "Trap States, Electric Fields, and Phase Segregation in Mixed-Halide Perovskite Photovoltaic Devices", *Advanced Energy Materials*, vol. 10, no. 9, p. 1 903 488, 2020.

[56] F. Peña-Camargo *et al.*, "Revealing the Doping Density in Perovskite Solar Cells and Its Impact on Device Performance", *Applied Physics Reviews*, vol. 9, no. 2, p. 021 409, 2022.

[57] J. Thiesbrummel *et al.*, "Ion-Induced Field Screening as a Dominant Factor in Perovskite Solar Cell Operational Stability", *Nature Energy*, vol. 9, no. 6, pp. 664–676, 2024.

[58] S. Shah *et al.*, "Impact of Ion Migration on the Performance and Stability of Perovskite-Based Tandem Solar Cells", *Advanced Energy Materials*, vol. 14, no. 48, p. 2 400 720, 2024.

[59] W. Xu *et al.*, "Impact of Interface Energetic Alignment and Mobile Ions on Charge Carrier Accumulation and Extraction in p-i-n Perovskite Solar Cells", *Advanced Energy Materials*, vol. 13, no. 36, p. 2 301 102, 2023.

[60] L. J. F. Hart *et al.*, "More Is Different: Mobile Ions Improve the Design Tolerances of Perovskite Solar Cells", *Energy & Environmental Science*, vol. 17, no. 19, pp. 7107–7118, 2024.

[61] S. P. Harvey, Z. Li, J. A. Christians, K. Zhu, J. M. Luther, and J. J. Berry, "Probing Perovskite Inhomogeneity beyond the Surface: TOF-SIMS Analysis of Halide Perovskite Photovoltaic Devices", *ACS Applied Materials & Interfaces*, vol. 10, no. 34, pp. 28 541–28 552, 2018.

[62] S. P. Harvey, F. Zhang, A. Palmstrom, J. M. Luther, K. Zhu, and J. J. Berry, "Mitigating Measurement Artifacts in TOF-SIMS Analysis of Perovskite Solar Cells", *ACS Applied Materials & Interfaces*, vol. 11, no. 34, pp. 30 911–30 918, 2019.

[63] C. Li, A. Guerrero, S. Huettner, and J. Bisquert, "Unravelling the Role of Vacancies in Lead Halide Perovskite Through Electrical Switching of Photoluminescence", *Nature Communications*, vol. 9, no. 1, p. 5113, 2018.

[64] X. Deng *et al.*, "Electric Field Induced Reversible and Irreversible Photoluminescence Responses in Methylammonium Lead Iodide Perovskite", *Journal of Materials Chemistry C*, vol. 4, no. 38, pp. 9060–9068, 2016.

[65] S. P. Senanayak *et al.*, "A General Approach for Hysteresis-Free, Operationally Stable Metal Halide Perovskite Field-Effect Transistors", *Science Advances*, vol. 6, no. 15, eaaz4948, 2020.

[66] H. J. Snaith *et al.*, "Anomalous Hysteresis in Perovskite Solar Cells", *The Journal of Physical Chemistry Letters*, vol. 5, no. 9, pp. 1511–1515, 2014.

[67] B. Chen, M. Yang, S. Priya, and K. Zhu, "Origin of JV Hysteresis in Perovskite Solar Cells", *The Journal of Physical Chemistry Letters*, vol. 7, no. 5, pp. 905–917, 2016.

[68] D. A. Jacobs *et al.*, "Hysteresis Phenomena in Perovskite Solar Cells: The Many and Varied Effects of Ionic Accumulation", *Physical Chemistry Chemical Physics*, vol. 19, no. 4, pp. 3094–3103, 2017.

[69] G. Richardson *et al.*, "Can Slow-Moving Ions Explain Hysteresis in the Current–Voltage Curves of Perovskite Solar Cells?", *Energy & Environmental Science*, vol. 9, no. 4, pp. 1476–1485, 2016.

[70] S. Van Reenen, M. Kemerink, and H. J. Snaith, "Modeling Anomalous Hysteresis in Perovskite Solar Cells", *The Journal of Physical Chemistry Letters*, vol. 6, no. 19, pp. 3808–3814, 2015.

[71] W. Clarke, G. Richardson, and P. Cameron, "Understanding the Full Zoo of Perovskite Solar Cell Impedance Spectra with the Standard Drift-Diffusion Model", *Advanced Energy Materials*, vol. 14, no. 32, p. 2 400 955, 2024.

[72] A. O. Alvarez, S. Ravishankar, and F. Fabregat-Santiago, "Combining Modulated Techniques for the Analysis of Photosensitive Devices", *Small Methods*, vol. 5, no. 10, p. 2 100 661, 2021.

[73] D. A. Jacobs *et al.*, "The Two Faces of Capacitance: New Interpretations for Electrical Impedance Measurements of Perovskite Solar Cells and Their Relation to Hysteresis", *Journal of Applied Physics*, vol. 124, no. 22, p. 225 702, 2018.

[74] C. Messmer *et al.*, "Understanding Ion-Related Performance Losses in Perovskite-Based Solar Cells by Capacitance Measurements and Simulation", *Solar RRL*, vol. 8, no. 24, p. 2 400 630, 2024.

[75] R. A. Awni *et al.*, "Influence of Charge Transport Layers on Capacitance Measured in Halide Perovskite Solar Cells", *Joule*, vol. 4, no. 3, pp. 644–657, 2020.

[76] D. V. Lang, "Deep-Level Transient Spectroscopy: A New Method to Characterize Traps in Semiconductors", *Journal of Applied Physics*, vol. 45, no. 7, pp. 3023–3032, 1974.

[77] M. H. Futscher, M. K. Gangishetty, D. N. Congreve, and B. Ehrler, "Quantifying Mobile Ions and Electronic Defects in Perovskite-Based Devices with Temperature-Dependent Capacitance Measurements: Frequency vs Time Domain", *The Journal of Chemical Physics*, vol. 152, no. 4, p. 044 202, 2020.

[78] A. O. Alvarez *et al.*, "Ionic Field Screening in $MAPbBr_3$ Crystals Revealed from Remnant Sensitivity in X-ray Detection", *ACS Physical Chemistry Au*, vol. 3, no. 4, pp. 386–393, 2023.

[79] A. O. Alvarez *et al.*, "Ion Migration and Space-Charge Zones in Metal Halide Perovskites Through Short-Circuit Transient Current and Numerical Simulations", *Advanced Electronic Materials*, vol. 10, no. 11, p. 2 400 241, 2024.

[80] M. Diethelm *et al.*, "Probing Ionic Conductivity and Electric Field Screening in Perovskite Solar Cells: a Novel Exploration Through Ion Drift Currents", *Energy & Environmental Science*, vol. 18, no. 3, pp. 1385–1397, 2025.

[81] D. A. Jacobs *et al.*, "Hysteresis Phenomena in Perovskite Solar Cells: the Many and Varied Effects of Ionic Accumulation", *Physical Chemistry Chemical Physics*, vol. 19, no. 4, pp. 3094–3103, 2017.

[82] E. A. Duijnstee, J. M. Ball, V. M. Le Corre, L. J. A. Koster, H. J. Snaith, and J. Lim, "Toward Understanding Space-Charge Limited Current Measurements on Metal Halide Perovskites", *ACS Energy Letters*, vol. 5, no. 2, pp. 376–384, 2020.

[83] V. M. Le Corre *et al.*, "Quantification of Efficiency Losses Due to Mobile Ions in Perovskite Solar Cells via Fast Hysteresis Measurements", *Solar RRL*, vol. 6, no. 4, p. 2 100 772, 2022.

[84] W. Tress, "Perovskite Solar Cells on the Way to Their Radiative Efficiency Limit – Insights Into a Success Story of High Open-Circuit Voltage and Low Recombination", *Advanced Energy Materials*, vol. 7, no. 14, p. 1 602 358, 2017.

[85] M. Koopmans, V. Corre, and L. Koster, "SIMsalabim: An Open-Source Drift-Diffusion Simulator for Semiconductor Devices", *Journal of Open Source Software*, vol. 7, no. 70, p. 3727, 2022.

[86] W. Clarke, L. J. Bennett, Y. Grudeva, J. M. Foster, G. Richardson, and N. E. Courtier, "IonMonger 2.0: Software for Free, Fast and Versatile Simulation of Current, Voltage and Impedance Response of Planar Perovskite Solar Cells", *Journal of Computational Electronics*, vol. 22, no. 1, pp. 364–382, 2023.

[87] N. E. Courtier, J. M. Cave, A. B. Walker, G. Richardson, and J. M. Foster, "IonMonger: a Free and Fast Planar Perovskite Solar Cell Simulator With Coupled Ion Vacancy and Charge Carrier Dynamics", *Journal of Computational Electronics*, vol. 18, no. 4, pp. 1435–1449, 2019.

[88] P. Calado, I. Gelmetti, B. Hilton, M. Azzouzi, J. Nelson, and P. R. F. Barnes, "Driftfusion: An Open Source Code for Simulating Ordered Semiconductor Devices with Mixed Ionic-Electronic Conducting Materials in One Dimension", *Journal of Computational Electronics*, vol. 21, no. 4, pp. 960–991, 2022.

[89] *Setfos Simulation Software*, `https://www.fluxim.com/setfos-intro`, Accessed: 2025-04-15.

2

Impact of Mobile Ions on Transient Capacitance Measurements

Abstract

Mitigating the migration of mobile ions within perovskite solar cells is a crucial step on the way to improving their stability. In the past, transient capacitance measurements have been applied to extract information about mobile ions, including their activation energy, diffusion coefficient, density, and polarity. However, in this work, we show that the interpretation of capacitance transients is more complex than originally proposed because of the intrinsic nature of the perovskite and the contributions of charge transport layers to the capacitance. Using drift-diffusion simulations and light intensity-dependent capacitance transient measurements we show that the direction of capacitance transients is not linked to the polarity of the migrating species. Instead, the direction of the transients is linked to the layer of the cell that dominates the capacitance modulation. This work illustrates that transport layers can be crucial for the capacitance and impedance response of perovskite solar cells, and therefore for characterizing mobile ions in perovskites.

Authors: Moritz C. Schmidt, Emilio Gutierrez-Partida, Martin Stolterfoht, and Bruno Ehrler

Published in: PRX Energy, Volume: 2, Issue: 4, Pages: 043011(01-10), November 2023

https://doi.org/10.1103/PRXEnergy.2.043011

2.1 Introduction

Even though the efficiency of perovskite solar cells (PSCs) has increased significantly to 26.7 % in 2024 [1], their commercialization is still hindered by their poor stability, which has been attributed to the migration of mobile ions in the perovskite layer [2]. Thus, in order to improve the stability of PSCs, significant efforts have been made to mitigate ion migration [3–5]. Based on calculations of defect formation energies, it has often been suggested that vacancy-mediated migration of iodide I^- and methylammonium MA^+ contribute to ion migration in methylammonium lead triiodide ($MAPbI_3$), where iodide vacancies V_I^+ generally show an activation energy around 0.25 – 0.4 eV lower than methylammonium vacancies V_{MA}^- [6–8]. Experimentally, a variety of characterization techniques have been applied to understand the formation and migration of mobile ions. Some of these techniques focus on qualitatively understanding which mobile ions are present in the perovskite. These techniques include Time-of-Flight Secondary Ion Mass Spectrometry [9, 10], photothermal induced resonance microscopy [11], and Kelvin probe force microscopy [12]. Other techniques focus on quantifying the density of mobile ions, their activation energy, or diffusion coefficient. These include electrical measurements like impedance spectroscopy [13], bias-assisted charge extraction [2], and ionic conductivity measurements [14, 15].

One popular technique that has been applied to quantify the density, diffusion coefficient, activation energy, and polarity of mobile ions is transient ion drift (TID) [16–20]. TID is closely related to impedance-based techniques and relies on measuring capacitance transients after an applied voltage pulse is released. The capacitance is modulated by mobile ions drifting within the perovskite layer, which allows measuring the properties of these ions. The physical model behind TID is typically based on a few core assumptions, namely that the perovskite has a high doping density, that the ion density is much smaller than the doping density, and that charge transport layers (CTLs) do not significantly contribute to the capacitance transients. Additionally, the direction of the capacitance transients was directly related to the polarity of ionic species, meaning that decreasing capacitance transients (for p-doped perovskites) were assigned to mobile anions (e.g. mobile I_i^-, Br_i^-), and increasing capacitance transients were assigned to mobile cations (e.g. mobile MA_i^+) [16, 18].

Here, by utilizing drift-diffusion simulations of capacitance transients, we show that the interpretation of TID is more complex than originally expected. We show that the direction of the transients is not related to the polarity of the ionic species. Instead, it depends on the layer in the device that dominates the capacitance modulation by mobile ions. When the perovskite is fully depleted (low doping density), the accumulation of mobile ions at the perovskite/CTL interface leads to a depletion of electronic carriers

in the CTLs, resulting in decreasing capacitance transients. In contrast, when the perovskite layer is only partially depleted, the modulation of the depletion layer in the perovskite results in increasing capacitance transients. Between these regimes, the transients consist of a mixed regime, with an initial decrease, followed by an increase in the capacitance. Lastly, we show experimentally that increasing the photogenerated carrier density of a PSC also leads to a change of the transient direction from decreasing to increasing, because of the change of the electric field distribution by photogenerated charges. Similar to doping, increasing the density of photogenerated carriers changes the layer that dominates the capacitance modulation by mobile ions.

2.2 Results and Discussion

To investigate the role of the polarity of mobile ions in capacitance measurements, we simulate the behavior of the capacitance as a function of time after a voltage pulse. This simulation emulates the TID measurement. For the simulation of capacitance transients, we used the drift-diffusion solver Setfos by Fluxim. The device structure resembling a perovskite solar cell is shown in Figure 2.1, and all simulation parameters are listed as parameters set 1 of Table 2.A.1 in the Appendix. For the charge transport layers (CTLs), we selected parameters that are in the range of typical organic semiconductors used in PSCs (e.g. PTAA and C_{60}). However, in order to simplify the device structure, we used the same band gaps, effective density of states, mobilities of electronic carriers, and dielectric constants for both the hole transport layer (HTL) and electron transport layer (ETL). The simulation parameters for the perovskite layer are based on $MAPbI_3$. Throughout this work, we assume that two ionic species with opposite charges are present in the perovskite, where one species is mobile within the perovskite, while the other one is immobile and homogeneously distributed throughout the perovskite [21, 22]. The density of immobile and mobile ions is the same to ensure charge neutrality. We differentiate between positive ions and negative ions, where positive ions refer to positively charged interstitials and vacancies (e.g. iodide vacancies V_I^+ or MA interstitials MA_i^+), while negative ions refer to negatively charged interstitials and vacancies (e.g. iodide interstitials I_i^- or MA vacancies V_{MA}^-). Additionally, we assume that the mobile ions are confined in the perovskite and cannot migrate into the CTLs.

2.2.1 Principle of Capacitance Transient Measurements

Figure 2.1 shows a schematic of transient ion drift, considering positive mobile ions. Note that the device is symmetric, so with negative mobile ions, we would see the same mechanism in the opposite direction. Initially, an external voltage equal to the built-in voltage $V_{\mathrm{app}} = V_{\mathrm{bi}}$ is applied to the device (see Figure 2.1(a)). Because of the compensation of the built-in field, mobile ions distribute homogeneously within the perovskite (see Figure 2.1(b)). We note that experimentally, the device might not reach this steady-state if the voltage pulse is too short, and that some potential drops across the transport layers [23]. When the applied voltage is removed, $V_{\mathrm{app}} = 0$ V, positive mobile ions drift to the perovskite/HTL interface to screen the built-in field (see Figure 2.1(c)). During the drift of ions, we simulate the modulation of the capacitance using a perturbation voltage with a frequency of 10 kHz and an amplitude of 10 mV. At 10 kHz, the capacitance is determined by the density and distribution of electronic charge carriers within the PSC. Mobile ions do not directly contribute to the capacitance because they cannot follow the perturbed electric field due to their low mobility. However, they impact the distribution of electronic carriers within the PSC and consequently indirectly change the capacitance [24]. In other words, at the frequency of the perturbation, we are measuring a static distribution of ions, but over the timescale of milliseconds to seconds, the change in ion distribution changes the electronic capacitance of the device, resulting in a capacitance transient as illustrated in Figure 2.1(d).

2.2.2 Does the Transient Direction Depend on the Ion Polarity?

We now use the drift-diffusion simulations to better understand the transient capacitance measurements. First, we investigate how the polarity of the mobile ions influences capacitance transients. So far, in literature, it has been assumed that the polarity of ionic charge carriers determines the direction of the capacitance transients. This was done in analogy to the polarity of trap states in deep-level transient spectroscopy [25], which is very similar to TID. More specifically, decreasing transients were assigned to negative mobile ions like $\mathrm{I_i^-}$ or $\mathrm{Br_i^-}$, while increasing transients were assigned to positive mobile ions like $\mathrm{MA_i^+}$ [16, 18] in a p-doped perovskite. The basis for this assignment was the assumption that the perovskite is doped, leading to a partially depleted perovskite, and the assumption that the density of mobile ionic carriers is smaller than the acceptor-like defect (or doping) density ($N_{\mathrm{A}} > N_{\mathrm{ion}}$). When applying a voltage pulse close to V_{bi}, the depletion layer would collapse, and mobile ionic charge carriers would distribute homogeneously within the perovskite. After removing the applied voltage, mobile negative/positive ions would drift out of the depletion layer, leading to an increase/decrease in the depletion

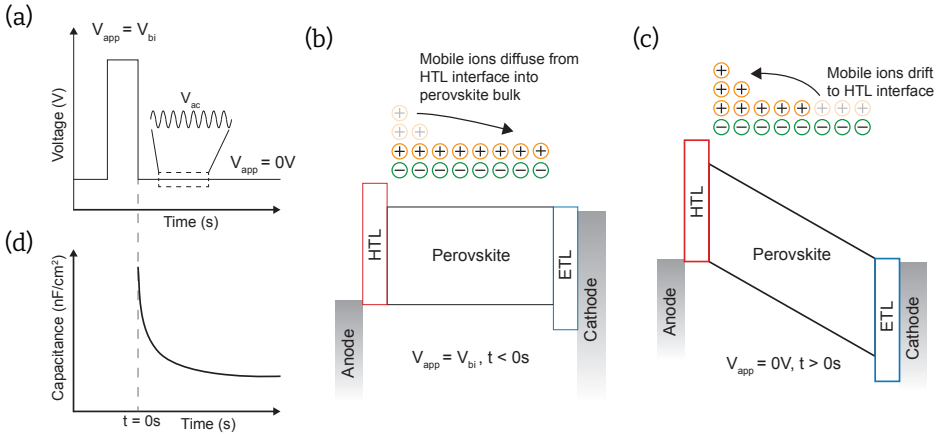

Figure 2.1: (a) Illustration of the voltage profile applied to a perovskite solar cell during transient ion drift. After the voltage pulse, the capacitance of the device is probed with a high-frequency perturbation voltage V_{ac}. (b) During the voltage pulse of $V_{\mathrm{app}} = V_{\mathrm{bi}}$, positive mobile ions that were previously accumulated at the HTL interface diffuse into the perovskite and distribute more homogeneously. (c) When the voltage pulse is removed ($V_{\mathrm{app}} = 0V$), positive mobile ions drift back to the HTL interface, changing the device capacitance. (d) Illustration of a capacitance transient.

layer width. Because the depletion layer capacitance is proportional to the inverse of the depletion layer width $C_{\mathrm{dl}} \sim 1/w_{\mathrm{dl}}$ this would ultimately result in increasing capacitance transients for negative ions and decreasing capacitance transients for positive ions [17]. Considering these conditions, we simulated capacitance transients for positive and negative mobile ions, respectively. We chose an acceptor doping density of $1 \cdot 10^{17}$ cm^{-3} and ionic carrier densities from $1 \cdot 10^{15}$ – $5 \cdot 10^{16}$ cm^{-3} (typical values for mobile ion densities extracted using TID lie between $1 \cdot 10^{13}$-$1 \cdot 10^{16}$ cm^{-3}, while the assumed doping densities were around 1-2 orders of magnitude higher than the extracted ion densities [16, 18–20]). The results are shown in Figure 2.2, where $\delta C(t)$ is the capacitance change compared to the initial capacitance value $\delta C(t) = C(t) - C_0$ (the transients of the absolute capacitance values are shown in Figure 2.C.1).

As expected, the capacitance transients for mobile positive ions are increasing. However, contrary to the original prediction, the capacitance transients for negative mobile ions are also increasing. To better understand why both positive and negative mobile ions lead to increasing transients, we can study the energy band diagram and charge carrier distributions within the device. These are shown in Figure 2.3(a)-(c) for positive mobile ions. As expected, the p-doping of the perovskite leads to the formation of a depletion layer at the perovskite/ETL interface, where the depletion

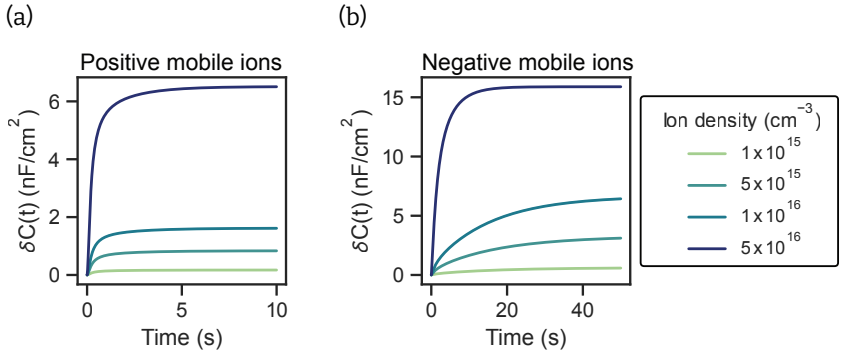

Figure 2.2: Simulated capacitance transients for different ion densities in the case of (a) positive mobile ions and (b) mobile negative ions. In both cases, the acceptor doping density is 10^{17} cm^{-3} (p-doping).

layer width (illustrated as w_0 in Figure 2.3(c)) depends on the doping density and the density of ionic charge carriers in the depletion layer. Initially, when V_{bi} is applied to the device, mobile positive ions are distributed across the perovskite. Then, after removing V_{bi}, these mobile ions drift out of the depletion region towards the HTL (see Figure 2.3(b)). Because the acceptor atoms N_{A} and the positive mobile ions have the opposite polarity, the net charge density in the depletion layer increases. This, in turn, reduces the depletion layer width (to w_1 in Figure 2.3(c)) and results in an increase in capacitance. In contrast, mobile negative ions accumulate at the perovskite/ETL interface after removing V_{bi} (see Figure 2.C.2). Now, the doping density and the mobile negative ions have the same polarity. Consequently, the net charge density within the depletion layer increases upon the accumulation of mobile negative ions, leading to a decrease in the depletion layer width and an increase in capacitance.

With this, we have established that the direction of capacitance transients cannot be correlated with the polarity of mobile ionic charge carriers. Instead, when considering high defect/doping densities, both negative and positive mobile ions lead to increasing capacitance transients. Comparing the duration of the transient in Figure 2.2(a) and (b), it is apparent that mobile negative ions lead to longer transients. These negative ions must partially diffuse through the field-free region of the perovskite before they accumulate in the depletion layer. In contrast, positive mobile ions only have to drift out of the depletion layer, leading to faster capacitance transients.

2.2.3 Origin of Decreasing Capacitance Transients

In the simulations shown so far, the capacitance transients were always increasing. However, decreasing or mixed transients are often observed in the literature, where

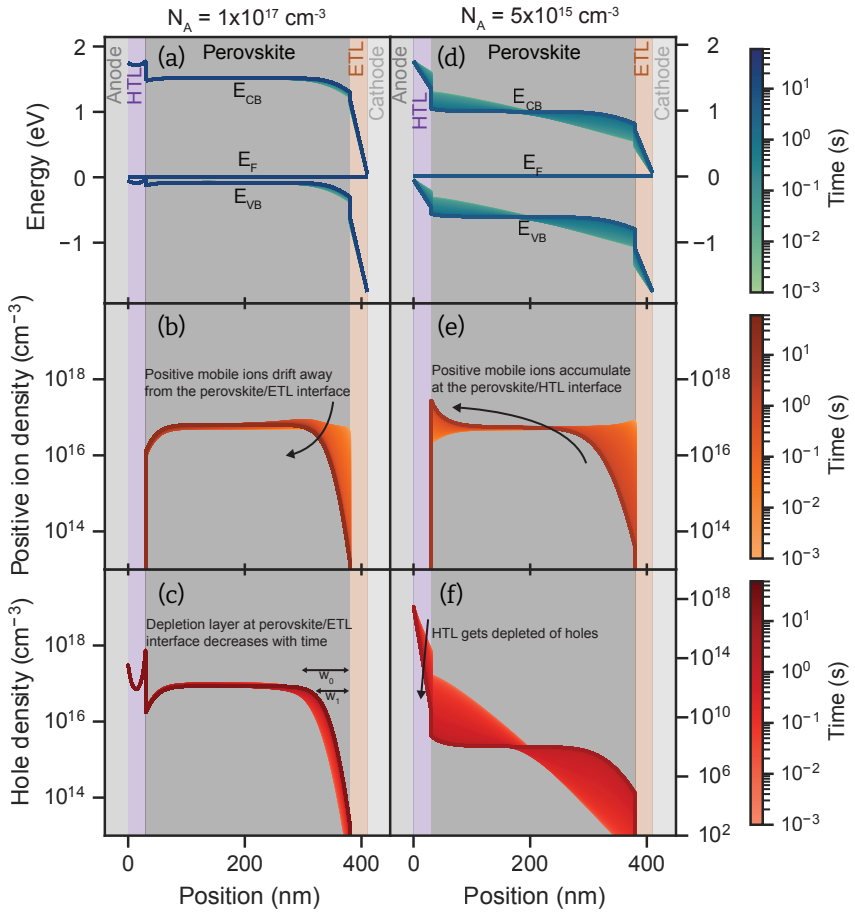

Figure 2.3: Simulated energy band diagrams, positive mobile ion densities, and hole densities at different times during the transients. The ion density is $5 \cdot 10^{16}$ cm^{-3}. Figures (a)-(c) contain the simulations in the case of an acceptor doping density of $1 \cdot 10^{17}$ cm^{-3} (p-doping). The corresponding increasing capacitance transient is shown in Figure 2.2(a) and panel C of Figure 2.4. Figures (d)-(f) show the simulations for an acceptor doping density of $5 \cdot 10^{15}$ cm^{-3}. The corresponding negative capacitance transient is shown in panel A of Figure 2.4. The electron density distributions are shown in Figure 2.C.5.

mixed transients consist of an initial decrease followed by an increase of the capacitance [17–20]. Additionally, recent studies using intensity-dependent transient photoluminescence measurements, Hall measurements, and charge extraction by linearly increasing voltage (CELIV) measurements suggest that Pb-based PSCs are not significantly doped [26]. Therefore, we investigate the influence of doping density on capacitance transients next. Figure 2.4 shows the capacitance change of the decreasing and increasing components of simulated transients when considering acceptor doping densities between $5 \cdot 10^{14}$ - 10^{18} cm^{-3}, positive mobile ions resembling halide vacan-

cies (as similarly done in [21, 22, 27]), and a mobile ion density of $5 \cdot 10^{16}$ cm^{-3}. Three different regimes are present (decreasing, mixed, and increasing), where one exemplary transient for each regime is shown in panels A-C (the transients with absolute capacitance values are shown in Figure 2.C.3). At doping densities until around $2 \cdot 10^{16}$ cm^{-3}, the capacitance transients decrease. Then, until $8 \cdot 10^{16}$ cm^{-3} the transients consist of a decreasing and an increasing part. For doping densities above $8 \cdot 10^{16}$ cm^{-3}, the capacitance transients increase. We note that the same three regimes are also observed for mobile negative ions, as shown in Figure 2.C.4. This suggests that rather than the polarity of mobile ionic species, the doping density of the perovskite determines the direction of the capacitance transients.

We have already established that the increasing capacitance transients for high perovskite doping densities originate from a decrease in the depletion layer width in the perovskite when positive mobile ions drift out of the depletion layer. In contrast, in the case of low perovskite doping densities, the perovskite layer is depleted of electronic charge carriers, and its capacitance is given by the geometrical capacitance $C_{\mathrm{geo,pero}}$. Because $C_{\mathrm{geo,pero}}$ is independent of the redistribution of ionic charge carriers, the perovskite layer does not contribute to the change of capacitance during the transient. Instead, the capacitance change originates from the transport layers. Upon application of the perturbation voltage, the density of the charge carriers injected into the device changes, which can be expressed as the capacitance

$$C_\mu = \frac{dQ_{\mathrm{inj}}}{dV_{\mathrm{app}}} = e\frac{d}{dV}\int_0^w \big(n(x) + p(x)\big)dx \tag{2.1}$$

where Q_{inj} is the injected charge, V_{app} is the applied voltage, e is the elementary charge, w is the thickness of the device, and $n(x)$ and $p(x)$ are the position-dependent electron and hole densities. This capacitance C_μ is sometimes termed chemical or charge storage capacitance [28, 29]. A more detailed explanation of C_μ and the influence of mobile ions on it is given in Section 2.B in the Appendix. Now, when positive mobile ions drift to the HTL/perovskite interface and accumulate there, the HTL gets more depleted of holes, as illustrated in Figure 2.3(d)-(f). At the same time, the depletion of positive ions at the perovskite/ETL interface leads to a reduction of electrons in the ETL (see Figure 2.C.5(b)), because they are repelled by the net negative charge at the perovskite/ETL interface. The difference between the Fermi-level and the VB on the HTL side, and the Fermi-level and the CB on the ETL side increases (see Figure 2.3(d)). This results in a reduction of injected charge carriers upon application of the perturbation voltage, leading to a decrease of the capacitance C_μ. We note that the injection of carriers into the perovskite could also contribute to C_μ. However, in the discussed case, the difference between the Fermi-level in the perovskite and its

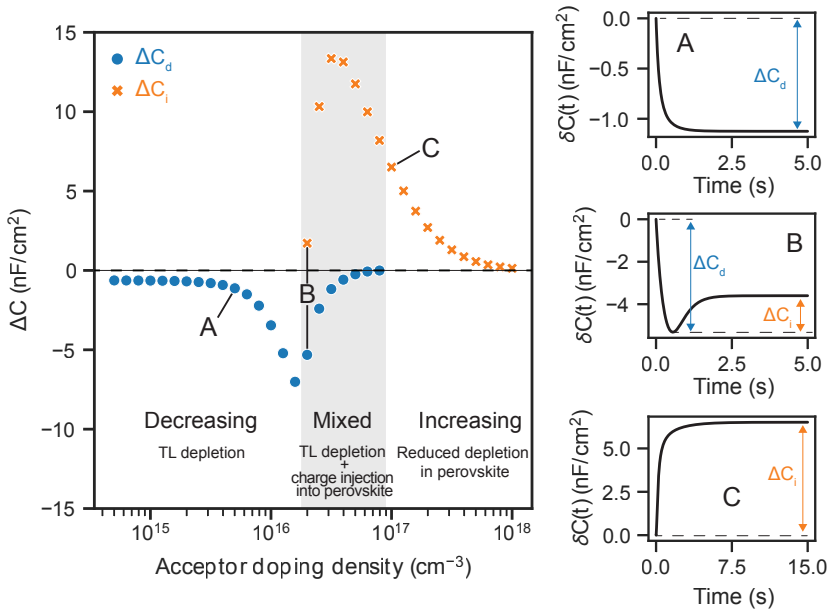

Figure 2.4: Capacitance change ΔC of simulated capacitance transients depending on the acceptor doping density of the perovskite. Simulated mobile ions are positive with a density of $5 \cdot 10^{16}$ cm^{-3}. ΔC is separated into ΔC_d of decreasing transients (blue circles) and ΔC_i of increasing transients (orange crosses). Depending on the acceptor doping density, three regimes are visible. The panels A, B, and C show example transients of the decreasing (A), mixed (B), and increasing (C) regimes.

CB and VB is too large, and no significant density of electronic carriers is injected into the perovskite bulk.

In the intermediate perovskite doping regime, the capacitance transients are mixed, consisting of an initial decrease followed by an increase in the capacitance. After releasing the voltage pulse, positive mobile ions start accumulating at the HTL/perovskite interface, decreasing the density of holes in the HTL and in the perovskite close to the HTL (see Figure 2.C.6). This decrease, similar to the low-doping case, results in the initial decrease of the capacitance. Then, as more positive mobile ions accumulate at the HTL/perovskite interface, the built-in field is screened, resulting in a large portion of the perovskite being field-free. In contrast to the low-doping case, the energy difference between the Fermi level and the VB in the perovskite is smaller. Consequently, the injection of holes into the perovskite upon application of a perturbation voltage is significantly higher and increases as a larger fraction of the built-in field is screened. This ultimately results in the observed increase of the capacitance.

Next to the doping density of the perovskite, other parameters of the PSC can impact

the density of injected electronic carriers into the perovskite and subsequently C_μ and the increasing part of the transient. Because we assume the mobile ions to be positive, the injection of holes dominates C_μ of the perovskite. We, therefore, focus on the parameters of the HTL and the perovskite. We simulated the onset of the mixed transient regime, i.e. at which doping density the transients switch from decreasing to mixed (in Figure 2.4 the onset would, for example, be at around a doping density of $2 \cdot 10^{16}$ cm^{-3}), as a function of ion density, thickness of the perovskite, VB offset between HTL and perovskite, doping density of the HTL, and dielectric constant of the perovskite. The results are shown in Figure 2.C.7. Increasing the density of mobile ions within the perovskite shifts the onset of the mixed regime to slightly higher doping densities (see Figure 2.C.7(a)). This shift is strongly sub-linear and can be explained in the following way: A higher ion density also leads to a higher density of accumulated positive ions at the HTL/perovskite interface. This results in a stronger depletion of holes at the HTL/perovskite interface and consequently reduces the overall density of injected holes in the perovskite, shifting the onset of the mixed regime to higher doping densities. When increasing the perovskite thickness, we observe that the onset of the mixed regime shifts almost linearly to lower doping densities because the built-in potential drops over an increasing distance (see Figure 2.C.7(b)). For thicker films, a lower density of accumulated ions at the HTL/perovskite interface is necessary to screen the electric field. Consequently, more holes are injected into the perovskite, which results in a lower onset of the mixed regime. A higher dielectric constant of the perovskite results in a higher fraction of the potential dropping over the CTLs. Consequently, the density of holes injected into the perovskite is reduced, shifting the onset of the mixed regime to higher doping densities (see Figure 2.C.7(c)). Changing the VB offset between the HTL and perovskite from −0.2 eV to 0.2 eV results in a stronger injection of holes into the perovskite. This leads to a shift of the onset of the mixed regime to lower doping densities (see Figure 2.C.7(d)). Lastly, increasing the doping density of the HTL leads to an increased injection of holes into the perovskite, shifting the onset of the mixed regime to dramatically lower doping densities (see Figure 2.C.7(e)). Here, at an HTL doping density of around $9 \cdot 10^{17}$ cm^{-3}, even undoped perovskites show a mixed transient, illustrating that injection of electronic carriers from the HTL into the perovskite is leading to an effectively doped perovskite layer.

2.2.4 Switching the Transient Direction

In the previous section, we established that the direction of capacitance transients depends on the layer that contributes to the capacitance. If the electronic carrier density of the perovskite is low, the CTLs dominate the change in capacitance, and

the transients decrease. A sufficiently high electronic carrier density within the perovskite introduces an increasing component. This increasing component can dominate the complete transient for significantly high doping in the perovskite. In order to verify these trends experimentally, we would ideally measure capacitance transients of PSCs with doping densities that span multiple orders of magnitude. However, accurate control of the doping density of perovskites is difficult to achieve to date [30]. Instead, we chose light excitation with a white high-power LED to alter the electronic charge carrier density within the PSC. The PSC was based on the stack ITO/PTAA/PFN-P2/$(Cs_{0.05}(FA_{0.83}MA_{0.17})_{0.95}Pb(I_{0.84}Br_{0.16})_3$/$C_{60}$/BCP/Cu. The fabrication is described in Section 2.A in the Appendix. These PSCs have been previously shown to have doping densities below 10^{13} cm^{-3} [26]. In addition, we use undoped organic CTLs to ensure decreasing transients in the absence of light excitation. Exemplary JV curves at different light intensities, showing a good diode character, are shown in Figure 2.C.8. In Figure 2.5(a), the measured capacitance transients for different illumination intensities (from dark to 27.8 mW/cm^2) at 300 K are shown. We find that the transient direction switches with increasing light intensity. In the dark, the transient decreases across the entire time range. This is expected for a PSC with a lowly doped perovskite. For low light intensities (e.g. 0.2 mW/cm^2), the transients show a decreasing and increasing component, where the magnitude of the increasing component strongly increases with light intensity. For the highest light intensity measured (27.8 mW/cm^2), we see a mostly increasing transient, with a small initial decrease remaining (see Figure 2.C.9 for a magnification at short times). We additionally measured the capacitance transients at a range of different temperatures (172-330 K in steps of 8 K, see Figure 2.C.10). At lower temperatures, both components become slower, which means that at lower temperatures the decreasing transient becomes

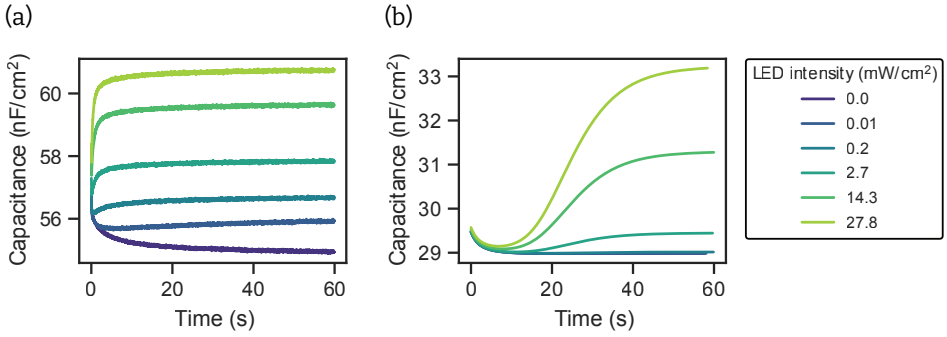

Figure 2.5: (a) Measured capacitance transients of a perovskite solar cell at 300 K and different LED intensities. (b) Simulated capacitance transients of a perovskite-like semiconductor stack at different LED intensities, assuming 10^{17} cm^{-3} ions and positive mobile ions with a mobility of $3 \cdot 10^{-11}$ cm^2/Vs.

more obvious (see Figure 2.C.10(d)). On the contrary, the decreasing component vanishes completely from the measurement at high temperatures (>318 K). This temperature dependence corresponds to the activation energy of the ionic processes leading to the transients.

We qualitatively reproduce the light-intensity dependence of the measured capacitance transients using the drift-diffusion simulations described above and in Section 2.A in the Appendix. The changes made to the model to approximate the device structure are listed as parameter set 2 in Table 2.A.1. The results are shown in Figure 2.5(b). We note that the simulations do not match the absolute capacitance values, which is most likely caused by differences in the doping density of the CTLs, and dielectric constants of the CTLs and the perovskite. However, qualitatively the simulations reproduce the trend that the capacitance transients transition from decreasing in the dark to mixed transients at higher light intensities. The light-induced splitting of the Fermi-level and the subsequently decreased difference to the CB and VB leads to an increase of C_μ of the perovskite. This is analogous to the case of higher doping, where an increase in the charge carrier density also led to a contribution of the perovskite layer to the capacitance transient. Interestingly, while the decreasing transient in the dark reproduces the time constant measured experimentally, the illuminated transients are much slower than the experimental data. A possible explanation for this discrepancy is that the mobility of mobile ions increases under illumination, as also found elsewhere [31, 32]. This change would result in faster transients as illustrated in Figure 2.C.11.

Finally, we note that the ionic contributions measured by the capacitance transients on these timescales (10s of seconds) are different from the ones typically measured by impedance spectroscopy and capacitance-frequency (C-f) methods. Because of low signal-to-noise ratios at low frequencies, C-f spectra are usually measured to around 0.1 Hz or 1 Hz, thus limiting the minimum resolvable mobility of ionic carriers. In contrast, capacitance transients can be measured for 10s of seconds, allowing the characterization of mobile ionic carriers with a lower mobility compared to C-f. To illustrate this point, we measured the capacitance of our PSCs as a function of frequency, varying the temperature and light intensity. The results are shown in Figure 2.C.12. In the dark, we observe an increase of the capacitance at around 1 kHz, which shifts to lower frequencies as the temperature decreases, in accordance with the literature [33]. We attribute this signature to mobile ions, whose mobility decreases with decreasing temperature. We can qualitatively reproduce the C-f measurements in simulations with ion mobilities of $1 \cdot 10^{-7}$ cm^2/Vs at 332 K to 10^{-10} cm^2/Vs at around 200 K, as shown in Figure 2.C.13. Under illumination, the measurements and simulations are also in good agreement, as depicted in Figures 2.C.12 and 2.C.13. Here, we

attribute the light-enhanced capacitance at low frequencies to phase-delayed recombination, as reported in the literature [34, 35]. From the simulations, we can estimate the mobility of mobile ions at 300 K to be around $5 \cdot 10^{-8}$ cm^2/Vs. This value is much higher compared to the ionic mobility needed to reproduce the capacitance transients in the dark ($\mu_{\mathrm{ion}} = 3 \cdot 10^{-11}$ cm^2/Vs, see Figure 2.5). This difference shows that the ionic response probed in the C-f measurements is not the same as the one observed at long times in the capacitance transients. Possibly, two mobile ionic species with very different mobilities are present in the perovskite, leading to dynamics on different timescales. This has similarly been proposed in [34, 36, 37] and shows the importance of both complementary methods. It also illustrates that a thorough investigation of the impact of multiple mobile ions with different ratios and mobilities on capacitance transients and C-f measurements is necessary. We note, however, that accounting for multiple mobile ions with varying mobilities and densities significantly increases the parameter space for drift-diffusion simulations and is, therefore, beyond the scope of this work.

2.3 Conclusion

To conclude, we have shown that the transient ion drift method, as applied in literature so far, is more complex than originally proposed. An assignment of the polarity of mobile ions to the direction of the capacitance transients is not possible. When, as assumed in the original transient ion drift model, the doping density of the perovskite is high, both positive and negative mobile ions result in an increase of the capacitance transient. When considering lower doping density, the direction of the capacitance transient depends on whether the capacitance of the perovskite or CTLs is modulated when mobile ions drift through the perovskite. An accumulation of ions at the CTLs leads to a decrease in the capacitance. Meanwhile, if the difference between Fermi level and VB or CB is low enough, i.e. the perovskite is slightly doped, the chemical capacitance of the perovskite is modulated when mobile ions accumulate at the perovskite/CTL interfaces due to increased injection into the perovskite, leading to an increase of the overall capacitance. Experimentally, we have verified these findings by decreasing the difference between Fermi level and VB/CB using illumination, which resulted in a change of the capacitance transients from decreasing to increasing. Finally, differences in time constants between C-f measurements and transient ion drift measurements suggest that multiple ionic species are present in the PSC. Hence, our results show the breadth of timescales that is required to understand ion migration and perovskites, and that further understanding of these techniques considering multiple mobile ionic species is needed.

Chapter appendix

2.A Experimental Details

Drift-Diffusion Simulations

For drift-diffusion simulations, we used the software Setfos by Fluxim. The device structures simulated are described in the main text, with the parameter sets outlined in Table 2.A.1. The capacitance transients were simulated using the transient voltage simulation module with an initial voltage V_{app} and a subsequently applied voltage of 0 V with a voltage modulation of 0.01 V at 10 kHz. The transients were simulated for a maximum time of 60 s or until they reached a steady state. We chose a logarithmic time step with the initial value being 0.1 ms and increasing to a maximum value of 50 ms. For simulations with illumination, we used the same spectrum and intensities of the High-Power LED Solis-3C used in the measurements.

Table 2.A.1: Parameters used for the drift-diffusion simulations.

	Parameter set 1	**Parameter set 2**
Applied voltage V_{app} (V)	1.3	1.4
Work function anode $W_{\mathrm{f,anode}}$ (eV)	5.35	5.4
Work function cathode $W_{\mathrm{f,cathode}}$ (eV)	4.05	4.0
Effective density of conduction band states HTL $N_{0,\mathrm{CB,HTL}}$ (cm^{-3})	$2.1 \cdot 10^{18}$ [38]	$2.1 \cdot 10^{18}$ [38]
Effective density of valence band states HTL $N_{0,\mathrm{VB,HTL}}$ (cm^{-3})	$2.1 \cdot 10^{18}$ [38]	$2.1 \cdot 10^{18}$ [38]
Dielectric constant HTL $\epsilon_{r,HTL}$	4.1 (same as ETL)	3.0 [39]
Acceptor doping density $N_{\mathrm{A,HTL}}$ (cm^{-3})	0	0
Thickness HTL d_{HTL} (nm)	30 (same as ETL)	10 [40]
Electron affinity HTL $E_{\mathrm{A,HTL}}$ (eV)	3.6	3.6
Band gap HTL $E_{\mathrm{g,HTL}}$ (eV)	1.8	1.85
Mobility holes in HTL $\mu_{\mathrm{h,HTL}}$ (cm^2/Vs)	0.02 (same as ETL)	$3 \cdot 10^{-5}$ [41]
Effective density of conduction band states perovskite $N_{0,\mathrm{CB,Pero}}$ (cm^{-3})	$2.1 \cdot 10^{18}$ [42]	$2.1 \cdot 10^{18}$ [42]

	Parameter set 1	Parameter set 2
Effective density of valence band states perovskite $N_{0,\mathrm{VB,Pero}}$ (cm^{-3})	$2.1 \cdot 10^{18}$ [42]	$2.1 \cdot 10^{18}$ [42]
Dielectric constant HTL $\epsilon_{\mathrm{r,Pero}}$	24.1 [43]	22.0 [36]
Acceptor doping density $N_{\mathrm{A,HTL}}$ (cm^{-3})	variable	0
Thickness perovskite d_{Pero} (nm)	350	400
Electron affinity perovskite $E_{\mathrm{A,HTL}}$ (eV)	3.9 [44]	3.9 [40]
Band gap perovskite $E_{\mathrm{g,Pero}}$ (eV)	1.6 [44]	1.6
Mobility electrons in perovskite $\mu_{\mathrm{e,Pero}}$ (cm^2/Vs)	17 [45]	1 [36]
Mobility holes in perovskite $\mu_{\mathrm{h,Pero}}$ (cm^2/Vs)	17 [45]	1 [36]
Radiative recombination constant perovskite $(\mathrm{cm}^3/\mathrm{s})$	10^{-9} [46]	10^{-9} [46]
Positive ion density N_{PI} (cm^{-3})	variable	$1 \cdot 10^{17}$
Negative ion density N_{NI} (cm^{-3})	variable	$1 \cdot 10^{17}$
Mobility positive ions μ_{PI} (cm^2/Vs)	10^{-9} or static	variable
Mobility negative ions μ_{NI} (cm^2/Vs)	10^{-9} or static	static
Effective density of conduction band states ETL $N_{0,\mathrm{CB,ETL}}$ (cm^{-3})	$2.1 \cdot 10^{18}$ [38]	$2.1 \cdot 10^{18}$ [38]
Effective density of valence band states ETL $N_{0,\mathrm{VB,ETL}}$ (cm^{-3})	$2.1 \cdot 10^{18}$ [38]	$2.1 \cdot 10^{18}$ [38]
Dielectric constant ETL $\epsilon_{\mathrm{r,ETL}}$	4.1 [47]	4.1 [47]
Donor doping density ETL $N_{\mathrm{D,ETL}}$ (cm^{-3})	0	0
Thickness ETL d_{ETL} (nm)	30 [40]	10 [40]
Electron affinity ETL $E_{\mathrm{A,ETL}}$ (eV)	4.0	3.95
Band gap ETL $E_{\mathrm{g,ETL}}$ (eV)	1.8	1.85
Mobility electrons in ETL $\mu_{\mathrm{e,ETL}}$ (cm^2/Vs)	0.02 [48]	0.02 [48]

Device Fabrication

Substrate: Pre-patterned 2.5x2.5 cm^2 15 Ω/sq ITO (Automatic Research, Germany), glass or fused silica substrates were cleaned with acetone, 3 % Hellmanex solution, DI-water, and isopropanol, by sonication for 10 min in each solution. Afterwards a microwave plasma treatment (4 min, 200 W) was performed. The samples were transferred to an N_2-filled glovebox where PTAA was spin-coated from solution.

Hole transport layers (HTLs): PTAA (Sigma Aldrich) was spin-coated from a 2 mg/ml Toluene solution at 6000 rpm for 30 s (acceleration 2000 rpm/s) onto the substrates and subsequently annealed at 100 °C for 10 min. Afterwards, a 60 µl solution of PFN-P2 (0.5 mg/mL in methanol) was added onto the spinning substrate at 4000 rpm for 30 s resulting in a film with a thickness below the detection limit of our AFM (< 5 nm).

Perovskite Layer: The triple cation perovskite solution was prepared by mixing two 1.2 M $FAPbI_3$ and $MAPbBr_3$ perovskite solutions in DMF: DMSO (4:1) in a ratio of 83:17, which we call "MAFA" solution. The 1.2 M $FAPbI_3$ solution was prepared by dissolving FAI (722 mg) and PbI_2 (2130 mg) in 2.8 ml DMF and 0.7 ml DMSO (note there is a 10% excess of PbI_2). The 1.2 M $MAPbBr_3$ solution was made by dissolving MABr (470 mg) and $PbBr_2$ (1696 mg) in 2.8 ml DMF and 0.7 ml DMSO (note there is a 10% excess of $PbBr_2$). Lastly, 40 µl of a 1.5 M CsI solution in DMSO (389 mg CsI in 1 ml DMSO) was mixed with 960 µl of the MAFA solution resulting in a final perovskite stoichiometry of $(CsPbI_3)_{0.05}[(FAPbI_3)_{0.83}(MAPbBr_3)_{0.17}]_{0.95}$ in solution. The perovskite film was deposited by spin-coating at 4000 rpm (acceleration 1300 rpm/s) for 40 seconds; 13 seconds after the start of the spinning process, the spinning substrate was washed with 300 µl of the anti-solvent Ethyl Acetate for approximately 1 s (the anti-solvent was placed in the center of the film). The perovskite film was then annealed at 100 °C for 1 hr on a preheated hot plate.

Electron transport layers (ETLs): After annealing, the samples were transferred to an evaporation chamber where 30 nm of fullerene-C_{60} (Sigma-Aldrich) followed by 8 nm of 2,9-Dimethyl-4,7-diphenyl-1,10-phenanthroline (BCP, Sigma-Aldrich) were thermally deposited under vacuum (pressure = 10^{-7} mbar).

Metal contacts: Similarly to the ETL, 100 nm copper (Sigma-Aldrich) at 0.6 Å/s were deposited under vacuum (pressure = 10^{-7} mbar). The overlap of the copper and the ITO electrodes defined the active area of the pixel (6 mm^2).

Electrical Characterization

The samples were loaded into a Janis VPF-100 liquid nitrogen cryostat in a glovebox under a nitrogen atmosphere. During the measurements, the pressure inside the cryostat was $5 \cdot 10^{-6}$ mbar, and the temperature was stabilized at 300 K using a Lakeshore 335 temperature controller. JV measurements were recorded using a Keithley 2401 in a voltage range from −0.2-1.2 V with a voltage step size of 0.04 V and a sweep speed of 0.1 V/s. All capacitance measurements were recorded using the Zurich Instruments MFIA with an AC voltage amplitude of 20 mV. The capacitance-frequency (C-f) measurements were acquired in a frequency range from 1 Hz-500 kHz. The capacitance transients were recorded by applying a 2 s-long voltage pulse of 1.2 V before measuring

the capacitance at 0 V for 30 s. For measurements with illumination, we used the high-power LED Solis-3C from Thorlabs and light-soaked the devices for 15 s. The LED's intensity was determined using a monocrystalline silicon solar cell by G2V. We measured the J_{sc} at different illumination intensities. Then, with the spectrum of the LED (measured with an OceanOptics spectrometer) and the EQE of the silicon solar cell, we determined the irradiance and the intensity.

2.B Chemical or Charge Storage Capacitance

The chemical or charge storage capacitance of a semiconductor is related to the filling of the density of states (DOS) of a semiconductor upon moving the Fermi-level by e.g. applying a voltage bias. We can generally define the chemical capacitance of the CB and VB as:

$$C_{\mu,\mathrm{CB}} = \frac{dQ_{\mathrm{CB}}}{dV_{\mathrm{app}}} = e\frac{d}{dV_{\mathrm{app}}}\int_0^w n(x)dx \tag{2.2}$$

$$C_{\mu,\mathrm{VB}} = \frac{dQ_{\mathrm{VB}}}{dV_{\mathrm{app}}} = e\frac{d}{dV_{\mathrm{app}}}\int_0^w p(x)dx \tag{2.3}$$

where Q_{CB}, and Q_{VB} are the charges of the conduction, and the valence band, respectively. V_{app} is the applied voltage, e is the elementary charge, w is the thickness of the device, and $n(x)$ and $p(x)$ are the electron and hole density as a function of position. In other words, the chemical capacitance describes the change of electrical charges in the semiconductor per change of applied voltage. In the case of a simple intrinsic semiconductor, this capacitance is mostly relevant at large forward bias when a significant density of electronic carriers is injected into the semiconductor (see [23, 28] for a more detailed explanation). When mobile ions are present, like in the perovskite, these ions screen the built-in potential and lead to a larger injection of electronic carriers upon changing the applied voltage. This can be seen in Figure 2.B.1(a), where the VB gets closer to the Fermi level as the ion density increases. The charge density scales exponentially with $E_{\mathrm{F}}(x) - E_{\mathrm{VB}}(x)$ as:

$$p(x) = N_{0,\mathrm{VB}}\, e^{-\frac{E_{\mathrm{F}}(x)-E_{\mathrm{VB}}(x)}{k_{\mathrm{B}}T}} \tag{2.4}$$

where $N_{0,\mathrm{VB}}$ are the effective density of states in the valence band. For holes, or symmetrically for electrons, assuming a parabolic band structure. Upon perturbation of the Fermi level, more charges are injected into the perovskite in the case of a high mobile ion density. For high mobile ion densities (from around 10^{16} cm^{-3}), this ultimately leads to a significant increase in the capacitance as a function of ion density as shown

in Figure 2.B.1(a). Then, an approximation of the device capacitance with the geometrical capacitance $C_{\mathrm{geo}} = \frac{\epsilon_0 \epsilon_r}{d}$ is not accurate anymore.

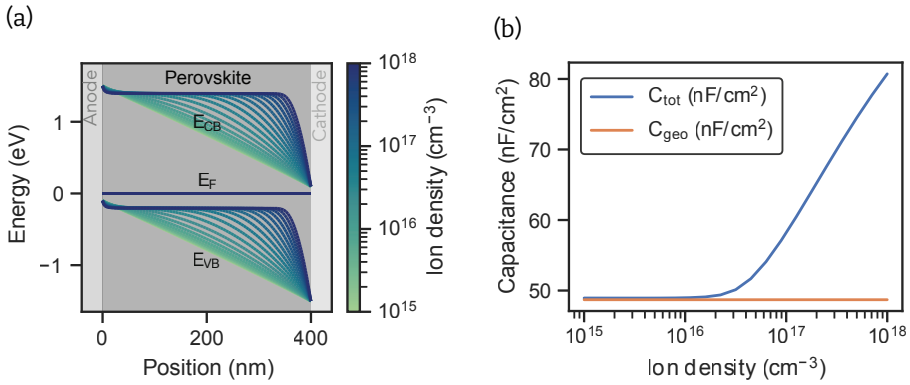

Figure 2.B.1: (a) Energy band diagram of an intrinsic perovskite with different mobile ion densities. (b) Simulated capacitance C_{tot} depending on the ion density and the geometrical capacitance C_{geo} of the perovskite.

2.C Additional Information

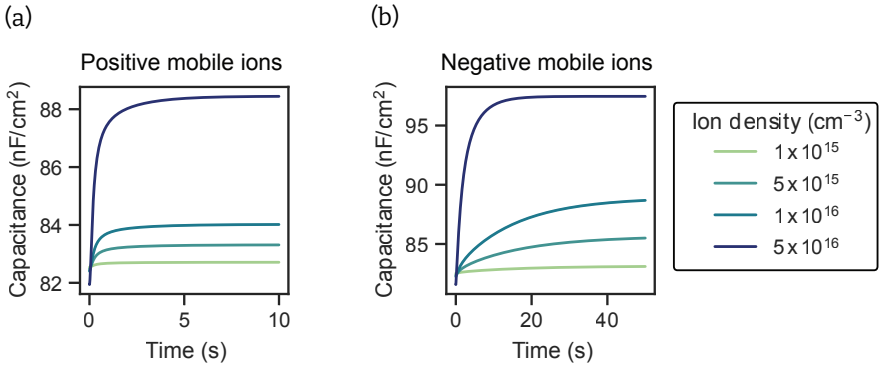

Figure 2.C.1: Capacitance transients of (a) mobile positive ions and (b) mobile negative ions. The acceptor doping density of the perovskite is 10^{17} cm^{-3}.

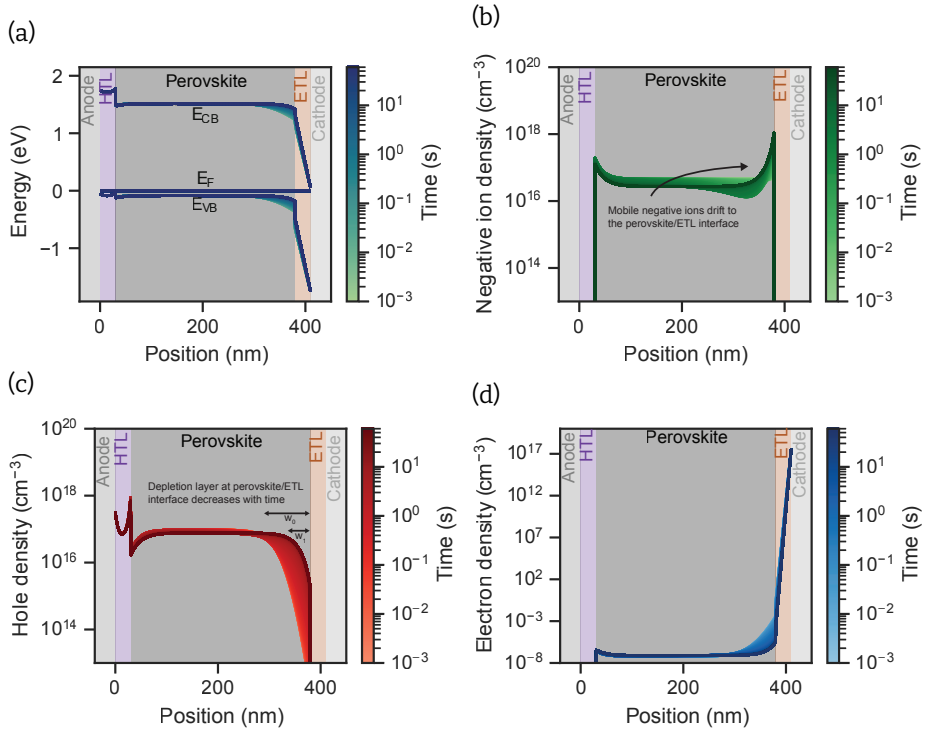

Figure 2.C.2: (a) Band diagram, (b) mobile negative ion distribution, (c) hole distribution, and (d) electron distribution of a PSC with a density of mobile negative ions of $5 \cdot 10^{16}$ cm^{-3} and an acceptor doping density of $1 \cdot 10^{17}$ cm^{-3}. As mobile negative ions drift to the perovskite/ETL interface, into the depletion layer, the depletion layer width in the perovskite decreases from w_0 to w_1, as illustrated in (c). Because of $C_{\mathrm{dl}} \propto 1/w_{\mathrm{dl}}$, the capacitance of the device increases.

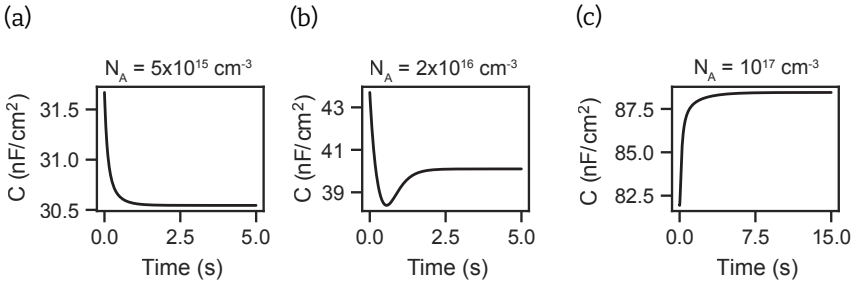

Figure 2.C.3: Absolute value of the capacitance of the example transients shown in panel A-C of Figure 2.4 in the main text. The mobile ion density is $5 \cdot 10^{16}$ cm^{-3}, while the acceptor doping densities of the perovskite are (a) $5 \cdot 10^{15}$ cm^{-3}, (b) $2 \cdot 10^{16}$ cm^{-3}, and (c) $1 \cdot 10^{17}$ cm^{-3}.

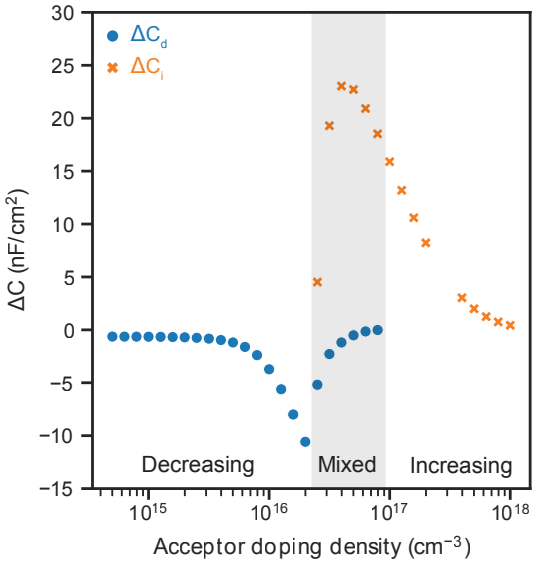

Figure 2.C.4: Capacitance change ΔC of simulated capacitance transients depending on the acceptor doping density of the perovskite with mobile negative ions and an ion density of $5 \cdot 10^{16}$ cm^{-3}. The only difference to Figure 2.3 of the main text is the polarity of the mobile ions. ΔC is separated into ΔC_d of decreasing transients (blue circles) and ΔC_i of the increasing transients (orange crosses). Depending on the acceptor doping density, three regimes are visible.

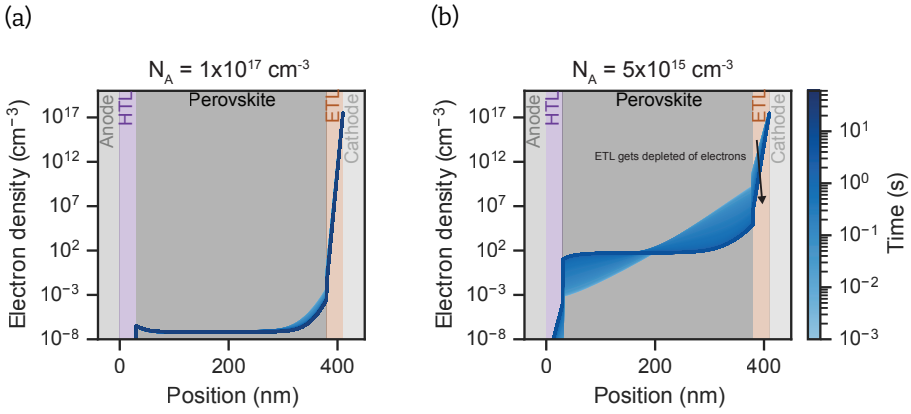

Figure 2.C.5: Simulated electron distributions of a PSC during the transient for an acceptor doping density of (a) $1 \cdot 10^{17}$ cm^{-3}, and (b) $5 \cdot 10^{15}$ cm^{-3}. The corresponding energy band diagram, positive mobile ion density, and hole density are shown in Figure 2.3 of the main text.

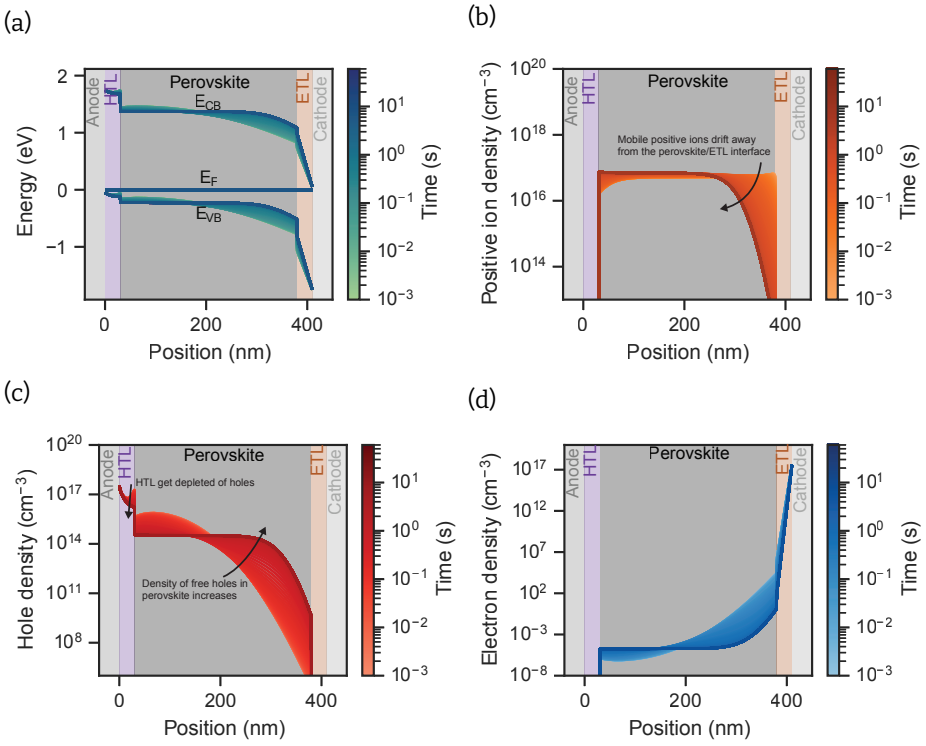

Figure 2.C.6: (a) Band diagram, (b) mobile positive ion distribution, (c) hole distribution, and (d) electron distribution of a PSC with a density of mobile positive ions of $5 \cdot 10^{16}$ cm^{-3} and an acceptor doping density of $2 \cdot 10^{16}$ cm^{-3}. Initially, when mobile positive ions accumulate at the perovskite/HTL interface, the HTL gets depleted of holes, leading to a decrease of the capacitance. At later times, because of the field-free region in the perovskite and the small difference between Fermi level and VB, the chemical capacitance of the perovskite increases, overall resulting in a mixed transient.

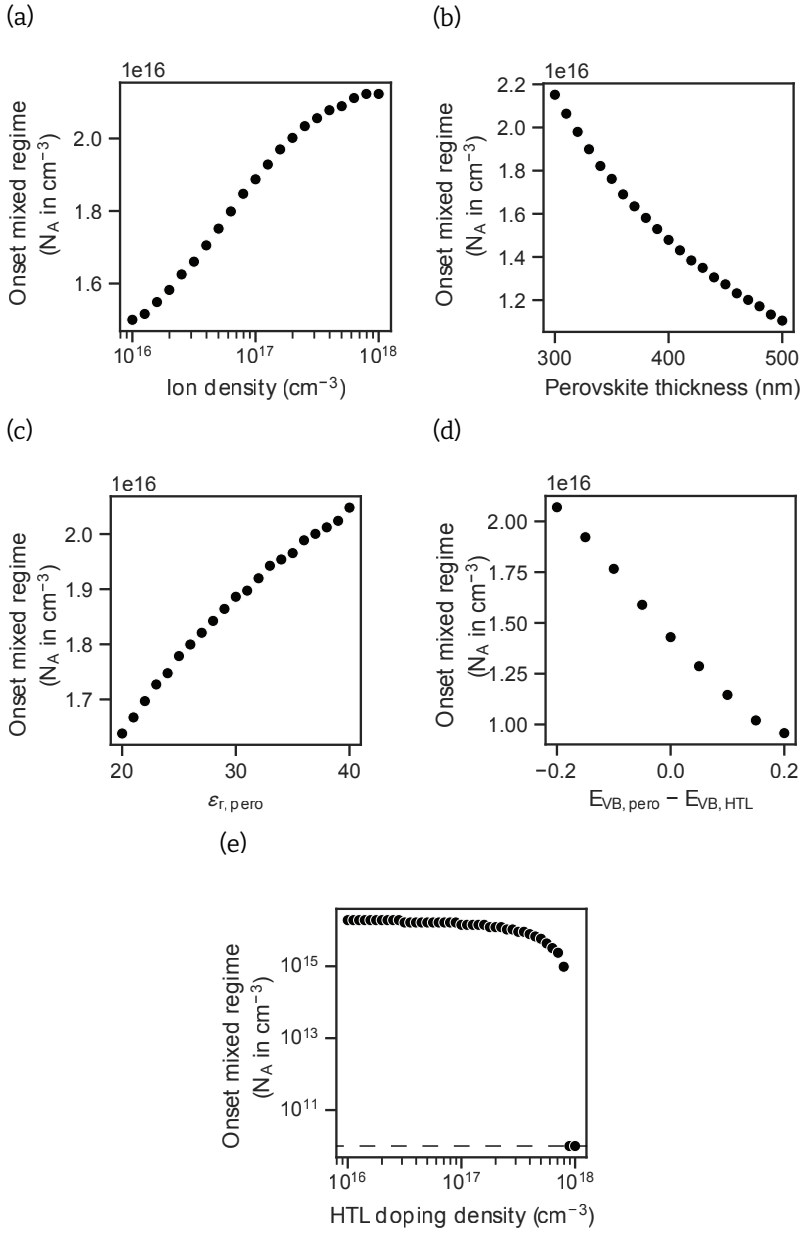

Figure 2.C.7: Simulated onset of mixed capacitance transient regime as a function of (a) mobile ion density, (b) perovskite thickness, (c) dielectric constant in perovskite, (d) offset between the valence band (VB) of perovskite and VB of the HTL, and (e) HTL doping density. The dashed line in (e) at 10^{10} cm^{-3} marks the minimum value considered in the simulations.

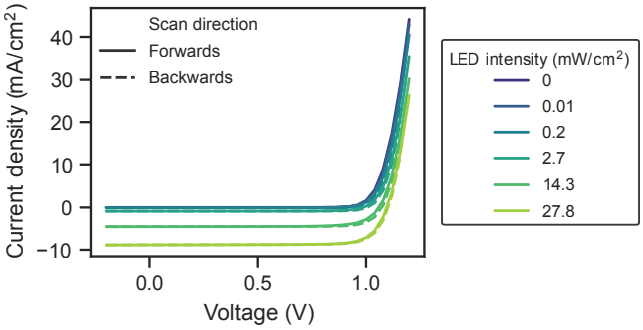

Figure 2.C.8: Current density-voltage measurements of the PSCs at various illumination intensities in forward and backward direction.

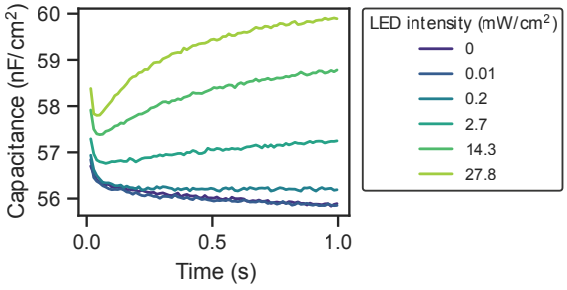

Figure 2.C.9: Zoomed-in capacitance transients of Figure 2.5(a) in the main text. Here, the initial decrease of the capacitance at higher illumination intensities is visible.

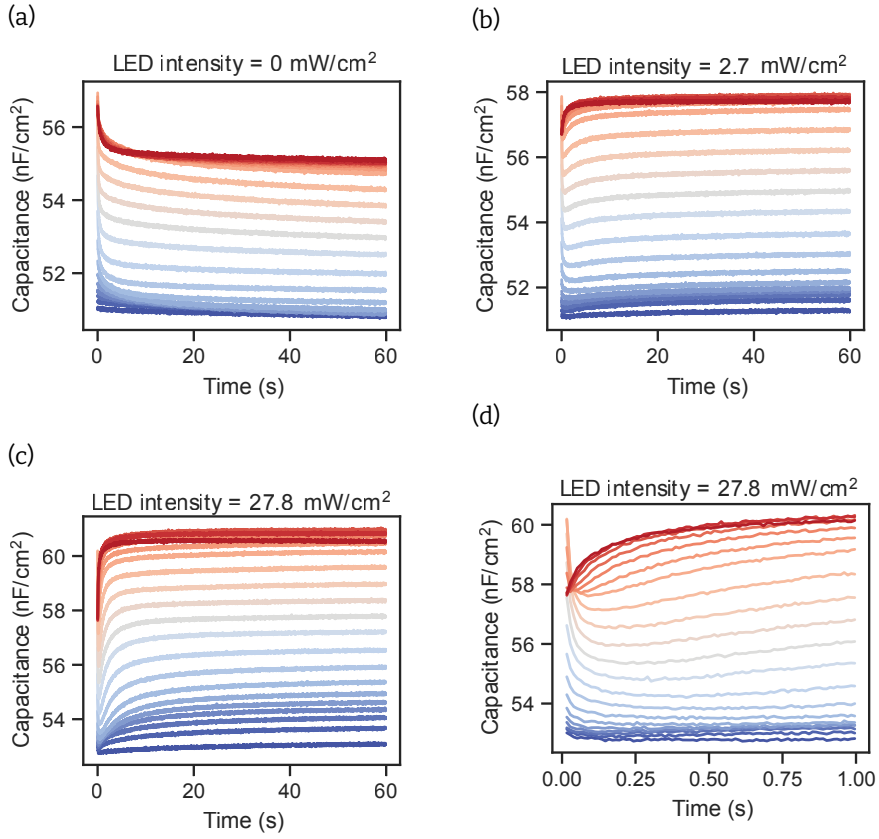

Figure 2.C.10: Measured capacitance transients at different temperatures (172-330 K in steps of 8 K) and different illumination intensities of (a) 0 mW/cm^2 (dark), (b) 2.7 mW/cm^2, (c) 27.8 mW/cm^2, (d) also 27.8 mW/cm^2, but zoomed into shorter times.

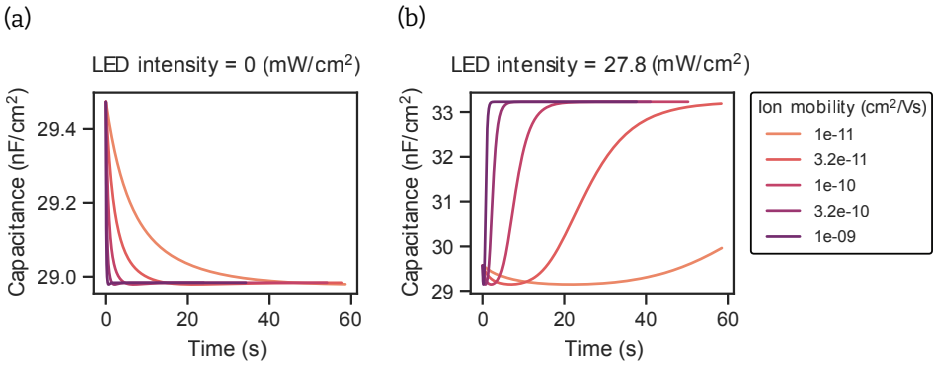

Figure 2.C.11: Simulated capacitance transients depending on different ion mobilities in (a) the dark and (b) under illumination.

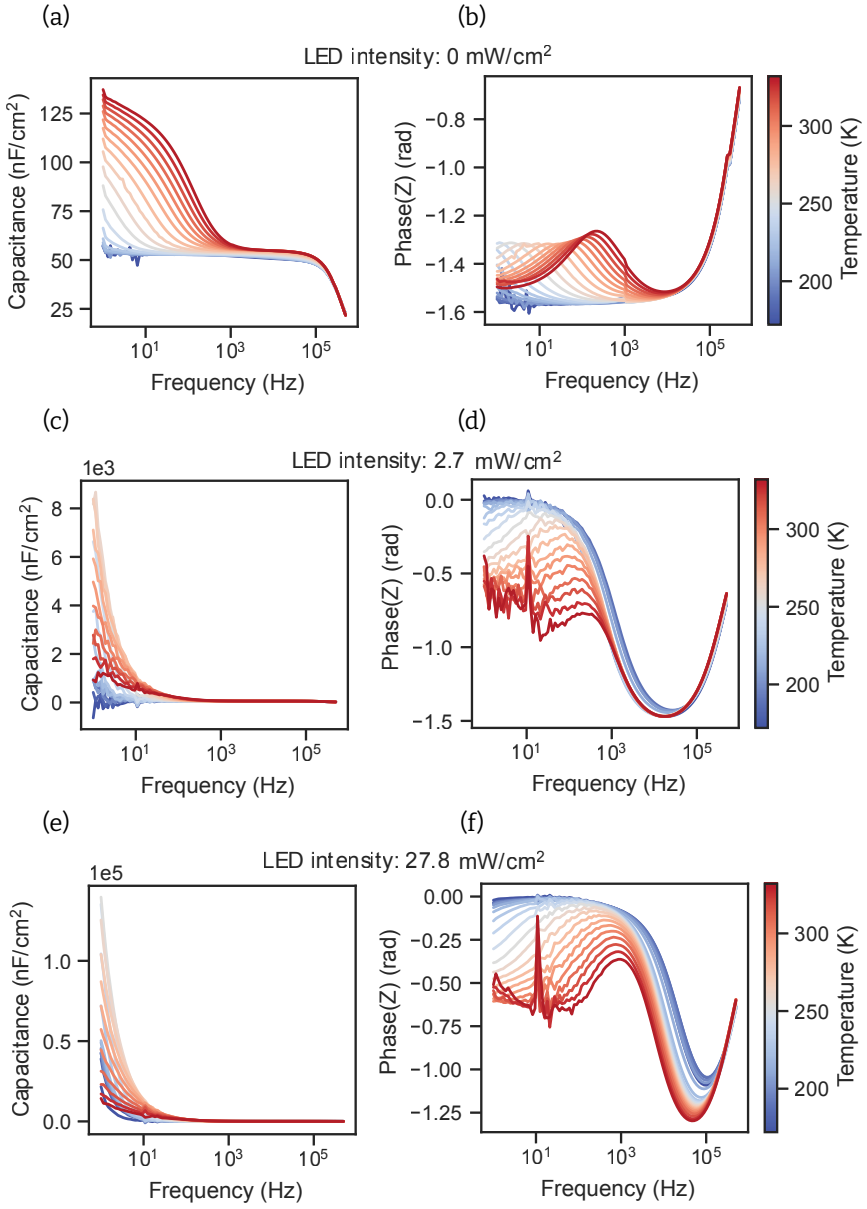

Figure 2.C.12: Capacitance frequency (C-f) measurements of the PSC at different temperatures (172-330 K in steps of 8 K) and light intensities. (a) and (b) show the capacitance and phase in the dark, (c) and (d) show the capacitance and phase under 2.7 mW/cm^2 illumination, and (e) and (f) show the capacitance and phase under 27.8 mW/cm^2 illumination.

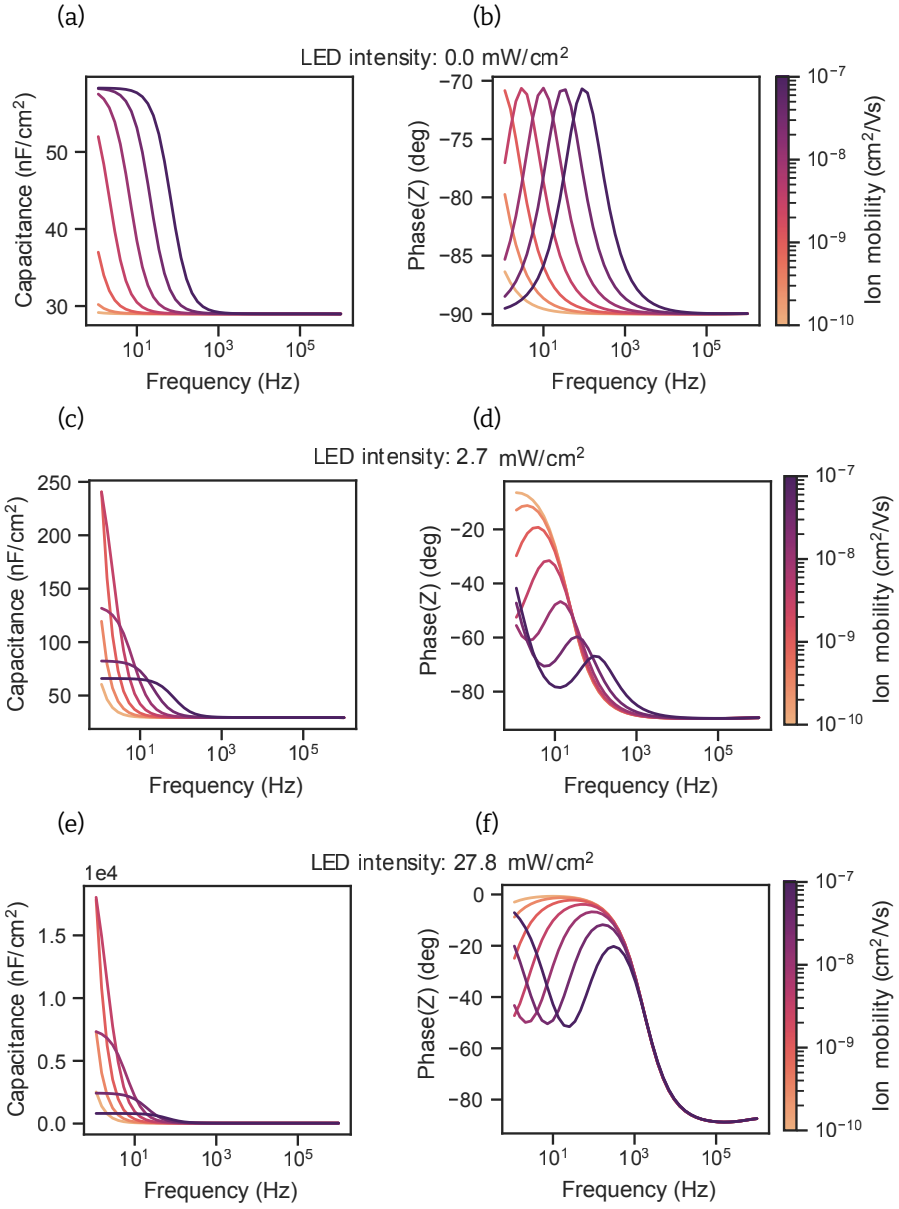

Figure 2.C.13: Drift diffusion simulations of capacitance frequency spectra using the parameters set 2 in Table 2.A.1 at different ion mobilities and light intensities. (a) and (b) show the capacitance and phase in the dark, (c) and (d) show the capacitance and phase under 2.7 mW/cm^2 illumination, and (e) and (f) show the capacitance and phase under 27.8 mW/cm^2 illumination.

Bibliography

[1] M. A. Green *et al.*, "Solar Cell Efficiency Tables (Version 64)", *Progress in Photovoltaics: Research and Applications*, vol. 32, no. 7, pp. 425–441, 2024.

[2] J. Thiesbrummel *et al.*, "Universal Current Losses in Perovskite Solar Cells Due to Mobile Ions", *Advanced Energy Materials*, vol. 11, no. 34, p. 2 101 447, 2021.

[3] E. Bi, Z. Song, C. Li, Z. Wu, and Y. Yan, "Mitigating Ion Migration in Perovskite Solar Cells", *Trends in Chemistry*, vol. 3, no. 7, pp. 575–588, 2021.

[4] C. Kan *et al.*, "Mitigating Ion Migration by Polyethylene Glycol-Modified Fullerene for Perovskite Solar Cells with Enhanced Stability", *ACS Energy Letters*, vol. 6, no. 11, pp. 3864–3872, 2021.

[5] J.-W. Lee, S.-G. Kim, J.-M. Yang, Y. Yang, and N.-G. Park, "Verification and Mitigation of Ion Migration in Perovskite Solar Cells", *APL Materials*, vol. 7, no. 4, p. 041 111, 2019.

[6] J. M. Azpiroz, E. Mosconi, J. Bisquert, and F. De Angelis, "Defect Migration in Methylammonium Lead Iodide and Its Role in Perovskite Solar Cell Operation", *Energy & Environmental Science*, vol. 8, no. 7, pp. 2118–2127, 2015.

[7] J. Haruyama, K. Sodeyama, L. Han, and Y. Tateyama, "First-Principles Study of Ion Diffusion in Perovskite Solar Cell Sensitizers", *Journal of the American Chemical Society*, vol. 137, no. 32, pp. 10 048–10 051, 2015.

[8] C. Eames, J. M. Frost, P. R. F. Barnes, B. C. O'Regan, A. Walsh, and M. S. Islam, "Ionic Transport in Hybrid Lead Iodide Perovskite Solar Cells", *Nature Communications*, vol. 6, no. 1, p. 7497, 2015.

[9] Z. Li *et al.*, "Extrinsic Ion Migration in Perovskite Solar Cells", *Energy & Environmental Science*, vol. 10, no. 5, pp. 1234–1242, 2017.

[10] D. Wei *et al.*, "Ion-Migration Inhibition by the Cation-π Interaction in Perovskite Materials for Efficient and Stable Perovskite Solar Cells", *Advanced Materials*, vol. 30, no. 31, p. 1 707 583, 2018.

[11] Y. Yuan *et al.*, "Photovoltaic Switching Mechanism in Lateral Structure Hybrid Perovskite Solar Cells", *Advanced Energy Materials*, vol. 5, no. 15, p. 1 500 615, 2015.

[12] J. S. Yun *et al.*, "Critical Role of Grain Boundaries for Ion Migration in Formamidinium and Methylammonium Lead Halide Perovskite Solar Cells", *Advanced Energy Materials*, vol. 6, no. 13, p. 1 600 330, 2016.

[13] W. Peng, C. Aranda, O. M. Bakr, G. Garcia-Belmonte, J. Bisquert, and A. Guerrero, "Quantification of Ionic Diffusion in Lead Halide Perovskite Single Crystals", *ACS Energy Letters*, vol. 3, no. 7, pp. 1477–1481, 2018.

[14] D. Moia and J. Maier, "Ion Transport, Defect Chemistry, and the Device Physics of Hybrid Perovskite Solar Cells", *ACS Energy Letters*, vol. 6, no. 4, pp. 1566–1576, 2021.

[15] G. Y. Kim, A. Senocrate, Y.-R. Wang, D. Moia, and J. Maier, "Photo-Effect on Ion Transport in Mixed Cation and Halide Perovskites and Implications for Photo-Demixing**", *Angewandte Chemie International Edition*, vol. 60, no. 2, pp. 820–826, 2021.

[16] M. H. Futscher *et al.*, "Quantification of Ion Migration in $CH_3NH_3PbI_3$ Perovskite Solar Cells by Transient Capacitance Measurements", *Materials Horizons*, vol. 6, no. 7, pp. 1497–1503, 2019.

[17] M. H. Futscher, M. K. Gangishetty, D. N. Congreve, and B. Ehrler, "Quantifying Mobile Ions and Electronic Defects in Perovskite-Based Devices with Temperature-Dependent Capacitance Measurements: Frequency vs Time Domain", *The Journal of Chemical Physics*, vol. 152, no. 4, p. 044 202, 2020.

[18] L. McGovern, M. H. Futscher, L. A. Muscarella, and B. Ehrler, "Understanding the Stability of $MAPbBr_3$ versus $MAPbI_3$: Suppression of Methylammonium Migration and Reduction of Halide Migration", *The Journal of Physical Chemistry Letters*, vol. 11, no. 17, pp. 7127–7132, 2020.

[19] L. McGovern, I. Koschany, G. Grimaldi, L. A. Muscarella, and B. Ehrler, "Grain Size Influences Activation Energy and Migration Pathways in $MAPbBr_3$ Perovskite Solar Cells", *The Journal of Physical Chemistry Letters*, vol. 12, no. 9, pp. 2423–2428, 2021.

[20] S. Reichert, Q. An, Y.-W. Woo, A. Walsh, Y. Vaynzof, and C. Deibel, "Probing the Ionic Defect Landscape in Halide Perovskite Solar Cells", *Nature Communications*, vol. 11, no. 1, p. 6098, 2020.

[21] L. Bertoluzzi *et al.*, "Mobile Ion Concentration Measurement and Open-Access Band Diagram Simulation Platform for Halide Perovskite Solar Cells", *Joule*, vol. 4, no. 1, pp. 109–127, 2020.

[22] G. Richardson *et al.*, "Can Slow-Moving Ions Explain Hysteresis in the Current–Voltage Curves of Perovskite Solar Cells?", *Energy & Environmental Science*, vol. 9, no. 4, pp. 1476–1485, 2016.

[23] S. Ravishankar, Z. Liu, U. Rau, and T. Kirchartz, "Multilayer Capacitances: How Selective Contacts Affect Capacitance Measurements of Perovskite Solar Cells", *PRX Energy*, vol. 1, no. 1, p. 013 003, 2022.

[24] J. Diekmann *et al.*, "Determination of Mobile Ion Densities in Halide Perovskites via Low-Frequency Capacitance and Charge Extraction Techniques", *The Journal of Physical Chemistry Letters*, vol. 14, no. 18, pp. 4200–4210, 2023.

[25] D. V. Lang, "Deep-Level Transient Spectroscopy: A New Method to Characterize Traps in Semiconductors", *Journal of Applied Physics*, vol. 45, no. 7, pp. 3023–3032, 1974.

[26] F. Peña-Camargo *et al.*, "Revealing the Doping Density in Perovskite Solar Cells and Its Impact on Device Performance", *Applied Physics Reviews*, vol. 9, no. 2, p. 021 409, 2022.

[27] N. E. Courtier, J. M. Cave, J. M. Foster, A. B. Walker, and G. Richardson, "How Transport Layer Properties Affect Perovskite Solar Cell Performance: Insights from a Coupled Charge Transport/Ion Migration Model", *Energy & Environmental Science*, vol. 12, no. 1, pp. 396–409, 2019.

[28] J. Bisquert, "Chemical Capacitance of Nanostructured Semiconductors: Its Origin and Significance for Nanocomposite Solar Cells", *Physical Chemistry Chemical Physics*, vol. 5, no. 24, p. 5360, 2003.

[29] Chih-Tang Sah, "The Equivalent Circuit Model in Solid-State Electronics—Part I: The Single Energy Level Defect Centers", *Proceedings of the IEEE*, vol. 55, no. 5, pp. 654–671, 1967.

[30] J. Euvrard, Y. Yan, and D. B. Mitzi, "Electrical Doping in Halide Perovskites", *Nature Reviews Materials*, vol. 6, no. 6, pp. 531–549, 2021.

[31] W. Zhou *et al.*, "Light-Independent Ionic Transport in Inorganic Perovskite and Ultrastable Cs-Based Perovskite Solar Cells", *The Journal of Physical Chemistry Letters*, vol. 8, no. 17, pp. 4122–4128, 2017.

[32] J. Xing, Q. Wang, Q. Dong, Y. Yuan, Y. Fang, and J. Huang, "Ultrafast Ion Migration in Hybrid Perovskite Polycrystalline Thin Films under Light and Suppression in Single Crystals", *Physical Chemistry Chemical Physics*, vol. 18, no. 44, pp. 30 484–30 490, 2016.

[33] R. A. Awni *et al.*, "Influence of Charge Transport Layers on Capacitance Measured in Halide Perovskite Solar Cells", *Joule*, vol. 4, no. 3, pp. 644–657, 2020.

[34] D. A. Jacobs *et al.*, "The Two Faces of Capacitance: New Interpretations for Electrical Impedance Measurements of Perovskite Solar Cells and Their Relation to Hysteresis", *Journal of Applied Physics*, vol. 124, no. 22, p. 225 702, 2018.

[35] N. Filipoiu *et al.*, "Capacitive and Inductive Effects in Perovskite Solar Cells: The Different Roles of Ionic Current and Ionic Charge Accumulation", *Physical Review Applied*, vol. 18, no. 6, p. 064 087, 2022.

[36] J. Thiesbrummel *et al.*, "Ion-Induced Field Screening as a Dominant Factor in Perovskite Solar Cell Operational Stability", *Nature Energy*, vol. 9, no. 6, pp. 664–676, 2024.

[37] D. Walter *et al.*, "Transient Photovoltage in Perovskite Solar Cells: Interaction of Trap-Mediated Recombination and Migration of Multiple Ionic Species", *The Journal of Physical Chemistry C*, vol. 122, no. 21, pp. 11 270–11 281, 2018.

[38] N. Tessler and Y. Vaynzof, "Insights from Device Modeling of Perovskite Solar Cells", *ACS Energy Letters*, vol. 5, no. 4, pp. 1260–1270, 2020.

[39] M. Sendner, J. Trollmann, and A. Pucci, "Dielectric Function and Degradation Process of poly(triarylamine) (PTAA)", *Organic Electronics*, vol. 15, no. 11, pp. 2959–2963, 2014.

[40] M. Stolterfoht *et al.*, "The Impact of Energy Alignment and Interfacial Recombination on the Internal and External Open-Circuit Voltage of Perovskite Solar Cells", *Energy & Environmental Science*, vol. 12, no. 9, pp. 2778–2788, 2019.

[41] Y. Ko, Y. Kim, C. Lee, Y. Kim, and Y. Jun, "Investigation of Hole-Transporting Poly(triarylamine) on Aggregation and Charge Transport for Hysteresisless Scalable Planar Perovskite Solar Cells", *ACS Applied Materials & Interfaces*, vol. 10, no. 14, pp. 11 633–11 641, 2018.

[42] F. Staub *et al.*, "Beyond Bulk Lifetimes: Insights into Lead Halide Perovskite Films from Time-Resolved Photoluminescence", *Physical Review Applied*, vol. 6, no. 4, p. 044 017, 2016.

[43] F. Brivio, K. T. Butler, A. Walsh, and M. van Schilfgaarde, "Relativistic Quasiparticle Self-Consistent Electronic Structure of Hybrid Halide Perovskite Photovoltaic Absorbers", *Physical Review B*, vol. 89, no. 15, p. 155 204, 2014.

[44] M. Caputo *et al.*, "Electronic Structure of $MAPbI_3$ and $MAPbCl_3$: Importance of Band Alignment", *Scientific Reports*, vol. 9, no. 1, p. 15 159, 2019.

[45] C. Q. Xia *et al.*, "Limits to Electrical Mobility in Lead-Halide Perovskite Semiconductors", *The Journal of Physical Chemistry Letters*, vol. 12, no. 14, pp. 3607–3617, 2021.

[46] C. Wehrenfennig, G. E. Eperon, M. B. Johnston, H. J. Snaith, and L. M. Herz, "High Charge Carrier Mobilities and Lifetimes in Organolead Trihalide Perovskites", *Advanced Materials*, vol. 26, no. 10, pp. 1584–1589, 2014.

[47] P. C. Eklund *et al.*, "Optical Properties of C_{60} and C_{70}-based Solid Films", *Thin Solid Films*, vol. 257, no. 2, pp. 211–232, 1995.

[48] C. H. Lee, G. Yu, D. Moses, V. I. Srdanov, X. Wei, and Z. V. Vardeny, "Transient and Steady-State Photoconductivity of a Solid C_{60} Film", *Physical Review B*, vol. 48, no. 11, pp. 8506–8509, 1993.

3

Time- and Frequency-Domain Traces of Ion Migration

Abstract

The migration of mobile ions through the metal halide perovskite layer is still one of the main reasons for the poor stability of perovskite solar cells, LEDs, and photodetectors. To characterize mobile ions in the perovskite layer, time- and frequency-based electrical measurements are promising techniques. However, the presence of transport layers complicates their interpretation, limiting the information about mobile ions that can be extracted, and it is not clear how different features in frequency- and time-domain measurements relate to mobile ions. Here, we characterize a transport-layer-free device with capacitance frequency, capacitance transients, and current transient measurements in the dark, under illumination, and at different temperatures. We extract characteristic ionic signatures from the measurements, which we reproduce with drift-diffusion simulations for each technique. This allows us to explain the origins of the different ionic signatures, advancing the understanding of how electronic characterization techniques can be used to study the properties of mobile ions.

Authors: Moritz C. Schmidt, Agustin O. Alvarez, Jeroen J. de Boer, Larissa J.M. van de Ven, and Bruno Ehrler

Published in: ACS Energy Letters, Volume: 9, Issue: 12, Pages: 5850-5858, November 2024

https://doi.org/10.1021/acsenergylett.4c02446

3.1 Introduction

All commercial applications of perovskite semiconductors are currently hampered by their poor intrinsic stability [1]. Long-term degradation occurs due to several mechanisms. For example, thermally induced reactions of the soft perovskite crystal release volatile methylammonium (MA) from $MAPbI_3$ [2, 3]. Humidity and light introduce the decomposition of the perovskite into photo-inactive PbI_2 [4]. Some of these degradation pathways can be avoided by encapsulation, reducing the evaporation of volatile species and the intrusion of moisture [5, 6]. Additionally, perovskite layers exhibit large densities of mobile ions [7, 8], which dominate the potential distribution within perovskite devices. Recently, these mobile ions have been shown to be the leading cause of the reduction of current extraction of perovskite solar cells, introducing significant efficiency losses on short time scales [9]. Other perovskite-based devices, such as LEDs and photo-detectors, also suffer from ion-induced degradation [10–12]. However, mobile ions can also lead to the recovery of perovskite-based devices, also known as self-healing [13], and increase the design tolerance for efficient solar cells [14]. Consequently, reliable ways to quantify mobile ions in perovskite layers are necessary. However, so far, most techniques to study ion migration have significant downsides. Optical techniques, for example, using photoluminescence spectroscopy to study phase segregation [15], only extract quantitative information about the timescale of ion migration and provide no chemical resolution or sensitivity to ions that do not change optical properties. Techniques that offer chemical resolution, such as X-ray fluorescence [16] and Time-of-Flight Secondary Ion Mass Spectrometry (ToF-SIMS) [17], require elaborate measurement equipment. Furthermore, X-ray fluorescence requires special sample geometries, usually with larger distances between electrodes, and ToF-SIMS is a destructive technique, not allowing the study of ion migration while applying a bias. A common way to study ion migration is by electrical measurements, for example, impedance spectroscopy [18, 19], transient current [20], transient voltage [21, 22], or transient capacitance measurements [23, 24]. While these techniques are often used to extract quantitative information, their interpretation is not trivial, as they are based on complex interactions between ionic and electronic carriers and recombination [8, 25, 26]. In addition, it has been shown that transport layers in complete devices complicate the interpretation of many electronic measurements [26–28].

To circumvent these issues, this work focuses on characterizing the simplest possible perovskite device, a $MAPbI_3$ perovskite layer sandwiched between two electrodes without charge transport layers. We compare three different electronic measurements: capacitance frequency (Cf), capacitance transients (Ct), and current transients (Jt) in

the dark and under illumination. In most of the measurements, we can identify a signature of an ion migration process. Tracing this feature for various temperatures allows us to extract its activation energy. With drift-diffusion simulations, we can qualitatively reproduce and explain all measurements when considering a non-radiative recombination process in addition to the mobile ions. While focusing on a single technique to study ion migration often leaves parameters ambiguously defined, using several techniques to measure the same system narrows down the parameter set used for the simulations to reproduce the experimental observations. Therefore, we can estimate the mobile ion density, mobility, and activation energy.

3.2 Results and Discussion

We fabricated a simple perovskite device by sandwiching a polycrystalline thin film of $MAPbI_3$ between an ITO and a gold electrode (see Figure 3.1(a)). The $MAPbI_3$ thin film covers the ITO pinhole-free, as shown in a scanning electron microscopy image in Figure 3.D.1. Using X-ray diffraction, we can identify all the characteristic peaks for $MAPbI_3$ (see Figure 3.D.2). Figures 3.D.3(a) and (b) show current-density vs. voltage (JV) measurements at 280, 300, and 320 K in the dark and light. The JV measurements are mostly symmetric except for a diode behavior at forward bias. This diode shape is temperature-dependent, and we attribute it to an interfacial barrier. Under illumination, the overall current density of the device increases due to photoconductivity. We chose this device structure to avoid the influence of transport layers on the frequency and time-dependent electrical measurements. We [26] and others [27, 28] have previously shown that the transport layers can influence these measurements, complicating their interpretation.

The techniques we focus on are capacitance frequency, capacitance transients, and current transients, illustrated in Figure 3.1(b). In the capacitance frequency technique, we measure the capacitance with a small voltage perturbation of 20 mV at frequencies ranging from 1 Hz to 500 kHz at 0 V DC voltage. This technique is often applied to perovskite solar cells to study ion migration [24]. However, it has been shown that the interpretation is difficult, especially when applied to complete devices [8]. Capacitance transient measurements, originating from deep-level transient spectroscopy [29], are less established when characterizing perovskite solar cells. Here, we apply a DC voltage pulse of 1 V and 2.5 s to the ITO (anode). After the voltage pulse, thus at 0 V DC voltage, we measure the change of the capacitance using a high-frequency voltage perturbation of 20 mV and 10 kHz. Even though capacitance transients are difficult to interpret, they contain valuable information about the device properties, as the transients are influenced by the mobility and density of mobile ions [26]. In

current transients, we apply the same DC voltage pulse of 1 V and 2.5 s to the device and then measure the current as a function of time once the voltage pulse is switched off. This technique has been previously used in complete devices, thin films, and single crystals in attempts to quantify the density of mobile ions [20, 30, 31].

We perform all measurements in the dark and under moderate illumination with a 2.3 mW/cm^2 white light LED. Additional information about the fabrication process and the experimental setup is available in the Appendix. To understand the mechanism behind the measurements, we additionally carry out drift-diffusion simulations with the software Setfos by Fluxim. For the ionic parameters, we choose mobile positive ions, accounting for mobile iodide vacancies V_I^+, and immobile negative ions to conserve charge neutrality (e.g. iodide interstitials I_i^- and MA vacancies V_{MA}^-) [7, 32]. To reproduce the measurements, we choose a work function difference of 0.3 eV between the electrodes, leading to accumulation of mobile positive ions at the anode at steady-state when no voltage is applied. We note that the choice of work function difference affects the steady-state ion distribution, which has a large effect on the simulation results. Furthermore, we additionally include hole traps in the semiconductor layer. We note, however, that we do not know the polarity of the traps in the semiconductor. Therefore, electron traps are also a possibility. Table 3.D.1 shows the complete list of simulation parameters.

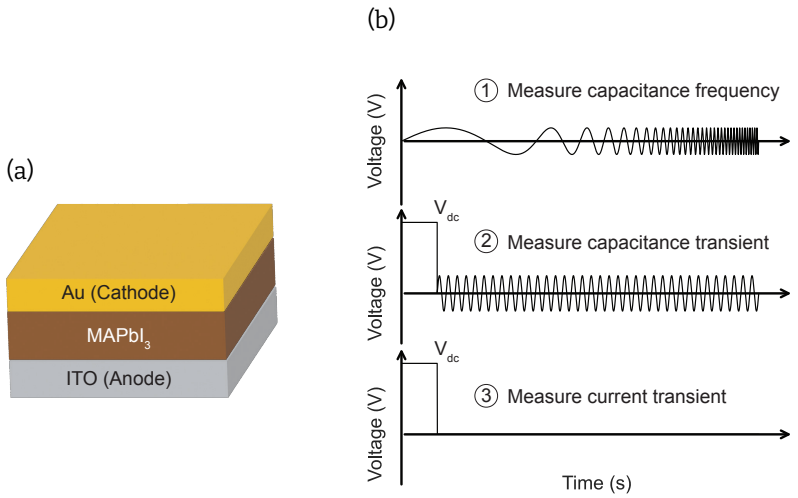

Figure 3.1: (a) Schematic of the device stack. (b) The three different techniques used in this work: capacitance frequency, capacitance transient, and current transient.

3.2.1 Capacitance Frequency Measurements

The first technique we focus on is capacitance frequency, where we measure the capacitance C of the device at different frequencies f. The capacitance can be determined from the impedance Z:

$$C = \frac{1}{2\pi f} \operatorname{Im}\left(\frac{1}{Z}\right) \tag{3.1}$$

The measured capacitance in the dark for different temperatures from 280-320 K is plotted in Figure 3.2(a). At intermediate frequencies from 50 Hz to 50 kHz, we observe a plateau in the capacitance value. Because no transport layers are present, we can assume that the geometrical capacitance dominates the capacitance in this regime. Using the approximation of a parallel plate capacitor:

$$C = \frac{\epsilon_0 \epsilon_r}{d} \tag{3.2}$$

with ϵ_0 being the vacuum permittivity and d the thickness of the perovskite of 330 nm, we can approximate the permittivity ϵ_r of the perovskite to be 54 at 300 K, close to values previously observed in literature [33]. At frequencies below 50 Hz, mobile ions in the perovskite start to polarize, increasing the capacitance [34, 35]. We reproduce this capacitance increase at low frequencies using drift-diffusion simulations, as shown in Figure 3.D.4(a). The drift-diffusion simulations allow us to distinguish between the contributions to the total capacitance C_{tot} from electrons C_{n}, holes C_{p}, positive ions C_{ion}, and the time-dependent change of the electric field, i.e., displacement, C_{disp}. These contributions are shown in Figure 3.2(c) for a capacitance frequency simulation in the dark at 300 K. At frequencies smaller than 20 Hz, mobile ions dominate the total capacitance. At higher frequencies, the device's capacitance is entirely dominated by the displacement current, confirming that an approximation of the geometrical capacitance is valid.

The characteristic time of the ionic signature can be estimated with the peak of the phase of the impedance. The measurement of the phase angle is shown in Figure 3.2(a), and the simulations in Figure 3.D.4(a). This characteristic time is inversely proportional to the ionic conductivity:

$$f_{\mathrm{ion}} = \frac{1}{\tau_{\mathrm{ion}}} \propto \sigma_{\mathrm{ion}} = e\mu_{\mathrm{ion}} N_{\mathrm{ion}} \tag{3.3}$$

where σ_{ion} is the ionic conductivity, μ_{ion} is the mobility of ions, and N_{ion} is the density of mobile ions. This relationship between phase peak and ionic conductivity is illustrated in Figure 3.D.5. As the mobility of the ions decreases with temperature [36], the

characteristic frequency also decreases with decreasing temperature.
Next, we perform the same Cf measurements while illuminating the device with a low-intensity white light LED. Compared to the dark measurements, the capacitance increases around one order of magnitude at low frequencies, as shown in Figure 3.2(b). We can reproduce this large capacitance rise with illumination at different temperatures in drift-diffusion simulations, as shown in Figure 3.D.4(b). We attribute this to the contribution of electronic carriers in the device in combination with a phase delay due to mobile ions. According to Jacobs et al. [25], electronic carriers contribute to the impedance of a device with a charge storage Z_{Q} and recombination Z_{R} term. Based on the current continuity equation, these contributions for e.g. electrons can be expressed as:

$$Z_{\mathrm{n}} = V_{\mathrm{ac}}(\underbrace{i\omega \int e\tilde{n}\,\mathrm{dx}}_{Z_{\mathrm{Q}}} + \underbrace{\int e\tilde{R}_{\mathrm{n}}\,\mathrm{dx} + \tilde{j}_{\mathrm{Rn0}}}_{Z_{\mathrm{R}}})^{-1} \tag{3.4}$$

where V_{ac} is the perturbation voltage, $\tilde{n}$ is the AC electronic carrier density, $\tilde{R}_{\mathrm{n}}$ is the AC recombination rate of electrons in the bulk, and $\tilde{j}_{\mathrm{Rn0}}$ is the AC recombination current of photogenerated electrons at the anode. By substituting Equation 3.4 into Equation 3.1, we get the contributions of the charge storage and recombination term to the capacitance:

$$C_{\mathrm{n}} = \frac{1}{2\pi f}\,\mathrm{Im}\left(\frac{1}{Z_{\mathrm{n}}}\right) = \underbrace{\frac{1}{V_{\mathrm{ac}}}\int e\,\mathrm{Re}(\tilde{n})\,\mathrm{dx}}_{C_{\mathrm{Q}}} + \underbrace{\frac{1}{V_{\mathrm{ac}}}\frac{1}{2\pi f}\int e\,\mathrm{Im}(\tilde{R}_{\mathrm{n}})\,\mathrm{dx} + \mathrm{Im}(\tilde{j}_{\mathrm{Rn0}})}_{C_{\mathrm{R}}} \tag{3.5}$$

We want to emphasize that the contribution C_{R} is not a capacitance in the classical sense, i.e., it does not describe the device's ability to store charge. Instead, recombination processes can lead to phase-delayed currents similar to the conventional charge storage capacitance C_{Q}. Therefore, the capacitances of, e.g., electrons C_{n} mentioned here only describe the phase delay of the electron current and the applied voltage rather than the device's ability to store electrons. At low frequencies, mobile ions introduce a phase shift in the potential and the electronic carrier densities, resulting in significant contributions of the recombination term C_{R} to the capacitance, which is responsible for the large rise of the capacitance. In other words, the photogenerated carriers recombine, and the phase delay that the mobile ions induce in this recombination process leads to a large increase in capacitance.
In the simulations, we again break down the different contributions to the capacitance at 300 K and see that the electron and hole capacitances dominate the total capacitance at low frequencies (see Figure 3.2(d)). Furthermore, we calculate the con-

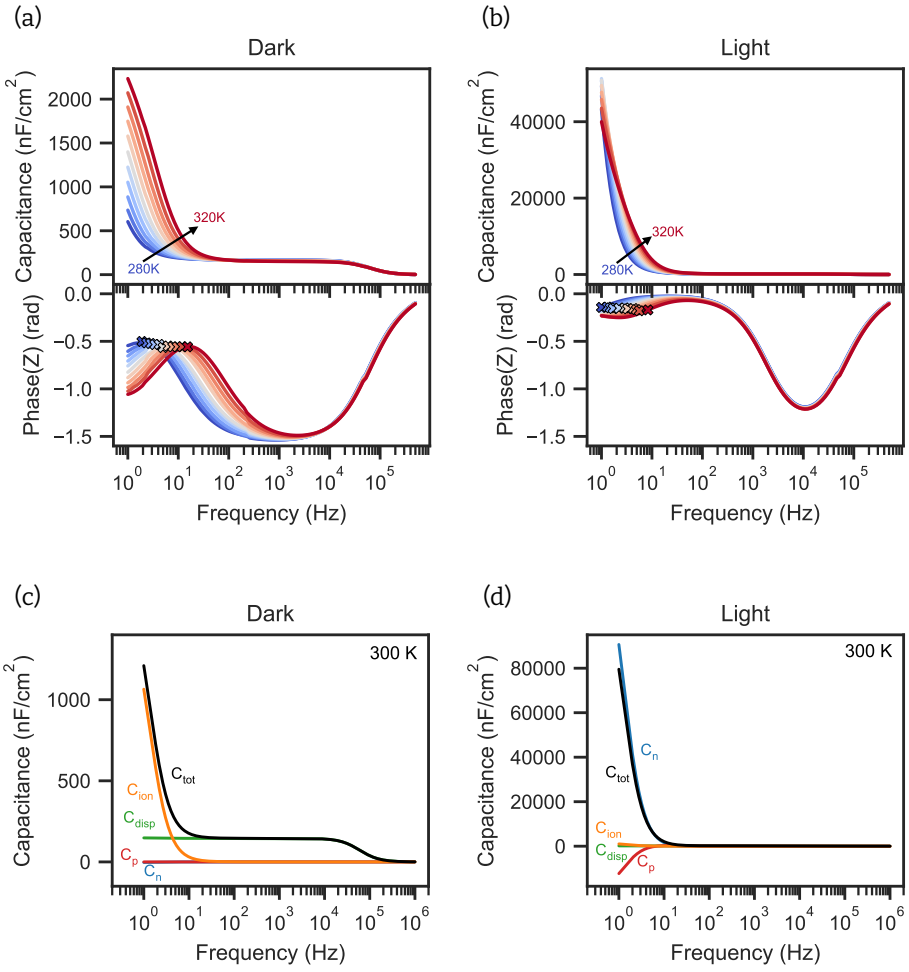

Figure 3.2: (a) Capacitance frequency measurements and corresponding phase angle in the dark at temperatures from 280 to 320 K in steps of 4 K. (b) Capacitance frequency measurements and corresponding phase angle in light. (c) Simulated contributions of electrons C_{n}, holes C_{p}, ions C_{ion}, and displacement C_{disp} to the total capacitance C_{tot} for the capacitance frequency simulations in the dark at 300 K. (d) Simulated contributions to the capacitance in light at 300 K.

tributions of charge storage and recombination to the overall capacitance according to Equation 3.5 (the derivation of the AC recombination is described in the Appendix). The result in Figure 3.D.6(a) illustrates that the out-of-phase recombination of electrons and holes, i.e., C_{R} in Equation 3.5 for electrons, dominates the capacitance rise at low frequencies. As this out-of-phase recombination is caused by the movement of ions, we can still estimate a characteristic time, for example, by choosing the inflection point between the low-frequency dip and peak, as illustrated in Figure 3.2(b) and reproduced with simulations in Figure 3.D.4(b). We note that we would ideally choose the minimum of the phase as the characteristic time, as it correlates to the characteristic time of the low-frequency semicircle in the Nyquist plot of the impedance. However, we cannot resolve this characteristic point at low temperatures because it is too slow to be measured within a reasonable time. This effect is also illustrated in the Nyquist plots in Figure 3.D.7, where only a small fraction of the low-frequency arc is visible at low temperatures (280 K). It is noteworthy that the observed large increase of the capacitance at low frequency is not limited to devices with perovskite/metal interfaces, i.e., devices with high interfacial recombination. It is commonly observed in high-performing perovskite solar cells and can generally be attributed to phase-delayed recombination due to mobile ions [25, 26].

3.2.2 Capacitance Transient Measurements

Next, we focus on the impact of mobile ions on transient capacitance measurements. In these, we measure the capacitance after applying a voltage pulse to the device. During the voltage pulse, mobile ions drift and accumulate at the perovskite/cathode interface. After the pulse, mobile ions drift back into the perovskite bulk, and we measure the capacitance. Figure 3.3(a) shows the transients measured in the dark. While the capacitance decreases with increasing temperature, the transients do not show significant changes over time. We attribute this to the fact that we mainly probe the geometrical capacitance at 10 kHz, which is not significantly modulated when ionic carriers redistribute within the device. In simulations, we only see a slight modulation of the capacitance in the dark (see Figure 3.D.4(c)), which might be hidden by noise in the experiment. This minor change of the capacitance originates from a modulation of C_{disp} as illustrated in 3.3(c). The observed temperature shift could originate from a temperature-dependent dielectric constant of the perovskite, as similarly observed in the literature [37]. In contrast to the device studied here, significant dynamics are usually observed when measuring capacitance transients of complete solar cells in the dark [23, 24], which we mainly attribute to the modulation of the transport layer capacitances in our previous work [26]. As no charge transport layers are present in

the devices studied here, the measured transients do not show any dynamics.

Interestingly, we observe significant dynamics when measuring capacitance transients while illuminating the device, as shown in Figure 3.3(b). The capacitance first decreases, followed by a rise before it stabilizes. The dip is strongly temperature-dependent, shifting from around 1 s at 280 K to 0.2 s at 320 K. We carry out drift-diffusion simulations of the capacitance transients with the same device parameters used in the capacitance frequency simulations. Initially, the mobile ions are accumulated at the cathode. Then, after removing the voltage pulse, the ions drift away from the cathode and accumulate at the anode (see Figure 3.D.8). Simulating the capacitance transient during the redistribution of ions reproduces the temperature-dependent dip of the capacitance, as shown in Figure 3.D.4(d). We can again distinguish between the different contributions to the capacitance, or more specifically, the modulation of the capacitance ΔC. These are illustrated in Figure 3.3(d) for 300 K. The capacitance decrease originates mainly from a decrease of C_{disp} and C_{n}, whereas the rise is dominated almost entirely by C_{p}. The contributions of C_{n} and C_{p} are again a result of the out-of-phase recombination, as Figure 3.D.6(b) clarifies. In contrast to the low-frequency capacitance, however, the out-of-phase recombination at 10 kHz is not impacted by the slow response of mobile ionic carriers to the AC perturbation. Instead, it mainly depends on the AC recombination dynamics at the electrode and the bulk due to electronic trap states. These AC recombination dynamics depend on a complex interplay between the electronic carrier distributions, capture coefficients, and the frequency of the applied AC potential. This can be seen in Equations 3.16 and 3.17 for the AC recombination rates of holes and electrons. When, for example, the trap capture rates of electrons c_n or holes c_p are varied, the amplitude of the rise of the capacitance changes (see Figure 3.D.9(a) and (b)). The probing frequency also impacts the rise of the capacitance, as illustrated in Figure 3.D.9(c). Even though the recombination rates are not directly dependent on mobile ions, they are indirectly dependent, as the distribution of mobile ions impacts the band profile. This is illustrated in Figure 3.3(e) for four specific times marked with dashed lines in Figure 3.3(d). Initially, when most ions are still accumulated at the cathode, the valence band at the anode and the conduction band at the cathode side have a high electronic carrier density. Then, as mobile ions drift away from the cathode and redistribute, the conduction and valence bands are flatter and populated more homogeneously across the perovskite. This change of the electronic carrier distribution across the perovskite ultimately impacts the AC recombination, resulting in the dip of the capacitance transients.

Interestingly, we have observed a dependency of the capacitance rise on illumination intensity in full perovskite solar cells in our previous work [26], which we attributed to

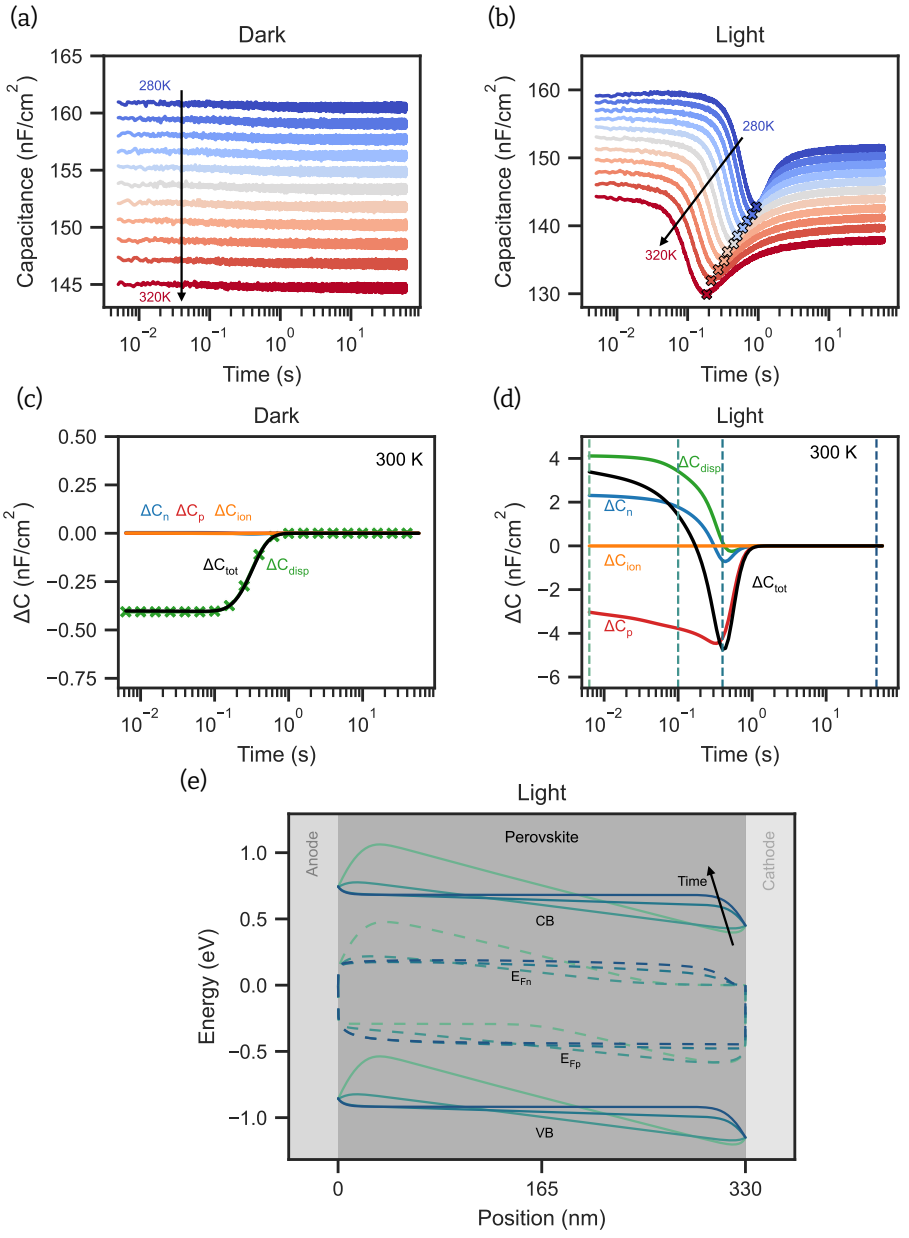

Figure 3.3: (a) Capacitance transient measurements and in the dark at temperatures from 280 to 320 K in steps of 4 K. (b) Capacitance transient measurements in light. (c) Simulated contributions of electrons ΔC_{n}, holes ΔC_{p}, ions ΔC_{ion}, and displacement ΔC_{disp} to the total capacitance ΔC_{tot} for the capacitance transient simulations in the dark at 300 K. (d) Simulated contributions to the capacitance transient in light at 300 K. Different points in time are marked with vertical dashed lines. (e) Band diagram under illumination at these times.

the modulation of the charge storage capacitance due to mobile ions. However, based on the results presented here, we hypothesize that the modulation of phase-delayed recombination can also impact the capacitance transients of complete devices.

3.2.3 Current Transient Measurements

Finally, we carry out current transient measurements. The results in the dark are shown in Figure 3.4(a). Here, we measure the current density after applying the same voltage pulse as in the capacitance transient measurements. Mobile ions are first accumulated at the cathode and then drift into the perovskite bulk, leading to a compensation current on the electrodes that can be extracted from the device. With drift-diffusion simulations, we can reproduce this behavior (see Figure 3.4(c)) and observe that the entire current is dominated by the ionic current J_{ion}. A decrease of the amplitude with lower temperatures is observed in Figure 3.4(a). This trend can be explained by the lower mobility of mobile ionic carriers at lower temperatures and can also be seen in the corresponding temperature-dependent simulations in Figure 3.D.4(e). To extract a characteristic time of the ionic signature, we fit a stretched exponential to the transients (see the Appendix for more details) and extract the amplitude J_0 and the characteristic times τ of the transients, which are shown in Figure 3.5(a).

The current transients under illumination are shown in Figure 3.4(b). Here, the current is not dominated by mobile ions, in contrast to the dark measurements. Instead, we are measuring the extraction of photogenerated carriers from the device. After the voltage pulse, mobile ions are accumulated at the cathode and depleted at the anode, as illustrated in Figure 3.D.8. This leads to a non-zero electric field in the perovskite bulk and, consequently, the extraction of electronic carriers. However, when the mobile ions redistribute, the electric field in the bulk vanishes (the conduction and valence bands in the bulk are flat at later times, see Figure 3.3(e)), and the recombination of photogenerated carriers in the bulk increases. This reduces the extracted electron and hole current, as shown in the simulations in Figure 3.4(d). Notably, the total currents of the simulations in Figure 3.4(d) and 3.D.4(f) do not match the absolute values of the measurements. We attribute this discrepancy to differences in the trap distribution in the measurements and simulations. From the measurements, we extract a characteristic time similar to the dark current transient measurements by fitting a stretched exponential to the transients.

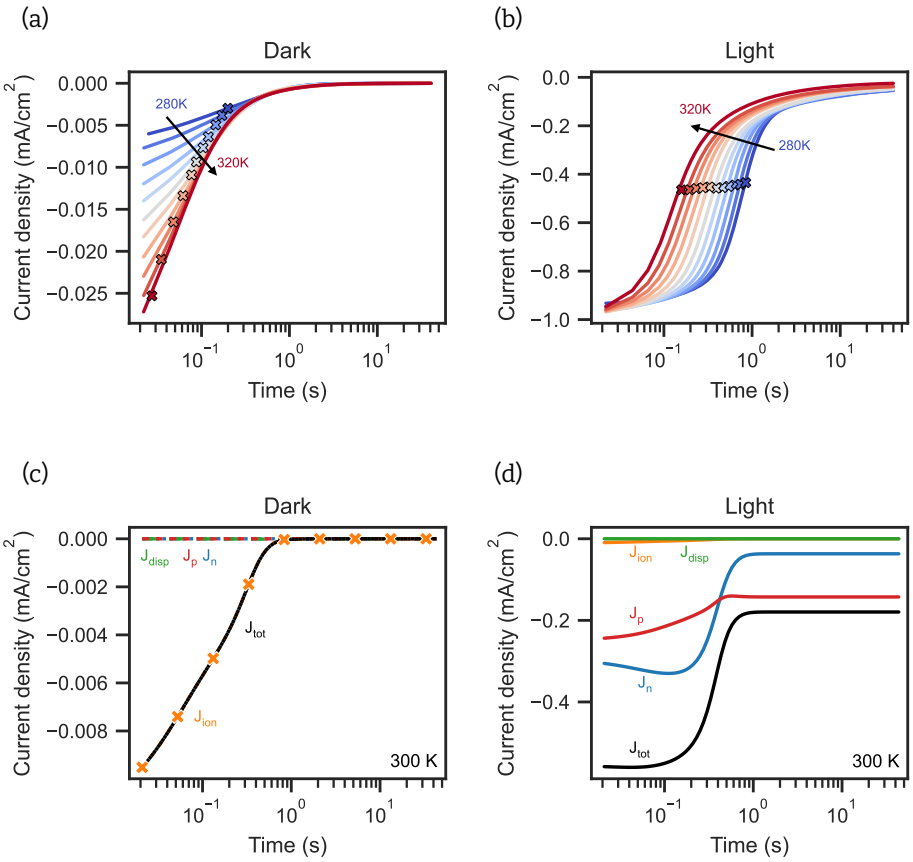

Figure 3.4: (a) Current transient measurements and in the dark at temperatures from 280 to 320 K in steps of 4 K.(b) Current transient measurements in light. (c) Simulated contributions of electrons J_{n}, holes J_{p}, ions J_{ion}, and displacement J_{disp} to the total current J_{tot} for the current transient simulations in the dark at 300 K. (d) Simulated contributions to the current transient in light at 300 K.

3.2.4 Extraction of Ionic Parameters

Now, we have qualitatively understood the origin of the different ionic signatures of the different measurements, and we can compare their characteristic times quantitatively. The extracted time constants are shown in Figure 3.5. Assuming a temperature-activated diffusion coefficient of the mobile ionic carriers [36, 38]:

$$D_{\mathrm{ion}}(T) = D_{\mathrm{ion},0} e^{-\frac{E_{\mathrm{A}}}{k_{\mathrm{B}} T}} \tag{3.6}$$

where k_{B} is the Boltzmann constant, and T is the temperature, we extract the activation energies E_{A} for each technique, listed in Table 3.1. For the capacitance frequency measurements in the dark and light, we extract activation energies of 0.40 eV and 0.42 eV, respectively. For the current transients, we extract 0.40 eV for the dark measurements and 0.35 eV for the light measurements from fitting the time constants. We additionally used the fitted amplitude of the current transients to determine the activation energy to be 0.40 eV in the dark, as shown in Figure 3.D.10. Lastly, we extract 0.34 eV for the capacitance transient measurement under illumination.

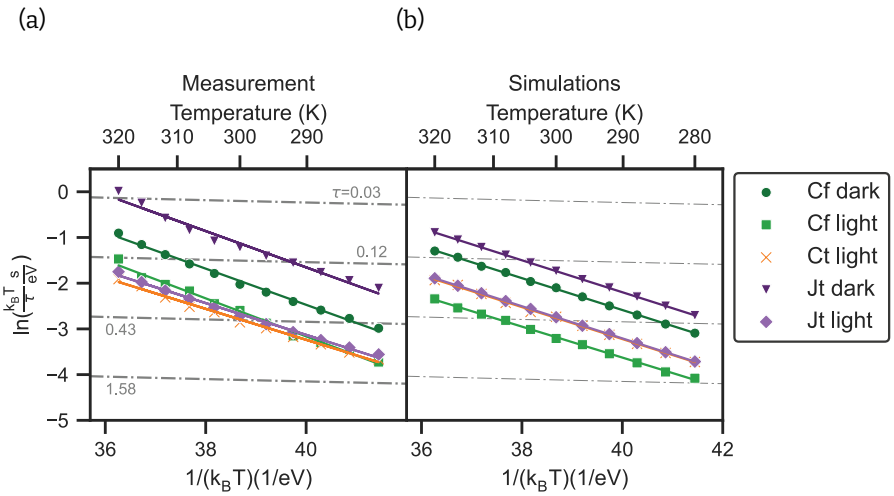

Figure 3.5: (a) Characteristic times of the ionic signatures at various temperatures of capacitance frequency (Cf), capacitance transient (Ct), and current transient (Jt) measurements. (b) Characteristic times of the simulations shown in Figure 3.D.4. The lines represent exponential fits accounting for the temperature-activated diffusion coefficient of the mobile ions to extract their activation energies listed in Table 3.1.

When comparing the extracted characteristic times for the different techniques, it is apparent that the ones measured under illumination are similar. The characteristic time of the capacitance frequency measurement in the dark is lower, followed by the characteristic time of the current transient measurements in the dark. We can roughly reproduce this trend when extracting the same characteristic time constants from simulated data, assuming an activation energy of 0.35 eV, as depicted in Figure 3.5(b). The capacitance transient and current transient simulations under illumination show the same time constants. In contrast, the extracted time constants of the capacitance frequency simulations under illumination are slightly higher. We attribute this to the fact that the low-frequency response of capacitance frequency is heavily influenced by the recombination dynamics in the device, leaving more parameters to influence the characteristic time. This also becomes clear in the extracted activation energy for the capacitance frequency simulation under illumination, which is 0.01 eV off from the set value of 0.35 eV. In contrast, the extracted activation energies of the other techniques are accurate. Lastly, the extracted time constants of the two dark methods, capacitance frequency and current transient, lie at lower values than the light simulations, following the same trend observed in the measurements.

Because we can reproduce all the different features observed in the different methods in the dark and under illumination, and the extracted characteristic times follow a similar trend, we can estimate the mobile ion density for the $MAPbI_3$ thin film to be around the values used for the drift-diffusion simulation, i.e., $2 \cdot 10^{18}\,cm^{-3}$ and a diffusion coefficient of $3.96 \cdot 10^{-11}\,cm^2/s$ at 300 K. Lastly, we estimate the activation energy as the average of the different measurements to be around 0.38 ± 0.03 eV.

	Activation energy (eV)	
Technique	Measurement	Simulation
Cf dark	0.40 ± 0.01	0.35
Cf light	0.42 ± 0.01	0.34
Ct light	0.34 ± 0.01	0.35
Jt dark	0.40 ± 0.02	0.35
Jt light	0.35 ± 0.01	0.35

Table 3.1: Extracted activation energies of the different techniques capacitance frequency (Cf), capacitance transient (Ct), and current transient (Jt) in dark and light. The error corresponds to the error of the fit. If a value does not have an error, the error of the fit is lower than the least significant digit. The corresponding fits to extract the activation energies are shown in Figure 3.5.

3.3 Conclusion

In this work, we have successfully combined three different measurements, namely capacitance frequency, capacitance transient, and current transient, to characterize mobile ions in a simple ITO/$MAPbI_3$/Au device. By choosing this simple structure, we could avoid the impact of transport layers, which often complicate the characterization of mobile ions. We measured all techniques at various temperatures, both in the dark and under low illumination conditions. We were able to identify ionic signatures in all measurements except for the dark capacitance transients. Using drift-diffusion simulations, we offered explanations for the origins of the different ionic features. In the dark, the observed features originate directly from the ionic carriers within the device. In contrast, the features in the light measurements are dominated by the modulation of recombination dynamics due to mobile ions. More specifically, the mobile ion distribution within the device directly impacts the electronic carrier distribution and, in turn, the recombination dynamics, ultimately resulting in observable ionic features in the different measurements. These findings underline the importance of taking mobile ions into account when characterizing recombination dynamics of perovskite semiconductors. Lastly, we extracted and compared the characteristic time constants of the different ionic features in the measurements and the simulations. This allowed us to estimate the mobile ions' density, diffusion coefficient, and activation energy in the $MAPbI_3$ semiconductor.

Chapter appendix

3.A Experimental Details

Device Fabrication

Materials: Acetone (anhydrous, ≥99.8%) and iso-propanol (IPA, anhydrous, ≥99.8%) were purchased from Biosolve. PbI_2 (99.99%) was purchased from TCI. Methylammonium iodide (MAI, purity not listed) was purchased from Solaronix. N,N-Dimethylamine (DMF, anhydrous, ≥99.8%) and chlorobenzene (anhydrous, ≥99.8%) were purchased from Sigma Aldrich. All materials were used without further purification.

Substrates: Patterned quartz/ITO substrates were cleaned by scrubbing with water and soap, followed by sequential sonication in deionized water, acetone, and IPA (15 min. per liquid).

Perovskite layer: All processing steps were performed in a nitrogen-filled glovebox. For the precursor solution, 322.8 mg MAI was dissolved in 2 ml dimethylformamide in a vial. The vial was stirred vigorously, and the clear, colorless liquid was added to another vial containing 936.0 mg PbI_2. The solution was then stirred overnight (400 rpm, 50 °C) to ensure complete dissolution of the powders. The $MAPbI_3$ precursor solution was then filtered with a 0.2 µm PTFE filter. The resulting bright yellow mixture was spin-coated using a spin coating robot (Sciprios SpinBot, 4000 rpm, 30 s, 4000 rpm/s acceleration) on the quartz/ITO substrates. As an anti-solvent, 250 µl of chlorobenzene was added to the spinning substrates after 5 s of spinning. The substrates were annealed (100 °C for 10 min) immediately after spin coating, resulting in $MAPbI_3$ perovskite thin films.

Top electrode: For the top electrode, a thermal evaporator was used to evaporate 100 nm of gold through a shadow mask at a pressure of $1 \cdot 10^{-6}$ mbar onto the perovskite layer.

Electrical Characterization

All electrical measurements were carried out inside a Janis VPF-100 liquid nitrogen cryostat. During the measurements, the pressure in the cryostat was below $5 \cdot 10^{-6}$ mbar. The temperature was controlled using a Lakeshore 335 temperature controller and was stabilized for 10 min before each measurement cycle. We used the

white-light LED SOLIS-3C by Thorlabs for measurements with illumination.
The capacitance frequency measurements were carried out using the MFIA by Zurich instruments with an AC voltage perturbation of 20 mV and sweeping the frequency from 1 Hz to 500 kHz. The capacitance transient measurements were carried out with the same voltage perturbation of 20 mV at a constant frequency of 10 kHz. For the voltage pulse, 1 V was applied to the ITO electrode for 2.5 s. The current transient measurements were acquired using an Agilent B2902A. Here, we also applied a voltage pulse of 1 V for 2.5 s. The JV measurements were acquired with the Agilent B2902A from −1 to 1 V with a scan speed of 0.5 V/s.

Thin Film Characterization

Scanning electron microscopy (SEM) images of the perovskite devices on ITO were recorded in vacuum on a FEI Verios 460. The accelerating voltage used was 5 kV and 100 pA current was used.
X-ray diffraction (XRD) patterns of the perovskite solar cell devices on ITO were recorded on a Bruker D2 Phaser with Cu $\mathrm{K}\alpha$ X-rays with $\lambda = 1.54\,\text{Å}$ as the X-ray source. A 0.1 s exposure time, 0.6 mm slit width, 1 mm knife height, and 0.016° (2θ) step size were used.

Drift-Diffusion Simulations

Drift-diffusion simulations were carried out with Setfos by Fluxim, and the parameter set in Table 3.D.1.

3.B Fitting of Current Transients

To extract characteristic times from the current transient measurements, we fit the decays with stretched exponential decays:

$$J(t) = J_0 e^{-(\frac{t}{\tau})^{\alpha}} + J_{\text{offset}}$$

We chose to fit the transients with a stretched exponential because the quality of fits was better compared to single exponential fits. The stretched exponential function could indicate that a distribution of timescales describes the long-time decay most accurately [39]. Figure 3.B.1 shows an example fit of the current transient in the dark at 300 K.

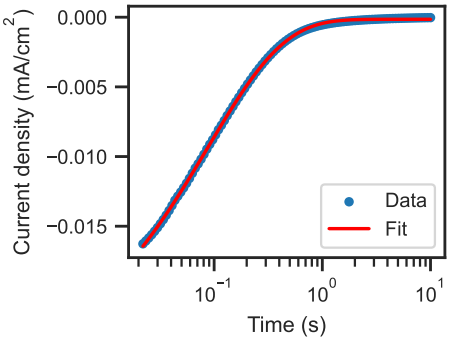

Figure 3.B.1: Example fit of a current transient measured in the dark at 300 K

3.C Derivation of AC Recombination

We can derive the AC recombination constants of electrons $\tilde{R}_\mathrm{n}$ and holes $\tilde{R}_\mathrm{p}$ assuming hole traps similar to [40]. We start with the DC recombination rates R_p and R_n [41]:

$$R_\mathrm{p} = c_\mathrm{p} p (N_\mathrm{t} - p_\mathrm{t}) - e_\mathrm{p} p_\mathrm{t} \tag{3.7}$$

$$R_\mathrm{n} = c_\mathrm{n} n p_\mathrm{t} - e_\mathrm{n} (N_\mathrm{t} - p_\mathrm{t}) \tag{3.8}$$

where c_n and c_p are the capture coefficients for electrons and holes, n and p are the electron and hole densities, N_t is the trap density, p_t is the density of trapped holes, and e_n and e_p are the electron and hole emission rates. The rate of change of trapped holes is:

$$\frac{dp_\mathrm{t}}{dt} = R_\mathrm{p} - R_\mathrm{n} \tag{3.9}$$

We then extend the different variables into DC and AC parts, for example, for holes by:

$$p = p_0 + \tilde{p} e^{i\omega t} \tag{3.10}$$

If we assume that emission is negligible compared to recombination (as is the case for deep traps in our simulations), we can omit the emission terms in Equations 3.7 and 3.8. Together with Equation 3.9 this results in:

$$i\omega \tilde{p}_\mathrm{t} e^{i\omega t} = c_\mathrm{p}(p_0 + \tilde{p} e^{i\omega t})(N_\mathrm{t} - (p_{\mathrm{t}0} + \tilde{p}_\mathrm{t} e^{i\omega t})) - c_\mathrm{n}(n_0 + \tilde{n} e^{i\omega t})(p_{\mathrm{t}0} + \tilde{p}_\mathrm{t} e^{i\omega t}) \tag{3.11}$$

We divide this into an DC and an AC part, where we omit the terms of higher order frequency:

$$0 = c_\mathrm{p} p_0 (N_\mathrm{t} - p_{\mathrm{t}0}) - c_\mathrm{n} n_0 p_{\mathrm{t}0} \tag{3.12}$$

$$i\omega \tilde{p}_\mathrm{t} = c_\mathrm{p}(\tilde{p}(N_\mathrm{t} - p_{\mathrm{t}0}) - p_0 \tilde{p}_\mathrm{t}) - c_\mathrm{n}(n_0 \tilde{p}_\mathrm{t} + \tilde{n} p_{\mathrm{t}0}) \tag{3.13}$$

Solving for $p_{\mathrm{t}0}$ and $\tilde{p}_t$ we get:

$$p_{\mathrm{t}0} = \frac{N_\mathrm{t} c_\mathrm{p} p_0}{c_\mathrm{n} n_0 + c_\mathrm{p} p_0} \tag{3.14}$$

$$\tilde{p}_t = \frac{c_\mathrm{p}\tilde{p}(N_\mathrm{t} - p_{\mathrm{t}0}) - c_\mathrm{n}\tilde{n} p_{\mathrm{t}0}}{i\omega + c_\mathrm{p} p_0 + c_\mathrm{n} n_0} \tag{3.15}$$

Substituting Equation 3.15 into the AC extension of Equation 3.7 and 3.8, we finally get an expression for the AC recombination rate for holes and electrons:

$$\begin{aligned} \tilde{R}_\mathrm{p} &= c_\mathrm{p}(\tilde{p}(N_\mathrm{t} - p_{\mathrm{t}0}) - p_0 \tilde{p}_\mathrm{t}) \\ &= c_\mathrm{p} c_\mathrm{n} \frac{\tilde{p}(N_\mathrm{t} - p_{\mathrm{t}0})(n_0 + i\omega/c_\mathrm{n}) + \tilde{n} p_{\mathrm{t}0} p_0}{i\omega + c_\mathrm{p} p_0 + c_\mathrm{n} n_0} \end{aligned} \tag{3.16}$$

$$\begin{aligned} \tilde{R}_\mathrm{n} &= c_\mathrm{n} n_0 \tilde{p}_\mathrm{t} + c_\mathrm{n} \tilde{n} p_{\mathrm{t}0} \\ &= c_\mathrm{n} c_\mathrm{p} \frac{n_0 \tilde{p}(N_\mathrm{t} - p_{\mathrm{t}0}) + \tilde{n} p_{\mathrm{t}0}(p_0 + i\omega/c_\mathrm{p})}{i\omega + c_\mathrm{p} p_0 + c_\mathrm{n} n_0} \end{aligned} \tag{3.17}$$

3.D Additional Information

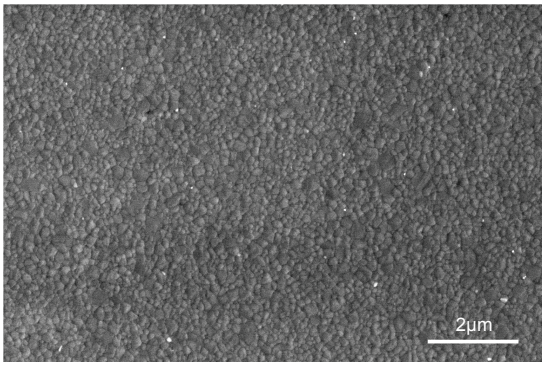

Figure 3.D.1: Scanning electron microscopy image of a $MAPbI_3$ thin film on ITO.

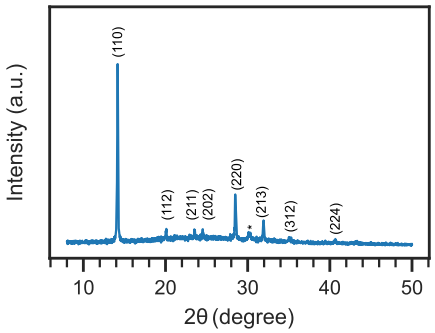

Figure 3.D.2: X-ray diffraction pattern of the $MAPbI_3$ thin film on ITO. The crystal planes were assigned by comparing the 2θ angles to literature [42]. The peak at 30° is due to the ITO.

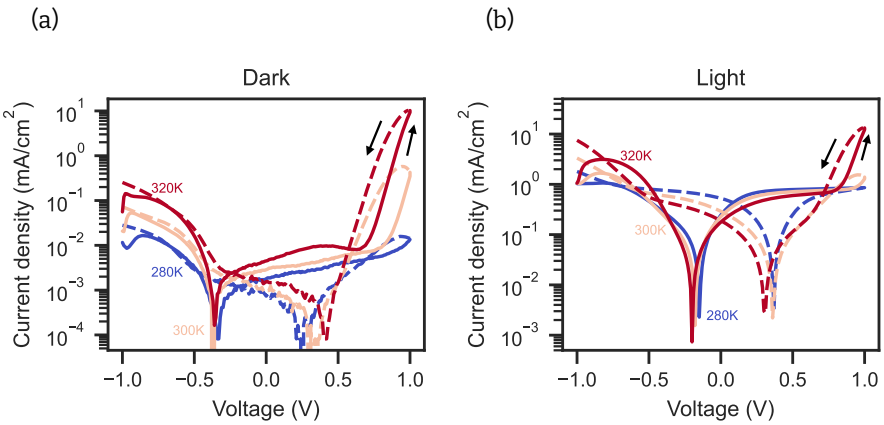

Figure 3.D.3: Current-density vs. voltage measurements of a ITO/$MAPbI_3$/Au device in (a) dark and (b) light (2.3 mW/cm^2) at three different temperatures. The measurements were carried out with a scan speed of 0.5 V/s from −1 to 1 V. The arrows indicate the measurement direction.

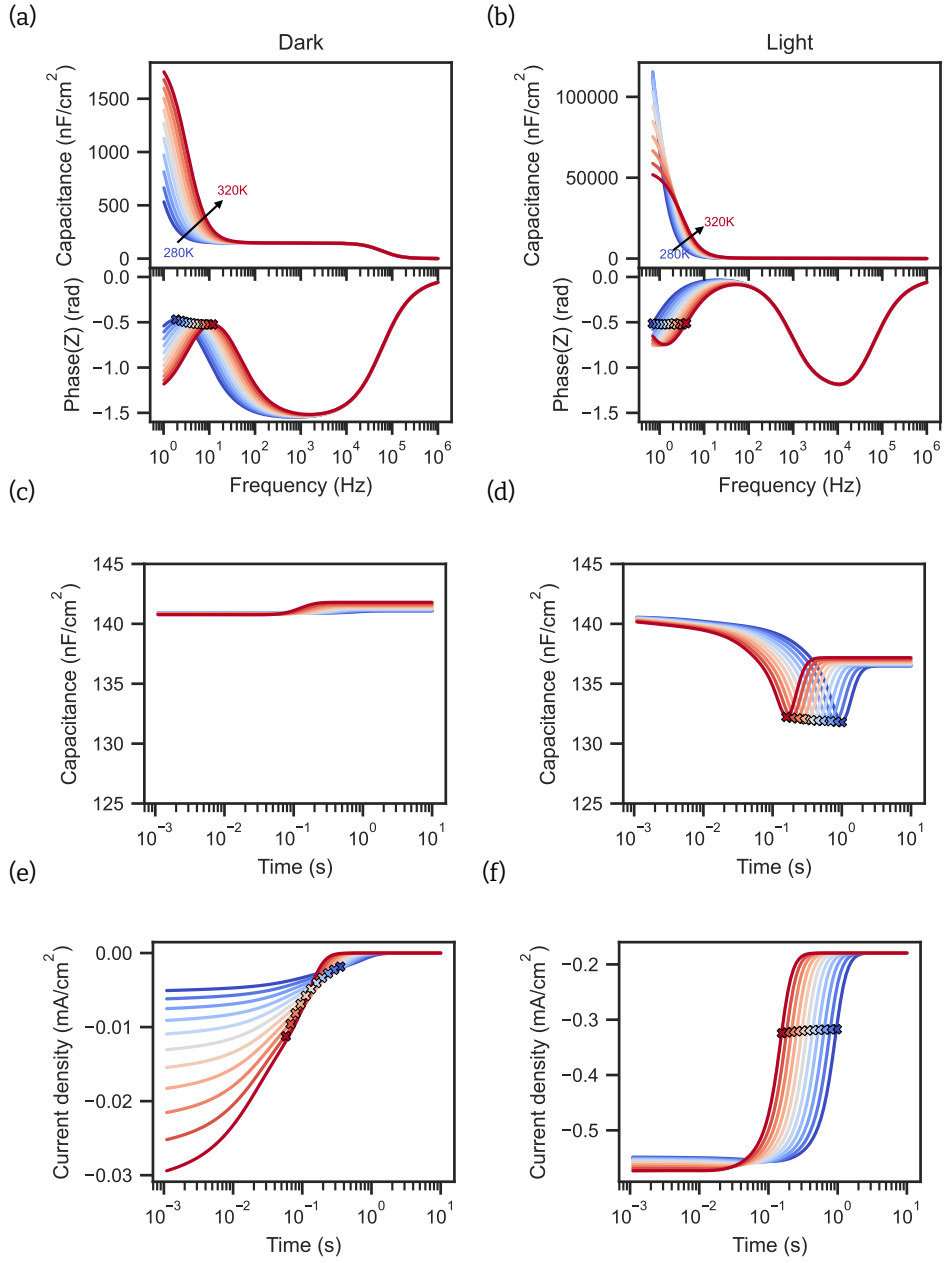

Figure 3.D.4: Different simulations of a perovskite semiconductor at temperatures from 280-320 K in steps of 4 K, using the parameters in Table 3.D.1. All figures in the left column contain simulations in the dark. The right column contains simulations under illumination with a white LED at an irradiance of 2.3 mW/cm^2. (a) Capacitance frequency simulations in the dark and (b) in the light. (a) Phase(Z) simulations in the dark and (b) under illumination. (c) Capacitance transient simulations in the dark and (d) in light. (e) Current transient simulations in the dark and (f) in light.

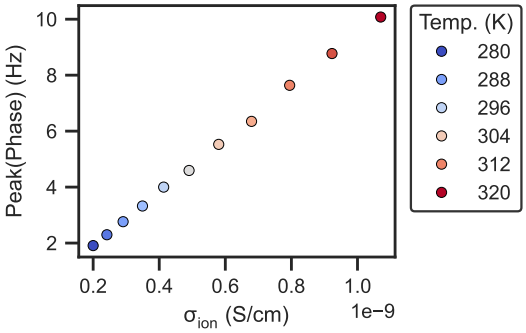

Figure 3.D.5: Illustration of the proportionality between the characteristic time of the phase peak of the Cf simulations in the dark of Figure 3.D.4(a) and the ionic conductivity of the perovskite layer.

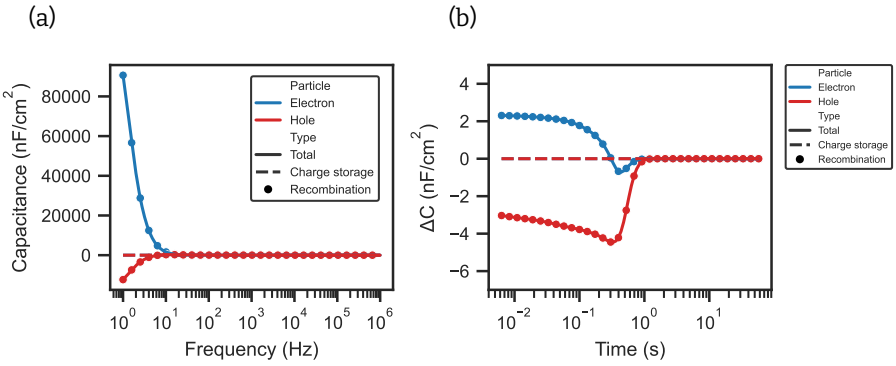

Figure 3.D.6: Contributions of the charge storage and recombination of electrons and holes to the capacitance for (a) the capacitance frequency simulations under illumination shown in Figure 3.2(d) and (b) capacitance transient simulations under illumination in 3.3(d).

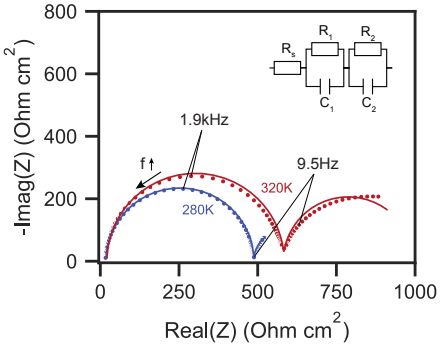

Figure 3.D.7: Nyquist plots of the impedance measurements of the device under illumination at 280 K and 320 K. The lines correspond to fits with the illustrated equivalent circuit. At 280 K, the majority of the low-frequency semicircle is not resolved. At 320 K, the low-frequency fit diverges from the data, presumably because of the distribution of timescales for the low-frequency regime.

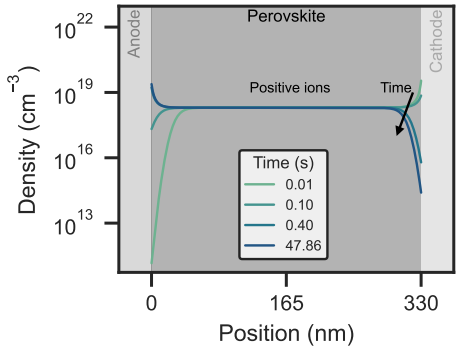

Figure 3.D.8: Simulations of mobile positive ions at 300 K within the perovskite at different times after removing a voltage pulse.

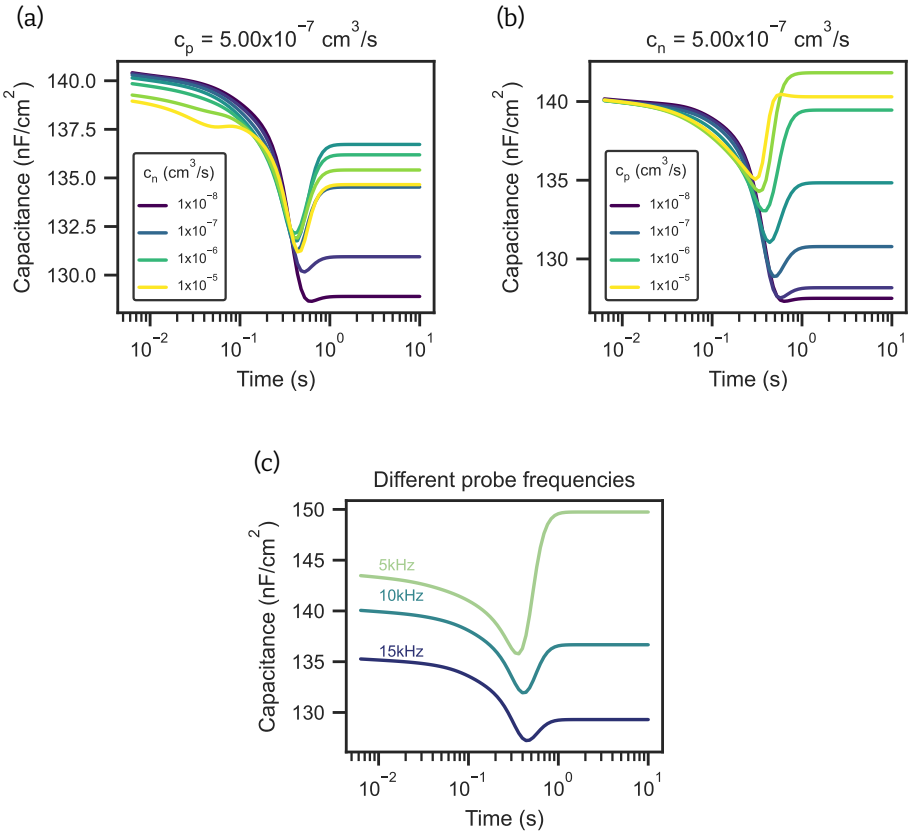

Figure 3.D.9: Simulations of capacitance transients, illustrating the dependency of the capacitance rise on the (a) electron capture rate, (b) hole capture rate, and (c) probing frequency.

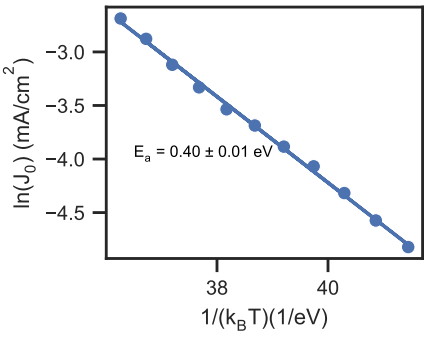

Figure 3.D.10: Extracted activation energy of the amplitude J_0 of the stretched exponential decay of the transient current measurements shown in Figure 3.4(a) in the main text.

Table 3.D.1: Parameters used for the drift-diffusion simulations.

Parameter	Value	Comment
Band gap perovskite (eV)	1.6	From [43]
Electron affinity (eV)	3.9	From [43]
Dielectric constant ϵ_{r}	54	Estimated from capacitance at 10 kHz and 300 K
Thickness perovskite (nm)	330	Measured with profilometer
Effective density of states conduction band $N_{0,\mathrm{CB}}$ (cm^{-3})	$8 \cdot 10^{18}$	
Effective density of states valence band $N_{0,\mathrm{VB}}$ (cm^{-3})	$8 \cdot 10^{18}$	
Bimolecular recombination coefficient (cm^3/s)	$1 \cdot 10^{-11}$	
Hole trap density N_{t} (cm^{-3})	$9 \cdot 10^{15}$	
Capture rate electrons c_{n} (cm^3/s)	$5 \cdot 10^{-7}$	
Capture rate holes c_{p} (cm^3/s)	$5 \cdot 10^{-7}$	
Trap energy with respect to VB E_{t} (eV)	0.7	
Mobility electrons μ_{n} ($\mathrm{cm}^2/\mathrm{Vs}$)	11	In the range of [25, 44]
Mobility holes μ_{p} ($\mathrm{cm}^2/\mathrm{Vs}$)	11	In the range of [25, 44]
Mobile positive ion density N_{ion} (cm^{-3})	$2 \cdot 10^{18}$	
Immobile negative ion density N_{nion} (cm^{-3})	$2 \cdot 10^{18}$	
Diffusion coefficient of ions at 300 K $D_{\mathrm{ion},300\mathrm{K}}$ (cm^2/s)	$3.96 \cdot 10^{-11}$	
Activation energy of diffusion coefficient of ions $E_{\mathrm{a,ion}}$ (eV)	0.35	
Anode work function $W_{\mathrm{f,anode}}$ (eV)	4.65	
Cathode work function $W_{\mathrm{f,cathode}}$ (eV)	4.35	
Series resistance R_{s} ($\Omega\ \mathrm{cm}^2$)	18.375	

Bibliography

[1] W. Fu *et al.*, "Stability of Perovskite Materials and Devices", *Materials Today*, vol. 58, pp. 275–296, 2022.

[2] E. J. Juarez-Perez, L. K. Ono, M. Maeda, Y. Jiang, Z. Hawash, and Y. Qi, "Photodecomposition and Thermal Decomposition in Methylammonium Halide Lead Perovskites and Inferred Design Principles to Increase Photovoltaic Device Stability", *Journal of Materials Chemistry A*, vol. 6, no. 20, pp. 9604–9612, 2018.

[3] B. Conings *et al.*, "Intrinsic Thermal Instability of Methylammonium Lead Trihalide Perovskite", *Advanced Energy Materials*, vol. 5, no. 15, p. 1 500 477, 2015.

[4] R. Gottesman *et al.*, "Photoinduced Reversible Structural Transformations in Free-Standing $CH_3NH_3PbI_3$ Perovskite Films", *The Journal of Physical Chemistry Letters*, vol. 6, no. 12, pp. 2332–2338, 2015.

[5] L. Xiang *et al.*, "Progress on the Stability and Encapsulation Techniques of Perovskite Solar Cells", *Organic Electronics*, vol. 106, p. 106 515, 2022.

[6] Y. Wang *et al.*, "Encapsulation and Stability Testing of Perovskite Solar Cells for Real Life Applications", *ACS Materials Au*, vol. 2, no. 3, pp. 215–236, 2022.

[7] L. Bertoluzzi *et al.*, "Mobile Ion Concentration Measurement and Open-Access Band Diagram Simulation Platform for Halide Perovskite Solar Cells", *Joule*, vol. 4, no. 1, pp. 109–127, 2020.

[8] J. Diekmann *et al.*, "Determination of Mobile Ion Densities in Halide Perovskites via Low-Frequency Capacitance and Charge Extraction Techniques", *The Journal of Physical Chemistry Letters*, vol. 14, no. 18, pp. 4200–4210, 2023.

[9] J. Thiesbrummel *et al.*, "Ion-Induced Field Screening as a Dominant Factor in Perovskite Solar Cell Operational Stability", *Nature Energy*, vol. 9, no. 6, pp. 664–676, 2024.

[10] Q. Dong, L. Lei, J. Mendes, and F. So, "Operational Stability of Perovskite Light Emitting Diodes", *Journal of Physics: Materials*, vol. 3, no. 1, p. 012 002, 2020.

[11] L. Zhang *et al.*, "Suppressing Ion Migration Enables Stable Perovskite Light-Emitting Diodes with All-Inorganic Strategy", *Advanced Functional Materials*, vol. 30, no. 40, p. 2 001 834, 2020.

[12] J. Cai *et al.*, "Ion Migration in the All-Inorganic Perovskite $CsPbBr_3$ and Its Impacts on Photodetection", *The Journal of Physical Chemistry C*, vol. 126, no. 23, pp. 10 007–10 013, 2022.

[13] B. P. Finkenauer, Akriti, K. Ma, and L. Dou, "Degradation and Self-Healing in Perovskite Solar Cells", *ACS Applied Materials & Interfaces*, vol. 14, no. 21, pp. 24 073–24 088, 2022.

[14] L. J. F. Hart *et al.*, "More is Different: Mobile Ions Improve the Design Tolerances of Perovskite Solar Cells", *Energy & Environmental Science*, vol. 17, no. 19, pp. 7107–7118, 2024.

[15] D. J. Slotcavage, H. I. Karunadasa, and M. D. McGehee, "Light-Induced Phase Segregation in Halide-Perovskite Absorbers", *ACS Energy Letters*, vol. 1, no. 6, pp. 1199–1205, 2016.

[16] H. Jun *et al.*, "Soft X-ray Characterization of Halide Perovskite Film by Scanning Transmission X-Ray Microscopy", *Scientific Reports*, vol. 12, no. 1, p. 4520, 2022.

[17] S. P. Harvey, Z. Li, J. A. Christians, K. Zhu, J. M. Luther, and J. J. Berry, "Probing Perovskite Inhomogeneity beyond the Surface: TOF-SIMS Analysis of Halide Perovskite Photovoltaic Devices", *ACS Applied Materials & Interfaces*, vol. 10, no. 34, pp. 28 541–28 552, 2018.

[18] V. Srivastava, A. Alexander, B. Anitha, and M. A. G. Namboothiry, "Impedance Spectroscopy Study of Defect/Ion Mediated Electric Field and Its Effect on the Photovoltaic Performance of Perovskite Solar Cells Based on Different Active Layers", *Solar Energy Materials and Solar Cells*, vol. 237, p. 111 548, 2022.

[19] E. von Hauff and D. Klotz, "Impedance Spectroscopy for Perovskite Solar Cells: Characterisation, Analysis, and Diagnosis", *Journal of Materials Chemistry C*, vol. 10, no. 2, pp. 742–761, 2022.

[20] J. Thiesbrummel *et al.*, "Universal Current Losses in Perovskite Solar Cells Due to Mobile Ions", *Advanced Energy Materials*, vol. 11, no. 34, p. 2 101 447, 2021.

[21] G. Y. Kim, A. Senocrate, Y.-R. Wang, D. Moia, and J. Maier, "Photo-Effect on Ion Transport in Mixed Cation and Halide Perovskites and Implications for Photo-Demixing", *Angewandte Chemie International Edition*, vol. 60, no. 2, pp. 820–826, 2021.

[22] D. Walter *et al.*, "Transient Photovoltage in Perovskite Solar Cells: Interaction of Trap-Mediated Recombination and Migration of Multiple Ionic Species", *The Journal of Physical Chemistry C*, vol. 122, no. 21, pp. 11 270–11 281, 2018.

[23] M. H. Futscher *et al.*, "Quantification of Ion Migration in $CH_3NH_3PbI_3$ Perovskite Solar Cells by Transient Capacitance Measurements", *Materials Horizons*, vol. 6, no. 7, pp. 1497–1503, 2019.

[24] S. Reichert, Q. An, Y.-W. Woo, A. Walsh, Y. Vaynzof, and C. Deibel, "Probing the Ionic Defect Landscape in Halide Perovskite Solar Cells", *Nature Communications*, vol. 11, no. 1, p. 6098, 2020.

[25] D. A. Jacobs *et al.*, "The Two Faces of Capacitance: New Interpretations for Electrical Impedance Measurements of Perovskite Solar Cells and Their Relation to Hysteresis", *Journal of Applied Physics*, vol. 124, no. 22, p. 225 702, 2018.

[26] M. C. Schmidt, E. Gutierrez-Partida, M. Stolterfoht, and B. Ehrler, "Impact of Mobile Ions on Transient Capacitance Measurements of Perovskite Solar Cells", *PRX Energy*, vol. 2, no. 4, p. 043 011, 2023.

3

[27] S. Ravishankar, Z. Liu, U. Rau, and T. Kirchartz, "Multilayer Capacitances: How Selective Contacts Affect Capacitance Measurements of Perovskite Solar Cells", *PRX Energy*, vol. 1, no. 1, p. 013 003, 2022.

[28] R. A. Awni *et al.*, "Influence of Charge Transport Layers on Capacitance Measured in Halide Perovskite Solar Cells", *Joule*, vol. 4, no. 3, pp. 644–657, 2020.

[29] D. V. Lang, "Deep-Level Transient Spectroscopy: A New Method to Characterize Traps in Semiconductors", *Journal of Applied Physics*, vol. 45, no. 7, pp. 3023–3032, 1974.

[30] A. O. Alvarez *et al.*, "Ion Migration and Space-Charge Zones in Metal Halide Perovskites Through Short-Circuit Transient Current and Numerical Simulations", *Advanced Electronic Materials*, vol. 10, no. 11, p. 2 400 241, 2024.

[31] A. O. Alvarez *et al.*, "Ionic Field Screening in $MAPbBr_3$ Crystals Revealed from Remnant Sensitivity in X-ray Detection", *ACS Physical Chemistry Au*, vol. 3, no. 4, pp. 386–393, 2023.

[32] G. Richardson *et al.*, "Can Slow-Moving Ions Explain Hysteresis in the Current–Voltage Curves of Perovskite Solar Cells?", *Energy & Environmental Science*, vol. 9, no. 4, pp. 1476–1485, 2016.

[33] I. Anusca *et al.*, "Dielectric Response: Answer to Many Questions in the Methylammonium Lead Halide Solar Cell Absorbers", *Advanced Energy Materials*, vol. 7, no. 19, p. 1 700 600, 2017.

[34] M. H. Futscher, M. K. Gangishetty, D. N. Congreve, and B. Ehrler, "Quantifying Mobile Ions and Electronic Defects in Perovskite-Based Devices with Temperature-Dependent Capacitance Measurements: Frequency vs Time Domain", *The Journal of Chemical Physics*, vol. 152, no. 4, p. 044 202, 2020.

[35] O. Almora, I. Zarazua, E. Mas-Marza, I. Mora-Sero, J. Bisquert, and G. Garcia-Belmonte, "Capacitive Dark Currents, Hysteresis, and Electrode Polarization in Lead Halide Perovskite Solar Cells", *The Journal of Physical Chemistry Letters*, vol. 6, no. 9, pp. 1645–1652, 2015.

[36] W. Zhu, S. Wang, X. Zhang, A. Wang, C. Wu, and F. Hao, "Ion Migration in Organic–Inorganic Hybrid Perovskite Solar Cells: Current Understanding and Perspectives", *Small*, vol. 18, no. 15, p. 2 105 783, 2022.

[37] M. N. F. Hoque, N. Islam, Z. Li, G. Ren, K. Zhu, and Z. Fan, "Ionic and Optical Properties of Methylammonium Lead Iodide Perovskite across the Tetragonal–Cubic Structural Phase Transition", *ChemSusChem*, vol. 9, no. 18, pp. 2692–2698, 2016.

[38] C. Eames, J. M. Frost, P. R. F. Barnes, B. C. O'Regan, A. Walsh, and M. S. Islam, "Ionic Transport in Hybrid Lead Iodide Perovskite Solar Cells", *Nature Communications*, vol. 6, no. 1, p. 7497, 2015.

[39] S. Reichert, J. Flemming, Q. An, Y. Vaynzof, J.-F. Pietschmann, and C. Deibel, "Ionic-Defect Distribution Revealed by Improved Evaluation of Deep-Level Transient Spectroscopy on Perovskite Solar Cells", *Physical Review Applied*, vol. 13, no. 3, p. 034 018, 2020.

[40] M. Gaitan and I. D. Mayergoyz, "A Numerical Analysis for the Small-Signal Response of the MOS Capacitor", *Solid-State Electronics*, vol. 32, no. 3, pp. 207–213, 1989.

[41] W. Shockley and W. T. Read, "Statistics of the Recombinations of Holes and Electrons", *Physical Review*, vol. 87, no. 5, pp. 835–842, 1952.

[42] X. Guo, C. McCleese, C. Kolodziej, A. C. S. Samia, Y. Zhao, and C. Burda, "Identification and Characterization of the Intermediate Phase in Hybrid Organic–Inorganic $MAPbI_3$ Perovskite", *Dalton Transactions*, vol. 45, no. 9, pp. 3806–3813, 2016.

[43] M. Caputo *et al.*, "Electronic Structure of $MAPbI_3$ and $MAPbCl_3$: Importance of Band Alignment", *Scientific Reports*, vol. 9, no. 1, p. 15 159, 2019.

[44] C. Q. Xia *et al.*, "Limits to Electrical Mobility in Lead-Halide Perovskite Semiconductors", *The Journal of Physical Chemistry Letters*, vol. 12, no. 14, pp. 3607–3617, 2021.

4

How Many Ions Can Electrical Measurements Detect?

Abstract

Mobile ions in perovskite solar cells are one of the main reasons for their limited stability. Electrical measurements like current transient, capacitance transient, capacitance frequency, and low-frequency Mott-Schottky measurements are becoming increasingly popular in quantifying the density of mobile ions. However, here, we show that these techniques suffer from a limit for the maximum determinable ion density. With the help of drift-diffusion simulations, we show that when mobile ions screen the built-in field, current transient, capacitance transient, capacitance frequency, and low-frequency Mott-Schottky measurements saturate. Then, only the ionic conductivity can be determined, but not the ion density. The exact value of this upper limit depends on many device parameters. Therefore, a reasonable estimation of various device parameters, like the potential drops in the charge transport layers, is necessary when quantifying mobile ion densities.

Authors: Moritz C. Schmidt and Bruno Ehrler

Published in: ACS Energy Letters, Volume: 10, Issue: 5, Pages: 2457–2460, April 2025

https://doi.org/10.1021/acsenergylett.5c00887

4.1 Introduction

In recent years, mobile ions have been assigned to various degradation mechanisms in perovskite solar cells. Some of these include non-reversible degradation like migration into charge transport layers (CTLs) [1], or reaction with electrodes [2]. Others focus on the electrostatic effects due to mobile ions. Most importantly, the accumulation of a large density of mobile ions at the interface between perovskite and charge transport layers can lead to screening of the built-in potential, which can result in enhanced interface and bulk recombination, reducing the short-circuit current density and fill-factor [3]. The accumulation of mobile ions has also been connected to a decrease in open-circuit voltage [4]. To obtain a comprehensive understanding of the impact of mobile ions on the device physics of perovskite solar cells, accurately determining the density and diffusion coefficient of mobile ions in perovskites is of utmost importance. However, measured ion densities cover multiple orders of magnitude from 10^{15} cm^{-3} to 10^{19} cm^{-3} [3, 5–7]. To determine ion densities, electrical measurements like transient current measurements, also known as bias-assisted charge extraction [3], capacitance-frequency, also known as impedance spectroscopy [8, 9], transient capacitance measurements, also known as transient ion drift measurements [9], and low-frequency Mott-Schottky measurements [5] have been applied. Here, we illustrate that it becomes impossible to determine the ion density if it is high enough to screen a significant portion of the built-in field.

4.2 Results and Discussion

To illustrate the difficulty of extracting high ion densities from the different electrical measurements, we carried out drift-diffusion simulations. For the transport layers, we chose parameters resembling thin organic transport layers 2PACz and C_{60}. We assume that ionic transport is mediated by halide vacancies [10–12], and their charge is compensated by non-mobile negatively charged ions [13]. We carried out the simulations for different mobile ion densities ranging from 10^{16} cm^{-3} to 10^{20} cm^{-3}, and a typical ionic conductivity $\sigma_{\mathrm{ion}} = e\mu_{\mathrm{ion}}N_{\mathrm{ion}}$ of $1.6 \cdot 10^{-10}$ S/cm, where e is the elementary charge, μ_{ion} is the ionic mobility, and N_{ion} is the density of mobile ions. The complete simulation parameters are listed in Table 4.A.1 in the Appendix. We emphasize that the absolute values of the presented results are only valid for the parameter set studied in this work.

4.2.1 Impact of Ionic Field Screening on Electrical Measurements

The resulting simulations of the potential distribution at 0 V, steady state JV simulations, and simulations of the various techniques are shown in Figure 4.1. At low ion densities of 10^{16} cm^{-3}, the ion density is not high enough to screen the built-in field, resulting in a significant potential drop in the perovskite, as shown in Figure 4.1(a). Increasing the ion density leads to increased screening of the built-in field until almost no potential drops in the perovskite bulk for ion densities of 10^{18} cm^{-3} and higher. Due to the increased field screening, the bulk and surface recombination around J_{sc} and at low forward bias increases, resulting in a significant drop of J_{sc} with increasing ion densities (see Figure 4.1(b)), which has been experimentally observed [3].

Next, we illustrate how the screening of the built-in potential impacts the different techniques used to quantify ion densities. First, we focus on the transient measurements, transient capacitance, and transient current. In both techniques, a forward bias is applied to the device, resulting in mobile ions diffusing away from the perovskite/CTL interface into the perovskite bulk [3, 14]. Then, after removing the applied bias, ions drift back to the interface, resulting in an ionic current. Additionally, the screening of the built-in potential and the change of the bulk electric field result in a displacement current. The sum of these currents is measured. Generally, the amplitude of the ionic current depends on the ionic conductivity. The integral of the current has been used to approximate the overall ion density [3]. However, as illustrated in Figure 4.1(c), the transients saturate for ion densities at around 10^{18} cm^{-3}. With increasing ion density, more potential drops close to the interface between perovskite and CTLs, resulting in only a fraction of the ions contributing to the current. This limit for extracting high ion densities for transient current measurements has also been observed elsewhere [5]. We note that higher ion densities than the theoretical maximum for one ion have been observed in degraded devices [3, 5], suggesting that additional effects, like additional ions may contribute to the current transients.

In transient capacitance measurements, the modulation of the device capacitance is measured while mobile ions accumulate at the perovskite/CTL interface following a voltage pulse [14]. This leads to a reduction of capacitance, as the accumulation of ions leads to a depletion of electronic carriers from the CTLs and consequently a reduction of the high-frequency capacitance [14]. Both, the initial capacitance and the steady state capacitance can be impacted by mobile ions, as illustrated in Figure 4.1(d). In the presented case, the higher ion densities lead to a larger potential drop in the perovskite layer and, consequently, a lower depletion of electronic carriers from the transport layers, resulting in a higher initial capacitance. As can be seen, at ion densities of 10^{18} cm^{-3} and higher, the initial capacitance is saturating. The

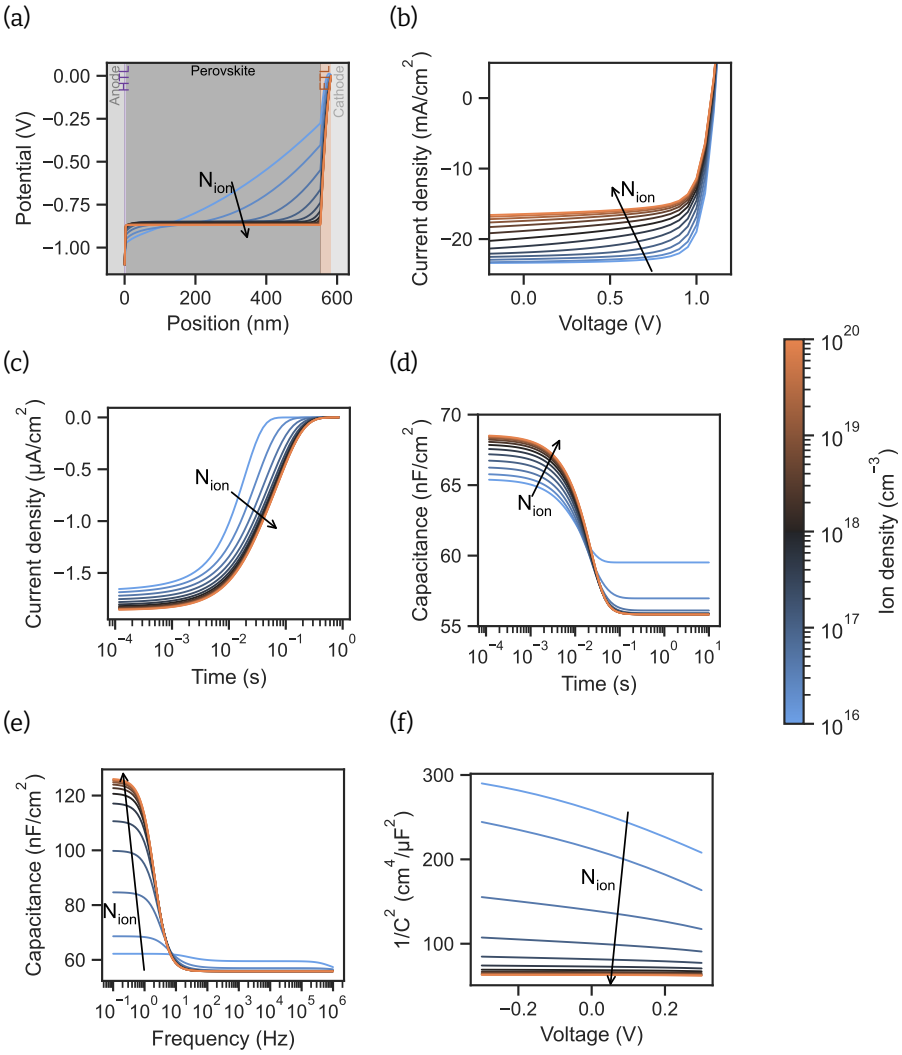

Figure 4.1: Drift diffusion simulations of a device resembling a perovskite solar cell with different ion densities. Simulation of (a) potential distribution, (b) current-density vs. voltage, (c) current transient (d), capacitance transients (e), capacitance vs. frequency, and (f) low-frequency Mott-Schottky measurements.

steady-state capacitance depends on the level of depletion when ions accumulate at the perovskite/CTL interfaces. Here, starting at 10^{17} cm^{-3}, the transport layers are depleted, leading to the same capacitance values for these ion densities. Due to the saturation of the initial capacitance, ion densities higher than 10^{18} cm^{-3} cannot be accurately determined.

Next, we focus on impedance (capacitance vs. frequency) measurements. Here, the

device capacitance at 0 V is measured at various frequencies. At 0 V, the mobile ions are accumulated at the perovskite/HTL interface and depleted from the perovskite/ETL interface. At high frequencies, the dielectric capacitance of the semiconductor stack, i.e., the series connection of the dielectric capacitance of the perovskite and the depletion layer capacitances of the transport layers, is probed. At low frequencies, the polarization capacitance due to mobile ions is probed, resulting in a rise, as shown in Figure 4.1(e). The ionic conductivity determines the onset of the rise, while the amplitude depends, to some extent, on the density of ions. As shown in Figure 4.1(e), as the density of ions increases, the low-frequency capacitance also increases until a density of around $3 \cdot 10^{18}\,\mathrm{cm}^{-3}$. At higher ion density, more ions are accumulated at the perovskite/CTL interfaces. However, the AC-potential drops in an increasingly small region close to the perovskite/CTL interface, limiting the density of excited ions and, therefore, also the capacitance.

Lastly, in low-frequency Mott-Schottky measurements, the low-frequency capacitance at small DC voltages around 0 V is measured. The DC bias modulates the depletion/accumulation layer of mobile ions at the perovskite/CTL interfaces. This modulation is then probed by determining the low-frequency capacitance [5]. Figure 4.1(f) shows the low-frequency Mott-Schottky plot for various ion densities. For low ion densities, the slope changes considerably. However, for ion densities of around $10^{18}\,\mathrm{cm}^{-3}$, the Mott-Schottky response stabilizes, and an accurate determination of the ion density is no longer possible. Interestingly, similar to the limitation of extracting ion densities, it was previously shown that the conventional Mott-Schottky analysis also suffers from limitations when applied to perovskite solar cells to extract electronic defect densities. [15, 16]

We note that the upper limit for determinable ion densities of around $10^{18}\,\mathrm{cm}^{-3}$ is only valid for the presented device and can not be generalized. The ion density necessary to screen the built-in potential depends on numerous device parameters. These include all parameters that impact the potential of the device, specifically the potential under dark conditions. These parameters include the built-in potential, the thicknesses, doping densities, and the dielectric constants of the individual layers. For example, a smaller built-in potential would decrease the density of ions necessary to screen the built-in potential. Consequently, the maximum determinable ion density would decrease. Similarly, a larger potential drop in the CTLs, for example, due to lower dielectric constants or thicker layers, would also decrease the necessary ion density to screen the built-in potential, lowering the maximum ion density that can be determined. Parameters like the ionic diffusion coefficient or recombination velocities do not significantly impact the device's potential in the dark. Therefore, these parameters will also not impact the maximum determinable ion density. We

note that we only account for effects covered by drift-diffusion simulations. Processes like the annihilation of ionic defects [17] can lead to a reduced field screening effect due to ionic carriers and, therefore, impact the maximum determinable ion density. Additional polarization effects at the transport layers [18] can also impact how many ions can accumulate at the perovskite/CTL interface before the built-in potential is screened. In very small devices, collection from the sides next to the contacts could also add to the measured ion density. These effects could also explain why high ion densities of up to $5 \cdot 10^{18}$ cm^{-3} have been measured [3]. Generally, a good approximation of the potential drop within the different layers is necessary to ensure that the extracted ion density lies in a regime where an accurate extraction is possible. For ion densities above the maximum that is possible to determine with electrical measurements, only the ionic conductivity can be accurately determined.

4.3 Conclusion

In summary, we have shown that accurately determining ion densities becomes impossible if mobile ions screen significant parts of the built-in potential. The current transient, capacitance transient, and capacitance frequency measurements saturate at high ion densities. In low-frequency Mott-Schottky measurements, the slope saturates. Accordingly, ion densities can not be determined accurately anymore. We also note that the built-in potential and the potential drops in the device can impact the maximum determinable ion density. Therefore, a good understanding and estimation of the device parameters are crucial when applying any of the studied measurement techniques to extract ion densities. To ensure ion densities can be determined, drift-diffusion simulation can be of great help. After extracting an ion density using one of the discussed techniques, one can, for example, simulate the technique with various ion densities to determine if the regime is suitable to accurately extract ion densities.

Chapter appendix

4.A Drift-Diffusion Parameters

Table 4.A.1: Parameters used for the drift-diffusion simulations.

Parameter	Value
Band gap perovskite (eV)	1.6
Electron affinity perovskite (eV)	3.9
Dielectric constant perovskite	62
Thickness perovskite (nm)	550
Effective density of states conduction band perovskite (cm^{-3})	$2.1 \cdot 10^{18}$
Effective density of states valence band (cm^{-3})	$2.1 \cdot 10^{18}$
Mobility electrons in perovskite (cm^2/Vs)	1
Mobility holes in perovskite (cm^2/Vs)	1
Mobile positive ion density in perovskite (cm^{-3})	variable
Electron SRH lifetime in perovskite (ns)	200
Hole SRH lifetime in perovskite (ns)	200
Electron recombination velocity at HTL/perovskite interface (cm/s)	100
Hole recombination velocity at HTL/perovskite interface (cm/s)	100
Electron recombination velocity at perovskite/ETL interface (cm/s)	1000
Hole recombination velocity at perovskite/ETL interface (cm/s)	1000
Immobile negative ion density (cm^{-3})	variable
Ionic conductivity (S/cm)	$1.6 \cdot 10^{-10}$
Band gap HTL (eV)	1.9
Electron affinity HTL (eV)	3.4
Dielectric constant HTL	3.0
Thickness HTL (nm)	3
Effective density of states conduction band HTL (cm^{-3})	$2.1 \cdot 10^{18}$
Effective density of states valence band (cm^{-3})	$2.1 \cdot 10^{18}$

Parameter	Value
Mobility holes in HTL (cm^2/Vs)	$1 \cdot 10^{-4}$
Work function anode (eV)	5.2
Band gap ETL (eV)	2.0
Electron affinity ETL (eV)	4.0
Dielectric constant ETL	5.0
Thickness ETL (nm)	30
Effective density of states conduction band ETL (cm^{-3})	$2.1 \cdot 10^{18}$
Effective density of states valence band (cm^{-3})	$2.1 \cdot 10^{18}$
Mobility electrons in ETL (cm^2/Vs)	$1 \cdot 10^{-4}$
Donor doping density in ETL (cm^{-3})	$3 \cdot 10^{17}$
Work function cathode (eV)	4.1
Capacitance transient probing frequency (Hz)	$20 \cdot 10^3$
Capacitance transient voltage pulse amplitude (V)	1.2
Current transient voltage pulse amplitude (V)	1.2

Bibliography

[1] S. Kim *et al.*, "Relationship Between Ion Migration and Interfacial Degradation of $CH_3NH_3PbI_3$ Perovskite Solar Cells Under Thermal Conditions", *Scientific Reports*, vol. 7, no. 1, p. 1200, 2017.

[2] C. Besleaga *et al.*, "Iodine Migration and Degradation of Perovskite Solar Cells Enhanced by Metallic Electrodes", *The Journal of Physical Chemistry Letters*, vol. 7, no. 24, pp. 5168–5175, 2016.

[3] J. Thiesbrummel *et al.*, "Ion-Induced Field Screening as a Dominant Factor in Perovskite Solar Cell Operational Stability", *Nature Energy*, vol. 9, no. 6, pp. 664–676, 2024.

[4] L. J. F. Hart *et al.*, "More is Different: Mobile Ions Improve the Design Tolerances of Perovskite Solar Cells", *Energy & Environmental Science*, vol. 17, no. 19, pp. 7107–7118, 2024.

[5] J. Diekmann *et al.*, "Determination of Mobile Ion Densities in Halide Perovskites via Low-Frequency Capacitance and Charge Extraction Techniques", *The Journal of Physical Chemistry Letters*, vol. 14, no. 18, pp. 4200–4210, 2023.

[6] L. Bertoluzzi *et al.*, "Mobile Ion Concentration Measurement and Open-Access Band Diagram Simulation Platform for Halide Perovskite Solar Cells", *Joule*, vol. 4, no. 1, pp. 109–127, 2020.

[7] M. Sajedi Alvar, P. W. Blom, and G.-J. A. H. Wetzelaer, "Device Model for Methylammonium Lead Iodide Perovskite With Experimentally Validated Ion Dynamics", *Advanced Electronic Materials*, vol. 6, no. 6, p. 1 900 935, 2020.

[8] C. Messmer *et al.*, "Understanding Ion-Related Performance Losses in Perovskite-Based Solar Cells by Capacitance Measurements and Simulation", *Solar RRL*, vol. 8, no. 24, p. 2 400 630, 2024.

[9] M. C. Schmidt, A. O. Alvarez, J. J. De Boer, L. J. Van De Ven, and B. Ehrler, "Consistent Interpretation of Time- and Frequency-Domain Traces of Ion Migration in Perovskite Semiconductors", *ACS Energy Letters*, vol. 9, no. 12, pp. 5850–5858, 2024.

[10] J. M. Azpiroz, E. Mosconi, J. Bisquert, and F. De Angelis, "Defect Migration in Methylammonium Lead Iodide and Its Role in Perovskite Solar Cell Operation", *Energy & Environmental Science*, vol. 8, no. 7, pp. 2118–2127, 2015.

[11] J. Haruyama, K. Sodeyama, L. Han, and Y. Tateyama, "First-Principles Study of Ion Diffusion in Perovskite Solar Cell Sensitizers", *Journal of the American Chemical Society*, vol. 137, no. 32, pp. 10 048–10 051, 2015.

[12] E. Mosconi and F. De Angelis, "Mobile Ions in Organohalide Perovskites: Interplay of Electronic Structure and Dynamics", *ACS Energy Letters*, vol. 1, no. 1, pp. 182–188, 2016.

[13] A. Walsh, D. O. Scanlon, S. Chen, X. G. Gong, and S.-H. Wei, "Self-Regulation Mechanism for Charged Point Defects in Hybrid Halide Perovskites", *Angewandte Chemie International Edition*, vol. 54, no. 6, pp. 1791–1794, 2015.

[14] M. C. Schmidt, E. Gutierrez-Partida, M. Stolterfoht, and B. Ehrler, "Impact of Mobile Ions on Transient Capacitance Measurements of Perovskite Solar Cells", *PRX Energy*, vol. 2, no. 4, p. 043 011, 2023.

[15] S. Ravishankar, Z. Liu, U. Rau, and T. Kirchartz, "Multilayer Capacitances: How Selective Contacts Affect Capacitance Measurements of Perovskite Solar Cells", *PRX Energy*, vol. 1, no. 1, p. 013 003, 2022.

[16] O. Almora, C. Aranda, E. Mas-Marzá, and G. Garcia-Belmonte, "On Mott-Schottky Analysis Interpretation of Capacitance Measurements in Organometal Perovskite Solar Cells", *Applied Physics Letters*, vol. 109, no. 17, p. 173 903, 2016.

[17] S. T. Birkhold, J. T. Precht, R. Giridharagopal, G. E. Eperon, L. Schmidt-Mende, and D. S. Ginger, "Direct Observation and Quantitative Analysis of Mobile Frenkel Defects in Metal Halide Perovskites Using Scanning Kelvin Probe Microscopy", *The Journal of Physical Chemistry C*, vol. 122, no. 24, pp. 12 633–12 639, 2018.

[18] L. Li, F. Wang, X. Wu, H. Yu, S. Zhou, and N. Zhao, "Carrier-Activated Polarization in Organometal Halide Perovskites", *The Journal of Physical Chemistry C*, vol. 120, no. 5, pp. 2536–2541, 2016.

5

Approximating Drift-Diffusion Simulations to Characterize Mobile Ions

Abstract

The migration of mobile ions is one of the leading causes of the degradation of perovskite solar cells. However, quantifying mobile ions in complete perovskite solar cells is challenging due to the complex device stacks and the impact of charge transport layers on the measurement techniques. Here, we develop a simple and openly accessible *step model* that approximates drift-diffusion simulations. The step model is based on expressing the charge density in the ionic and electronic accumulation and depletion layers as step functions. We can then accurately determine the impact of mobile ions on the DC potential distribution of perovskite solar cells. Furthermore, we can simulate electrical measurement techniques commonly used to quantify mobile ions: capacitance transient, current transient, and capacitance frequency measurements. By validating the step model with drift-diffusion simulations, we show that an accurate extraction of ion density, diffusion coefficient, and activation energy is possible in an accessible range. We finally apply the developed step model to estimate the ionic conductivity and activation energy of perovskite solar cells.

Authors: Moritz C. Schmidt, Agustin O. Alvarez, Biruk A. Seid, Felix Lang, and Bruno Ehrler

Accepted in: PRX Energy, August 2025

5.1 Introduction

The efficiency of single-junction perovskite solar cells reached 27.0 % in 2024, directly competing with silicon-based solar cells, with an efficiency of 27.8 % [1, 2]. Also, the longevity of perovskite solar cells has significantly improved in recent years, with operational stability now reaching thousands of hours [3, 4]. This value, however, is still not enough and hinders the commercialization of perovskite-based solar cells. Stability issues are often related to mobile ions in the perovskite. These can migrate into the charge transport layers (CTLs), introducing traps and decreasing the conductivity [5]. Ion-induced phase segregation in mixed-halide perovskites has been linked to open-circuit voltage losses [6, 7]. Additionally, mobile ions can significantly alter the potential distribution of perovskite solar cells by screening the built-in voltage, which can lead to significant short-circuit current losses [8–10]. To better understand the impact of mobile ions on the stability of perovskite solar cells, an accurate characterization of the ionic conductivity and the ion density is important. Electrical measurements are becoming increasingly popular to quantify mobile ions due to their ease of use and non-destructive nature. These techniques include transient current measurements (also known as bias-assisted charge extraction) [9, 11–13], impedance and capacitance spectroscopy [14–16], and capacitance transients (also known as transient ion drift) [17, 18]. However, the interpretation of these techniques is difficult, as transport layers can significantly impact electrical measurements [19, 20]. One prominent example is capacitance transient measurements. Contrary to our initially proposed interpretation [18], we have later shown that most of the dynamics in this measurement technique occur due to a modulation of the transport layer capacitances [21].

One option to circumvent the impact of transport layers on electrical measurements is to focus on the characterization of transport-layer-free devices [13, 14, 16]. Another option is to account for the impact of transport layers using drift-diffusion simulations, a common tool to understand the device physics of perovskite solar cells [22, 23]. However, drift-diffusion simulations can be computationally intensive, which makes screening large ranges of device parameters difficult. A compromise between accuracy and simplicity is to approximate drift-diffusion simulations with a model that is computationally less intensive and still describes the device reasonably accurately. One example is the surface polarization model developed by Courtier et al. [24, 25], which is based on an accurate, yet still complex approximation of the Debye accumulation layers. Bertoluzzi et al. developed an elegant approximation of the potential distribution in the perovskite by approximating the net charge density of the ionic accumulation and depletion layers as step functions and estimated mobile

ion densities based on current transient measurements [26]. However, their model did not account for potential drops in the transport layers and only allowed for the approximation of current transients.
Here, we extend the model proposed by Bertoluzzi et al. to approximate current transient, capacitance transient, and capacitance frequency measurements of complete devices in the dark. The model is based on approximating the net charge density in the ionic accumulation and depletion layers in the perovskite and the depletion layers in the CTLs with step functions. This description allows for an accurate approximation of the potential through perovskite solar cells. We further extend the model by computing the time-dependent charge and potential distributions depending on the ionic conductivity of the perovskite, resulting in an approximation of current transient measurements. Additionally, we solve the small-signal solution, allowing us to compute capacitance transient measurements and capacitance frequency measurements at 0 V DC bias. From hereon, we will refer to the approximation as the *step model*. By benchmarking the step model with drift-diffusion simulations, we demonstrate that we can accurately determine the ionic conductivity and, in a range, also the ion density of perovskite solar cells. Lastly, we experimentally determine the ionic conductivity of triple cation perovskite solar cells by fitting the step model to capacitance transient, current transient, and capacitance frequency measurements.
In combination with the simplicity of the measurements, the model developed here offers a powerful tool to quantify mobile ions in perovskite solar cells and is openly accessible [27].

5.2 Results and Discussion

To derive a model for the capacitance transient, current transient, and capacitance frequency measurements, we first have to make some assumptions about the perovskite solar cell. Similar to other studies [26, 28, 29], we assume that halide vacancies V_X^+ are the dominant migrating species due to their lower activation energy, which has been theoretically predicted [30–32]. We further assume that these mobile halide vacancies are compensated by immobile anion vacancies V_A^- [33] or halide interstitials X_i^- [34], leading to overall charge neutrality in the perovskite. We additionally assume that defect doping is negligible, which has been shown for well-performing lead-based perovskite solar cells [35]. Consequently, we assume that the mobile ionic carriers dominate the potential profile in the perovskite. The impact of mobile halide vacancies on the potential of a device is illustrated in Figure 5.1. In Figure 5.1(a), positively charged mobile halide vacancies are distributed homogeneously throughout the perovskite. In this case, because the net charge density in the perovskite is zero (due to

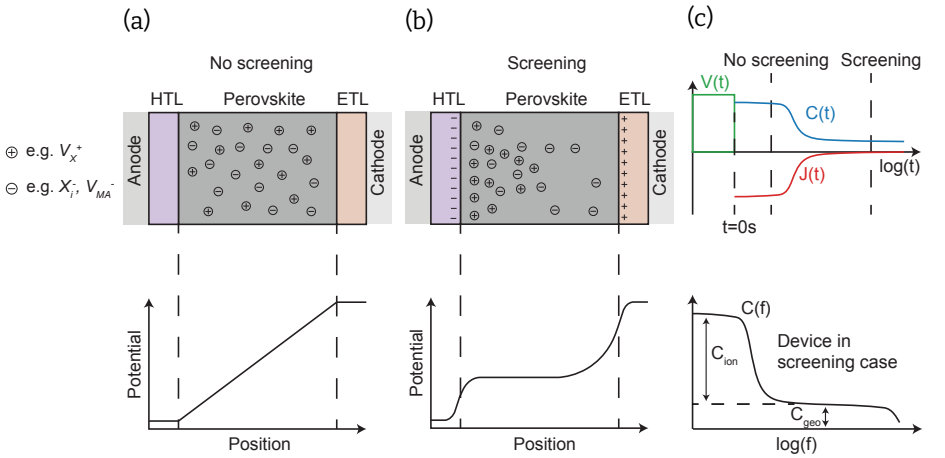

Figure 5.1: Illustration of the impact of mobile ions on the potential in a perovskite solar cell. In the *No screening* case in (a), the mobile ions are distributed homogeneously, and the potential drops linearly across the perovskite. In the *Screening* case in (b), the mobile ions are accumulated at the HTL/perovskite interface, screening the built-in voltage of the device, resulting in a flat potential in the perovskite bulk. (c) Illustrations of a capacitance C(t) and a current transient J(t) after a voltage pulse V(t), and a capacitance frequency C(f) measurement.

compensation by negative ions), the potential drops linearly within the perovskite. We refer to this case as *No screening*. In the second case in Figure 5.1(b), the halide vacancies accumulate at the HTL/perovskite interface, screening the built-in voltage of the device. The accumulation of halide vacancies comes with a simultaneous depletion of halide vacancies at the perovskite/ETL interface and a depletion of electronic carriers in the CTLs [21]. Altogether, the potential drops mainly in the CTLs and the ionic accumulation and depletion layers. We refer to this case as *Screening*. In equilibrium at 0 V applied bias, the device is in the *Screening* case. When a voltage pulse is applied to the device, like in current transient or capacitance transient measurements, as illustrated in Figure 5.1(c), mobile ions diffuse away from the interface. Then, after removing the applied bias, the device potential is similar to the *No screening* case. With increasing time, more and more ions drift to the HTL/perovskite interface, ultimately resulting in the *Screening* case. In capacitance frequency measurements at 0 V, the device is in the *Screening* case. At high frequencies, the geometrical capacitance C_{geo} of the device is probed, as illustrated in Figure 5.1(c). At low frequencies, the capacitance increases due to ionic polarization [20, 36].

To illustrate the step model, we will compare it to drift-diffusion simulations of a semiconductor stack resembling a perovskite solar cell. The device stack is illustrated in Figure 5.1(a), and the simulation parameters are listed in Table 5.A.1 in the Appendix. For illustration purposes, we use a slightly doped hole transport layer (HTL) and elec-

tron transport layer (ETL), $N_{\mathrm{D,ETL}} = N_{\mathrm{A,HTL}} = 5 \cdot 10^{17}\,\mathrm{cm}^{-3}$ with different dielectric constants ($\epsilon_{\mathrm{r,HTL}} = 4$ and $\epsilon_{\mathrm{r,ETL}} = 8$). First, we will focus on approximating the DC solution of the potential and net charge density, which will enable the calculation of current transients. Then, we will focus on applying the sinusoidal steady state analysis [37] to approximate capacitance transient and capacitance frequency measurements.

5.2.1 Approximation of the DC Solution

Our first focus is to approximate the DC potential profile within the perovskite solar cell, which is dominated by mobile ions. Bertoluzzi et al. showed that approximating the charge density of the ionic accumulation and depletion layers within the perovskite with step functions leads to good agreement compared to drift-diffusion simulations [26]. However, their model only accounted for the approximation of the potential in the perovskite layer (not taking CTLs into account). Therefore, we extend the step function approximation and apply it to the depletion layers in the CTLs. Figure 5.2(a) and (b) illustrate the approximation of the net charge densities for the earlier described *No screening* and *Screening* cases. We divide the device into five regions, shown in Figure 5.2(a) and (b). At the interfaces between the perovskite and the CTLs, we define the ionic accumulation and the ionic depletion layer in the perovskite (regions II and IV). Their widths and net charge densities are en_{II}, w_{II}, and en_{IV}, w_{IV}, respectively. In the perovskite bulk, the net charge density en_{III} is zero, as the mobile ions and the immobile ions compensate each other. The accumulation of mobile ions at the HTL/perovskite interface leads to a depletion of holes from the HTL (region I). We define the charge density and width of this depletion layer as en_{I} and w_{I}. Similarly, the depletion of mobile ions at the perovskite/ETL interface leads to a depletion of electrons from the ETL (region V), which we describe with the charge density and width en_{V} and w_{V}. With this, we can summarize the net charge density in the device as:

$$\rho(x) = \begin{cases} -e\,n_{\mathrm{I}} & \text{in region I} \\ e\,n_{\mathrm{II}} & \text{in region II} \\ 0 & \text{in region III} \\ -e\,n_{\mathrm{IV}} & \text{in region IV} \\ e\,n_{\mathrm{V}} & \text{in region V} \\ 0 & \text{otherwise} \end{cases} \tag{5.1}$$

where e is the elementary charge. Now, we can calculate the position-dependent one-dimensional electric field $E(x)$ through the device with Gauss' law [38]:

$$\frac{dE(x)}{dx} = \frac{\rho(x)}{\epsilon} \tag{5.2}$$

and the potential profile $\Phi(x)$ through the device with:

$$\frac{d\Phi(x)}{dx} = -E(x) \tag{5.3}$$

A detailed derivation of the electric field and potential is given in the Appendix.

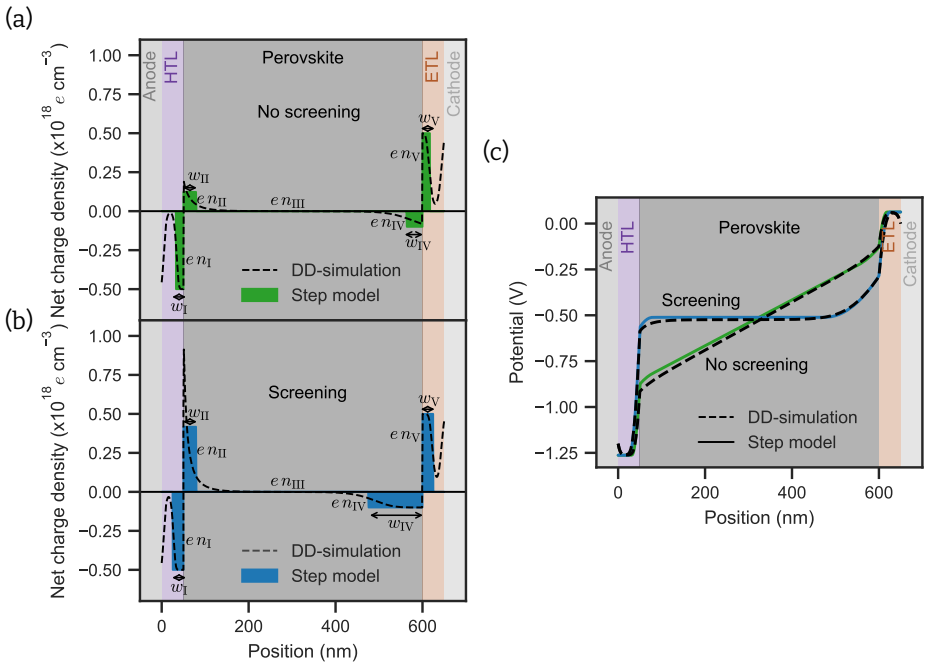

Figure 5.2: Comparison of the net charge density simulated with drift-diffusion simulations and the step model for the (a) *No screening* and (b) *Screening* case. (c) Comparison of the potentials simulated with the step model and drift-diffusion simulations.

Ultimately, we arrive at an expression for the individual potential drops within the different regions:

$$\Delta\Phi = \begin{cases} \frac{en_{\mathrm{I}}w_{\mathrm{I}}^2}{2\epsilon_0\epsilon_{\mathrm{r,HTL}}} & \text{in region I} \\ \frac{en_{\mathrm{II}}w_{\mathrm{II}}^2}{2\epsilon_0\epsilon_{\mathrm{r,Pero}}} - E_{\mathrm{bulk}}w_{\mathrm{II}} & \text{in region II} \\ -E_{\mathrm{bulk}}(d_{\mathrm{pero}} - w_{\mathrm{II}} - w_{\mathrm{IV}}) & \text{in region III} \\ \frac{en_{\mathrm{IV}}w_{\mathrm{IV}}^2}{2\epsilon_0\epsilon_{\mathrm{r,Pero}}} - E_{\mathrm{bulk}}w_{\mathrm{IV}} & \text{in region IV} \\ \frac{en_{\mathrm{V}}w_{\mathrm{V}}^2}{2\epsilon_0\epsilon_{\mathrm{r,ETL}}} & \text{in region V} \end{cases} \tag{5.4}$$

where E_{bulk} is the electric field in region III, ϵ_0 is vacuum permittivity, and $\epsilon_{\mathrm{r,HTL}}$, $\epsilon_{\mathrm{r,Pero}}$, and $\epsilon_{\mathrm{r,ETL}}$ are the relative permittivities in the different layers.
The overall sum of these potential drops has to equal the potential difference at the electrodes, which is dependent on the built-in potential V_{bi} and the externally applied bias V_{app} [25]:

$$V_{\mathrm{bi}} - V_{\mathrm{app}} = \Delta\Phi_I + \Delta\Phi_{II} + \Delta\Phi_{III} + \Delta\Phi_{IV} + \Delta\Phi_V \tag{5.5}$$

$$= \frac{e}{2\epsilon_0}\left(\frac{n_{\mathrm{I}}w_{\mathrm{I}}^2}{\epsilon_{\mathrm{r,HTL}}} + \frac{n_{\mathrm{II}}w_{\mathrm{II}}^2}{\epsilon_{\mathrm{r,Pero}}} + \frac{n_{\mathrm{IV}}w_{\mathrm{IV}}^2}{\epsilon_{\mathrm{r,Pero}}} + \frac{n_{\mathrm{V}}w_{\mathrm{V}}^2}{\epsilon_{\mathrm{r,ETL}}}\right) - E_{\mathrm{bulk}}d_{\mathrm{pero}} \tag{5.6}$$

Some of the densities and widths are readily accessible from the device parameters. For example, the carrier density in the ionic depletion region n_{IV} can be approximated with the density of immobile negative ions, which is simply the ion density N_{ion}. Furthermore, the carrier densities in the depletion layers are the doping densities of the transport layers $N_{\mathrm{A,HTL}}$ and $N_{\mathrm{D,ETL}}$. Additionally, the total charge in the ionic accumulation and depletion layer has to be equal ($en_{\mathrm{II}}w_{\mathrm{II}} = en_{\mathrm{IV}}w_{\mathrm{IV}}$). The electric displacement field through the device has to be constant, resulting in expressions for the depletion and accumulation widths in the transport layers as a function of n_{II}. Lastly, we can approximate the width of the ionic accumulation layer with the Debye length [26]:

$$L_{\mathrm{D}} = \sqrt{\frac{\epsilon_0\epsilon_{\mathrm{r,Pero}}k_{\mathrm{B}}T}{e^2N_{\mathrm{ion}}}} \tag{5.7}$$

where k_{B} is the Boltzmann constant, and T is the temperature. With these constraints and simplifications, we finally arrive at an expression for the bulk electric field E_{bulk} that depends only on the density of accumulated ions at the HTL/perovskite interface (see Section 5.A in the Appendix for the complete derivation).
Next, we introduce time dependence into the step model. The starting point is the *No screening* case depicted in Figure 5.2(a) and (c), which illustrates the charge densities and potential after applying a voltage pulse. In this case, the density of accumulated

ions at the HTL/perovskite interface is low (see Figure 5.2(a)), leading to a large potential drop in the perovskite bulk (see Figure 5.2(c)), and consequently a large bulk electric field E_{bulk}. This electric field drives mobile ions to the HTL/perovskite interface when the voltage pulse is removed. We can, therefore, express the time-dependent change of accumulated ions at the interface as [29, 39]:

$$\frac{dn_{\mathrm{II}}(t)}{dt} = -\frac{1}{ew_{\mathrm{II}}} \underbrace{eN_{\mathrm{ion}}\mu_{\mathrm{ion}}E_{\mathrm{bulk}}(t)}_{J_{\mathrm{ion}}(t)} \tag{5.8}$$

$$= -\frac{1}{w_{\mathrm{II}}k_{\mathrm{B}}T}eN_{\mathrm{ion}}D_{\mathrm{ion}}E_{\mathrm{bulk}}(t) \tag{5.9}$$

5

where μ_{ion} is the mobility and D_{ion} is the diffusion coefficient of mobile ions. This is an ordinary differential equation, as the electric field $E_{\mathrm{bulk}}(t)$ depends on the density of accumulated ions $n_{\mathrm{II}}(t)$ (see Equation 5.59 in the Appendix). After the applied bias is removed, more and more mobile ions accumulate at the HTL/perovskite interface. Simultaneously, the potential drops in all depletion and accumulation layers increase, resulting in a smaller bulk electric field and, consequently, a smaller ionic current. Finally, when enough mobile ions accumulate at the HTL/perovskite interface, the built-in potential is screened, and no more ions will accumulate at the interface, resulting in the *Screening* case in Figure 5.2(b) and the corresponding potential in Figure 5.2(c). We can solve the differential equation numerically. The result is a time-dependent density of accumulated ions at the HTL/perovskite interface $n_{\mathrm{II}}(t)$. With $n_{\mathrm{II}}(t)$, we can calculate the time-dependent net charge densities in all other regions and approximate the time-dependent potential within the device. Figure 5.2(a) and (b) show good agreement between the approximated net charge densities and drift-diffusion simulations. The approximated potential distribution within the device for both the *No screening* and the *Screening* case also agree well with the drift-diffusion simulations, as shown in Figure 5.2(c).

When the applied bias is high enough, mobile ions can accumulate at the opposite perovskite/ETL interface. Then, the ionic depletion layer is at the HTL/perovskite interface, whereas the ionic accumulation layer is at the perovskite/ETL interface, which is illustrated in Figure 5.A.5(a). At even higher voltages, electronic carriers will screen the accumulated ions at the perovskite/CTL interfaces (see Figure 5.A.5(b)). The step model can also approximate the potential in undoped CTLs as shown in Figure 5.A.6.

With the DC solution of the potential, we can compute the current transient after applying a voltage pulse. In the center of the perovskite, the current density depends on the ionic current and the displacement current due to the change in the electric field. Because the current density is constant throughout the device, we can define the ex-

tracted current as:

$$J_{\mathrm{dc}}(t) = eN_{\mathrm{ion}}\mu_{\mathrm{ion}}E_{\mathrm{bulk}}(t) + \epsilon_0\epsilon_{\mathrm{r,Pero}}\frac{dE_{\mathrm{bulk}}(t)}{dt} \tag{5.10}$$

A comparison of the approximated current transient simulations with drift-diffusion simulations is discussed in Section 5.A in the Appendix.

5.2.2 Approximation of the AC Solution

Now that we have found an approximation of the DC potential and net charge density, we can focus on solving the device capacitance. We aim to approximate the high-frequency capacitance as a function of time after applying a voltage pulse (capacitance transients) and the capacitance at 0 V at different frequencies (capacitance frequency). To compute the capacitance, we choose the sinusoidal steady state analysis (S3A), first introduced by Laux [37] and previously applied to organic and inorganic semiconductors [40–42]. This method is based on linearizing the Poisson equation and the electron and hole current continuity equations around a DC operating point. To simplify the derivation, we first express the non-time-dependent terms in the Poisson and current continuity equations in terms of F_Φ, F_{n}, and F_{p}:

$$F_\Phi(\Phi, n, p) = \frac{\epsilon}{e}\frac{d^2\Phi}{dx^2} + (p - n) = 0 \tag{5.11}$$

$$F_{\mathrm{n}}(\Phi, n, t) - \frac{dn}{dt} = \frac{1}{e}\frac{dj_{\mathrm{n}}}{dx} - r_{\mathrm{n}} - \frac{dn}{dt} = 0 \tag{5.12}$$

$$F_{\mathrm{p}}(\Phi, n, t) - \frac{dp}{dt} = -\frac{1}{e}\frac{dj_{\mathrm{p}}}{dx} - r_{\mathrm{p}} - \frac{dp}{dt} = 0 \tag{5.13}$$

where j_n, and j_p are the electron and hole current density, r_n, and r_p are the electron and hole recombination. Because the techniques we focus on are carried out in the dark, we can assume that r_n and r_p are negligible. We then extend the electron and hole density and the potential into a DC and an AC term:

$$\Phi = \Phi^{\mathrm{dc}} + \Phi^{\mathrm{ac}}e^{i\omega t} \tag{5.14}$$

$$n = n^{\mathrm{dc}} + n^{\mathrm{ac}}e^{i\omega t} \tag{5.15}$$

$$p = p^{\mathrm{dc}} + p^{\mathrm{ac}}e^{i\omega t} \tag{5.16}$$

where i is the imaginary unit, and $\omega = 2\pi f$ is the angular perturbation frequency. After linearizing the Poisson and current continuity equations, we arrive at a system

of equations:

$$\begin{bmatrix} \frac{dF_\Phi}{d\Phi} & \frac{dF_\Phi}{dn} & \frac{dF_\Phi}{dp} \\ \frac{dF_\mathrm{n}}{d\Phi} & \frac{dF_\mathrm{n}}{dn} - i\omega & \frac{dF_\mathrm{n}}{dp} \\ \frac{dF_\mathrm{p}}{d\Phi} & \frac{dF_\mathrm{p}}{dn} & \frac{dF_\mathrm{p}}{dp} - i\omega \end{bmatrix} \cdot \begin{bmatrix} \Phi^\mathrm{ac} \\ n^\mathrm{ac} \\ p^\mathrm{ac} \end{bmatrix} = 0 \tag{5.17}$$

which we can solve numerically for the position-dependent AC potential Φ^ac, AC electron density n^ac, and AC hole density p^ac. We can add a time dependency by solving Equation 5.17 for the DC potentials and carrier densities during the transient. A detailed explanation of this derivation and the discretization of the semiconductor equations following Selberherr [43] is given in Section 5.A in the Appendix. In the case of capacitance transient simulations, we do not account for the contribution of ions to the small signal solution. We can make this simplification because the perturbation frequency is high. Thus, the contribution due to ionic polarization to the AC current can be disregarded. When simulating capacitance frequency measurements, we take mobile ions into account when computing the AC solution, as mobile ions dominate the AC solution at low frequencies. A comparison of capacitance transient and capacitance frequency measurements with drift-diffusion simulations is given in Section 5.A in the Appendix.

5.2.3 Validation of the Step Model

We can now approximate the three measurement techniques: capacitance transient, current transient, and capacitance frequency. For the capacitance transient and current transient approximation, we solve the DC solution after applying a voltage pulse. The current density then follows from Equation 5.10. For the capacitance transients, we solve the AC solution at each point in time at a perturbation frequency that is high enough so we can assume that no mobile ions contribute to the capacitance, in this case 20 kHz. For the capacitance frequency technique, we solve the AC solution at 0 V DC bias and various frequencies. When directly comparing the step model with drift-diffusion simulations, as illustrated in Figures 5.A.7, 5.A.10, and 5.A.11 in the Appendix, we generally observe only a slight offset between the step model and the drift-diffusion simulations. This difference illustrates that these techniques are sensitive to the minor differences in the DC solution between the step model and the drift-diffusion solution.

To validate the developed step model, we, therefore, choose to fit data generated with drift-diffusion simulations. We use the parameter set in Table 5.A.1 in the Appendix for the drift-diffusion simulations and the step model. We simulate transients with voltage pulses of 0.8, 0.9, 1.0, and 1.1 V with drift-diffusion simulations and use the step model to fit the free parameters. We are mainly interested in determining the

density and diffusion coefficient of the mobile ions. However, to account for the offset between the step model and the drift-diffusion simulations, we need to add additional fitting parameters. Here, we choose to also fit the doping density of the ETL $N_{\mathrm{D,ETL}}$ and the dielectric constant of the perovskite $\epsilon_{\mathrm{r,Pero}}$. Figure 5.3 shows the three different techniques for an ion density of 10^{17} cm^{-3} and an ionic diffusion coefficient of $9.1 \cdot 10^{-11}$ cm^2/s at 300 K fitted with the step model. The extracted ion density is $1.1 \cdot 10^{17}$ cm^{-3}, which is in good agreement with the density set in the drift-diffusion simulations. The extracted diffusion coefficient of $1.0 \cdot 10^{-10}$ cm^2/s also matches the diffusion coefficient set in the drift-diffusion simulations well.

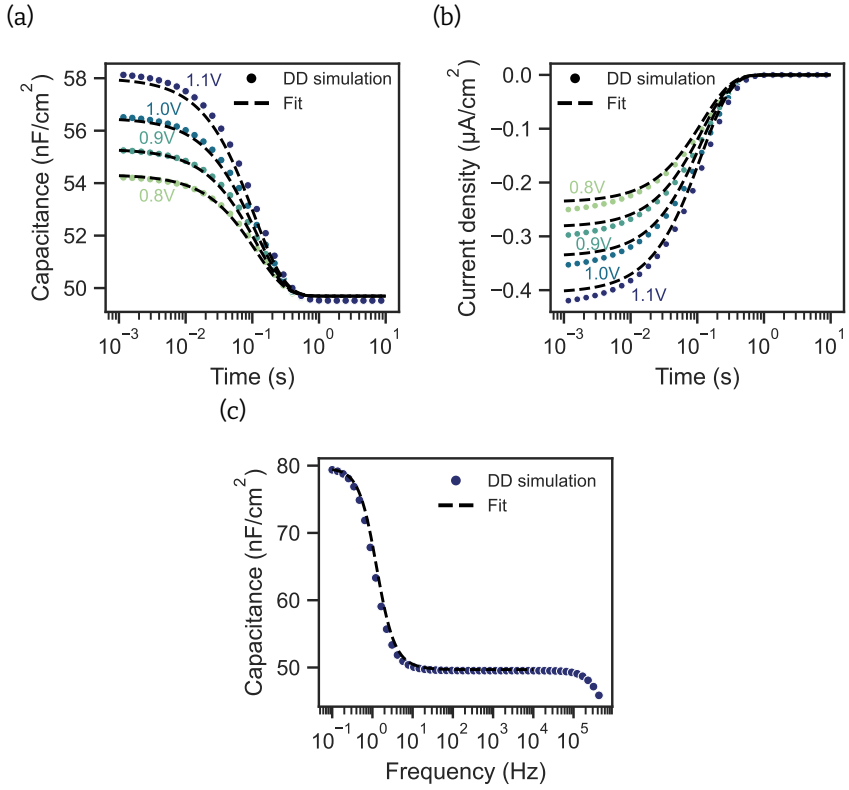

Figure 5.3: Drift-diffusion simulations of (a) capacitance transients, (b) current transients, and (c) capacitance frequency measurements. The dashed lines are fits with the step model. The ion density set in the drift-diffusion simulations is 10^{17} cm^{-3}. The fitted ion density and diffusion coefficient are listed in Table 5.1.

To test the limitations of the step model, we then fit a range of ion densities between $5 \cdot 10^{16}$ cm^{-3} and $5 \cdot 10^{18}$ cm^{-3}, which are shown in Figure 5.B.1 in the Appendix. The extracted ion densities, diffusion coefficients, and ionic conductivities are listed in

Table 5.1. Ion densities below $5 \cdot 10^{17}\,\mathrm{cm}^{-3}$ can be determined accurately. For ion densities of $5 \cdot 10^{17}$ and higher, the drift-diffusion simulations can be fitted with a range of ion densities and diffusion coefficients. Consequently, ion densities can not be determined anymore [44]. This is illustrated in Figure 5.B.2 in the Appendix, where we compare the fit residual of the drift-diffusion simulations with ion densities of $10^{17}\,\mathrm{cm}^{-3}$ and $10^{18}\,\mathrm{cm}^{-3}$. For an ion density of $10^{17}\,\mathrm{cm}^{-3}$, the fit in Figure 5.B.2(a) converges to one ion density and diffusion coefficient. In contrast, for an ion density of $10^{18}\,\mathrm{cm}^{-3}$, the fit converges to a product of ion density and diffusion coefficient, which is proportional to the ionic conductivity (see Figure 5.B.2(b)). This limitation is further illustrated in Figure 5.B.2(c), where a clear minimum for a set ion density of $10^{17}\,\mathrm{cm}^{-3}$ is visible. In contrast, for a set ion density of $10^{18}\,\mathrm{cm}^{-3}$, the residual decreases as the ion density increases and does not show a significant difference for ion densities of $5 \cdot 10^{17}\,\mathrm{cm}^{-3}$ and higher. Even though we can not determine the ion density, we can still accurately estimate the ionic conductivity, which is listed in Table 5.1. We additionally fit temperature-activated capacitance transients, current transients, and capacitance frequency measurements, shown in Figure 5.B.3. With the developed step model, we can accurately predict the activation energy of 0.3 eV, set in the drift-diffusion simulations.

Table 5.1: Ion densities N_{ion}, diffusion coefficients $D_{\mathrm{ion,300K}}$, and ionic conductivities $\sigma_{\mathrm{ion,300K}}$ when fitting drift-diffusion simulations with the step model. For ion densities of $5 \cdot 10^{17}\,\mathrm{cm}^{-3}$ and higher, only the ionic conductivity can be determined.

N_{ion} (cm^{-3})		$D_{\mathrm{ion,300K}}$ (cm^2/s)		$\sigma_{\mathrm{ion,300K}}$ (S/cm)	
Set	Fit	Set	Fit	Set	Fit
$5.0 \cdot 10^{16}$	$5.8 \cdot 10^{16}$	$9.1 \cdot 10^{-11}$	$1.2 \cdot 10^{-10}$	$2.8 \cdot 10^{-11}$	$4.3 \cdot 10^{-11}$
$1.0 \cdot 10^{17}$	$1.1 \cdot 10^{17}$	$9.1 \cdot 10^{-11}$	$1.0 \cdot 10^{-10}$	$5.7 \cdot 10^{-11}$	$7.1 \cdot 10^{-11}$
$5.0 \cdot 10^{17}$	-	$9.1 \cdot 10^{-11}$	-	$2.8 \cdot 10^{-10}$	$3.1 \cdot 10^{-10}$
$1.0 \cdot 10^{18}$	-	$9.1 \cdot 10^{-11}$	-	$5.7 \cdot 10^{-10}$	$6.5 \cdot 10^{-10}$
$5.0 \cdot 10^{18}$	-	$9.1 \cdot 10^{-11}$	-	$2.8 \cdot 10^{-9}$	$3.1 \cdot 10^{-9}$

5.2.4 Application of the Step Model to a Measured Device

Now, we can apply the step model to quantify the properties of mobile ions in an experimental realization of a perovskite solar cell in the configuration ITO/Meo-2PACz/$Cs_{0.05}$ $(MA_{0.05}$ $FA_{0.95})_{0.95}$ $Pb(I_{0.95}$ $Br_{0.05})_3$/C_{60}/BCP/Cu [45]. An exemplary current

density vs. voltage measurement is shown in Figure 5.D.1 in the Appendix. We carried out capacitance transient, current transient, and capacitance frequency measurements at different temperatures, which are shown in Figure 5.D.2. Details about the fabrication process and the characterization are described in Section 5.C in the Appendix. With increasing temperature, the capacitance transient measurements in Figure 5.D.2(a) shift to shorter times, while the capacitance in Figure 5.D.2(c) shifts to higher frequencies. This trend is in line with a temperature-activated ionic conductivity. Interestingly, we observe a decrease of the initial current amplitude in the current transient measurements in Figure 5.D.2(b) for temperatures greater than 280 K. However, we expect the current amplitude to increase with increasing temperature due to the higher ionic conductivity, as illustrated in the temperature-dependent current transient simulations in Figure 5.B.3. Possibly, the current transient measurements at higher temperatures are impacted by additional temperature-activated processes influencing, for example, the charge transport layers [20], or creating additional ions [32]. The unexpected temperature dependency of the current transients illustrates the complexity of their interpretation. The precise origin of the decrease in the current amplitude is out of the scope of this work. We therefore focus on the regime between 260 K and 280 K, the region where we observe the expected behavior of an increasing current amplitude. The measurements at 260 K are shown in Figure 5.4. Because we do not know the initial distribution of the mobile ions, we measure the capacitance and current transients at different voltage pulses from 0.8 to 1.1 V. In the capacitance transient measurements in Figure 5.4(a), the capacitance remains almost unchanged for voltages of 0.8 V and 0.9 V. Then, at 1.0 V and 1.1 V the initial capacitance increases significantly. Also, in the current transient measurements in Figure 5.4(b), we observe an increase in the current amplitude with applied voltage. The capacitance frequency measurement in Figure 5.4(c) shows the expected increase of the capacitance at low frequencies due to ionic polarization [20, 36].

To unravel the device parameters and ionic properties, we fit the measurements with the developed step model. The device parameters used in the step model are listed in Table 5.D.1. We assume that the ETL is moderately doped. If that were not the case, most of the potential would drop in the ETL, and there would be almost no accumulation of ions at the HTL/perovskite interface. This situation would lead to little change in the amplitude of the capacitance transient measurements and only a small increase in the low-frequency capacitance in the capacitance frequency measurements. For many device parameters, including the doping density of the ETL, the conduction band offset of the ETL, the work function of the anode, and the dielectric constants of the different layers, we can only estimate a range. We, therefore, start by globally fitting the capacitance transient and capacitance frequency measurements

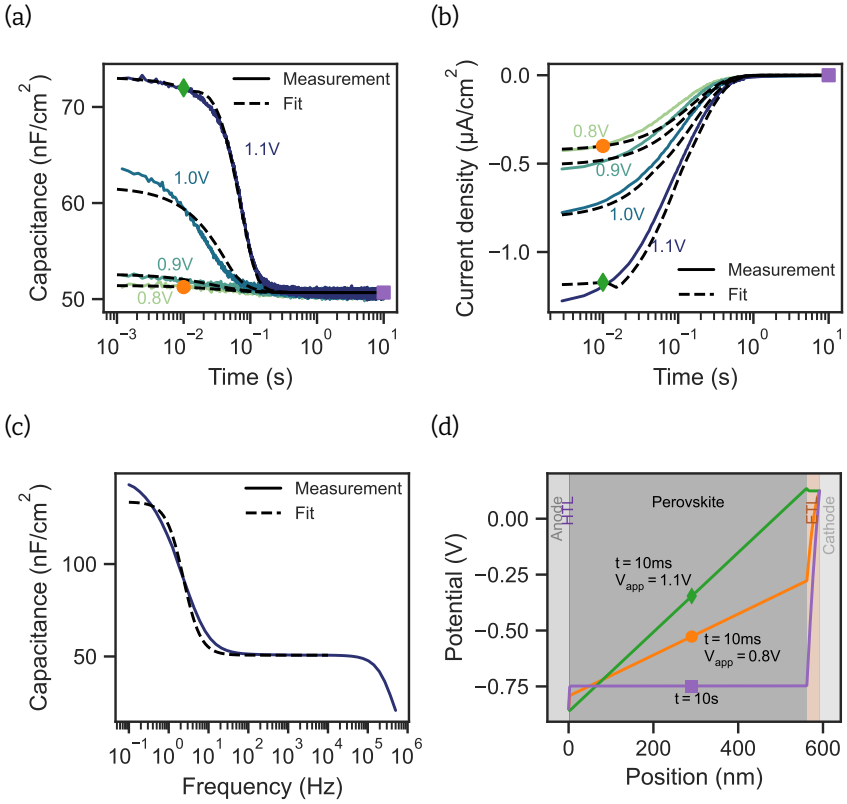

Figure 5.4: (a) Capacitance transient, (b) current transient, and (c) capacitance frequency measurements of a perovskite solar cell. The dashed lines are fits with the step model. (d) Approximated potential 10 ms and 10 s after the voltage pulse for voltages of 0.8 V and 1.1 V. The markers link the potential distributions to the capacitance and current transient plots.

to estimate these parameters. The results are listed in Table 5.D.2 in the Appendix. We can estimate the built-in potential of the device (the difference between the work function of the anode and the conduction band of the doped ETL), an often unknown parameter, to be around 1.0 V. We then individually fit the different techniques, focusing only on the ionic parameters, which are illustrated as dashed lines in Figure 5.4 and show good agreement with the measurements.

As a result, we get insight into the approximated potential and net charge density (see Figure 5.4(d)) and can explain the origin of the increasing amplitude in the capacitance transient measurements and current transients. The increase of the capacitance at voltages of 1.0 and 1.1 V is due to mobile ions that accumulate at the perovskite/ETL interface during the voltage pulses. Simultaneously, mobile ions are depleted from the HTL/perovskite interfaces. The accumulated ions at the perovskite/ETL interface are

then screened by electrons at the interface (evident in the flat and slightly increasing potential for $V_{\mathrm{app}} = 1.1\,\mathrm{V}$ and $t = 10\,\mathrm{ms}$ at the perovskite/ETL interface in Figure 5.4(d)). The accumulation of electronic charges then leads to the larger initial capacitance. In contrast, for a voltage pulse of 0.8 V, the ETL is already depleted at 10 ms (see Figure 5.4(d)), explaining the low value of the initial capacitance. The increased accumulation of ions at the ETL interface with increasing voltage also leads to a higher bulk electric field (higher slope of the potential in Figure 5.4(d)), explaining the increased amplitude in the current transient measurements. We note that the shoulder at short times in the 1.1 V current transients originates from a slight discontinuity in the electric field solution when switching from the reverse accumulation case (ions accumulated at the ETL interface) to the normal accumulation case (ions accumulated at the HTL interface).

Regarding the ionic parameters, we are in the range where only the conductivity can be extracted from electronic measurements (see Figure 5.D.3 in the Appendix). At 260 K, the extracted ionic conductivities show good agreement between the techniques with ionic conductivities of $1.0 \cdot 10^{-10}$ S/cm for capacitance transient measurements, $0.7 \cdot 10^{-10}$ S/cm for the current transient measurements, and $2.0 \cdot 10^{-10}$ S/cm for capacitance frequency measurements (see Table 5.2).

Table 5.2: Average values for the ionic conductivity at 260 and 300 K and the activation energy of the diffusion coefficient $E_{\mathrm{a,ion}}$ extracted from fitting capacitance transient (Ct), current transient (Jt), and capacitance frequency (Cf) measurements. The values are the average values and standard deviations from fitting three different devices.

Technique	$\sigma_{\mathrm{ion,260K}}$ (S/cm)	$\sigma_{\mathrm{ion,300K}}$ (S/cm)	$E_{\mathrm{a,ion}}$ (eV)
Ct	$1.0 \pm 0.4 \cdot 10^{-10}$	$4.0 \pm 1.6 \cdot 10^{-10}$	0.25 ± 0.01
Jt	$0.7 \pm 0.2 \cdot 10^{-10}$	-	-
Cf	$2.0 \pm 0.8 \cdot 10^{-10}$	$1.4 \pm 0.3 \cdot 10^{-9}$	0.36 ± 0.03

Lastly, we determine the activation energy based on the capacitance transient and capacitance frequency measurements at different temperatures. We do not extract the activation energy from the current transient measurements because we cannot capture the decreased current amplitude at higher temperatures with the step model. Assuming a temperature-activated ionic diffusion coefficient [46, 47]

$$D_{\mathrm{ion}} = D_0 e^{-\frac{E_{\mathrm{a,ion}}}{k_{\mathrm{B}} T}} \tag{5.18}$$

with prefactor D_0 and activation energy $E_{\mathrm{a,ion}}$, we fit the capacitance transients and frequency measurements, as Figure 5.5 illustrates. We extract an activation

energy of 0.25 eV for the capacitance transient measurements and an activation energy of 0.36 eV for the capacitance frequency measurements. We attribute the discrepancy between the activation energies to the difference in the operation point of the techniques. In transient techniques, we apply a bias before the measurement during which we possibly activate mobile ions. In contrast, the capacitance frequency measurement is carried out at 0 V DC bias. Additionally, the capacitance and current transient measurements are mainly sensitive to the perovskite bulk, whereas the capacitance frequency measurements mainly probe the interface between the perovskite and the CTLs. Local differences between the bulk and the interfaces can, therefore, result in differences between the extracted properties of the mobile ions. Finally, we calculate the ionic conductivities at 300 K, which are listed in Table 5.2. For the capacitance transient measurements, we extract an ionic conductivity of $4.0 \cdot 10^{-10}$ S/cm. For the capacitance frequency measurement, we get a value of $1.4 \cdot 10^{-9}$ S/cm. These values lie in a typical range of ionic conductivities observed in perovskite solar cells [12, 48].

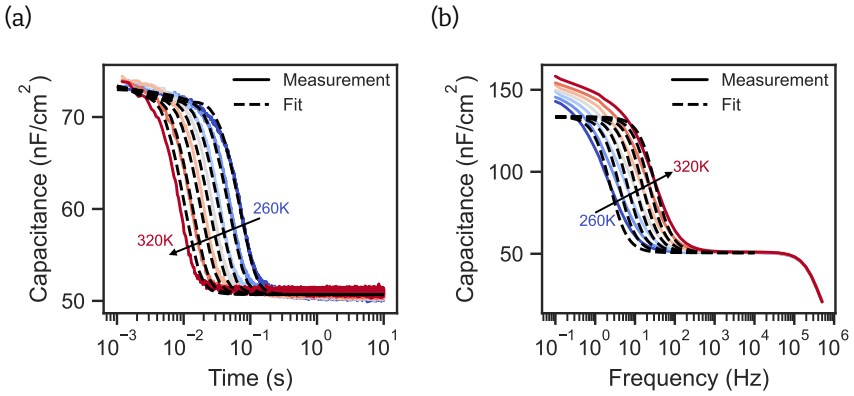

Figure 5.5: (a) Capacitance transient and (b) capacitance frequency measurements at temperatures from 260 K to 320 K in steps of 10 K. The dashed lines are fits with the step model.

5.3 Conclusion

In this work, we have developed a novel approach to characterize mobile ions based on capacitance transient, current transient, and capacitance frequency measurements. The approach is based on approximating drift-diffusion simulations with a computationally inexpensive model. Expressing the net charge density of ionic accumulation and depletion layers and, crucially, the depletion layers in the CTLs leads to an accurate approximation of the DC potential. After introducing a time de-

pendency in the DC solution and calculating the AC solution based on the sinusoidal steady-state analysis, we could approximate capacitance transient, current transient, and capacitance frequency measurements. We then validated the step model by extracting ionic parameters from drift-diffusion simulations. Within the accessible regime, we could accurately determine the ion densities and diffusion coefficients. Above an upper threshold where electrical measurements do not allow an accurate estimation of ion densities, we could still accurately determine the ionic conductivity. Lastly, we applied the step model to characterize perovskite solar cells. We fit the three measurement techniques, capacitance transient, current transient, and capacitance frequency, with the step model, resulting in valuable information about device parameters like the built-in potential, which we determined to be around 1.0 V. With the step model, we could then extract an ionic conductivity between $4.0 \cdot 10^{-10}$ and $1.4 \cdot 10^{-9}$ S/cm and an activation energy between 0.25 and 0.36 eV.

Overall, the balance between the simplicity and accuracy of the developed step model allows for an accurate characterization of mobile ionic carriers in perovskite solar cells. Furthermore, in combination with the simplicity of electrical measurements, the step model offers a powerful tool to study ion migration in perovskite solar cells and is openly accessible [27].

Chapter appendix

5.A Derivation of the Step Model

In this section, we derive the approximation of the capacitance transient, current transient, and capacitance frequency techniques, which we call *step model*. We will start with deriving the approximation of the DC potential and charge densities, followed by a detailed explanation of how we calculate the device's capacitance. For illustration purposes, we will compare the step model to drift-diffusion simulations, where both are simulated with the parameter set listed in Table 5.A.1. We will compare the step model with drift-diffusion simulations of a transient simulation, where we apply a 1.1 V voltage pulse and then approximate the device properties 0.1 ms and 10 s after removing the voltage pulse. These points are equal to the *No Screening* and *Screening* cases in the main text.

Derivation of the DC Solution

Electric Field

We start with the derivation of the DC solution. Our goal is to compute the time-dependent charge carrier densities and the time-dependent potential. As described in the main text, we define the accumulation and depletion layers within the device, as illustrated in Figure 5.A.1. The net charge density $\rho(x)$ in the device is then:

$$\rho(x) = \begin{cases} -e\, n_{\mathrm{I}} & \text{in region I} \\ e\, n_{\mathrm{II}} & \text{in region II} \\ 0 & \text{in region III} \\ -e\, n_{\mathrm{IV}} & \text{in region IV} \\ e\, n_{\mathrm{V}} & \text{in region V} \\ 0 & \text{otherwise} \end{cases} \tag{5.19}$$

where e is the elementary charge, and n_{I}, n_{II}, n_{IV}, and n_{V} are the net carrier densities in the different regions. We can then calculate the electric field $E(x)$ at position x following Gauss' law in one dimension $\frac{dE(x)}{dx} = \frac{\rho(x)}{\epsilon}$ for every region.

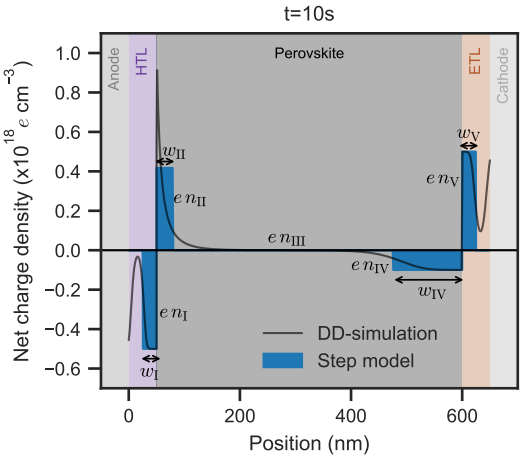

Figure 5.A.1: Comparison of the approximated net charge densities with drift-diffusion simulations of a transient simulation 10 s after the voltage pulse.

5

Region I:

$$\begin{aligned} E_{\mathrm{I}}(x) &= \int_{d_{\mathrm{HTL}}-w_{\mathrm{I}}}^{x} -\frac{en_{\mathrm{I}}}{\epsilon_0\epsilon_{\mathrm{r,HTL}}}dx' \\ &= -\frac{en_{\mathrm{I}}}{\epsilon_0\epsilon_{\mathrm{r,HTL}}}(x-(d_{\mathrm{HTL}}-w_{\mathrm{I}}))+C \end{aligned} \tag{5.20}$$

where ϵ_0 is the vacuum permittivity $\epsilon_{\mathrm{r,HTL}}$ is the relative permittivity of the HTL, d_{HTL} is the thickness of the HTL, and w_{I} is the width of region I. At the contacts, the electric field is zero:

$$E_{\mathrm{I}}(d_{\mathrm{HTL}}-w_{\mathrm{I}}) = C \overset{!}{=} 0 \tag{5.21}$$

We finally get:

$$E_{\mathrm{I}}(x) = -\frac{en_{\mathrm{I}}}{\epsilon_0\epsilon_{\mathrm{r,HTL}}}(x-(d_{\mathrm{HTL}}-w_{\mathrm{I}})) \tag{5.22}$$

Region II:

$$\begin{aligned} E_{\mathrm{II}}(x) &= \int_{d_{\mathrm{HTL}}}^{x} \frac{en_{\mathrm{II}}}{\epsilon_0\epsilon_{\mathrm{r,Pero}}}dx' \\ &= \frac{en_{\mathrm{II}}}{\epsilon_0\epsilon_{\mathrm{r,Pero}}}(x-d_{\mathrm{HTL}})+C \end{aligned} \tag{5.23}$$

where $\epsilon_{\mathrm{r,Pero}}$ is the relative permittivity of the perovskite. Assuming no surface

charges at the interface, the electric displacement field must be constant, leading to:

$$E_{\mathrm{II}}(d_{\mathrm{HTL}} + w_{\mathrm{II}}) = \frac{en_{\mathrm{II}}w_{\mathrm{II}}}{\epsilon_0\epsilon_{\mathrm{r,Pero}}} + C \overset{!}{=} E_{\mathrm{III}} \tag{5.24}$$

where w_{II} is the width of region II. We finally get:

$$E_{\mathrm{II}}(x) = \frac{en_{\mathrm{II}}}{\epsilon_0\epsilon_{\mathrm{r,Pero}}}(x - (d_{\mathrm{HTL}} + w_{\mathrm{II}})) + E_{\mathrm{III}} \tag{5.25}$$

5

Region III:
In region III the electric field is constant:

$$E_{\mathrm{III}}(x) = E_{\mathrm{bulk}} \tag{5.26}$$

Region IV:

$$\begin{aligned} E_{\mathrm{IV}}(x) &= \int_{d_{\mathrm{HTL}}+d_{\mathrm{Pero}}-w_{\mathrm{IV}}}^{x} -\frac{en_{\mathrm{IV}}}{\epsilon_0\epsilon_{\mathrm{r,Pero}}}dx' \\ &= -\frac{en_{\mathrm{IV}}}{\epsilon_0\epsilon_{\mathrm{r,Pero}}}(x - (d_{\mathrm{HTL}} + d_{\mathrm{Pero}} - w_{\mathrm{IV}})) + C \end{aligned} \tag{5.27}$$

where d_{Pero} is the thickness of the perovskite, and w_{IV} is the width of region IV. Again, assuming no surface charges, the electric displacement field must be constant, leading to:

$$E_{\mathrm{IV}}(d_{\mathrm{HTL}} + d_{\mathrm{Pero}} - w_{\mathrm{IV}}) = C \overset{!}{=} E_{\mathrm{III}} \tag{5.28}$$

We finally get:

$$E_{\mathrm{IV}}(x) = -\frac{en_{\mathrm{IV}}}{\epsilon_0\epsilon_{\mathrm{r,Pero}}}(x - (d_{\mathrm{HTL}} + d_{\mathrm{Pero}} - w_{\mathrm{IV}})) + E_{\mathrm{III}} \tag{5.29}$$

Region V:

$$E_{\mathrm{V}}(x) = \int_{d_{\mathrm{HTL}}+d_{\mathrm{Pero}}}^{x} \frac{en_{\mathrm{V}}}{\epsilon_0\epsilon_{\mathrm{r,ETL}}}dx' \tag{5.30}$$

$$= \frac{en_{\mathrm{V}}}{\epsilon_0\epsilon_{\mathrm{r,ETL}}}(x - (d_{\mathrm{HTL}} + d_{\mathrm{Pero}})) + C \tag{5.31}$$

where $\epsilon_{\mathrm{r,ETL}}$ is the relative permittivity of the ETL. At the contacts, the electric field is zero, leading to:

$$E_{\mathrm{V}}(d_{\mathrm{HTL}} + d_{\mathrm{Pero}} + w_{\mathrm{V}}) = \frac{en_{\mathrm{V}}w_{\mathrm{V}}}{\epsilon_0\epsilon_{\mathrm{r,ETL}}} + C \overset{!}{=} 0 \tag{5.32}$$

where w_{V} is the width of region V. We finally get:

$$E_{\mathrm{V}}(x) = \frac{en_{\mathrm{V}}}{\epsilon_0 \epsilon_{\mathrm{r,ETL}}}(x - (d_{\mathrm{HTL}} + d_{\mathrm{Pero}} + w_{\mathrm{V}})) \tag{5.33}$$

Summarizing Equations 5.22, 5.25, 5.26, 5.29, and 5.33, we get:

$$E(x) = \begin{cases} -\frac{en_{\mathrm{I}}}{\epsilon_0 \epsilon_{\mathrm{r,HTL}}}(x - (d_{\mathrm{HTL}} - w_{\mathrm{I}})) & \text{in region I} \\ \frac{en_{\mathrm{II}}}{\epsilon_0 \epsilon_{\mathrm{r,Pero}}}(x - (d_{\mathrm{HTL}} + w_{\mathrm{II}})) + E_{\mathrm{bulk}} & \text{in region II} \\ E_{\mathrm{bulk}} & \text{in region III} \\ -\frac{en_{\mathrm{IV}}}{\epsilon_0 \epsilon_{\mathrm{r,Pero}}}(x - (d_{\mathrm{HTL}} + d_{\mathrm{Pero}} - w_{\mathrm{IV}})) + E_{\mathrm{bulk}} & \text{in region IV} \\ \frac{en_{\mathrm{V}}}{\epsilon_0 \epsilon_{\mathrm{r,ETL}}}(x - (d_{\mathrm{HTL}} + d_{\mathrm{Pero}} + w_{\mathrm{V}})) & \text{in region V} \\ 0 & \text{otherwise} \end{cases} \tag{5.34}$$

5

Potential

With the relationship

$$\frac{d\Phi(x)}{dx} = -E(x) \tag{5.35}$$

we can now calculate the potential $\Phi(x)$ within the different regions of the device. The potential needs to be continuous throughout the device.
Region I:

$$\begin{aligned} \Phi_{\mathrm{I}}(x) &= -\int_{d_{\mathrm{HTL}} - w_{\mathrm{I}}}^{x} E_{\mathrm{I}}(x')dx' \\ &= -\int_{d_{\mathrm{HTL}} - w_{\mathrm{I}}}^{x} -\frac{en_{\mathrm{I}}}{\epsilon_0 \epsilon_{\mathrm{r,HTL}}}(x' - (d_{\mathrm{HTL}} - w_{\mathrm{I}}))dx' \\ &= \frac{en_{\mathrm{I}}}{2\epsilon_0 \epsilon_{\mathrm{r,HTL}}}(x - (d_{\mathrm{HTL}} - w_{\mathrm{I}}))^2 + C \end{aligned} \tag{5.36}$$

$$\Phi_{\mathrm{I}}(d_{\mathrm{HTL}} - w_{\mathrm{I}}) = C \stackrel{!}{=} V_{+} \tag{5.37}$$

where V_{+} is the potential at the anode.

$$\Phi_{\mathrm{I}}(x) = \frac{en_{\mathrm{I}}}{2\epsilon_0 \epsilon_{\mathrm{r,HTL}}}(x - (d_{\mathrm{HTL}} - w_{\mathrm{I}}))^2 + V_{+} \tag{5.38}$$

Region II:

$$\begin{aligned}\Phi_{\mathrm{II}}(x) &= \Phi_{\mathrm{I}}(d_{\mathrm{HTL}}) - \int_{d_{\mathrm{HTL}}}^{x} E_{\mathrm{II}}(x')dx' \\ &= \Phi_{\mathrm{I}}(d_{\mathrm{HTL}}) - \int_{d_{\mathrm{HTL}}}^{x} \frac{en_{\mathrm{II}}}{\epsilon_0\epsilon_{\mathrm{r,Pero}}}(x' - (d_{\mathrm{HTL}} + w_{\mathrm{II}})) + E_{\mathrm{III}}dx' \\ &= \Phi_{\mathrm{I}}(d_{\mathrm{HTL}}) - \frac{en_{\mathrm{II}}}{2\epsilon_0\epsilon_{\mathrm{r,Pero}}}(x - (d_{\mathrm{HTL}} + w_{\mathrm{II}}))^2 - E_{\mathrm{bulk}}(x - d_{\mathrm{HTL}}) \end{aligned} \tag{5.39}$$

Region III:

$$\begin{aligned}\Phi_{\mathrm{III}}(x) &= \Phi_{\mathrm{II}}(d_{\mathrm{HTL}} + w_{\mathrm{II}}) - \int_{d_{\mathrm{HTL}}+w_{\mathrm{II}}}^{x} E_{\mathrm{bulk}}dx' \\ &= \Phi_{\mathrm{II}}(d_{\mathrm{HTL}} + w_{\mathrm{II}}) - E_{\mathrm{bulk}}(x - (d_{\mathrm{HTL}} + w_{\mathrm{II}})) \end{aligned} \tag{5.40}$$

Region IV:

$$\begin{aligned}\Phi_{\mathrm{IV}}(x) &= \Phi_{\mathrm{III}}(d_{\mathrm{HTL}} + d_{\mathrm{Pero}} - w_{\mathrm{IV}}) - \int_{d_{\mathrm{HTL}}+d_{\mathrm{Pero}}-w_{\mathrm{IV}}}^{x} E_{\mathrm{IV}}(x')dx' \\ &= \Phi_{\mathrm{III}}(d_{\mathrm{HTL}} + d_{\mathrm{Pero}} - w_{\mathrm{IV}}) \\ &\quad - \int_{d_{\mathrm{HTL}}+d_{\mathrm{Pero}}-w_{\mathrm{IV}}}^{x} -\frac{en_{\mathrm{IV}}}{\epsilon_0\epsilon_{\mathrm{r,Pero}}}(x' - (d_{\mathrm{HTL}} + d_{\mathrm{Pero}} - w_{\mathrm{IV}})) + E_{\mathrm{bulk}}dx' \\ &= \Phi_{\mathrm{III}}(d_{\mathrm{HTL}} + d_{\mathrm{Pero}} - w_{\mathrm{IV}}) + \frac{en_{\mathrm{IV}}}{2\epsilon_0\epsilon_{\mathrm{r,Pero}}}(x - (d_{\mathrm{HTL}} + d_{\mathrm{Pero}} - w_{\mathrm{IV}}))^2 \\ &\quad - E_{\mathrm{bulk}}(x - (d_{\mathrm{HTL}} + d_{\mathrm{Pero}} - w_{\mathrm{IV}})) \end{aligned} \tag{5.41}$$

Region V:

$$\begin{aligned}\Phi_{\mathrm{V}}(x) &= \Phi_{\mathrm{IV}}(d_{\mathrm{HTL}} + d_{\mathrm{Pero}}) - \int_{d_{\mathrm{HTL}}+d_{\mathrm{Pero}}}^{x} E_{\mathrm{V}}(x')dx' \\ &= \Phi_{\mathrm{IV}}(d_{\mathrm{HTL}} + d_{\mathrm{Pero}}) \\ &\quad - \int_{d_{\mathrm{HTL}}+d_{\mathrm{Pero}}}^{x} \frac{en_{\mathrm{V}}}{\epsilon_0\epsilon_{\mathrm{r,ETL}}}(x' - (d_{\mathrm{HTL}} + d_{\mathrm{Pero}} + w_{\mathrm{V}}))dx' \\ &= \Phi_{\mathrm{IV}}(d_{\mathrm{HTL}} + d_{\mathrm{Pero}}) - \frac{en_{\mathrm{V}}}{2\epsilon_0\epsilon_{\mathrm{r,ETL}}}(x^2 - 2x(d_{\mathrm{HTL}} + d_{\mathrm{Pero}} + w_{\mathrm{V}}) \\ &\quad + (d_{\mathrm{HTL}} + d_{\mathrm{Pero}})^2 + 2w_{\mathrm{V}}(d_{\mathrm{HTL}} + d_{\mathrm{Pero}})) \end{aligned} \tag{5.42}$$

With the expression of the potential in the different regions, we can now define the voltage drops in the regions:

Region I:

$$\begin{aligned}\Delta\Phi_{\mathrm{I}} &= \Phi_{\mathrm{I}}(d_{\mathrm{HTL}}) - \Phi_{\mathrm{I}}(d_{\mathrm{HTL}} - w_{\mathrm{I}}) \\ &= \frac{e n_{\mathrm{I}} w_{\mathrm{I}}^2}{2\epsilon_0 \epsilon_{\mathrm{r,HTL}}}\end{aligned} \tag{5.43}$$

Region II:

$$\begin{aligned}\Delta\Phi_{\mathrm{II}} &= \Phi_{\mathrm{II}}(d_{\mathrm{HTL}} + w_{\mathrm{II}}) - \Phi_{\mathrm{II}}(d_{\mathrm{HTL}}) \\ &= \frac{e n_{\mathrm{II}} w_{\mathrm{II}}^2}{2\epsilon_0 \epsilon_{\mathrm{r,Pero}}} - E_{\mathrm{bulk}} w_{\mathrm{II}}\end{aligned} \tag{5.44}$$

Region III:

$$\begin{aligned}\Delta\Phi_{\mathrm{I}} &= \Phi_{\mathrm{III}}(d_{\mathrm{HTL}} + d_{\mathrm{Pero}} - w_{\mathrm{IV}}) - \Phi_{\mathrm{III}}(d_{\mathrm{HTL}} + w_{\mathrm{II}}) \\ &= -E_{\mathrm{bulk}}(d_{\mathrm{Pero}} - w_{\mathrm{II}} - w_{\mathrm{IV}})\end{aligned} \tag{5.45}$$

Region IV:

$$\begin{aligned}\Delta\Phi_{\mathrm{IV}} &= \Phi_{\mathrm{IV}}(d_{\mathrm{HTL}} + d_{\mathrm{Pero}}) - \Phi_{\mathrm{IV}}(d_{\mathrm{HTL}} + d_{\mathrm{Pero}} - w_{\mathrm{IV}}) \\ &= \frac{e n_{\mathrm{IV}} w_{\mathrm{IV}}^2}{2\epsilon_0 \epsilon_{\mathrm{r,Pero}}} - E_{\mathrm{bulk}} w_{\mathrm{IV}}\end{aligned} \tag{5.46}$$

Region V:

$$\begin{aligned}\Delta\Phi_{\mathrm{V}} &= \Phi_{\mathrm{V}}(d_{\mathrm{HTL}} + d_{\mathrm{Pero}} + w_{\mathrm{IV}}) - \Phi_{\mathrm{V}}(d_{\mathrm{HTL}} + d_{\mathrm{Pero}}) \\ &= \frac{e n_{\mathrm{V}} w_{\mathrm{V}}^2}{2\epsilon_0 \epsilon_{\mathrm{r,ETL}}}\end{aligned} \tag{5.47}$$

Summarizing Equations 5.43, 5.44, 5.45, 5.46, and 5.47 leads to:

$$\Delta\Phi = \begin{cases} \frac{e n_{\mathrm{I}} w_{\mathrm{I}}^2}{2\epsilon_0 \epsilon_{\mathrm{r,HTL}}} & \text{in region I} \\ \frac{e n_{\mathrm{II}} w_{\mathrm{II}}^2}{2\epsilon_0 \epsilon_{\mathrm{r,Pero}}} - E_{\mathrm{bulk}} w_{\mathrm{II}} & \text{in region II} \\ -E_{\mathrm{bulk}}(d_{\mathrm{Pero}} - w_{\mathrm{II}} - w_{\mathrm{IV}}) & \text{in region III} \\ \frac{e n_{\mathrm{IV}} w_{\mathrm{IV}}^2}{2\epsilon_0 \epsilon_{\mathrm{r,Pero}}} - E_{\mathrm{bulk}} w_{\mathrm{IV}} & \text{in region IV} \\ \frac{e n_{\mathrm{V}} w_{\mathrm{V}}^2}{2\epsilon_0 \epsilon_{\mathrm{r,ETL}}} & \text{in region V} \end{cases} \tag{5.48}$$

The sum of all potential drops in all layers equals the built-in voltage V_{bi} minus the applied voltage V_{app}. Expressing the potential drops as functions of the charge densities

leads to:

$$\begin{aligned} V_{\mathrm{bi}} - V_{\mathrm{app}} &= \Delta\Phi_I + \Delta\Phi_{\mathrm{II}} + \Delta\Phi_{\mathrm{III}} + \Delta\Phi_{\mathrm{IV}} + \Delta\Phi_{\mathrm{V}} \\ &= \frac{e}{2\epsilon_0}\left(\frac{n_{\mathrm{I}} w_{\mathrm{I}}^2}{\epsilon_{\mathrm{r,HTL}}} + \frac{n_{\mathrm{II}} w_{\mathrm{II}}^2}{\epsilon_{\mathrm{r,Pero}}} + \frac{n_{\mathrm{IV}} w_{\mathrm{IV}}^2}{\epsilon_{\mathrm{r,Pero}}} + \frac{n_{\mathrm{V}} w_{\mathrm{V}}^2}{\epsilon_{\mathrm{r,ETL}}}\right) - E_{\mathrm{bulk}} d_{\mathrm{Pero}} \end{aligned} \tag{5.49}$$

Ultimately, we aim to arrive at an expression for the bulk electric field E_{bulk} as a function of the density of accumulated ions in region II, n_{II}, as that will allow us to solve a simple differential equation for n_{II}. Therefore, we express the charge in the other accumulation and depletion regions in terms of the accumulated ion density.

5

In region IV the charge density is dominated by the immobile anions N_{ion}. We can therefore assume that:

$$n_{\mathrm{IV}} = N_{\mathrm{ion}} \tag{5.50}$$

The charge density in the depletion regions in the CTLs can just be approximated with the doping densities of the CTLs:

$$n_{\mathrm{I}} = N_{\mathrm{A,HTL}} \tag{5.51}$$

$$n_{\mathrm{V}} = N_{\mathrm{D,ETL}} \tag{5.52}$$

The total charge in regions II and IV must be equal. We can therefore express w_{IV} as:

$$\begin{aligned} n_{\mathrm{IV}} w_{\mathrm{IV}} &\overset{!}{=} n_{\mathrm{II}} w_{\mathrm{II}} \\ \Rightarrow w_{\mathrm{IV}} &= \frac{n_{\mathrm{II}} w_{\mathrm{II}}}{n_{\mathrm{IV}}} \end{aligned} \tag{5.53}$$

Furthermore, the electric displacement field at the perovskite/CTL interfaces is constant (assuming no surface charge). Consequently, we can find an expression for w_{I}:

$$\epsilon_0 \epsilon_{\mathrm{r,HTL}} E_I(d_{\mathrm{HTL}}) \overset{!}{=} \epsilon_0 \epsilon_{\mathrm{r,Pero}} E_{II}(d_{\mathrm{HTL}}) \tag{5.54}$$

$$\begin{aligned} -e n_{\mathrm{I}} w_{\mathrm{I}} &= \epsilon_0 \epsilon_{\mathrm{r,Pero}} E_{\mathrm{bulk}} - e w_{\mathrm{II}} n_{\mathrm{II}} \\ \Rightarrow w_{\mathrm{I}} &= \frac{e w_{\mathrm{II}} n_{\mathrm{II}} - \epsilon_0 \epsilon_{\mathrm{r,Pero}} E_{\mathrm{III}}}{e n_{\mathrm{I}}} \end{aligned} \tag{5.55}$$

And similarly for w_{V}.

$$\epsilon_0 \epsilon_{\mathrm{r,ETL}} E_V(d_{\mathrm{HTL}} + d_{\mathrm{Pero}}) \overset{!}{=} \epsilon_0 \epsilon_{\mathrm{r,Pero}} E_{IV}(d_{\mathrm{HTL}} + d_{\mathrm{Pero}}) \tag{5.56}$$

$$\begin{aligned} -e n_{\mathrm{V}} w_{\mathrm{V}} &= \epsilon_0 \epsilon_{\mathrm{r,Pero}} E_{\mathrm{bulk}} - e w_{\mathrm{IV}} n_{\mathrm{IV}} \\ \Rightarrow w_{\mathrm{V}} &= \frac{e w_{\mathrm{IV}} n_{\mathrm{IV}} - \epsilon_0 \epsilon_{\mathrm{r,Pero}} E_{\mathrm{III}}}{e n_{\mathrm{V}}} \end{aligned} \tag{5.57}$$

Lastly, we approximate the accumulation width of ions in regions II w_{II} with the Debye length L_{D} [26]:

$$w_{\mathrm{II}} = L_{\mathrm{D}} = \sqrt{\frac{\epsilon_0 \epsilon_{\mathrm{r,Pero}} V_{\mathrm{T}}}{e N_{\mathrm{ion}}}} \tag{5.58}$$

where V_{T} is the thermal voltage $V_{\mathrm{T}} = \frac{k_B T}{e}$. With these relationships, we can express the overall potential dependent on only n_{II} (because replacing all variables with the simplifications defined in Equations 5.50 - 5.58 leads to large expressions, we omit this step here).

$$\begin{aligned} V_{\mathrm{bi}} - V_{\mathrm{app}} &= \frac{e}{2\epsilon_0}\Big(\frac{n_{\mathrm{I}} w_{\mathrm{I}}^2}{\epsilon_{\mathrm{r,HTL}}} + \frac{n_{\mathrm{II}} w_{\mathrm{II}}^2}{\epsilon_{\mathrm{r,Pero}}} + \frac{n_{\mathrm{IV}} w_{\mathrm{IV}}^2}{\epsilon_{\mathrm{r,Pero}}} + \frac{n_{\mathrm{V}} w_{\mathrm{V}}^2}{\epsilon_{\mathrm{r,ETL}}}\Big) - E_{\mathrm{bulk}} d_{\mathrm{Pero}} \\ &= \frac{e n_{\mathrm{I}}}{2\epsilon_0 \epsilon_{\mathrm{r,HTL}}}\Big(\frac{e n_{\mathrm{II}} w_{\mathrm{II}} - \epsilon_0 \epsilon_{\mathrm{r,Pero}} E_{\mathrm{bulk}}}{e n_{\mathrm{V}}}\Big)^2 \\ &\quad + \frac{e n_{\mathrm{II}} w_{\mathrm{II}}}{2\epsilon_0 \epsilon_{\mathrm{r,Pero}}} + \frac{e n_{\mathrm{IV}}}{2\epsilon_0 \epsilon_{\mathrm{r,Pero}}}\Big(\frac{n_{\mathrm{II}} w_{\mathrm{II}}}{n_{\mathrm{IV}}}\Big)^2 \\ &\quad + \frac{e n_{\mathrm{V}}}{2\epsilon_0 \epsilon_{\mathrm{r,ETL}}}\Big(\frac{e n_{\mathrm{II}} w_{\mathrm{II}} - \epsilon_0 \epsilon_{\mathrm{r,Pero}} E_{\mathrm{bulk}}}{e n_{\mathrm{V}}}\Big)^2 - E_{\mathrm{bulk}} d_{\mathrm{Pero}} \end{aligned} \tag{5.59}$$

This is a quadratic equation that can be solved for E_{bulk}.

Time Dependence

Next, we focus on introducing the time-dependence of the solution. The ionic current in the perovskite bulk leads to a time-dependent change of the accumulated charge in region II [29, 39]:

$$\begin{aligned} \frac{dq_{\mathrm{II}}}{dt} &= -J_{\mathrm{ion}}(t) \\ e w_{\mathrm{II}} \frac{dn_{\mathrm{II}}}{dt} &= -\sigma_{\mathrm{ion}} E_{\mathrm{bulk}}(t) \\ \frac{dn_{\mathrm{II}}}{dt} &= -\frac{\sigma_{\mathrm{ion}}}{e w_{\mathrm{II}}} E_{\mathrm{bulk}}(t) \\ \frac{dn_{\mathrm{II}}}{dt} &= -\frac{e N_{\mathrm{ion}} \mu_{\mathrm{ion}}}{e w_{\mathrm{II}}} E_{\mathrm{bulk}}(t) \end{aligned} \tag{5.60}$$

where $J_{\mathrm{ion}}(t)$ is the time-dependent ionic current in the bulk and σ_{ion} is the ionic conductivity. According to Equation 5.59, $E_{\mathrm{bulk}}(t)$ is dependent on $n_{\mathrm{II}}(t)$. Hence, Equation 5.60 is an ordinary differential equation that can be solved numerically for $n_{\mathrm{II}}(t)$. After solving for $n_{\mathrm{II}}(t)$, we can compute the potential $\Phi(x)$ through the device as a function of time. Figure 5.A.2 shows the potential 0.1 ms and 10 s after removing a voltage pulse. They show good agreement when compared to the potential simulated with drift-diffusion simulations.

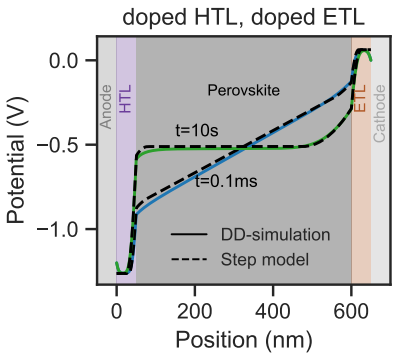

Figure 5.A.2: Comparison of the approximated potential with drift-diffusion simulations of a transient simulation 0.1 ms and 10 s after the voltage pulse.

Charge Carrier Densities

In order to later compute the AC charge carrier densities of the device, we first need to approximate the DC charge carrier densities. With the potential $\Phi(x)$, we can approximate the energy of the conduction and valence band with respect to the Fermi level:

$$E_{\mathrm{CB}}(x) - E_{\mathrm{F}} = E_{\mathrm{CB,ETL},0} - E_{\mathrm{F}} - e\Phi(x) \tag{5.61}$$

$$E_{\mathrm{F}} - E_{\mathrm{VB}}(x) = E_{\mathrm{F}} - [E_{\mathrm{VB,HTL},0} - e(\Phi(x) + (V_{\mathrm{bi}} - V_{\mathrm{app}}))] \tag{5.62}$$

where $E_{\mathrm{CB,ETL},0}$ and $E_{\mathrm{VB,HTL},0}$ are the energy of the conduction and valence band at the cathode and anode, respectively. At the interfaces between transport layers and perovskite, we adapt the energies of E_{CB} and E_{VB} according to the band offset between the perovskite and the CTLs. Figure 5.A.3(a) and (b) show the approximated energy of the conduction band (CB) and valence band (VB) with respect to the Fermi level (defined at 0 eV) 0.1 ms and 10 s after removing a voltage pulse. The step model shows good agreement with the drift-diffusion simulations.
We can then calculate the electron and hole densities at each position:

$$n(x) = n_{0,\mathrm{CB}}(x) e^{-\frac{E_{\mathrm{CB}}(x) - E_{\mathrm{F}}}{k_{\mathrm{B}} T}} \tag{5.63}$$

$$p(x) = p_{0,\mathrm{VB}}(x) e^{-\frac{E_{\mathrm{F}} - E_{\mathrm{VB}}(x)}{k_{\mathrm{B}} T}} \tag{5.64}$$

where $n_{0,\mathrm{CB}}(x)$ and $p_{0,\mathrm{VB}}(x)$ are the effective density of states of the conduction and valence band, respectively. We note that we generally assume that the electric charges do not significantly impact the potential. This is valid as long as the densities of elec-

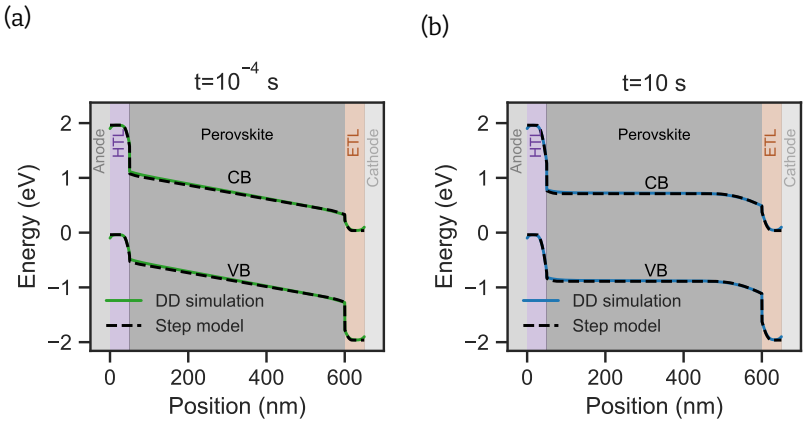

Figure 5.A.3: Comparison of the approximated conduction and valence band with drift-diffusion simulations of a transient simulations (a) 0.1 ms and (b) 10 s after the voltage pulse.

trons and holes are not very high. This assumption is valid for the presented device because the device is not doped and not illuminated. The results compared to drift-diffusion simulations are shown in Figure 5.A.4(a) and (b) 0.1 ms and 10 s after removing a voltage pulse, respectively.

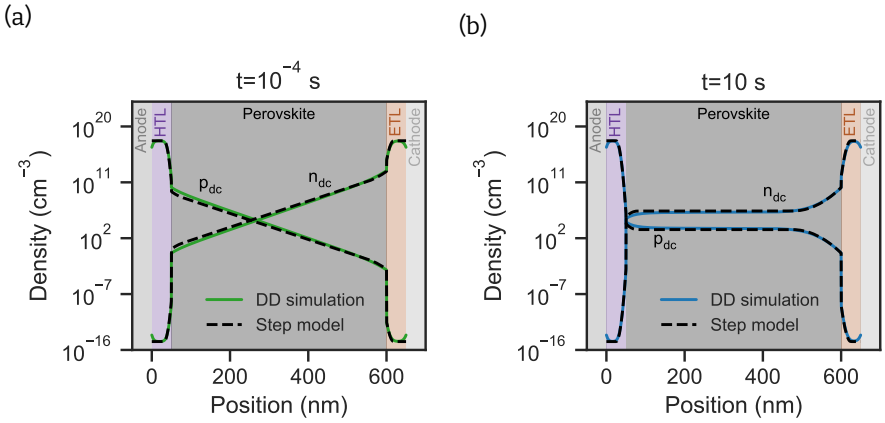

Figure 5.A.4: Comparison of the approximated DC electron and hole densities with drift-diffusion simulations of a transient simulations (a) 0.1 ms and (b) 10 s after the voltage pulse.

Reverse Accumulation

In cases of initial applied biases in the range of the built-in potential or higher, the depletion and accumulation layers can be reversed. We can generally distinguish between two special cases:
First, when the ionic accumulation and depletion layers are reversed. This means that after the voltage pulse, mobile ions are accumulated at the perovskite/ETL interface. We then still assume the same properties of the accumulation and depletion region as before, but define the Debye accumulation layer at the perovskite/ETL interface and the ion depletion layer at the perovskite/HTL interface. This is illustrated in Figure 5.A.5(a).
In the second case, electronic carriers within the transport layers accumulate at the perovskite/CTL interfaces. We assume that their accumulation can also be approximated with a Debye layer. This case is illustrated in Figure 5.A.5(b).
Switching between these cases can lead to discontinuities in the calculation of the capacitance transients and current transients, because the potential drops within the accumulation and depletion layers are different. Therefore, when transitioning between the different regimes, the time-dependent derivative of, e.g., the electric field, can be discontinuous.

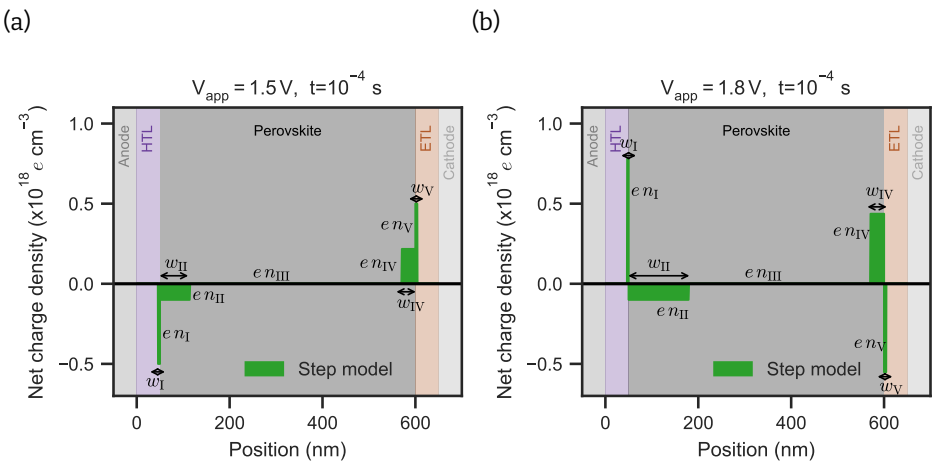

Figure 5.A.5: Approximated net charge density for a transient simulation 0.1 s after the voltage pulse of (a) 1.5 V and (b) 1.8 V.

Undoped Transport Layers

In case of undoped transport layers, we simply adapt the derived solution and assume a constant electric field and linear potential drop within the transport layers. If both CTLs are undoped, the potential drops, for example, become:

$$\Delta\Phi = \begin{cases} \frac{en_{\mathrm{II}}w_{\mathrm{II}}}{\epsilon_0\epsilon_{\mathrm{r,HTL}}}d_{\mathrm{HTL}} - \frac{\epsilon_{\mathrm{r,Pero}}}{\epsilon_{\mathrm{r,HTL}}}E_{\mathrm{bulk}}d_{\mathrm{HTL}} & \text{in region I} \\ \frac{en_{\mathrm{II}}w_{\mathrm{II}}^2}{2\epsilon_0\epsilon_{\mathrm{r,Pero}}} - E_{\mathrm{bulk}}w_{\mathrm{II}} & \text{in region II} \\ -E_{\mathrm{bulk}}(d_{\mathrm{Pero}} - w_{\mathrm{II}} - w_{\mathrm{IV}}) & \text{in region III} \\ \frac{en_{\mathrm{IV}}w_{\mathrm{IV}}^2}{2\epsilon_0\epsilon_{\mathrm{r,Pero}}} - E_{\mathrm{bulk}}w_{\mathrm{IV}} & \text{in region IV} \\ \frac{en_{\mathrm{IV}}w_{\mathrm{IV}}}{\epsilon_0\epsilon_{\mathrm{r,ETL}}}d_{\mathrm{ETL}} - \frac{\epsilon_{\mathrm{r,Pero}}}{\epsilon_{\mathrm{r,ETL}}}E_{\mathrm{bulk}}d_{\mathrm{ETL}} & \text{in region V} \end{cases} \tag{5.65}$$

When only one CTL is doped, the solution is adapted accordingly. Figure 5.A.6 shows good agreement between the drift-diffusion simulations and the step model for (a) both HTL and ETL being undoped, (b) HTL being undoped and ETL being doped, and (c) HTL being doped and ETL being undoped.

Comparison Current Transients

We can now compute current density transients using the time-dependent ionic current $J_{\mathrm{ion}} = eN_{\mathrm{ion}}\mu_{\mathrm{ion}}E_{\mathrm{bulk}}(t)$ and displacement current $J_{\mathrm{disp}} = \epsilon\frac{dE_{\mathrm{bulk}}(t)}{dt}$. Throughout the device, the current density is constant. If we assume that the current in the center of the perovskite bulk is dominated by the ionic current and the displacement current (which is valid if we assume that contributions by electronic carriers are negligible, because the perovksite is undoped and the measurement is carried out in the dark), we can define the current density of the transient $J_{\mathrm{dc}}(t)$:

$$J_{\mathrm{dc}}(t) = eN_{\mathrm{ion}}\mu_{\mathrm{ion}}E_{\mathrm{bulk}}(t) + \epsilon_0\epsilon_{\mathrm{r,Pero}}\frac{dE_{\mathrm{bulk}}(t)}{dt} \tag{5.66}$$

Figure 5.A.7 shows the approximated current density transient compared to one computed using drift-diffusion simulations. Here, the step model and drift-diffusion simulation slightly deviate from each other due to small differences in the computed electric field, but the timescales match well.

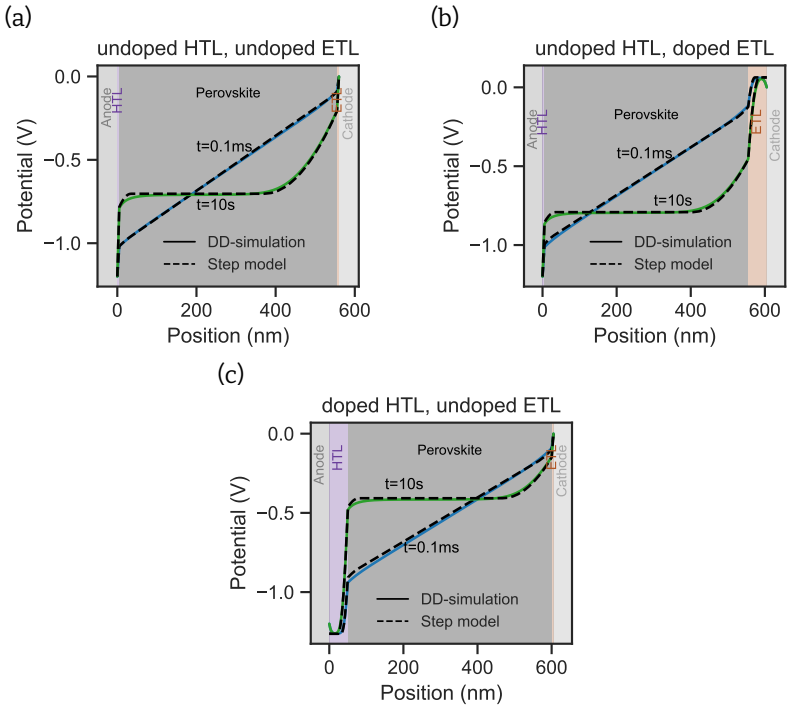

Figure 5.A.6: Comparison of the approximated DC potential with drift-diffusion simulations of a transient simulations 0.1 ms and 10 s after the voltage pulse for (a) undoped HTL and ETL, (b) undoped HTL and doped ETL, and (c) doped HTL undoped ETL.

Derivation of the AC Solution

AC Semiconductor Equations

Next, we derive the device's AC solution to approximate its capacitance at 0 V DC bias. Generally, the solution is based on the sinusoidal steady state analysis (S3A), first introduced by Laux [37]. Compared to a parallel plate capacitor approximation, the S3A approximation accounts for the charge injection capacitance within the perovskite, which can lead to increasing capacitance transients [21]. Additionally, we can easily calculate the capacitance of the device when it is in different accumulation and depletion regimes. Lastly, the S3A solution of the step model will allow us to compute the frequency-dependent capacitance.

To simplify the derivation, we start by combining the time-independent terms in the DC Poisson equation and the current continuity equations for electrons and holes. For

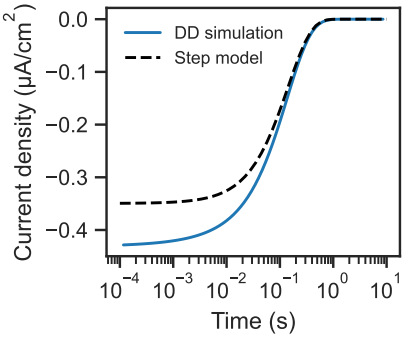

Figure 5.A.7: Drift-diffusion simulation and step model approximation of a current transient measurement with the parameters listed in Table 5.A.1 and an ion density of 10^{17} cm^{-3}.

this purpose, we define F_Φ, F_n, and F_p [49]:

$$\begin{aligned} \frac{dE}{dx} &= -\frac{d^2\Phi}{dx^2} = \frac{e}{\epsilon}(p-n) \\ \Rightarrow F_\Phi(\Phi,n,p) &= \frac{\epsilon}{e}\frac{d^2\Phi}{dx^2} + (p-n) = 0 \end{aligned} \tag{5.67}$$

$$\begin{aligned} \frac{dn}{dt} &= \frac{1}{e}\frac{dj_\mathrm{n}}{dx} - r_\mathrm{n} \\ \Rightarrow -\frac{dn}{dt} + F_\mathrm{n}(\Phi,n,p) &= -\frac{dn}{dt} + \frac{1}{e}\frac{dj_\mathrm{n}}{dx} - r_\mathrm{n} = 0 \end{aligned} \tag{5.68}$$

$$\begin{aligned} \frac{dp}{dt} &= -\frac{1}{e}\frac{dj_\mathrm{p}}{dx} - r_\mathrm{p} \\ \Rightarrow -\frac{dp}{dt} + F_\mathrm{p}(\Phi,n,p) &= -\frac{dp}{dt} - \frac{1}{e}\frac{dj_\mathrm{p}}{dx} - r_\mathrm{p} = 0 \end{aligned} \tag{5.69}$$

where we simplify the permittivity of a layer to $\epsilon = \epsilon_0\epsilon_\mathrm{r}$.
Next, we extend the potential and the electron and hole density into a DC and a complex AC part [49].

$$\Phi = \Phi^\mathrm{dc} + \Phi^\mathrm{ac}e^{i\omega t} \tag{5.70}$$

$$n = n^\mathrm{dc} + n^\mathrm{ac}e^{i\omega t} \tag{5.71}$$

$$p = p^\mathrm{dc} + p^\mathrm{ac}e^{i\omega t} \tag{5.72}$$

We can then linearize the semiconductor equations around a DC operating point with a first-order Taylor series expansion [49]. For the Poisson equation we get:

$$\begin{aligned} 0 &= F_\Phi(\Phi^{\mathrm{dc}} + \Phi^{\mathrm{ac}} e^{i\omega t}, n^{\mathrm{dc}} + n^{\mathrm{ac}} e^{i\omega t}, p^{\mathrm{dc}} + p^{\mathrm{ac}} e^{i\omega t}) \\ &\approx F_\Phi(\Phi^{\mathrm{dc}}, n^{\mathrm{dc}}, p^{\mathrm{dc}}) + e^{i\omega t}\left(\frac{dF_\Phi}{d\Phi}\Phi^{\mathrm{ac}} + \frac{dF_\Phi}{dn}n^{\mathrm{ac}} + \frac{dF_\Phi}{dp}p^{\mathrm{ac}}\right) \end{aligned} \tag{5.73}$$

According to Equation 5.67, $F_\Phi(\Phi^{\mathrm{dc}}, n^{\mathrm{dc}}, p^{\mathrm{dc}})$ equation at steady state is zero. We can therefore simplify the equation and get:

$$0 = \frac{dF_\Phi}{d\Phi}\Phi^{\mathrm{ac}} + \frac{dF_\Phi}{dn}n^{\mathrm{ac}} + \frac{dF_\Phi}{dp}p^{\mathrm{ac}} \tag{5.74}$$

Similarly, we treat the current continuity equation for electrons:

$$\begin{aligned} 0 &= -\frac{d(n^{\mathrm{dc}} + n^{\mathrm{ac}} e^{iwt})}{dt} + F_{\mathrm{n}}(\Phi^{\mathrm{dc}} + \Phi^{\mathrm{ac}} e^{i\omega t}, n^{\mathrm{dc}} + n^{\mathrm{ac}} e^{i\omega t}, p^{\mathrm{dc}} + p^{\mathrm{ac}} e^{i\omega t}) \\ &\overset{\text{Taylor}}{\approx} -\frac{d(n^{\mathrm{dc}} + n^{\mathrm{ac}} e^{iwt})}{dt} + F_{\mathrm{n}}(\Phi^{\mathrm{dc}}, n^{\mathrm{dc}}, p^{\mathrm{dc}}) + e^{i\omega t}\left(\frac{dF_{\mathrm{n}}}{d\Phi}\Phi^{\mathrm{ac}} + \frac{dF_{\mathrm{n}}}{dn}n^{\mathrm{ac}} + \frac{dF_{\mathrm{n}}}{dp}p^{\mathrm{ac}}\right) \\ &= -i\omega n^{\mathrm{ac}} e^{i\omega t} + F_{\mathrm{n}}(\Phi^{\mathrm{dc}}, n^{\mathrm{dc}}, p^{\mathrm{dc}}) + e^{i\omega t}\left(\frac{dF_{\mathrm{n}}}{d\Phi}\Phi^{\mathrm{ac}} + \frac{dF_{\mathrm{n}}}{dn}n^{\mathrm{ac}} + \frac{dF_{\mathrm{n}}}{dp}p^{\mathrm{ac}}\right) \end{aligned} \tag{5.75}$$

Again, the DC solution $F_{\mathrm{n}}(\Phi^{\mathrm{dc}}, n^{\mathrm{dc}}, p^{\mathrm{dc}})$ at steady state is zero. The equation simplifies to:

$$0 = -i\omega n^{\mathrm{ac}} + \frac{dF_{\mathrm{n}}}{d\Phi}\Phi^{\mathrm{ac}} + \frac{dF_{\mathrm{n}}}{dn}n^{\mathrm{ac}} + \frac{dF_{\mathrm{n}}}{dp}p^{\mathrm{ac}} \tag{5.76}$$

We can derive the expression for the hole current continuity equation in the same way:

$$0 = -i\omega p^{\mathrm{ac}} + \frac{dF_{\mathrm{p}}}{d\Phi}\Phi^{\mathrm{ac}} + \frac{dF_{\mathrm{p}}}{dn}n^{\mathrm{ac}} + \frac{dF_{\mathrm{p}}}{dp}p^{\mathrm{ac}} \tag{5.77}$$

We can write Equations 5.74, 5.76, and 5.77 in matrix notation.

$$\begin{bmatrix} \frac{dF_\Phi}{d\Phi} & \frac{dF_\Phi}{dn} & \frac{dF_\Phi}{dp} \\ \frac{dF_{\mathrm{n}}}{d\Phi} & \frac{dF_{\mathrm{n}}}{dn} - i\omega & \frac{dF_{\mathrm{n}}}{dp} \\ \frac{dF_{\mathrm{p}}}{d\Phi} & \frac{dF_{\mathrm{p}}}{dn} & \frac{dF_{\mathrm{p}}}{dp} - i\omega \end{bmatrix} \cdot \begin{bmatrix} \Phi^{\mathrm{ac}} \\ n^{\mathrm{ac}} \\ p^{\mathrm{ac}} \end{bmatrix} = 0 \tag{5.78}$$

This is the linear system of equations that we can solve at different frequencies ω to compute the AC potential, electron, and hole density of the device. To solve this linear system of equations, we first have to define boundary conditions.

Boundary Conditions at Interfaces

At the contacts, we impose AC Dirichlet boundary conditions [37], $n_{\mathrm{ac}} = p_{\mathrm{ac}} = 0$, implying that charge carrier recombination is infinite at the contacts. Furthermore, we excite the system with an AC voltage perturbation $\Phi_{\mathrm{ac},0} = V_{\mathrm{ac}}$ [37]. With these boundary conditions, the solution of the system of Equations in 5.78 will yield the AC solutions for the potential Φ_{ac}, electrons n_{ac}, and holes p_{ac}.

Grid

Before we can solve Equation 5.78 numerically, we have to choose a suitable grid to carry out the discretization. Often, a linear grid is possible. However, as we expect most dynamics to occur at the interface between perovskite and CTLs, we choose a grid suggested by Courtier et al. [50] with a higher resolution at the interfaces. The position x_{i} of grid point i in for example the perovskite is then:

$$x_{\mathrm{i,Pero}} = d_{\mathrm{HTL}} + d_{\mathrm{Pero}} \frac{x'_{\mathrm{i,Pero}} - x'_{\mathrm{0,Pero}}}{x'_{\mathrm{N_{Pero}-1,Pero}} - x'_{\mathrm{0,Pero}}} \tag{5.79}$$

where $x'_{\mathrm{i,Pero}}$ is:

$$x'_{\mathrm{i,Pero}} = \frac{1}{2}\left(\frac{\tanh\left(\sigma(\frac{2i}{N_{\mathrm{Pero}}-1} - 1)\right)}{\tanh(\sigma)} + 1\right) \tag{5.80}$$

for $i = 0, \ldots, N_{\mathrm{Pero}} - 1$ and N_{Pero} the total number of grid points in the perovskite. σ impacts the resolution at the interface. For HTL and ETL, we choose a similar grid but with a higher resolution only at the perovskite/CTL interface. For the HTL, we, for example, get

$$x_{\mathrm{i,HTL}} = d_{\mathrm{HTL}} \frac{x'_{\mathrm{i,HTL}} - x'_{\mathrm{0,HTL}}}{x'_{\mathrm{N_{HTL}-1,HTL}} - x'_{\mathrm{0,HTL}}} \tag{5.81}$$

where $x'_{\mathrm{i,HTL}}$ is:

$$x'_{\mathrm{i,HTL}} = \frac{1}{2}\left(\frac{\tanh\left(\sigma(\frac{2(i+N_{\mathrm{HTL}})}{N_{\mathrm{HTL}}-1} - 1)\right)}{\tanh(\sigma)} + 1\right) \tag{5.82}$$

$$\tag{5.83}$$

for $i = 0, \ldots, N_{\mathrm{HTL}} - 1$ and N_{HTL} the total number of grid points in the HTL.
Based on the total number of grid points N, we can define the potential, electron den-

sity, and hole density at grid point i as Φ_i, n_i, and p_i. We additionally define h_i as

$$h_i = x_{i+1} - x_i \tag{5.84}$$

Variable Scaling

To solve the linear system of equations numerically, we have to scale the variables. Here, we choose the same scaling as suggested by Selberherr [43], with some modifications. We first define the scaling factors:

$$x_s = \max(h) \tag{5.85}$$
$$\Phi_s = \frac{k_\mathrm{B}T}{e} \tag{5.86}$$
$$C_s = \max(p_{HTL}, n_{ETL}) \tag{5.87}$$
$$D_s = \max(D_{n,Pero}, D_{p,Pero}) \tag{5.88}$$

where p_{HTL} is the hole density in the HTL, n_{ETL} is the electron density in the ETL, and $D_{n,Pero}$ and $D_{p,Pero}$ are the diffusion coefficients of electrons and holes in the perovskite. The scaled variables, indicated with a prime, are then:

$$x' = \frac{x}{x_s} \tag{5.89}$$
$$\Phi' = \frac{\Phi}{\Phi_s} \tag{5.90}$$
$$n' = \frac{n}{C_s} \tag{5.91}$$
$$p' = \frac{p}{C_s} \tag{5.92}$$
$$D_n' = \frac{D_n}{D_s} \tag{5.93}$$
$$D_p' = \frac{D_p}{D_s} \tag{5.94}$$
$$t' = \frac{t}{x_s^2} D_s \tag{5.95}$$

We group the scaled variables, resulting in the variable λ:

$$\lambda^2 = \frac{\Phi_s \epsilon}{e C_s x_s^2} \tag{5.96}$$

For simplicity, we omit the prime in the following derivation.

Discretization of Semiconductor Equations

To solve for the AC solution in Equation 5.78 numerically, we need to express the solution in a discretized fashion. If we define a one-dimensional grid with N grid points, the linear system of equations at each grid point i can be expressed as:

$$\sum_{j=0}^{N-1} \begin{bmatrix} \frac{dF_{\Phi_i}}{d\Phi_j} & \frac{dF_{\Phi_i}}{dn_j} & \frac{dF_{\Phi_i}}{dp_j} \\ \frac{dF_{n_i}}{d\Phi_j} & \frac{dF_{n_i}}{dn_j} - i\omega & \frac{dF_{n_i}}{dp_j} \\ \frac{dF_{p_i}}{d\Phi_j} & \frac{dF_{p_i}}{dn_j} & \frac{dF_{p_i}}{dp_j} - i\omega \end{bmatrix} \cdot \begin{bmatrix} \Phi_j^{\mathrm{ac}} \\ n_j^{\mathrm{ac}} \\ p_j^{\mathrm{ac}} \end{bmatrix} = 0 \tag{5.97}$$

In order to solve Equation 5.97, we need to take the partial derivative of the discretized Poisson and current continuity equations. As a starting point, we refer to the discretized semiconductor equations derived by Selberherr [43]. The discretized Poisson equation in one dimension is:

$$F_{\Phi_i} = \lambda^2 \Big(\frac{\Phi_{i-1}}{h_{i-1}} - \frac{\Phi_i}{h_{i-1}} - \frac{\Phi_i}{h_i} + \frac{\Phi_{i+1}}{h_i} \Big) \frac{2}{h_{i-1} + h_i} - (n_i - p_i) = 0 \tag{5.98}$$

where λ is a scaling factor, which we introduced in Section 5.A.
Based on Equation 5.98 we can now derive the partial derivatives of the discretized Poisson equation.
Generally, the partial derivatives of the Poisson equation are zero in most cases. We can, therefore, distinguish between only a few cases:
If $j = i$:

$$\frac{dF_{\Phi_i}}{d\Phi_i} = -\lambda^2 \Big(\frac{1}{h_{i-1}} + \frac{1}{h_i} \Big) \frac{2}{h_{i-1} + h_i} \tag{5.99}$$

$$\frac{dF_{\Phi_i}}{dn_i} = -1 \tag{5.100}$$

$$\frac{dF_{\Phi_i}}{dp_i} = 1 \tag{5.101}$$

$j = i - 1$:

$$\frac{dF_{\Phi_i}}{d\Phi_{i-1}} = \lambda^2 \frac{1}{h_{i-1}} \frac{2}{h_{i-1} + h_i} \tag{5.102}$$

$$\frac{dF_{\Phi_i}}{dn_{i-1}} = 0 \tag{5.103}$$

$$\frac{dF_{\Phi_i}}{dp_{i-1}} = 0 \tag{5.104}$$

If $j = i + 1$:

$$\frac{dF_{\Phi_i}}{d\Phi_{i+1}} = \lambda^2 \frac{1}{h_i} \frac{2}{h_{i-1} + h_i} \tag{5.105}$$

$$\frac{dF_{\Phi_i}}{dn_{i+1}} = 0 \tag{5.106}$$

$$\frac{dF_{\Phi_i}}{dp_{i+1}} = 0 \tag{5.107}$$

Else:

$$\frac{dF_{\Phi_i}}{d\Phi_j} = 0 \tag{5.108}$$

$$\frac{dF_{\Phi_i}}{dn_j} = 0 \tag{5.109}$$

$$\frac{dF_{\Phi_i}}{dp_j} = 0 \tag{5.110}$$

Next, we derive the partial derivatives of the electron current continuity equation. Following Selberherr, the one-dimensional discretized current continuity equation for electrons is [43]:

$$\begin{aligned} F_{n,i} = \Bigg[& n_{i-1} D_{n,i-\frac{1}{2}} B\left(\frac{\Phi_{i-1} - \Phi_i}{V_t}\right) \frac{1}{h_{i-1}} \\ & + n_{i+1} D_{n,i+\frac{1}{2}} B\left(\frac{\Phi_{i+1} - \Phi_i}{V_t}\right) \frac{1}{h_i} \\ & - n_i \Bigg[D_{n,i-\frac{1}{2}} B\left(\frac{\Phi_i - \Phi_{i-1}}{V_t}\right) \frac{1}{h_{i-1}} \\ & + D_{n,i+\frac{1}{2}} B\left(\frac{\Phi_i - \Phi_{i+1}}{V_t}\right) \frac{1}{h_i} \Bigg] \Bigg] \frac{2}{h_i + h_{i-1}} \\ & - r_i = 0 \end{aligned} \tag{5.111}$$

where D_n is the diffusion coefficient of electrons, r is the recombination term, and $B(x)$ is the Bernoulli function, which is defined as:

$$B(x) = \frac{x}{e^x - 1} \tag{5.112}$$

The derivative of the Bernoulli function is $\beta(x) = \frac{dB(x)}{dx}$. We can now write down the partial derivatives of the electron continuity equation:

If $j = i$:

$$\begin{aligned}\frac{dF_{n,i}}{d\Phi_i} =& \Bigg[- n_{i-1} D_{n,i-\frac{1}{2}} \frac{1}{V_t} \beta(\frac{\Phi_{i-1} - \Phi_i}{V_t}) \frac{1}{h_{i-1}} \\ & - n_{i+1} D_{n,i+\frac{1}{2}} \frac{1}{V_t} \beta(\frac{\Phi_{i+1} - \Phi_i}{V_t}) \frac{1}{h_i} \\ & - n_i \Bigg[D_{n,i-\frac{1}{2}} \frac{1}{V_t} \beta(\frac{\Phi_i - \Phi_{i-1}}{V_t}) \frac{1}{h_{i-1}} \\ & + D_{n,i+\frac{1}{2}} \frac{1}{V_t} \beta(\frac{\Phi_i - \Phi_{i+1}}{V_t}) \frac{1}{h_i} \Bigg] \Bigg] \frac{2}{h_i + h_{i-1}}\end{aligned} \tag{5.113}$$

$$\begin{aligned}\frac{dF_{n,i}}{dn_i} =& \Bigg[- D_{n,i-\frac{1}{2}} B(\frac{\Phi_i - \Phi_{i-1}}{V_t}) \frac{1}{h_{i-1}} \\ & - D_{n,i+\frac{1}{2}} B(\frac{\Phi_i - \Phi_{i+1}}{V_t}) \frac{1}{h_i} \Bigg] \frac{2}{h_i + h_{i-1}}\end{aligned} \tag{5.114}$$

$$\frac{dF_{n,i}}{dp_i} = 0 \tag{5.115}$$

If $j = i - 1$:

$$\begin{aligned}\frac{dF_{n,i}}{d\Phi_{i-1}} =& D_{n,i-\frac{1}{2}} \frac{1}{V_t} \Bigg[n_{i-1} \beta(\frac{\Phi_{i-1} - \Phi_i}{V_t}) \\ & + n_i \beta(\frac{\Phi_i - \Phi_{i-1}}{V_t}) \Bigg] \frac{1}{h_{i-1}} \frac{2}{h_i + h_{i-1}}\end{aligned} \tag{5.116}$$

$$\frac{dF_{n,i}}{dn_{i-1}} = D_{n,i-\frac{1}{2}} B(\frac{\Phi_{i-1} - \Phi_i}{V_t}) \frac{1}{h_{i-1}} \frac{2}{h_i + h_{i-1}} \tag{5.117}$$

$$\frac{dF_{n,i}}{dp_{i-1}} = 0 \tag{5.118}$$

If $j = i + 1$:

$$\begin{aligned}\frac{dF_{n,i}}{d\Phi_{i+1}} =& D_{n,i+\frac{1}{2}} \frac{1}{V_t} \Bigg[n_{i+1} \beta(\frac{\Phi_{i+1} - \Phi_i}{V_t}) \\ & + n_i \beta(\frac{\Phi_i - \Phi_{i+1}}{V_t}) \Bigg] \frac{1}{h_i} \frac{2}{h_i + h_{i-1}}\end{aligned} \tag{5.119}$$

$$\frac{dF_{n,i}}{dn_{i+1}} = D_{n,i+\frac{1}{2}} B(\frac{\Phi_{i+1} - \Phi_i}{V_t}) \frac{1}{h_i} \frac{2}{h_i + h_{i-1}} \tag{5.120}$$

$$\frac{dF_{n,i}}{dp_{i+1}} = 0 \tag{5.121}$$

Else:

$$\frac{dF_{n,i}}{d\Phi_j} = 0 \tag{5.122}$$

$$\frac{dF_{n,i}}{dn_j} = 0 \tag{5.123}$$

$$\frac{dF_{n,i}}{dp_j} = 0 \tag{5.124}$$

Next, we derive the partial derivatives of the hole current continuity equation, which is defined as [43]:

$$\begin{aligned} F_{p,i} = & \Bigg[p_{i-1} D_{p,i-\frac{1}{2}} B(\frac{\Phi_i - \Phi_{i-1}}{V_t}) \frac{1}{h_{i-1}} \\ & + p_{i+1} D_{p,i+\frac{1}{2}} B(\frac{\Phi_i - \Phi_{i+1}}{V_t}) \frac{1}{h_i} \\ & - p_i \Bigg[D_{p,i-\frac{1}{2}} B(\frac{\Phi_{i-1} - \Phi_i}{V_t}) \frac{1}{h_{i-1}} \\ & + D_{p,i+\frac{1}{2}} B(\frac{\Phi_{i+1} - \Phi_i}{V_t}) \frac{1}{h_i} \Bigg] \Bigg] \frac{2}{h_i + h_{i-1}} \\ & - r_i = 0 \end{aligned} \tag{5.125}$$

The partial derivatives are then:

If $j = i$:

$$\begin{aligned} \frac{dF_{p,i}}{d\Phi_i} = & \Bigg[p_{i-1} D_{p,i-\frac{1}{2}} \frac{1}{V_t} \beta(\frac{\Phi_i - \Phi_{i-1}}{V_t}) \frac{1}{h_{i-1}} \\ & + p_{i+1} D_{n,i+\frac{1}{2}} \frac{1}{V_t} \beta(\frac{\Phi_i - \Phi_{i+1}}{V_t}) \frac{1}{h_i} \\ & + p_i \Bigg[D_{p,i-\frac{1}{2}} \frac{1}{V_t} \beta(\frac{\Phi_{i-1} - \Phi_i}{V_t}) \frac{1}{h_{i-1}} \\ & + D_{p,i+\frac{1}{2}} \frac{1}{V_t} \beta(\frac{\Phi_{i+1} - \Phi_i}{V_t}) \frac{1}{h_i} \Bigg] \Bigg] \frac{2}{h_i + h_{i-1}} \end{aligned} \tag{5.126}$$

$$\frac{dF_{p,i}}{dn_i} = 0 \tag{5.127}$$

$$\begin{aligned}\frac{dF_{p,i}}{dp_i} = \Bigg[&- D_{p,i-\frac{1}{2}} B(\frac{\Phi_{i-1} - \Phi_i}{V_t}) \frac{1}{h_{i-1}} \\ &- D_{p,i+\frac{1}{2}} B(\frac{\Phi_{i+1} - \Phi_i}{V_t}) \frac{1}{h_i} \Bigg] \frac{2}{h_i + h_{i-1}}\end{aligned} \tag{5.128}$$

If $j = i - 1$:

$$\begin{aligned}\frac{dF_{p,i}}{d\Phi_{i-1}} = &- D_{p,i-\frac{1}{2}} \frac{1}{V_t} \Bigg[p_{i-1} \beta(\frac{\Phi_i - \Phi_{i-1}}{V_t}) \\ &+ p_i \beta(\frac{\Phi_{i-1} - \Phi_i}{V_t}) \Bigg] \frac{1}{h_{i-1}} \frac{2}{h_i + h_{i-1}}\end{aligned} \tag{5.129}$$

$$\frac{dF_{p,i}}{dn_{i-1}} = 0 \tag{5.130}$$

$$\frac{dF_{p,i}}{dp_{i-1}} = D_{p,i-\frac{1}{2}} B(\frac{\Phi_i - \Phi_{i-1}}{V_t}) \frac{1}{h_{i-1}} \frac{2}{h_i + h_{i-1}} \tag{5.131}$$

(5.132)

If $j = i + 1$:

$$\frac{dF_{p,i}}{d\Phi_{i+1}} = - D_{p,i+\frac{1}{2}} \frac{1}{V_t} \Bigg[p_{i+1} \beta(\frac{\Phi_i - \Phi_{i+1}}{V_t}) + p_i \beta(\frac{\Phi_{i+1} - \Phi_i}{V_t}) \Bigg] \frac{1}{h_i} \frac{2}{h_i + h_{i-1}} \tag{5.133}$$

$$\frac{dF_{p,i}}{dn_{i+1}} = 0 \tag{5.134}$$

$$\frac{dF_{p,i}}{dp_{i+1}} = D_{p,i+\frac{1}{2}} B(\frac{\Phi_i - \Phi_{i+1}}{V_t}) \frac{1}{h_i} \frac{2}{h_i + h_{i-1}} \tag{5.135}$$

Else:

$$\frac{dF_{p,i}}{d\Phi_j} = 0 \tag{5.136}$$

$$\frac{dF_{p,i}}{dn_j} = 0 \tag{5.137}$$

$$\frac{dF_{p,i}}{dp_j} = 0 \tag{5.138}$$

Now, we can construct the matrix in Equation 5.97.

Calculation of AC Potential and Charge Densities

With the boundary conditions and the scaled variables, we can now numerically solve the linear system of Equations in 5.97 for the complex variables Φ_{ac}, n_{ac}, and p_{ac}. Figures 5.A.8(a) to (d) show the real and imaginary parts of these variables compared to drift-diffusion simulations 10 s after removing a voltage pulse at a frequency of 20 kHz. The real part of the potential and the real and imaginary parts of the hole and electron densities in Figures 5.A.8(a), (c), and (d) are in good agreement with the drift-diffusion simulations. The imaginary part of the potential in Figure 5.A.8(b) slightly deviates from the drift-diffusion simulations because we do not account for mobile cations in the AC solution in the step model (we will later introduce the ions in the AC solution), which impact the imaginary part of the potential. Note, however, that the imaginary part of the potential is orders of magnitude lower than the real part. Therefore, the error is negligible.

Calculation of Capacitance

Now that we have the AC potential, electron density, and hole density, we can calculate the device's impedance. Based on the current continuity equation for electrons and holes in Equations 5.68 and 5.69 and the AC extension of electrons and holes in Equations 5.71 and 5.72, we can define the AC electron and hole continuity equations:

$$i\omega n_{\mathrm{ac}}(x) = \frac{1}{e}\frac{d}{dx} j_{\mathrm{n,ac}}(x) - r_{\mathrm{n,ac}}(x) \tag{5.139}$$

$$i\omega p_{\mathrm{ac}}(x) = -\frac{1}{e}\frac{d}{dx} j_{\mathrm{p,ac}}(x) - r_{\mathrm{p,ac}}(x) \tag{5.140}$$

We assume that the recombination is negligible as we focus on techniques that are measured in the dark, and that the ETL and HTL completely block minority carriers. Therefore, the AC electron and hole currents are zero at the anode and cathode, respectively. To get $j_{\mathrm{n,ac}}$ and $j_{\mathrm{p,ac}}$ at position x, we can then simply integrate the current continuity equations across the device.

$$j_{\mathrm{n,ac}}(x) = i\omega e \int_0^x n_{\mathrm{ac}}(x')dx' \tag{5.141}$$

$$j_{\mathrm{p,ac}}(x) = -i\omega e \int_d^x p_{\mathrm{ac}}(x')dx' \tag{5.142}$$

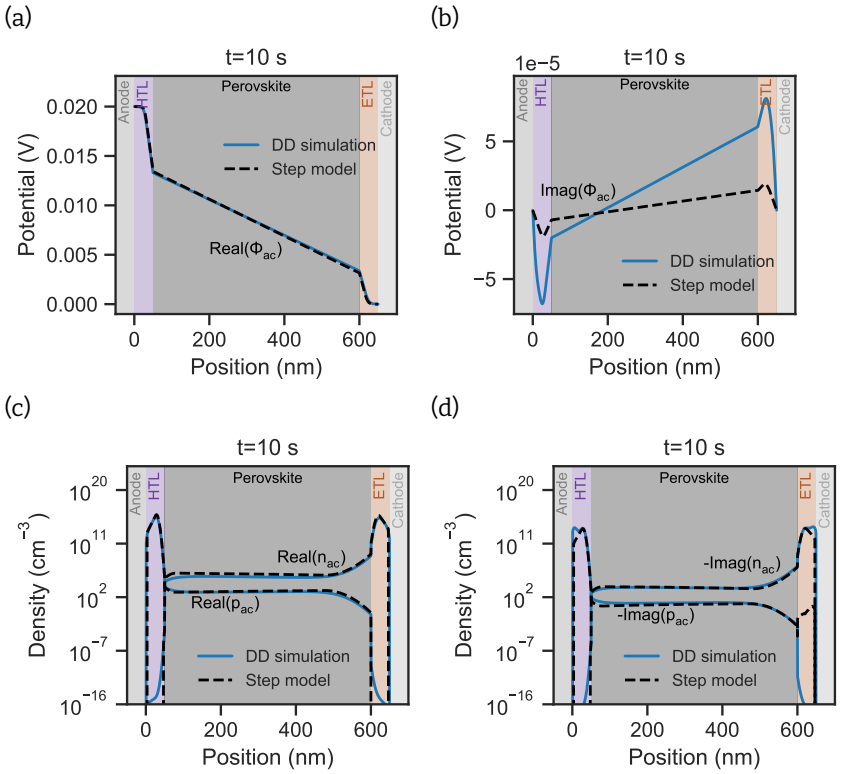

Figure 5.A.8: Comparison of approximated AC currents with drift-diffusion simulations of a capacitance transient simulation 10 s after the voltage pulse. The simulation parameters are listed in table 5.A.1. The ion density is 10^{17} cm^{-3}. (a) Real part of the AC potential, (b) imaginary part of the AC potential, (c) real part of the AC hole and electron density, and (d) imaginary part of the AC hole and electron density.

where d is the device thickness.

Additionally, we need to calculate the AC displacement current. The DC displacement current is defined as:

$$j_{\text{disp}}(x) = \epsilon \frac{dE(x)}{dt} \tag{5.143}$$

After expressing the displacement current j_{disp} and electric field E as a DC and AC part, we can define the equation for the AC displacement current.

$$j_{\text{disp,ac}}(x) = i\omega\epsilon E_{\text{ac}}(x) \tag{5.144}$$

where is AC electric field is accessible from the AC potential.

The approximated real and imaginary parts of the currents are shown in Figure 5.A.9(a) to (d) 10 s after removing a voltage pulse. The real parts deviate from the drift-diffusion simulation because we do not account for mobile ions when solving the AC solution for

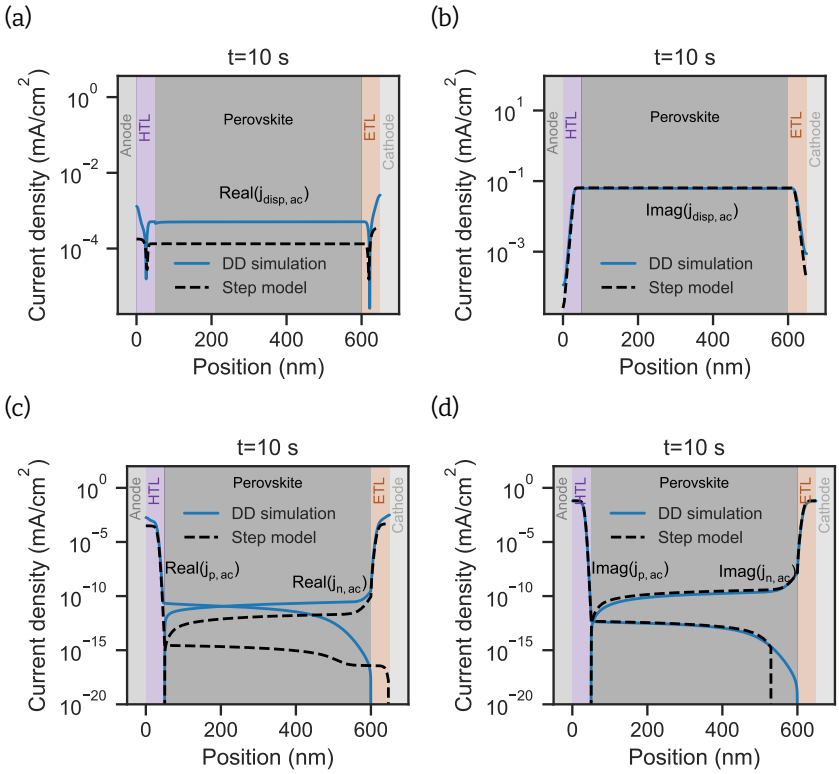

Figure 5.A.9: Comparison of approximated AC currents with drift-diffusion simulations of a capacitance transient simulation 10 s after the voltage pulse. The simulation parameters are listed in Table 5.A.1. The ion density is 10^{17} cm^{-3}. (a) Real part of the AC displacement currents, (b) imaginary part of the AC displacement currents, (c) real part of the AC hole and electron currents, and (d) imaginary part of the AC hole and electron currents.

capacitance transient simulations; the ions only influence the capacitance via the DC electric field. This is valid as long as we are in a frequency regime where we do not expect ions to impact the impedance significantly. This is the case at high frequencies, where we mainly probe the geometrical capacitance. We will later also account for ions in the AC solution. The imaginary parts are in good agreement with the drift-diffusion simulations. At each position through the device, the total AC current density is the sum of the individual current densities, which is constant:

$$J_{\mathrm{ac,tot}} = j_{\mathrm{n,ac}}(x) + j_{\mathrm{p,ac}}(x) + j_{\mathrm{disp,ac}}(x) \tag{5.145}$$

Now, with the total current density and the perturbation voltage V_{ac}, we can calculate the impedance of the device:

$$Z = \frac{V_{\mathrm{ac}}}{J_{\mathrm{ac,tot}}} \tag{5.146}$$

The capacitance is only dependent on the imaginary part of the impedance:

$$C = \frac{1}{\omega}\mathrm{Im}\left(\frac{1}{Z}\right) \tag{5.147}$$

Comparison Capacitance Transients

Now we can simulate the capacitance transients of a device, by first calculating the time-dependent DC solution, according to Section 5.A. Then, at every point in time we compute the capacitance according to Section 5.A, leading to capacitance transients. In Figure 5.A.10, the capacitance calculated with the step model is plotted compared with drift-diffusion simulation. We note that even though the previously shown AC solution is in good agreement with the drift-diffusion simulation, the capacitance transients have some offset compared to the drift-diffusion simulations due to slight differences at the depletion layer edges in the CTLs. This illustrates how sensitive the capacitance is to small differences in the solutions.

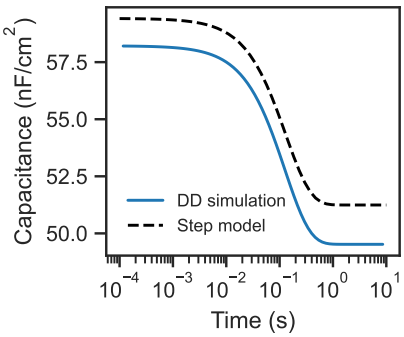

Figure 5.A.10: Drift-diffusion and step model simulation of a capacitance transient measurement with the parameters listed in Table 5.A.1 an ion density of 10^{17} cm^{-3}.

Frequency Dependent Capacitance

In order to simulate the frequency dependent capacitance of the device, we need to extend Equation 5.78 by an ionic term, because ionic carriers dominate the capacitance at low frequencies. As we assume that mostly halide vacancies contribute to the capac-

itance, we only add a term for cations. The system of Equations in 5.78 then becomes:

$$\begin{bmatrix} \frac{dF_\Phi}{d\Phi} & \frac{dF_\Phi}{dn} & \frac{dF_\Phi}{dp} & \frac{dF_\Phi}{dc} \\ \frac{dF_n}{d\Phi} & \frac{dF_n}{dn} - i\omega & \frac{dF_n}{dp} & \frac{dF_n}{dc} \\ \frac{dF_p}{d\Phi} & \frac{dF_p}{dn} & \frac{dF_p}{dp} - i\omega & \frac{dF_p}{dc} \\ \frac{dF_c}{d\Phi} & \frac{dF_c}{dn} & \frac{dF_c}{dp} & \frac{dF_c}{dc} - i\omega \end{bmatrix} \cdot \begin{bmatrix} \Phi^{\mathrm{ac}} \\ n^{\mathrm{ac}} \\ p^{\mathrm{ac}} \\ c^{ac} \end{bmatrix} = 0 \tag{5.148}$$

where c^{ac} is the AC cation density. The discrete partial derivatives of the Poisson equation and the current continuity equation for cations can be derived in a similar fashion compared to holes in Section 5.A. We extend the Poisson equation to:

5

If $j = i$:

$$\frac{dF_{\Phi_i}}{dc_i} = 1 \tag{5.149}$$

Else:

$$\frac{dF_{\Phi_i}}{dc_i} = 0 \tag{5.150}$$

The partial derivatives of the current continuity equations for cations become:

If $j = i$:

$$\begin{aligned} \frac{dF_{c,i}}{d\Phi_i} = & \Bigg[c_{i-1} D_{c,i-\frac{1}{2}} \frac{1}{V_t} \beta\left(\frac{\Phi_i - \Phi_{i-1}}{V_t}\right) \frac{1}{h_{i-1}} \\ & + c_{i+1} D_{c,i+\frac{1}{2}} \frac{1}{V_t} \beta\left(\frac{\Phi_i - \Phi_{i+1}}{V_t}\right) \frac{1}{h_i} \\ & + c_i \Bigg[D_{c,i-\frac{1}{2}} \frac{1}{V_t} \beta\left(\frac{\Phi_{i-1} - \Phi_i}{V_t}\right) \frac{1}{h_{i-1}} \\ & + D_{c,i+\frac{1}{2}} \frac{1}{V_t} \beta\left(\frac{\Phi_{i+1} - \Phi_i}{V_t}\right) \frac{1}{h_i} \Bigg] \Bigg] \frac{2}{h_i + h_{i-1}} \end{aligned} \tag{5.151}$$

$$\frac{dF_{c,i}}{dn_i} = 0 \tag{5.152}$$

$$\frac{dF_{c,i}}{dp_i} = 0 \tag{5.153}$$

$$\begin{aligned} \frac{dF_{c,i}}{dc_i} = & \Bigg[- D_{c,i-\frac{1}{2}} B\left(\frac{\Phi_{i-1} - \Phi_i}{V_t}\right) \frac{1}{h_{i-1}} \\ & - D_{c,i+\frac{1}{2}} B\left(\frac{\Phi_{i+1} - \Phi_i}{V_t}\right) \frac{1}{h_i} \Bigg] \frac{2}{h_i + h_{i-1}} \end{aligned} \tag{5.154}$$

If $j = i - 1$:

$$\frac{dF_{c,i}}{d\Phi_{i-1}} = - D_{c,i-\frac{1}{2}} \frac{1}{V_t} \left[c_{i-1} \beta \left(\frac{\Phi_i - \Phi_{i-1}}{V_t} \right) + c_i \beta \left(\frac{\Phi_{i-1} - \Phi_i}{V_t} \right) \right] \frac{1}{h_{i-1}} \frac{2}{h_i + h_{i-1}} \tag{5.155}$$

$$\frac{dF_{c,i}}{dn_{i-1}} = 0 \tag{5.156}$$

$$\frac{dF_{c,i}}{dp_{i-1}} = 0 \tag{5.157}$$

$$\frac{dF_{c,i}}{dc_{i-1}} = D_{c,i-\frac{1}{2}} B \left(\frac{\Phi_i - \Phi_{i-1}}{V_t} \right) \frac{1}{h_{i-1}} \frac{2}{h_i + h_{i-1}} \tag{5.158}$$

(5.159)

If $j = i + 1$:

$$\frac{dF_{c,i}}{d\Phi_{i+1}} = - D_{c,i+\frac{1}{2}} \frac{1}{V_t} \left[c_{i+1} \beta \left(\frac{\Phi_i - \Phi_{i+1}}{V_t} \right) + c_i \beta \left(\frac{\Phi_{i+1} - \Phi_i}{V_t} \right) \right] \frac{1}{h_i} \frac{2}{h_i + h_{i-1}} \tag{5.160}$$

$$\frac{dF_{c,i}}{dn_{i+1}} = 0 \tag{5.161}$$

$$\frac{dF_{c,i}}{dp_{i+1}} = 0 \tag{5.162}$$

$$\frac{dF_{c,i}}{dc_{i+1}} = D_{c,i+\frac{1}{2}} B \left(\frac{\Phi_i - \Phi_{i+1}}{V_t} \right) \frac{1}{h_i} \frac{2}{h_i + h_{i-1}} \tag{5.163}$$

Else:

$$\frac{dF_{c,i}}{d\Phi_j} = 0 \tag{5.164}$$

$$\frac{dF_{c,i}}{dn_j} = 0 \tag{5.165}$$

$$\frac{dF_{c,i}}{dp_j} = 0 \tag{5.166}$$

$$\frac{dF_{c,i}}{dc_j} = 0 \tag{5.167}$$

As we assume that the halide vacancies do not migrate into the charge transport layers, we impose the boundary conditions that the cation density at the perovskite/CTL interfaces is zero. We can then solve Equation 5.148 at different frequencies $\omega = 2\pi f$. Figure 5.A.11 shows the capacitance vs frequency simulation at 0 V of the drift-diffusion simulations and the step model. Here, we also see a slight difference between the step model and the drift-diffusion simulation, illustrating the sensitivity of the technique.

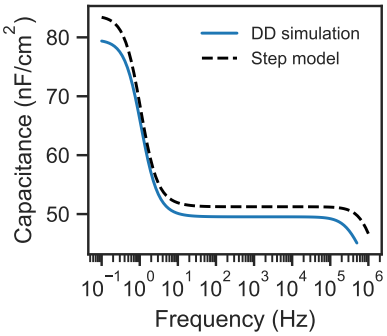

Figure 5.A.11: Drift-diffusion and step model simulation of a capacitance frequency measurement with the parameters listed in Table 5.A.1 and a mobile ion density of 10^{17} cm^{-3}.

Table 5.A.1: Parameters used for the drift-diffusion simulations.

Parameter	Value
Band gap perovskite $E_{\mathrm{g,Pero}}$ (eV)	1.6
Electron affinity perovskite $E_{\mathrm{aff,Pero}}$ (eV)	3.9
Dielectric constant perovskite $\epsilon_{\mathrm{r,Pero}}$	62
Thickness perovskite d_{Pero} (nm)	550
Effective density of states conduction band perovskite $N_{0,\mathrm{CB,Pero}}$ (cm^{-3})	$2.1 \cdot 10^{18}$
Effective density of states valence band perovskite $N_{0,\mathrm{VB,Pero}}$ (cm^{-3})	$2.1 \cdot 10^{18}$
Mobility electrons in perovskite $\mu_{\mathrm{n,Pero}}$ (cm^2/Vs)	1
Mobility holes in perovskite $\mu_{\mathrm{p,Pero}}$ (cm^2/Vs)	1
Mobile positive ion density in perovskite N_{ion} (cm^{-3})	variable
Immobile negative ion density $N_{\mathrm{nion,Pero}}$ (cm^{-3})	variable
Diffusion coefficient of ions at 300 K $D_{\mathrm{ion,300K}}$ (cm^2/s)	$9.1 \cdot 10^{-11}$
Band gap HTL $E_{\mathrm{g,HTL}}$ (eV)	2.0
Electron affinity HTL $E_{\mathrm{aff,HTL}}$ (eV)	3.4
Dielectric constant HTL $\epsilon_{\mathrm{r,HTL}}$	4.0
Thickness HTL d_{HTL} (nm)	50
Effective density of states conduction band HTL $N_{0,\mathrm{CB,HTL}}$ (cm^{-3})	$2.1 \cdot 10^{18}$
Effective density of states valence band HTL $N_{0,\mathrm{VB,HTL}}$ (cm^{-3})	$2.1 \cdot 10^{18}$
Mobility holes in HTL $\mu_{\mathrm{p,HTL}}$ (cm^2/Vs)	10^{-4}
Acceptor doping density in HTL $N_{\mathrm{A,HTL}}$ (cm^{-3})	$5 \cdot 10^{17}$
Band gap ETL $E_{\mathrm{g,ETL}}$ (eV)	2.0
Electron affinity ETL $E_{\mathrm{aff,HTL}}$ (eV)	4.0
Dielectric constant ETL $\epsilon_{\mathrm{r,ETL}}$	8.0
Thickness ETL d_{ETL} (nm)	50
Effective density of states conduction band ETL $N_{0,\mathrm{CB,ETL}}$ (cm^{-3})	$2.1 \cdot 10^{18}$
Effective density of states valence band ETL $N_{0,\mathrm{VB,ETL}}$ (cm^{-3})	$2.1 \cdot 10^{18}$
Mobility electrons in ETL $\mu_{\mathrm{n,ETL}}$ (cm^2/Vs)	10^{-4}
Donor doping density in ETL $N_{\mathrm{D,ETL}}$ (cm^{-3})	$5 \cdot 10^{17}$
Capacitance transient probing frequency (Hz)	$20 \cdot 10^{3}$
Capacitance measurements perturbation voltage amplitude (V)	$20 \cdot 10^{-3}$

5.B Fitting of Drift-Diffusion Simulations

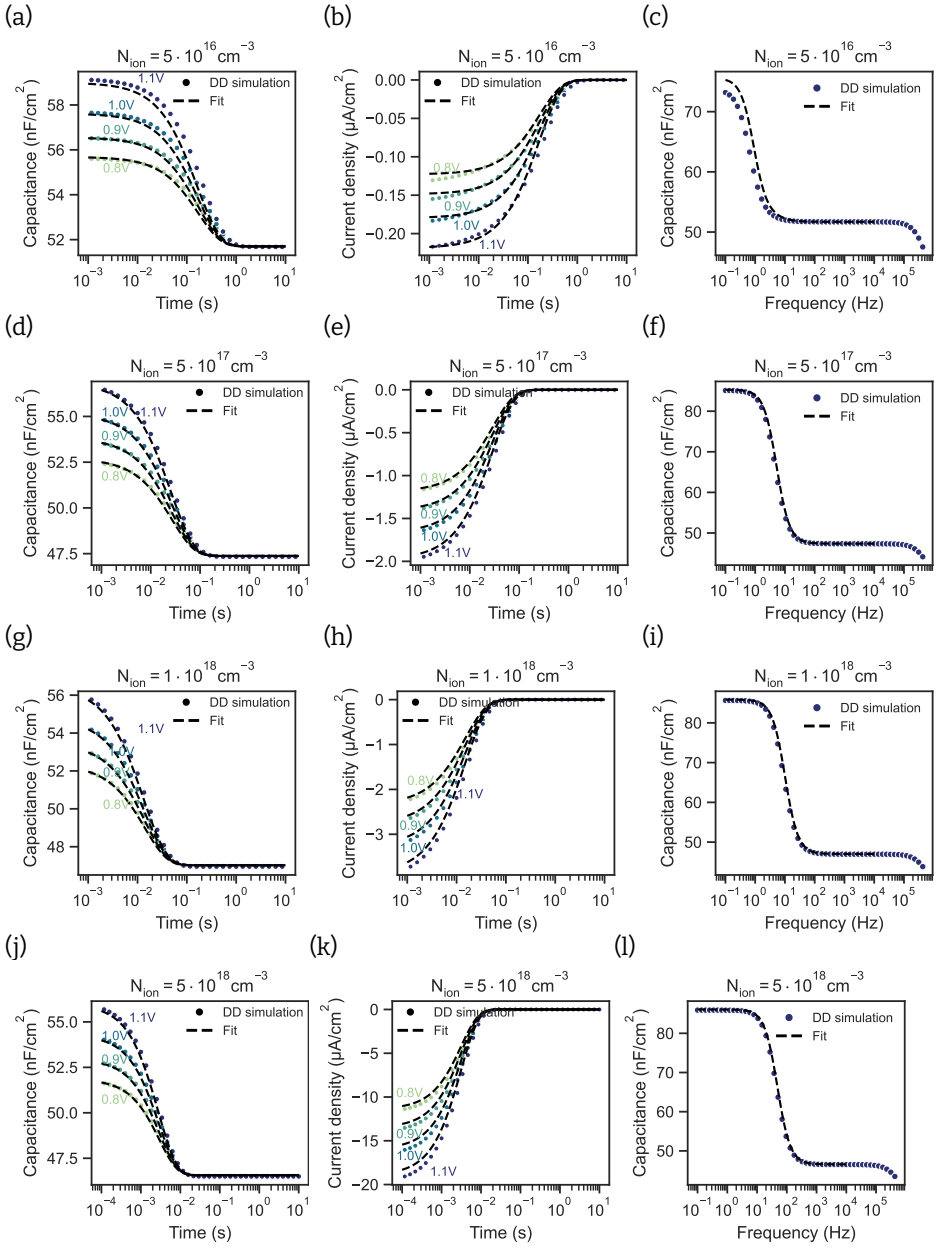

Figure 5.B.1: Drift-diffusion simulations of capacitance transient measurements (column 1), current transient measurements (column 2), and capacitance frequency measurements (column 3). The different rows are simulations with different ion densities. The dashed lines are the fits with the step model. For the ion density of $5 \cdot 10^{18}$ cm^{-3}, we used a higher time resolution to still be able to fit the amplitude accurately.

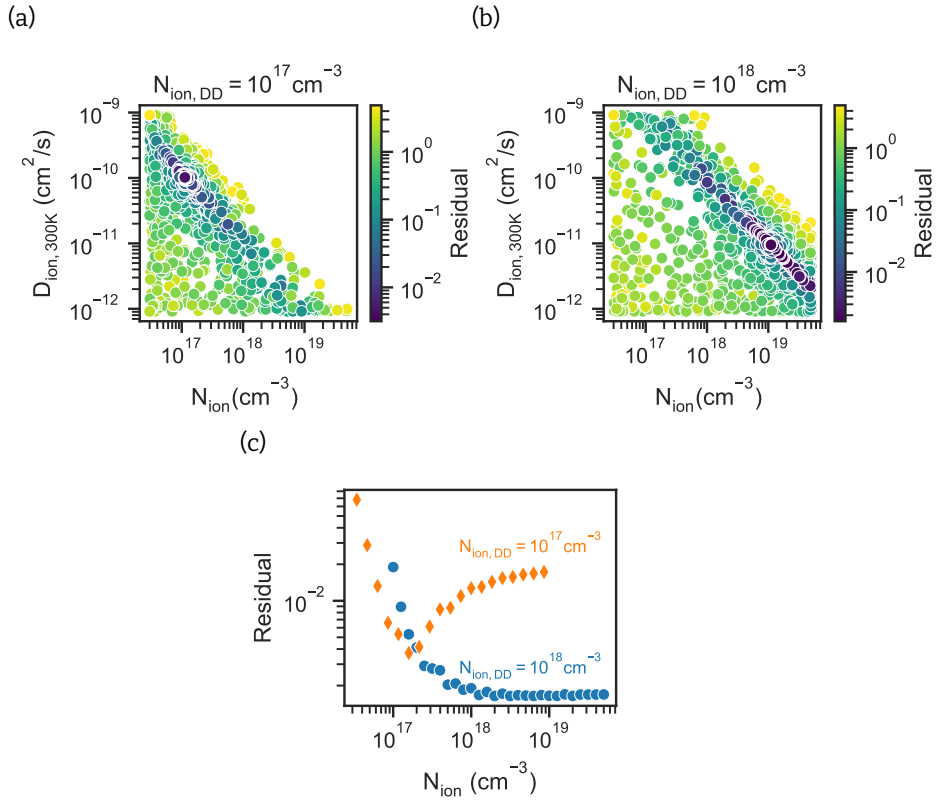

Figure 5.B.2: Residual of fits of drift-diffusion simulations dependent on ion density and diffusion coefficient at 300 K for set ion densities of (a) 10^{17} cm^{-3} and (b) 10^{18} cm^{-3}. (c) Minimum residuals of fits of the same drift-diffusion simulations as in (a) and (b), but keeping the ion density constant in individual fits.

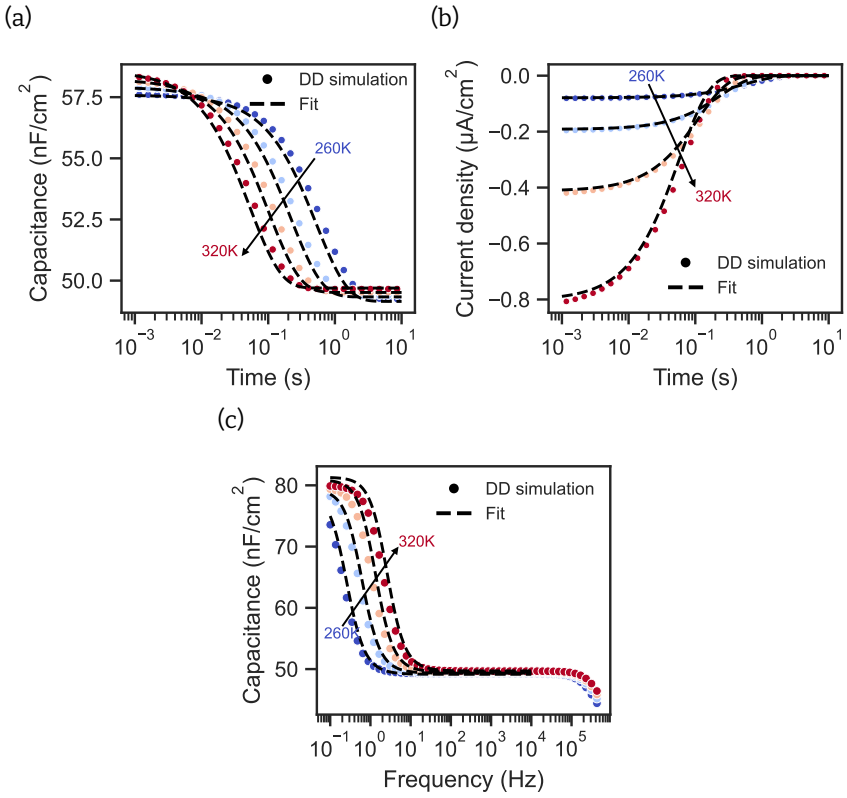

Figure 5.B.3: Global fit of (a) capacitance transient, (b) current transient, and (c) capacitance frequency drift-diffusion simulations at different temperatures with the developed model. The drift-diffusion simulation parameters are listed in Table 5.A.1. The ion density is 10^{17} cm^{-3}.

5.C Experimental Details

Device Fabrication

The solution was prepared by adopting the procedure reported by Seid et al. [45]. First, we mixed PbI_2 (909.00 mg), FAI (276.06 mg), MABr (3.68 mg), CsI (22.47 mg), and MACl (18.11 mg) in solvent mixture of DMF/DMSO (5/1 v/v). We stirred the solution for 4 hours at 60 °C, resulting in a 1.73 M $Cs_{0.05}(MA_{0.05}FA_{0.95})_{0.95}Pb(I_{0.95}Br_{0.05})_3$ perovskite solution. We fabricated planar inverted perovskite solar cells using the following layer structure: glass/ITO/MeO-2PACz/$Cs_{0.05}(MA_{0.05}FA_{0.95})_{0.95}Pb(I_{0.95}Br_{0.05})_3$/$C_{60}$/BCP/Cu. We started by cleaning the ITO-coated glass substrates in an ultrasonic bath using acetone, Hellmanex (3 % in deionized water), deionized water, ethanol, acetone, and isopropanol. Each cleaning step lasted 15 minutes. Then, we cleaned the substrates

with an ultraviolet ozone for 30 minutes before placing them in a nitrogen-filled glovebox.
Next, we spin-coated a MeO-2PACz layer from a 1 mmol mL^{-1} ethanol solution at 3000 rpm for 30 seconds, which was annealed at 100 °C for 10 minutes. Once cooled down, we spin-coated a triple-cation perovskite solution onto the substrate at 4000 rpm for 40 seconds with a 5-second acceleration time. As an antisolvent, we added 300 µl of chlorobenzene 7 seconds before the end of the process. Subsequently, the perovskite film was annealed at 100 °C for 1 hour. After transferring the samples into an evaporation chamber, 30 nm of C_{60} was deposited at 0.3 Å/s, followed by 8 nm of BCP and 100 nm of copper. BCP and copper were both evaporated at 0.3 Å/s and 0.6 Å/s, respectively, under a high vacuum of 10^{-7} mbar.

Electrical Characterization

The capacitance transient, current transient, and capacitance frequency measurements were carried out in a Janis VPF-100 liquid nitrogen cryostat. During the measurements, the pressure inside the cryostat was around $5 \cdot 10^{-6}$ mbar. The temperature was stabilized at each temperature step for 10 minutes. All capacitance measurements were recorded using the Zurich Instruments MFIA with an AC voltage amplitude of 20 mV at a frequency of 20 kHz. The capacitance-frequency measurements were acquired in a frequency range from 0.1 Hz-500 kHz. The capacitance transients were recorded by applying a 60 s-long voltage pulse before measuring the capacitance at 0 V for 60 s. The current transient measurements were carried out with an Agilent B2902A source-measure unit. After applying a voltage pulse, we measured the current at 0 V.
Current density vs voltage measurements were carried out in a nitrogen-filled glovebox with a Keithley 4200 source-measure unit. The devices were illuminated with a G2V Pico solar simulator.

5.D Measurements and Fitting

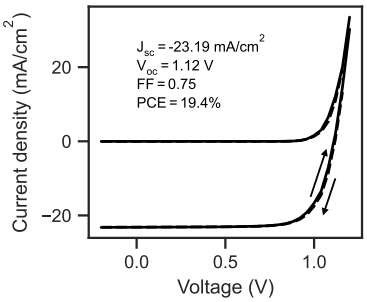

Figure 5.D.1: Exemplary current density vs. voltage measurement in the dark and under one-sun illumination. The extracted photovoltaic parameters are the average values of the forward and backward measurements.

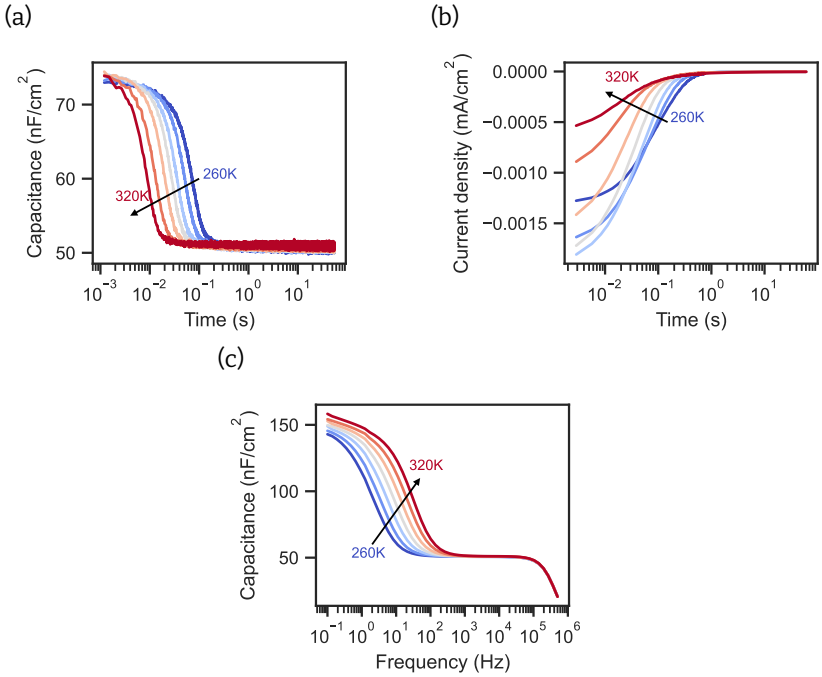

Figure 5.D.2: Temperature dependent measurements in 10 K steps from 260 K to 320 K. (a) Capacitance transient measurements, (b) current transient measurements, and (c) capacitance frequency measurements. In the capacitance transient and current transient measurements, a voltage pulse of 1.1 V was applied for 60 s at $t < 0$ s.

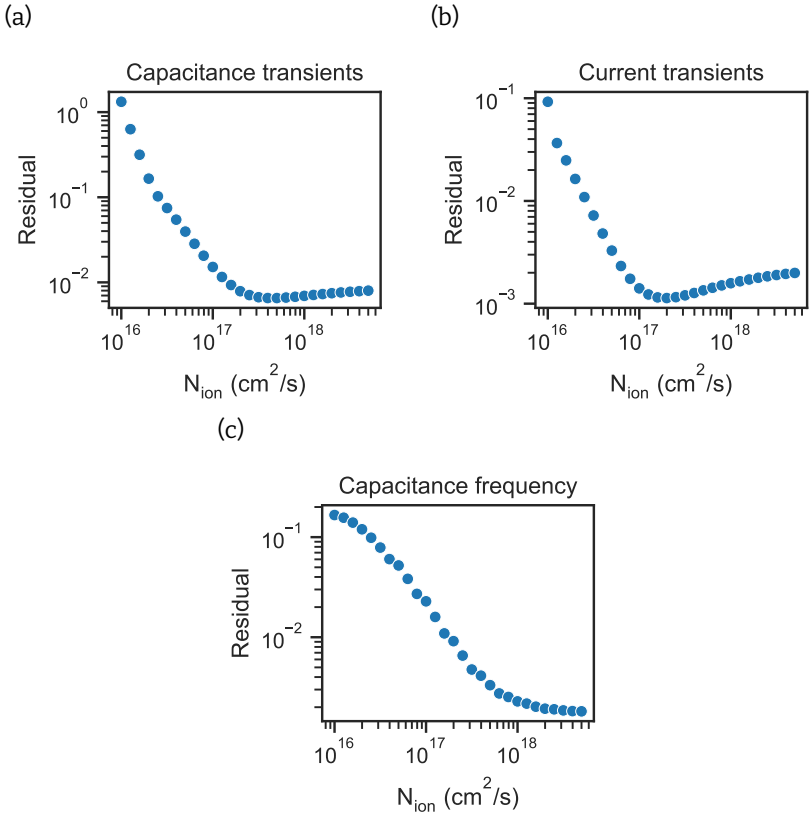

Figure 5.D.3: Fit residuals of (a) capacitance transient, (b) current transient, and (c) capacitance frequency measurements in Figure 5.4 in the main text. We note that residuals below 0.01 lead to similar fits. So, even though a local minimum is visible for the current transient measurements, the ion densities cannot be extracted from these fits.

Table 5.D.1: Parameters used for fitting the measurements.

Parameter	Value	Comment
Band gap perovskite $E_{\mathrm{g,Pero}}$ (eV)	1.63	[51]
Electron affinity perovskite $E_{\mathrm{aff,Pero}}$ (eV)	3.9	[51]
Dielectric constant perovskite $\epsilon_{\mathrm{r,Pero}}$	50-60	Fitting parameter
Thickness perovskite d_{Pero} (nm)	560	Measured with AFM
Effective density of states conduction band perovskite $N_{0,\mathrm{CB,Pero}}$ (cm^{-3})	$2 \cdot 10^{18}$	
Effective density of states valence band $N_{0,\mathrm{VB,Pero}}$ (cm^{-3})	$2 \cdot 10^{18}$	
Mobility electrons in perovskite $\mu_{\mathrm{n,Pero}}$ (cm^2/Vs)	1	
Mobility holes in perovskite $\mu_{\mathrm{p,Pero}}$ (cm^2/Vs)	1	
Mobile positive ion density in perovskite N_{ion} (cm^{-3})	$3 \cdot 10^{16}$ - $5 \cdot 10^{18}$	Fitting parameter
Immobile negative ion density N_{ion} (cm^{-3})	$3 \cdot 10^{16}$-$5 \cdot 10^{18}$	Fitting parameter
Diffusion coefficient prefactor $D_{0,ion}$ (cm^2/s)	$1 \cdot 10^{-10}$-$1 \cdot 10^{-3}$	Fitting parameter
Band gap HTL $E_{\mathrm{g,HTL}}$ (eV)	2.3	
Electron affinity HTL $E_{\mathrm{aff,HTL}}$ (eV)	3.0	
Dielectric constant HTL $\epsilon_{\mathrm{r,HTL}}$	3-4	Fitting parameter
Thickness HTL d_{HTL} (nm)	2	
Effective density of states conduction band HTL $N_{0,\mathrm{CB,HTL}}$ (cm^{-3})	$2 \cdot 10^{18}$	
Effective density of states valence band $N_{0,\mathrm{VB,HTL}}$ (cm^{-3})	$2 \cdot 10^{18}$	
Mobility holes in HTL $\mu_{\mathrm{p,HTL}}$ (cm^2/Vs)	0.02	
Work function anode $W_{\mathrm{f,anode}}$ (eV)	4.9-5.3	Fitting parameter
Valence band ETL $E_{\mathrm{g,ETL}}$ (eV)	6.0	
Electron affinity ETL $E_{\mathrm{aff,ETL}}$ (eV)	3.9-4.1	Fitting parameter
Dielectric constant ETL $\epsilon_{\mathrm{r,ETL}}$	4-5	Fitting parameter, around [52]
Thickness ETL d_{ETL} (nm)	30	
Effective density of states conduction band ETL $N_{0,\mathrm{CB,ETL}}$ (cm^{-3})	$2 \cdot 10^{18}$	
Effective density of states valence band $N_{0,\mathrm{VB,ETL}}$ (cm^{-3})	$2 \cdot 10^{18}$	
Mobility electrons in ETL $\mu_{\mathrm{n,ETL}}$ (cm^2/Vs)	0.02	
Donor doping density in ETL $N_{\mathrm{D,ETL}}$ (cm^{-3})	$5 \cdot 10^{16}$-$5 \cdot 10^{17}$	Fitting parameter
Capacitance transient probing frequency (Hz)	$20 \cdot 10^{3}$	
Capacitance measurements perturbation voltage amplitude (V)	$20 \cdot 10^{-3}$	

Table 5.D.2: Device parameters extracted from a global fit of the capacitance transient and capacitance frequency measurements at 260 K. The values are the average values and standard deviations of fits of three devices.

Parameter	Value
Dielectric constant perovskite $\epsilon_{\mathrm{r,Pero}}$	49.6±2.5
Dielectric constant HTL $\epsilon_{\mathrm{r,HTL}}$	4.0
Work function anode $W_{\mathrm{f,anode}}$ (eV)	5.0±0.1
Dielectric constant ETL $\epsilon_{\mathrm{r,ETL}}$	5.0
Conduction band ETL $E_{\mathrm{CB,ETL}}$ (eV)	4.01±0.08
Donor doping density ETL $N_{\mathrm{D,ETL}}$ (cm^{-3})	$2.1\pm0.4 \cdot 10^{17}$

Bibliography

[1] M. A. Green *et al.*, "Solar Cell Efficiency Tables (Version 64)", *Progress in Photovoltaics: Research and Applications*, vol. 32, no. 7, pp. 425–441, 2024.

[2] PV Magazine, *Longi Claims World's Highest Efficiency for Silicon Solar Cells*, `https://www.pv-magazine.com/2025/04/14/longi-claims-worlds-highest-efficiency-for-silicon-solar-cells/`, Accessed: 2025-05-14.

[3] Z. Shen *et al.*, "Efficient and Stable Perovskite Solar Cells with Regulated Depletion Region", *Nature Photonics*, vol. 18, no. 5, pp. 450–457, 2024.

[4] Y. Yang *et al.*, "Amidination of Ligands for Chemical and Field-Effect Passivation Stabilizes Perovskite Solar Cells", *Science*, vol. 386, no. 6724, pp. 898–902, 2024.

[5] Y. Zhao *et al.*, "Mobile-Ion-Induced Degradation of Organic Hole-Selective Layers in Perovskite Solar Cells", *The Journal of Physical Chemistry C*, vol. 121, no. 27, pp. 14 517–14 523, 2017.

[6] E. T. Hoke, D. J. Slotcavage, E. R. Dohner, A. R. Bowring, H. I. Karunadasa, and M. D. McGehee, "Reversible Photo-Induced Trap Formation in Mixed-Halide Hybrid Perovskites for Photovoltaics", *Chemical Science*, vol. 6, no. 1, pp. 613–617, 2015.

[7] Z. Fang, T. Nie, S. Liu, and J. Ding, "Overcoming Phase Segregation in Wide-Bandgap Perovskites: From Progress to Perspective", *Advanced Functional Materials*, vol. 34, no. 42, p. 2 404 402, 2024.

[8] V. M. Le Corre *et al.*, "Quantification of Efficiency Losses Due to Mobile Ions in Perovskite Solar Cells via Fast Hysteresis Measurements", *Solar RRL*, vol. 6, no. 4, p. 2 100 772, 2022.

[9] J. Thiesbrummel *et al.*, "Ion-Induced Field Screening as a Dominant Factor in Perovskite Solar Cell Operational Stability", *Nature Energy*, vol. 9, no. 6, pp. 664–676, 2024.

[10] S. Shah *et al.*, "Impact of Ion Migration on the Performance and Stability of Perovskite-Based Tandem Solar Cells", *Advanced Energy Materials*, vol. 14, no. 48, p. 2 400 720, 2024.

[11] J. Thiesbrummel *et al.*, "Universal Current Losses in Perovskite Solar Cells Due to Mobile Ions", *Advanced Energy Materials*, vol. 11, no. 34, p. 2 101 447, 2021.

[12] M. Diethelm *et al.*, "Probing Ionic Conductivity and Electric Field Screening in Perovskite Solar Cells: A Novel Exploration through Ion Drift Currents", *Energy & Environmental Science*, vol. 18, no. 3, pp. 1385–1397, 2025.

[13] A. O. Alvarez *et al.*, "Ion Migration and Space-Charge Zones in Metal Halide Perovskites Through Short-Circuit Transient Current and Numerical Simulations", *Advanced Electronic Materials*, vol. 10, no. 11, p. 2 400 241, 2024.

[14] C. Xu, M. S. Alvar, G.-J. A. H. Wetzelaer, and P. W. M. Blom, "Analysis of the Ionic and Dielectric Properties of Perovskites by Impedance Spectroscopy", *Journal of Applied Physics*, vol. 133, no. 4, p. 045 501, 2023.

[15] C. Messmer *et al.*, "Understanding Ion-Related Performance Losses in Perovskite-Based Solar Cells by Capacitance Measurements and Simulation", *Solar RRL*, vol. 8, no. 24, p. 2 400 630, 2024.

[16] M. C. Schmidt, A. O. Alvarez, J. J. De Boer, L. J. Van De Ven, and B. Ehrler, "Consistent Interpretation of Time- and Frequency-Domain Traces of Ion Migration in Perovskite Semiconductors", *ACS Energy Letters*, vol. 9, no. 12, pp. 5850–5858, 2024.

[17] L. McGovern *et al.*, "Reduced Barrier for Ion Migration in Mixed-Halide Perovskites", *ACS Applied Energy Materials*, vol. 4, no. 12, pp. 13 431–13 437, 2021.

[18] M. H. Futscher *et al.*, "Quantification of Ion Migration in $CH_3NH_3PbI_3$ Perovskite Solar Cells by Transient Capacitance Measurements", *Materials Horizons*, vol. 6, no. 7, pp. 1497–1503, 2019.

[19] S. Ravishankar, Z. Liu, U. Rau, and T. Kirchartz, "Multilayer Capacitances: How Selective Contacts Affect Capacitance Measurements of Perovskite Solar Cells", *PRX Energy*, vol. 1, no. 1, p. 013 003, 2022.

[20] R. A. Awni *et al.*, "Influence of Charge Transport Layers on Capacitance Measured in Halide Perovskite Solar Cells", *Joule*, vol. 4, no. 3, pp. 644–657, 2020.

[21] M. C. Schmidt, E. Gutierrez-Partida, M. Stolterfoht, and B. Ehrler, "Impact of Mobile Ions on Transient Capacitance Measurements of Perovskite Solar Cells", *PRX Energy*, vol. 2, no. 4, p. 043 011, 2023.

[22] V. M. Le Corre *et al.*, "Charge Transport Layers Limiting the Efficiency of Perovskite Solar Cells: How To Optimize Conductivity, Doping, and Thickness", *ACS Applied Energy Materials*, vol. 2, no. 9, pp. 6280–6287, 2019.

[23] E. A. Duijnstee, J. M. Ball, V. M. Le Corre, L. J. A. Koster, H. J. Snaith, and J. Lim, "Toward Understanding Space-Charge Limited Current Measurements on Metal Halide Perovskites", *ACS Energy Letters*, vol. 5, no. 2, pp. 376–384, 2020.

[24] N. E. Courtier, J. M. Foster, S. E. J. O'Kane, A. B. Walker, and G. Richardson, "Systematic Derivation of a Surface Polarisation Model for Planar Perovskite Solar Cells", *European Journal of Applied Mathematics*, vol. 30, no. 3, pp. 427–457, 2019.

[25] N. E. Courtier, J. M. Cave, J. M. Foster, A. B. Walker, and G. Richardson, "How Transport Layer Properties Affect Perovskite Solar Cell Performance: Insights from a Coupled Charge Transport/Ion Migration Model", *Energy & Environmental Science*, vol. 12, no. 1, pp. 396–409, 2019.

[26] L. Bertoluzzi *et al.*, "Mobile Ion Concentration Measurement and Open-Access Band Diagram Simulation Platform for Halide Perovskite Solar Cells", *Joule*, vol. 4, no. 1, pp. 109–127, 2020.

[27] *Code to Approximate Drift-Diffusion Simulation*, `https://github.com/AMOLF-Hybrid-Solar-Cells/DD-Approximation_CtJtCf`, 2025.

[28] S. G. McCallum, O. Nicholls, K. O. Jensen, M. V. Cowley, J. E. Lerpinière, and A. B. Walker, "Bayesian Parameter Estimation for Characterising Mobile Ion Vacancies in Perovskite Solar Cells", *Journal of Physics: Energy*, vol. 6, no. 1, p. 015 005, 2024.

[29] G. Richardson *et al.*, "Can Slow-Moving Ions Explain Hysteresis in the Current–Voltage Curves of Perovskite Solar Cells?", *Energy & Environmental Science*, vol. 9, no. 4, pp. 1476–1485, 2016.

[30] C. Eames, J. M. Frost, P. R. F. Barnes, B. C. O'Regan, A. Walsh, and M. S. Islam, "Ionic Transport in Hybrid Lead Iodide Perovskite Solar Cells", *Nature Communications*, vol. 6, no. 1, p. 7497, 2015.

[31] J. Haruyama, K. Sodeyama, L. Han, and Y. Tateyama, "First-Principles Study of Ion Diffusion in Perovskite Solar Cell Sensitizers", *Journal of the American Chemical Society*, vol. 137, no. 32, pp. 10 048–10 051, 2015.

[32] J. M. Azpiroz, E. Mosconi, J. Bisquert, and F. De Angelis, "Defect Migration in Methylammonium Lead Iodide and Its Role in Perovskite Solar Cell Operation", *Energy & Environmental Science*, vol. 8, no. 7, pp. 2118–2127, 2015.

[33] A. Walsh, D. O. Scanlon, S. Chen, X. G. Gong, and S.-H. Wei, "Self-Regulation Mechanism for Charged Point Defects in Hybrid Halide Perovskites", *Angewandte Chemie International Edition*, vol. 54, no. 6, pp. 1791–1794, 2015.

[34] E. Mosconi and F. De Angelis, "Mobile Ions in Organohalide Perovskites: Interplay of Electronic Structure and Dynamics", *ACS Energy Letters*, vol. 1, no. 1, pp. 182–188, 2016.

[35] F. Peña-Camargo *et al.*, "Revealing the Doping Density in Perovskite Solar Cells and Its Impact on Device Performance", *Applied Physics Reviews*, vol. 9, no. 2, p. 021 409, 2022.

[36] O. Almora, I. Zarazua, E. Mas-Marza, I. Mora-Sero, J. Bisquert, and G. Garcia-Belmonte, "Capacitive Dark Currents, Hysteresis, and Electrode Polarization in Lead Halide Perovskite Solar Cells", *The Journal of Physical Chemistry Letters*, vol. 6, no. 9, pp. 1645–1652, 2015.

[37] S. Laux, "Techniques for Small-Signal Analysis of Semiconductor Devices", *IEEE Transactions on Computer-Aided Design of Integrated Circuits and Systems*, vol. 4, no. 4, pp. 472–481, 1985.

[38] S. M. Sze and K. K. Ng, *Physics of Semiconductor Devices*, 3rd ed. Hoboken, N.J: Wiley-Interscience, 2007.

[39] S. E. J. O'Kane *et al.*, "Measurement and Modelling of Dark Current Decay Transients in Perovskite Solar Cells", *Journal of Materials Chemistry C*, vol. 5, no. 2, pp. 452–462, 2017.

[40] E. Knapp and B. Ruhstaller, "Numerical Impedance Analysis for Organic Semiconductors with Exponential Distribution of Localized States", *Applied Physics Letters*, vol. 99, no. 9, p. 093 304, 2011.

[41] Q. Li and R. Dutton, "Numerical Small-Signal AC Modeling of Deep-Level-Trap Related Frequency-Dependent Output Conductance and Capacitance for GaAs MESFET's on Semi-Insulating Substrates", *IEEE Transactions on Electron Devices*, vol. 38, no. 6, pp. 1285–1288, 1991.

[42] M. Gaitan and I. D. Mayergoyz, "A Numerical Analysis for the Small-Signal Response of the MOS Capacitor", *Solid-State Electronics*, vol. 32, no. 3, pp. 207–213, 1989.

[43] S. Selberherr, *Analysis and Simulation of Semiconductor Devices*. Vienna: Springer Vienna, 1984.

[44] M. C. Schmidt and B. Ehrler, "How Many Mobile Ions Can Electrical Measurements Detect in Perovskite Solar Cells?", *ACS Energy Letters*, vol. 10, no. 5, pp. 2457–2460, 2025.

[45] B. A. Seid *et al.*, "Understanding and Mitigating Atomic Oxygen-Induced Degradation of Perovskite Solar Cells for Near-Earth Space Applications", *Small*, vol. 20, no. 30, p. 2 311 097, 2024.

[46] S. Reichert, Q. An, Y.-W. Woo, A. Walsh, Y. Vaynzof, and C. Deibel, "Probing the Ionic Defect Landscape in Halide Perovskite Solar Cells", *Nature Communications*, vol. 11, no. 1, p. 6098, 2020.

[47] W. Zhu, S. Wang, X. Zhang, A. Wang, C. Wu, and F. Hao, "Ion Migration in Organic–Inorganic Hybrid Perovskite Solar Cells: Current Understanding and Perspectives", *Small*, vol. 18, no. 15, p. 2 105 783, 2022.

[48] T.-Y. Yang, G. Gregori, N. Pellet, M. Grätzel, and J. Maier, "The Significance of Ion Conduction in a Hybrid Organic–Inorganic Lead-Iodide-Based Perovskite Photosensitizer", *Angewandte Chemie International Edition*, vol. 54, no. 27, pp. 7905–7910, 2015.

[49] S. Wagner, *Small-Signal Device and Circuit Simulation*. TU Wien, 2005.

[50] N. E. Courtier, J. M. Cave, A. B. Walker, G. Richardson, and J. M. Foster, "IonMonger: A Free and Fast Planar Perovskite Solar Cell Simulator with Coupled Ion Vacancy and Charge Carrier Dynamics", *Journal of Computational Electronics*, vol. 18, no. 4, pp. 1435–1449, 2019.

[51] M. Stolterfoht *et al.*, "The Impact of Energy Alignment and Interfacial Recombination on the Internal and External Open-Circuit Voltage of Perovskite Solar Cells", *Energy & Environmental Science*, vol. 12, no. 9, pp. 2778–2788, 2019.

[52] G. B. Alers, B. Golding, A. R. Kortan, R. C. Haddon, and F. A. Theil, "Existence of an Orientational Electric Dipolar Response in C_{60} Single Crystals", *Science*, vol. 257, no. 5069, pp. 511–514, 1992.

6

Thermally Activated Ion Current Measurements

Abstract

Mobile ions play a key role in the degradation of perovskite solar cells, making their quantification essential for enhancing device stability. Various electrical measurements have been applied to characterize mobile ions. However, discerning between different ionic migration processes can be difficult. Furthermore, multiple measurements at different temperatures are usually required to probe different ions and their activation energies. Here, we demonstrate a new characterization technique based on measuring the thermally activated ion current (TAIC) of perovskite solar cells. The method reveals density, diffusion coefficient, and activation energy of mobile ions within a single temperature sweep and offers an intuitive way to distinguish mobile ion species. We apply the TAIC technique to quantify mobile ions of $MAPbI_3$ and triple-cation perovskite solar cells. We find a higher activation energy and a lower diffusion coefficient in the triple-cation devices. TAIC measurements are a simple yet powerful tool to better understand ion migration in perovskite solar cells.

Authors: Moritz C. Schmidt, Agustin O. Alvarez, Riccardo Pallotta, Biruk A. Seid, Jeroen J. de Boer, Jarla Thiesbrummel, Felix Lang, Giulia Grancini, and Bruno Ehrler

Submitted in May 2025

6.1 Introduction

In recent years, mobile ions have been assigned to various losses in perovskite solar cells. They have been attributed to losses in short-circuit current density (J_{sc}), open-circuit voltage (V_{oc}), and fill-factor (FF) [1–3]. To understand the impact of mobile ions on device characteristics, quantifying key parameters like the ion density, diffusion coefficient, and activation energy is essential. With the aim of extracting these parameters, various electrical measurements have been applied. The density of mobile ions has been estimated with current transient measurements (also known as bias-assisted charge extraction) [1] and low-frequency Mott-Schottky measurements [4, 5]. Techniques that are commonly employed to characterize electronic traps in semiconductor materials were transferred to quantify mobile ionic defects in perovskite solar cells, even though their interpretation must be adapted [6]. These techniques include thermal admittance spectroscopy (TAS) [7] and deep level transient spectroscopy (DLTS) [8], which have been employed in efforts to quantify the density, diffusion coefficient, and activation energy of mobile ions [6, 9–12]. All of these techniques can be used to quantify the diffusion coefficient and density of ions within some boundary conditions [13]. However, multiple measurements at different temperatures are necessary to extract the activation energy of the diffusion coefficient. Additionally, overlapping time constants can make it difficult to discern between different ionic species, especially in transient measurements.

Here, we propose an intuitive technique to quantify the density, diffusion coefficient, and activation energy of mobile ions within a single measurement. The method is inspired by thermally stimulated current (TSC) measurements, which have previously been applied to characterize traps in perovskite solar cells [14–20]. Similar to current transient measurements, we apply a bias during which mobile ions migrate away from the perovskite/charge transport layer (CTL) interfaces. While applying the bias, we decrease the temperature to 175 K, lowering the diffusion coefficient of the mobile ions. At 175 K, we then remove the applied bias, resulting in an electric field in the perovskite bulk due to the built-in potential of the device. However, because of the low diffusion coefficient of the mobile ions, they do not immediately drift to the interfaces. Mobile ions only begin to drift back to the perovskite/CTL interface when the temperature is increased at a constant rate, resulting in a thermally activated current. To emphasize that we are probing mobile ionic defects, we refer to this as the thermally activated ion current (TAIC).

6.2 Results and Discussion

We use the TAIC technique to quantify mobile ions of two different perovskite solar cells, one with a $MAPbI_3$ perovskite and one with a triple-cation perovskite. Figure 6.1(a) and (b) show the device stack and JV measurements of the $MAPbI_3$ device. In Figure 6.1(c) and (d), the device stack and JV measurements of the triple-cation device are shown. In both devices, we use the self-assembling monolayer MeO-2PACz as the hole transport layer (HTL). For the electron transport layer (ETL), we use PCBM in the case of the $MAPbI_3$ perovskite solar cell and C_{60} in the case of the triple-cation device. The surface of the triple-cation perovskite is passivated with a dual passivation of EDAI and PEAI. Details of the fabrication process are available in Section 6.A in the Appendix.

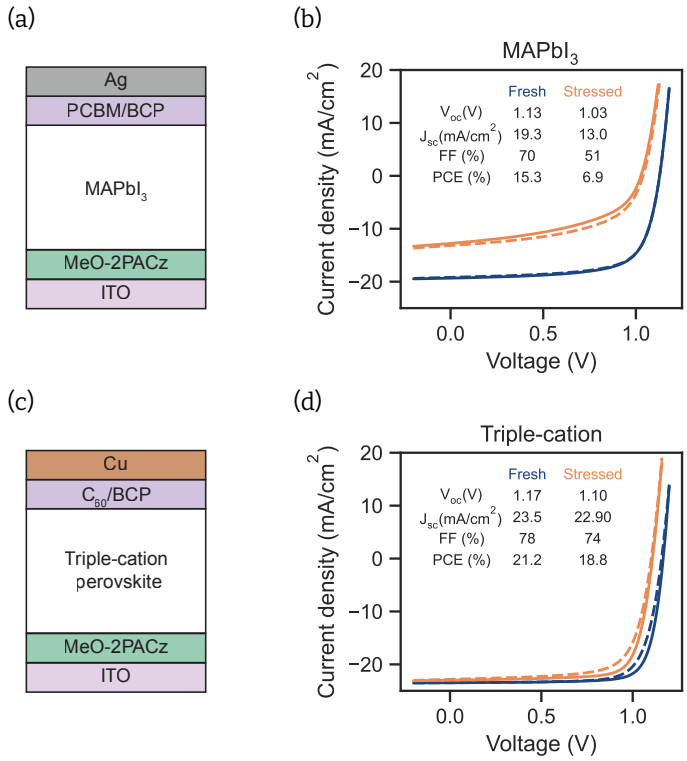

Figure 6.1: (a) Device stack of the $MAPbI_3$ perovskite solar cell. (b) JV measurement of a fresh $MAPbI_3$ device and the same device stressed for 32 h at V_{oc}. (c) Device stack of the triple-cation perovskite solar cell. (d) JV measurement of a fresh triple-cation device and the same device stressed for 78 h at V_{oc}. The dashed lines are the forward, and the solid lines are the reverse voltage scans. The extracted photovoltaic parameters are the mean values of the forward and reverse measurements.

It has previously been demonstrated that stressing perovskite solar cells at V_{oc} can lead to degradation by increased ion densities [1]. We therefore stress the devices at V_{oc} under a high-intensity white-light LED with 1-sun equivalent carrier excitation. During stressing, we repeatedly carry out electrical measurements, including JV, capacitance frequency, and TAIC measurements. For the $MAPbI_3$ device, for example, we perform measurements of the fresh device and after 12, 22, and 32 hours of stressing at V_{oc}. The JV measurements are measured under illumination, while the capacitance frequency and TAIC measurements are carried out in the dark. Figure 6.1(b) shows the JV measurement of a fresh $MAPbI_3$ device and the same device stressed for a total of 32 hours at V_{oc}, resulting in a significant decrease in V_{oc}, J_{sc}, and FF. The triple-cation device is more stable, with a decrease in mainly V_{oc} and FF after the maximum stressing time of 78 hours at V_{oc}, as shown in Figure 6.1(d).

6.2.1 Principle of TAIC

We then carry out TAIC measurements of the devices under the different stressing conditions. The principle of the TAIC measurements is illustrated in Figure 6.2. At steady state and no applied bias, mobile ions are accumulated at the perovskite/CTL interfaces due to the built-in field of the perovskite. In the first step, we apply a forward bias voltage to the device at 300 K. During this applied bias, mobile ions migrate away from the perovskite/CTL interface into the perovskite bulk, as illustrated in panel A in Figure 6.2.

While still applying the voltage bias, we then decrease the temperature, leading to a decrease in the diffusion coefficient of the mobile ions. Consequently, the ions are 'frozen' when the voltage pulse is removed at 175 K, and they do not drift back to the perovskite/CTL interface, as shown in panel B. In the last step, we slowly increase the temperature with the device at short-circuit. As the temperature increases, the temperature-activated diffusion coefficient of the mobile ions increases exponentially. Consequently, mobile ions start drifting back to the perovskite/CTL interfaces. This results in the thermally activated ion current, which is illustrated in panel C in Figure 6.2.

6.2.2 Extraction of Ionic Parameters

The TAIC measurements of the $MAPbI_3$ device and the triple-cation device after different stressing durations are shown in Figure 6.3(a) and (b), respectively. In both cases, we increase the temperature from 175 K to 300 K at a rate of 0.1 K/s and then stabilize at 300 K. Exemplary temperature sweeps are shown as gray lines in Figure 6.3(a) and (b). We expect the $MAPbI_3$ perovskite to be in the tetragonal phase during the entire

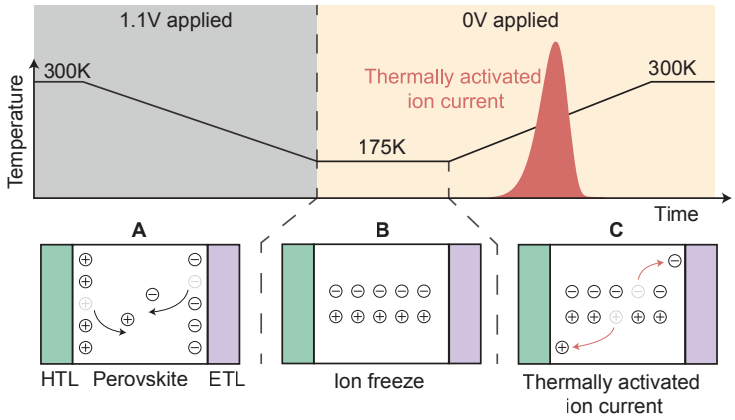

Figure 6.2: Illustration of the thermally activated ion current measurement. (A) At 300 K, a voltage is applied to the device, during which mobile ions migrate into the perovskite bulk. While the voltage is applied, the temperature is decreased, resulting in a decrease in the ionic diffusion coefficient. (B) At 175 K the applied voltage is removed. Because of the low temperature, the ions do not drift back to the interface. (C) When the temperature is gradually increased, the diffusion coefficient of the mobile ions increases, resulting in mobile ions drifting back to the perovskite/CTL interfaces, generating the thermally activated ion current (TAIC).

temperature sweep [21, 22] and see no obvious signs of a phase transition in the triple-cation devices. For both devices, we observe an increase in the current as the temperature increases. At some point, the current peaks and decreases again. For the $MAPbI_3$ device, this increase and decrease of the current occur during the temperature sweep. In contrast, the current peak in the triple-cation device occurs only when the temperature sweep is stopped at 300 K. Notably, in both cases, the integral of the current increases with increasing stressing time, suggesting that stressing the devices at V_{oc} increases the ion density in both devices. We also measured a second $MAPbI_3$ and triple-cation device, yielding similar trends but slightly different absolute values as shown in Figure 6.D.1.

We note that for both devices, some charges are extracted immediately after switching off the voltage at 175 K as shown in Figure 6.D.2(a) and (b). These could be caused by electrical or fast ionic carriers that are still mobile at low temperatures.

The current J_{tot} during the TAIC measurements depends on the density of mobile ions in the bulk $N_{\mathrm{ion,bulk}}$, the temperature activated diffusion coefficient with prefactor $D_{0,\mathrm{ion}}$ and activation energy E_{a} [23], and the electric field in the perovskite bulk E_{bulk} as:

$$J_{\mathrm{tot}}(t) = b\,e^2 N_{\mathrm{ion,bulk}}(t) D_{0,\mathrm{ion}} e^{-\frac{E_{\mathrm{a}}}{k_{\mathrm{B}}T(t)}} \frac{1}{k_{\mathrm{B}}T(t)} E_{\mathrm{bulk}}(t) \tag{6.1}$$

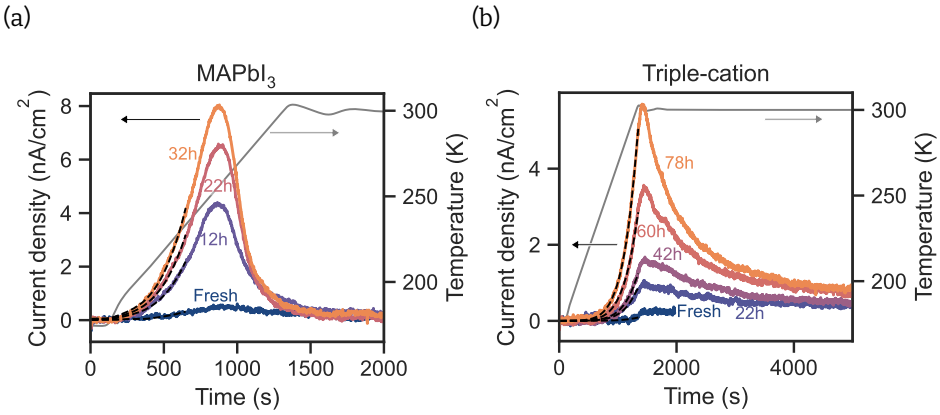

Figure 6.3: Thermally activated ion current measurements of (a) a $MAPbI_3$ and (b) a triple-cation perovskite solar cell for different stressing durations. The black dashed lines represent fits. The gray line represents an exemplary temperature sweep. The extracted ion parameters are shown in Table 6.1.

where b is a correction factor accounting for the displacement current in the perovskite, e is the elementary charge, k_B is the Boltzmann constant, and T is the temperature. A detailed derivation of Equation 6.1 is given in Section 6.B in the Appendix.

At low temperatures, we can assume that the density of ions in the bulk is constant $N_{\mathrm{ion,bulk}}(t) = N_{\mathrm{ion}}$, because the bulk is not yet depleted of mobile ions. Furthermore, we can approximate the bulk electric field based on an estimated built-in potential of the devices and a potential drop in the transport layers as described in Section 6.C in the Appendix. With these simplifications, we can then fit Equation 6.1 to the low-temperature part of the TAIC measurements to determine the activation energy and product of ion density and diffusion coefficient $N_{\mathrm{ion}} D_{0,\mathrm{ion}}$.

To verify this approach, we fit Equation 6.1 to drift-diffusion simulations of TAIC measurements, shown in Figure 6.4. We note that the drift-diffusion solver we use only allows for a temperature-activated mobility instead of the diffusion coefficient. We therefore extract the temperature-independent prefactor of the ionic conductivity $\sigma_{0,\mathrm{ion}} = eN_{\mathrm{ion}}\mu_{0,\mathrm{ion}}$, which we can estimate with good accuracy as shown in Table 6.D.3.

For the devices in Figure 6.3(a) and (b), we assume a built-in voltage of 1 V. With the correction factor described in Section 6.C in the Appendix, we estimate an electric field of 16 kV/cm for the $MAPbI_3$ device and 12 kV/cm for the triple-cation device. The fits of Equation 6.1 are illustrated as dashed lines in Figure 6.3(a) and (b). We fit the activation energy as a global parameter and the product of density and diffusion coefficient $N_{\mathrm{ion}} D_{0,\mathrm{ion}}$ as local parameters. For the $MAPbI_3$ and the triple-cation de-

vice, we extract activation energies of 0.28 eV and 0.35 eV, respectively. The extracted values for $N_{\mathrm{ion}}D_{0,\mathrm{ion}}$ are listed in Table 6.D.2 in the Appendix. With the activation energy, $N_{\mathrm{ion}}D_{0,\mathrm{ion}}$, and Equations 6.4, 6.5, and 6.6 we can now determine the ionic conductivity at different temperatures, for example 300 K, which are listed in Table 6.1. For both devices, we extract an increasing ionic conductivity with increasing stressing duration, most likely caused by an increasing ion density in the stressed devices. Furthermore, due to the higher activation energy, the ionic conductivity at 300 K of the triple-cation device is 1-2 orders of magnitude lower compared to the $MAPbI_3$ device.

To extract the density and diffusion coefficient from $N_{\mathrm{ion}}D_{0,\mathrm{ion}}$, we need to determine either the density N_{ion} or the diffusion coefficient $D_{0,\mathrm{ion}}$. In principle, the integral of the TAIC current can be used to determine the ion density. This is, however, only possible as long as the electric field within the perovskite bulk in Equation 6.1 does not significantly change over time. If the electric field is constant, more and more ions drift from the bulk to the perovskite/CTL interfaces, until the bulk becomes depleted of mobile ions, decreasing the current. Then, the integral of the current can be used to approximate the ion density. Because the depletion of ions in the bulk limits the current, we refer to this case as ion-limited.

In contrast, the electric field $E_{\mathrm{bulk}}(t)$ in Equation 6.1 can also limit the current. This occurs when ions that accumulate at the interface between perovskite and CTLs screen the built-in potential [1, 24], decreasing the electric field in the perovskite bulk and therefore the current. In this case, only a fraction of ions drift from the bulk to the interfaces, and the ion density is underestimated when integrating the current [5]. We refer to this case as the field-limited case.

To illustrate the ion-limited and the field-limited cases, we carried out drift-diffusion simulations of the TAIC measurements for different ion densities and activation energies, which are shown in Figure 6.4. In the ion limiting case for an activation energy of 0.3 eV, the peak of the TAIC measurements does not shift significantly when the ion density increases, as illustrated in Figure 6.4(a). For a higher activation energy of 0.6 eV in Figure 6.4(b), the TAIC currents decay similarly fast for the different ion densities. In contrast to these observations stands the field limiting case. Here, the peak shifts to shorter times for an activation energy of 0.3 eV due to the earlier screening of the built-in field, as shown in Figure 6.4(c). For an activation energy of 0.6 eV, the earlier screening of the built-in field results in faster decays for higher ion densities, as shown in Figure 6.4(d). Based on these observations, TAIC measurements can be used to determine if the device suffers from ionic field screening when devices with different ion densities are measured (e.g., during aging).

Table 6.1: Estimated values of the activation energy E_{a}, ionic conductivity at 300 K $\sigma_{\mathrm{ion,300K}}$, ion density N_{ion}, and diffusion coefficient at 300 K $D_{\mathrm{ion,300K}}$ for the $MAPbI_3$ and the triple-cation device at different stressing conditions. The values were extracted from the low-temperature fit and the integral of the TAIC measurements. The error of N_{ion} is estimated from the minimum detectable ion density based on the noise of the current and the diffusion coefficient at the temperature of the current peaks. The errors of the $\sigma_{\mathrm{ion,300K}}$ correspond to the fitting error. The error of $D_{\mathrm{ion,300K}}$ is propagated based on the errors of N_{ion} and $\sigma_{\mathrm{ion,300K}}$.

Device	Stressing	E_{a} (eV)	$\sigma_{\mathrm{ion,300K}}$ (S/cm)	N_{ion} (cm^{-3})	$D_{\mathrm{ion,300K}}$ (cm^2/s)
$MAPbI_3$	Fresh	0.28	$3.9 \pm 0.3 \cdot 10^{-13}$	$1.8 \pm 0.2 \cdot 10^{17}$	$3.5 \pm 0.4 \cdot 10^{-13}$
	12h		$2.6 \pm 0.2 \cdot 10^{-12}$	$8.8 \pm 0.1 \cdot 10^{17}$	$4.9 \pm 0.3 \cdot 10^{-13}$
	22h		$3.9 \pm 0.2 \cdot 10^{-12}$	$10.5 \pm 0.1 \cdot 10^{17}$	$6.0 \pm 0.3 \cdot 10^{-13}$
	32h		$5.1 \pm 0.3 \cdot 10^{-12}$	$13.7 \pm 0.1 \cdot 10^{17}$	$6.0 \pm 0.3 \cdot 10^{-13}$
Triple-cation	Fresh	0.35	$1.0 \pm 0.1 \cdot 10^{-14}$	$1.9 \pm 1.2 \cdot 10^{17}$	$8.7 \pm 5.4 \cdot 10^{-15}$
	22h		$9.7 \pm 0.3 \cdot 10^{-14}$	$15.9 \pm 1.2 \cdot 10^{17}$	$9.8 \pm 0.7 \cdot 10^{-15}$
	42h		$14.0 \pm 0.5 \cdot 10^{-14}$	$20.9 \pm 0.9 \cdot 10^{17}$	$10.8 \pm 0.6 \cdot 10^{-15}$
	60h		$31.8 \pm 1.0 \cdot 10^{-14}$	$32.1 \pm 0.6 \cdot 10^{17}$	$16.0 \pm 0.6 \cdot 10^{-15}$
	78h		$56.3 \pm 1.9 \cdot 10^{-14}$	$43.8 \pm 0.5 \cdot 10^{17}$	$20.8 \pm 0.7 \cdot 10^{-15}$

In the ion-limited case, most mobile ions drift from the bulk to the perovskite/CTL interfaces. We can therefore estimate the ion density by integrating the overall current according to:

$$N_{\mathrm{ion}} = \frac{1}{b\frac{d_{\mathrm{Pero}}}{2}e}\int_0^{\infty} J_{\mathrm{tot}}(t)dt \tag{6.2}$$

where b is a correction factor accounting for the drop of the potential in the CTLs. Section 6.C in the Appendix contains details about the correction factor. d_{Pero} is the perovskite thickness, and J_{tot} is the measured current. The factor $\frac{1}{2}$ originates from the assumption that the mobile ions are distributed homogeneously across the bulk. Then, the average distance that mobile ions migrate is $\frac{d_{\mathrm{Pero}}}{2}$. When applying Equation 6.2 to drift-diffusion simulations, we can accurately determine the ion density in the ion-limited case, as shown in Figure 6.4(e) and (f) and Table 6.D.3 in the Appendix. For increasing ion densities in the field limited case, the estimated ion density in Figure 6.4(e) and (f) plateaus, and the extracted ion densities are significantly underestimated. This is consistent with the observation that no electrical measurement can accurately extract ion densities in the field-limited case [13]. With the ionic conductivity and the density, we can now also determine the mobility of ions in the ion-limited case with good accuracy, as shown in Table 6.D.3.

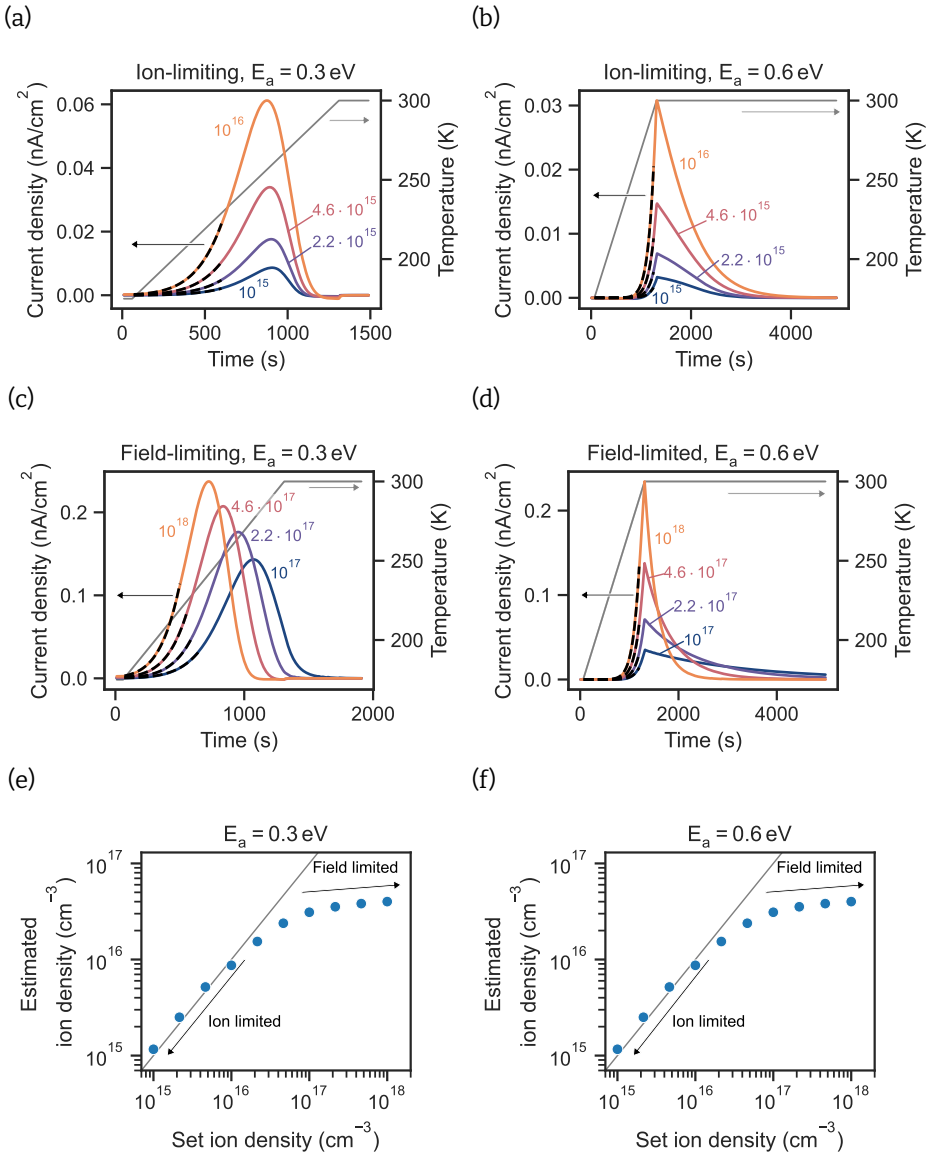

Figure 6.4: Drift-diffusion simulations of TAIC measurements with different ion densities for the ion-limiting case with (a) an activation energy of 0.3 eV and (b) 0.6 eV and the field limiting case with (c) an activation energy of 0.3 eV and (d) 0.6 eV. All other parameters used for the drift-diffusion simulations are listed in Table 6.A.1. The dashed black lines represent fits. (e) Estimated ion density for the simulations with activation energy of 0.3 eV and (f) 0.6 eV.

In the measurements in Figures 6.3(a) and (b), we do not observe a significant shift of the current peak or a faster decay for the more stressed devices. We can therefore assume that the TAIC current is ion-limited. Consequently, we estimate the ion density by integrating the current according to Equation 6.2. We note that the current in the triple-cation device does not fully decay within 5000 s. We therefore extrapolate the data with exponential decays. The estimated ion densities for the different stressing conditions are listed in Table 6.1. We determine that ion densities for both devices increase by around one order of magnitude due to stressing. For the $MAPbI_3$ device, the ion density increases from $1.8 \cdot 10^{17}$ cm^{-3} to $1.4 \cdot 10^{18}$ cm^{-3}. Similarly, stressing the triple-cation device increases the ion density from $1.9 \cdot 10^{17}$ cm^{-3} to $4.4 \cdot 10^{18}$ cm^{-3}. We can now also determine the diffusion coefficients at 300 K, which are listed in Table 6.1. For both devices, the diffusion coefficient increases slightly by a factor of two due to stressing. Notably, the diffusion coefficient and ionic conductivity of the $MAPbI_3$ device are higher than those of the triple-cation device, suggesting that ion migration in the triple-cation devices is suppressed.

We note that, just accounting for the electrostatic effects of mobile ions, we would expect ionic field screening to limit the extracted current for ion densities of 10^{17} cm^{-3} and higher (similar to the drift-diffusion simulations in Figure 6.4). However, we extract much higher ion density from the TAIC measurements. Possibly, more ions can accumulate at the interface between perovskite and CTLs before the field is screened, which has previously been suggested [25]. It is also possible that ions recombine when drifting back to the interfaces, not impacting the potential anymore [26], or that lateral ion migration [27] impacts the current, leading to an overestimation of the ion density. Pinpointing the exact cause for the high extracted ion densities is a crucial next step to better understand ion migration, but it is out of the scope of this work.

Interestingly, the extracted diffusion coefficients of both devices are significantly lower than those associated with halide vacancy-mediated ion migration, which is often assumed to be the dominating ionic species. For $MAPbI_3$, diffusion coefficients of around $4 \cdot 10^{-11}$ cm^2/s up to 10^{-9} cm^2/s have been previously assigned to iodide vacancy migration [28–30]. For double cation perovskite solar cells, diffusion coefficients were determined to be in the range of 10^{-10} cm^2/s [4]. Possibly, we probe the migration of a slower ionic migration process in the TAIC measurements. To verify this, we carried out capacitance frequency measurements, which allow us to probe faster ionic processes. The resulting capacitance frequency measurements for different stressing times are shown in Figure 6.D.3. We observe a rise of the capacitance at around 100 Hz for both the $MAPbI_3$ and the triple-cation device in Figure 6.D.3(a) and (b), respectively. A similar capacitance rise has been observed in other capacitance frequency measurements and can be associated with ionic defects

[9, 25, 30]. Interestingly, the capacitance at lower frequencies increases when the devices are stressed. This suggests the presence of another ionic migration process [25], which is slower than the ionic process at around 100 Hz. This process can not be completely resolved with capacitance frequency measurements. However, carrying out capacitance frequency measurements at 360 K shifts the fast defect to higher frequencies and also reveals more of the capacitance increase of the slower ionic defect, as shown in Figure 6.D.3(c) and (d) for the $MAPbI_3$ and the triple-cation device, respectively. Additionally, we extracted some current after switching off the voltage at 175 K, shown in the current transient measurements in Figure 6.D.2. Possibly, this current is due to the fast defect observed in the capacitance frequency measurements. From these current transient measurements, we estimate the densities of the fast ion migration process for the $MAPbI_3$ and the triple-cation device to be around 10^{16} cm^{-3} and $5 \cdot 10^{16}$ cm^{-3}, see Table 6.D.4. These low ion densities are difficult to resolve in TAIC measurements.

Altogether, we assign the fast process in the capacitance frequency and low temperature current transients to the migration of halide vacancies. In the TAIC measurements, we then measure the slower ionic migration process, which we probe only partially at low frequencies in the capacitance frequency measurements. The slow ionic process could be due to cation vacancies, which have been associated with lower diffusion coefficients [31, 32]. However, the activation energy associated with cation migration is expected to be around 0.8-1.2 eV [32–34], significantly larger than the values found here. A more likely explanation is, therefore, that the fast and slow migration processes are due to different migration pathways of the same ion. It has, for example, been previously reported that ion migration along grain boundaries is significantly faster than migration through perovskite grains [12, 35, 36]. Consequently, the current in the TAIC measurements and the slow process in the capacitance frequency measurements could originate from halide vacancies migrating through perovskite grains, whereas the fast process is caused by halide vacancy migration along grain boundaries.

To verify that the TAIC signal is due to ionic carriers, we also carried out the TAIC measurement with an applied voltage of 0 V during the cool-down. Then, as shown in Figure 6.D.4(a), we do not observe any current peak, because no ions were moved into the perovskite bulk. To exclude that we are probing trap emission, we illuminated a device at low temperatures, during which traps would be filled. The emission of electronic charges from these traps would result in a similar current to that with applied bias. However, we do not measure any significant current, as shown in Figure 6.D.4(b). We can therefore assign the measured TAIC signal to mobile ions in the perovskite.

Finally, we carried out TAIC measurements starting and finishing at a higher temperature of 360 K with the aim of observing additional ionic processes. Figure 6.D.5(a) and (b) show exemplary measurements of a $MAPbI_3$ and the triple-cation device, respectively. We note that the devices degrade while keeping them at 360 K for extended durations, complicating a controlled stressing profile. In the $MAPbI_3$ device, we observe an additional peak and a shoulder at around 310 K and 340 K, indicating additional ionic processes. For the triple-cation device in Figure 6.D.5(b), we observe a distinct second peak for which we can extract an activation energy of 0.94 eV. Similarly high activation energies have been previously associated and computationally predicted with the migration of cations in perovskites [32–34, 37].

6.2.3 Comparison to Other Techniques

These measurements illustrate that we can distinguish between different defects within a single temperature sweep. In other techniques like transient current, transient capacitance, and capacitance frequency measurements, multiple measurements at different temperatures are necessary to probe different defects. And even then, it can be difficult to distinguish between different defects in transient measurement, as their characteristic time constants can overlap. The main disadvantage of TAIC measurements is, however, that low ion densities cannot easily be resolved (like the fast defect probed in capacitance frequency measurements). To clarify the position of TAIC measurements within electrical characterization methods, we summarize the capabilities and limitations of commonly-used techniques in Table 6.2. We note that all the methods can only quantify mobile ion densities if mobile ions do not significantly screen the electric field [13].

6.3 Conclusion

In summary, we have introduced a new measurement technique, thermally activated ion current (TAIC), to characterize mobile ions in perovskite solar cells. TAIC is based on measuring the current due to thermally activated ions. With a simple expression for the TAIC current, we extracted the ionic conductivity by fitting the low-temperature tail of the TAIC measurements. Furthermore, the ion density can be determined by integrating the current in the TAIC measurements, if electric field screening does not limit the overall current. Conveniently, the peak shift in the TAIC data indicates if perovskite solar cells suffer from electric field screening. We applied TAIC measurements to quantify the mobile ion density, diffusion coefficient, and

Table 6.2: Comparison of capabilities and limitations of common electrical measurement techniques used to quantify mobile ions in perovskite solar cells.

Technique	Capabilities	Limitations
Thermally activated ion current (TAIC)	• Measurement of ion density and diffusion coefficient • Single temperature sweep to determine activation energy • Intuitive measurement to distinguish between different ions	• Difficult to measure low ion densities
Transient current [1, 4, 38, 39]	• Measurement of ion density and diffusion coefficient • Slow and fast ions can be measured • Sensitive to low ion densities	• Difficult to distinguish between different ions • Multiple measurements at different temperatures are necessary to determine the activation energy
Transient capacitance [10, 30, 31, 40]	• Measurement of ion density and diffusion coefficient • Slow and fast ions can be measured • Sensitive to low ion densities	• A more complex model is necessary to evaluate the data • Difficult to distinguish between different ions • Multiple measurements at different temperatures are necessary to determine the activation energy
Capacitance frequency [9, 25, 30]	• Measurement of ion density and diffusion coefficient • Sensitive to low ion densities	• A more complex model is necessary to evaluate the data • Measurement of slow ions takes a long time • Multiple measurements at different temperatures are necessary to determine the activation energy
Low-frequency Mott-Schottky [4, 5]	• Measurement of ion density • Sensitive to low ion densities	• Multiple ions can not be measured/distinguished • Does not contain information about the diffusion coefficient

activation energy in a $MAPbI_3$ and a triple-cation perovskite solar cell at different stressing conditions. For the $MAPbI_3$ device we determined an activation energy of 0.28 eV, mobile ion densities of $1.8 \cdot 10^{17}\,cm^{-3}$ to $1.4 \cdot 10^{18}\,cm^{-3}$ depending on the stressing condition and a diffusion coefficient of around $5 \cdot 10^{-13}\,cm^2/s$ at 300 K. For the triple-cation device we determined an activation energy of 0.35 eV, mobile ion densities of $1.9 \cdot 10^{17}\,cm^{-3}$ to $4.4 \cdot 10^{18}\,cm^{-3}$, and a diffusion coefficient of around $10^{-14}\,cm^2/s$ at 300 K, lower than that of the $MAPbI_3$ device. We attribute the migration process to halide vacancy migration within perovskite grains. We also observed a faster ionic process in capacitance frequency measurements, which we assign to halide vacancy migration along grain boundaries. Lastly, we showed that it is possible to distinguish between different ionic processes by increasing the temperature range of the TAIC measurements and found a third ion migration process with a high activation energy of 0.94 eV in the triple-cation devices, which we assign to cation migration. In total, TAIC measurements are a promising technique because they are easy to perform, their interpretation is straightforward, and they offer an intuitive visualization of ion migration in perovskite solar cells.

Chapter appendix

6.A Experimental Details

Fabrication of the $MAPbI_3$ Devices

Materials: Chlorobenzene (CB, extra dry, 99.8%), dimethyl sulfoxide (DMSO, $\geq$99.9% extra dry), N,N-dimethylformamide (DMF, extra dry, 99.8%), and chloroform (CF, extra dry 99.8%) were purchased from Acros Organics. 2-propanol (IPA, $\geq$ 99.8%), lead iodide (PbI_2, >98.0%), and MeO-2PACz were purchased from TCI. Methylammonium iodide (MAI, >99.99%) was purchased from GreatCell Solar Materials. Phenyl-C61-butyric acid methyl ester (PCBM, >99.99%) was purchased from Lumatec. Bathocuproine (BCP) was purchased from Sigma Aldrich. All solutions were prepared in an Ar-filled glovebox, while the deposition of each layer of the solar cell was performed in an N_2-filled glovebox.

Device Fabrication: For the fabrication of the $MAPbI_3$ devices, indium tin oxide (ITO)-coated glass substrates (purchased from Yingkou Shangneng Photoelectric material Co.,Ltd.) were consecutively cleaned in acetone and IPA by ultrasonicating for 15 min in each solvent. Substrates were dried with N_2 airflow and O_2 plasma treated for 10 min. MeO-2PACz was dissolved in ethanol in a concentration of 0.33 mg/ml and 50 µl were spin-coated onto ITO/glass substrates at 3000 rpm for 30 s and annealed at 100 °C for 10 min. The perovskite precursor solution was prepared by dissolving 0.553 g of PbI_2 and 0.191 g of MAI powders in 1 ml DMF/DMSO 4/1 v/v solvent. 25 µl of the final solution were deposited on the MeO-2PACz coated substrates and spin-coated with a three-step procedure: the first step proceeded at 1000 rpm (500 rpm/s) for 6 s, the second step proceeded at 5000 rpm for 27 s (2500 rpm/s), while the last step was a speed deceleration of 1250 rpm/s to 0 rpm/s. 150 µl of chlorobenzene were dropped onto the spinning substrate for an antisolvent procedure 6 seconds after the beginning of the second step. Subsequently, substrates were annealed at 100 °C for 15 min. To fabricate the ETL, PCBM was dissolved in chloroform to produce a 15 mg/ml solution. 20 µl of the solution were spin-coated at 2000 rpm for 20 s onto the perovskite layer. To prevent the diffusion of the metal contact into the perovskite, 50 µl of 1 mg/ml solution (in isopropanol) of bathocuproine was deposited on PCBM. For all the deposition, a vacuum-based chuck was used. Finally, 80 nm of Ag was thermally evaporated on the device with a shadow mask of 0.0825 cm^2 area. The evaporation speed was adjusted to

0.01 nm/s for the first 5 nm, 0.02 nm/s from 5 to 15 nm, and 0.06 nm/s for the rest of the procedure.

Fabrication of the Triple-Cation Devices

Solution preparation: The perovskite solution was prepared by adopting the procedure reported by Seid et al. [41]. PbI_2 (909.00 mg), FAI (276.06 mg), MABr (3.68 mg), CsI (22.47 mg), and MACl (18.11 mg) were mixed in a DMF/DMSO solvent mixture (5/1 v/v) and stirred for 4 hours at 60 °C to form a 1.73 M $Cs_{0.05}(MA_{0.05}FA_{0.95})_{0.95}Pb(I_{0.95}Br_{0.05})_3$ perovskite solution. The passivation layers were prepared using high-purity materials from Sigma-Aldrich: PEAI (98%) and $EDAI_2$ (>98%). 3.5 mg of PEAI was dissolved in 1 ml of isopropanol (IPA), sonicated for 30 minutes. The $EDAI_2$ solution was prepared by dissolving 2 mg of $EDAI_2$ in a 2 ml 1:1 (v/v) mixture of IPA and toluene

Device fabrication: Planar inverted perovskite solar cells were fabricated using the following layer structure: glass/ITO/MeO-2PACz/$Cs_{0.05}(MA_{0.05}FA_{0.95})_{0.95}Pb(I_{0.95}Br_{0.05})_3$/$C_{60}$ /BCP/Cu. The fabrication started with ITO-coated glass substrates, which were cleaned sequentially in an ultrasonic bath using acetone, Hellmanex (3 % in deionized water), deionized water, ethanol, acetone, and isopropanol, with each solvent being used for 15 minutes. The cleaned substrates were then exposed to ultraviolet ozone for 30 minutes before being placed in a nitrogen-filled glovebox.
Next, a MeO-2PACz layer was spin-coated from a 1 mmol ml^{-1} ethanol solution at 3000 rpm for 30 seconds, followed by annealing at 100 °C for 10 minutes. Once the substrates had cooled to room temperature, a triple-cation perovskite solution was spin-coated at 4000 rpm for 40 seconds with a 5-second acceleration time. 7 seconds before the end of the spin-coating process, 300 µl of chlorobenzene was added as an antisolvent, and the perovskite film was annealed at 100 °C for 1 hour. For the bi-layered passivation, the $EDAI_2$ solution was spin-coated onto the perovskite at 5000 rpm for 40 seconds, and annealed at 100°C for 10 minutes. Then, the PEAI solution was spin-coated onto the cooled sample at 5000 rpm for 40 seconds. Afterward, the samples were transferred to an evaporation chamber where 30 nm of C_{60} was deposited at 0.3 Å/s, followed by 8 nm of BCP and 100 nm of copper, which were evaporated at 0.3 Å/s and 0.6 Å/s, respectively, under a high vacuum of 10^{-7} mbar.

Electrical Characterization

All electrical measurements were carried out in a Janis VPF-100 liquid nitrogen cryostat. During the measurements, the pressure inside the cryostat was around $5 \cdot 10^{-6}$ mbar.

JV measurements: JV measurements were carried out with an Agilent B2902A source-measure unit and a SOLIS-3C high-power white-light LED from Thorlabs. The intensity of the LED was set so that the short-circuit current density of the devices matched with a JV measurement at AM-1.5G illumination (carried out with a Pico solar simulator by G2V inside a N_2 filled glovebox).
TAIC measurements: TAIC measurements were carried out using an Agilent B2902A source-measure unit. At 300 K or 360 K, a voltage of 1.1 V was applied to the devices. Subsequently, the devices were cooled down and stabilized at 175 K. When switching off the voltage, the current transient was measured. Then, the temperature was increased to 300 K or 360 K and stabilized there, while the current was constantly recorded.
Capacitance frequency measurements: Capacitance frequency measurements were carried out with the MFIA by Zurich Instruments with an AC amplitude of 20 mV in a frequency range of 0.1 Hz-500 kHz.

Thickness Measurements

The perovskite film thickness was determined by scratching the films with tweezers and measuring the depth of the scratch with a KLA Tencor P-7 Stylus Profiler.

Drift-Diffusion Simulations

Drift-diffusion simulations were carried out with Setfos by Fluxim, and the parameter set listed in Table 6.A.1.

Table 6.A.1: Parameters used for the drift-diffusion simulations.

Parameter	Value
Band gap perovskite $E_{\mathrm{g,Pero}}$ (eV)	1.6
Electron affinity perovskite $E_{\mathrm{aff,Pero}}$ (eV)	3.9
Dielectric constant perovskite $\epsilon_{\mathrm{r,Pero}}$	50
Thickness perovskite d_{Pero} (nm)	500
Effective density of states conduction band perovskite $N_{0,\mathrm{CB,Pero}}$ (cm^{-3})	$2.1 \cdot 10^{18}$
Effective density of states valence band perovskite $N_{0,\mathrm{VB,Pero}}$ (cm^{-3})	$2.1 \cdot 10^{18}$
Mobility electrons in perovskite $\mu_{\mathrm{n,Pero}}$ (cm^2/Vs)	1
Mobility holes in perovskite $\mu_{\mathrm{p,Pero}}$ (cm^2/Vs)	1
Mobile positive ion density in perovskite N_{ion} (cm^{-3})	variable
Immobile negative ion density N_{nion} (cm^{-3})	variable

Parameter	Value
Prefactor of mobility of ions $\mu_{0,\mathrm{ion}}$ (cm^2/Vs)	variable
Activation energy of mobility of ions E_a (eV)	variable
Band gap HTL $E_{\mathrm{g,HTL}}$ (eV)	1.9
Electron affinity HTL $E_{\mathrm{aff,HTL}}$ (eV)	3.4
Dielectric constant HTL $\epsilon_{\mathrm{r,HTL}}$	4.0
Thickness HTL d_{HTL} (nm)	3
Effective density of states conduction band HTL $N_{0,\mathrm{CB,HTL}}$ (cm^{-3})	$2.1 \cdot 10^{18}$
Effective density of states valence band HTL $N_{0,\mathrm{VB,HTL}}$ (cm^{-3})	$2.1 \cdot 10^{18}$
Mobility holes in HTL $\mu_{\mathrm{p,HTL}}$ (cm^2/Vs)	10^{-4}
Acceptor doping density in HTL $N_{\mathrm{A,HTL}}$ (cm^{-3})	0
Band gap ETL $E_{\mathrm{g,ETL}}$ (eV)	2.0
Electron affinity ETL $E_{\mathrm{aff,ETL}}$ (eV)	4.0
Dielectric constant ETL $\epsilon_{\mathrm{r,ETL}}$	5.0
Thickness ETL d_{ETL} (nm)	50
Effective density of states conduction band ETL $N_{0,\mathrm{CB,ETL}}$ (cm^{-3})	$2.1 \cdot 10^{18}$
Effective density of states valence band ETL $N_{0,\mathrm{VB,ETL}}$ (cm^{-3})	$2.1 \cdot 10^{18}$
Mobility electrons in ETL $\mu_{\mathrm{n,ETL}}$ (cm^2/Vs)	10^{-4}
Donor doping density in ETL $N_{\mathrm{D,ETL}}$ (cm^{-3})	$1 \cdot 10^{17}$
Work function anode $W_{\mathrm{f,anode}}\,(\mathrm{eV})$	5.1
Work function cathode $W_{\mathrm{f,cathode}}\,(\mathrm{eV})$	4.1
Applied voltage before TAIC simulation V_{app} (V)	1.1

6.B Derivation of TAIC

Generally, the ionic current J_{ion} can be expressed in terms of the ionic conductivity σ_{ion} and the electric field in the perovskite bulk E_{bulk} as:

$$J_{\mathrm{ion}}(t) = \sigma_{\mathrm{ion}}(t)\, E_{\mathrm{bulk}}(t) \tag{6.3}$$

The ionic conductivity is dependent on the ion density $N_{\mathrm{ion,bulk}}$ and mobility of the mobile ions μ_{ion}:

$$\sigma_{\mathrm{ion}}(t) = e\, N_{\mathrm{ion,bulk}}(t)\, \mu_{\mathrm{ion}}(t) \tag{6.4}$$

where e is the elementary charge. According to the Nernst-Einstein relation, the mobility depends on the ionic diffusion coefficient D_{ion} as[23]:

$$\mu_{\mathrm{ion}}(t) = \frac{D_{\mathrm{ion}}(t)\, e}{k_{\mathrm{B}} T(t)} \tag{6.5}$$

where k_{B} is the Boltzmann constant and $T(t)$ is the temperature at time t. The diffusion coefficient of mobile ions in perovskites is a temperature-activated process, following [23]:

$$D_{\mathrm{ion}}(t) = D_{0,\mathrm{ion}} e^{-\frac{E_{\mathrm{a}}}{k_{\mathrm{B}} T(t)}} \tag{6.6}$$

where $D_{0,\mathrm{ion}}$ is a temperature independent prefactor, and E_{a} is the activation energy associated with the diffusion coefficient. With these relationships, we can define the ionic current in Equation 6.3 in terms of the mobile ion density and diffusion coefficient:

$$J_{\mathrm{ion}}(t) = e^2 N_{\mathrm{ion,bulk}}(t) D_{0,\mathrm{ion}} e^{-\frac{E_{\mathrm{a}}}{k_{\mathrm{B}} T(t)}} \frac{1}{k_{\mathrm{B}} T(t)} E_{\mathrm{bulk}}(t) \tag{6.7}$$

Finally, the extracted current is the sum of the ionic current and the displacement current. If potential drops in the CTLs, the displacement current results in a lower total current J_{tot} compared to the ionic current J_{ion}. We can account for the impact of the displacement current with the correction factor b:

$$J_{\mathrm{tot}}(t) = b\, J_{\mathrm{ion}}(t) = b\, e^2 N_{\mathrm{ion,bulk}}(t) D_{0,\mathrm{ion}} e^{-\frac{E_{\mathrm{a}}}{k_{\mathrm{B}} T(t)}} \frac{1}{k_{\mathrm{B}} T(t)} E_{\mathrm{bulk}}(t) \tag{6.8}$$

Details about the correction factor are discussed in Section 6.C.

6.C Correction Factor

The drift current of mobile ions to the perovskite/CTL interfaces depends on the electric field in the perovskite bulk according to Equation 6.7. The electric field, in turn, depends on how much of the built-in potential of the perovskite solar cell drops over the perovskite. If organic CTLs are present, significant parts of the built-in potential can drop in the CTLs due to their low dielectric constant. Then, less potential drops over the perovskite, reducing the electric field in the perovskite bulk. This is illustrated in Figure 6.C.1(a) and (b), which show drift-diffusion simulations of the potential of a perovskite solar cell immediately after removing the voltage pulse in a TAIC measurement.

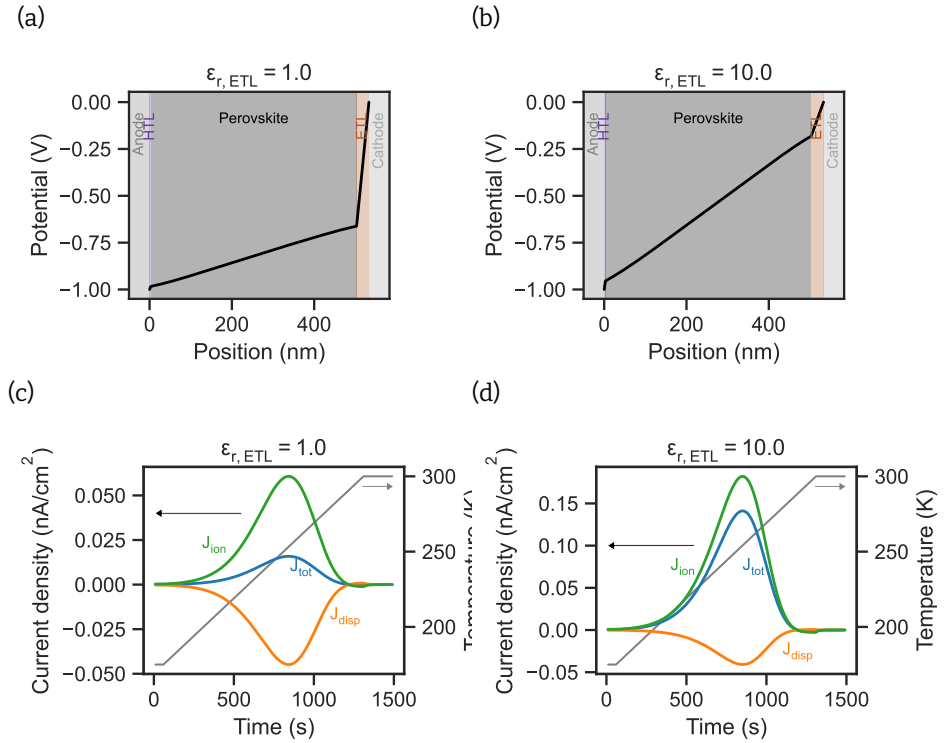

Figure 6.C.1: Simulated potential of a perovskite solar cell with a dielectric constant of (a) $\epsilon_{\mathrm{r,ETL}} = 1.0$ and (b) $\epsilon_{\mathrm{r,ETL}} = 10.0$ right after releasing the voltage pulse in a TAIC measurement. (c) Current contributions of the ionic current J_{ion} and the displacement current J_{disp} to the total current J_{tot} during the TAIC measurement of the devices with dielectric constant of $\epsilon_{\mathrm{r,ETL}} = 1.0$ and (d) $\epsilon_{\mathrm{r,ETL}} = 10.0$.

In Figure 6.C.1(a), a significantly higher fraction of the potential drops over the ETL compared to Figure 6.C.1(b) due the lower dielectric constant in the ETL ($\epsilon_{\mathrm{r,ETL}} = 1$ and $\epsilon_{\mathrm{r,ETL}} = 10$, with $\epsilon_{\mathrm{r,Pero}} = 50$). This difference results in a lower electric field inside the perovskite. We can estimate the potential drop in the perovskite by considering the dielectric constants of the individual layers. We first assume that the electric displacement field D throughout the device is constant:

$$D = \epsilon_0 \epsilon_{\mathrm{r,HTL}} E_{\mathrm{HTL}} = \epsilon_0 \epsilon_{\mathrm{r,Pero}} E_{\mathrm{Pero}} = \epsilon_0 \epsilon_{\mathrm{r,ETL}} E_{\mathrm{ETL}} \tag{6.9}$$

where ϵ_0 is the vacuum permittivity and $\epsilon_{\mathrm{r,HTL}}$, $\epsilon_{\mathrm{r,Pero}}$, and $\epsilon_{\mathrm{r,ETL}}$ are the relative dielectric constants of the different layers. E_{HTL}, E_{Pero}, and E_{ETL} refer to the electric field in the individual layers. Next, we express the potential drops in the individual lay-

ers in terms of the electric field and the dielectric constant in the perovskite:

$$\Delta V_{\mathrm{HTL}} = E_{\mathrm{HTL}} d_{\mathrm{HTL}} = \frac{\epsilon_{\mathrm{r,Pero}}}{\epsilon_{\mathrm{r,HTL}}} d_{\mathrm{HTL}} E_{\mathrm{Pero}} \tag{6.10}$$

$$\Delta V_{\mathrm{Pero}} = E_{\mathrm{Pero}} d_{\mathrm{Pero}} \tag{6.11}$$

$$\Delta V_{\mathrm{ETL}} = E_{\mathrm{ETL}} d_{\mathrm{ETL}} = \frac{\epsilon_{\mathrm{r,Pero}}}{\epsilon_{\mathrm{r,ETL}}} d_{\mathrm{ETL}} E_{\mathrm{Pero}} \tag{6.12}$$

where d_{HTL}, d_{Pero}, and d_{ETL} are the thicknesses of the different layers. The sum of the potential drops has to equal the built-in voltage V_{bi}:

$$V_{\mathrm{bi}} = \Delta V_{\mathrm{HTL}} + \Delta V_{\mathrm{Pero}} + \Delta V_{\mathrm{ETL}} \tag{6.13}$$

$$= E_{\mathrm{Pero}} \big(d_{\mathrm{Pero}} + \frac{\epsilon_{\mathrm{r,Pero}}}{\epsilon_{\mathrm{r,HTL}}} d_{\mathrm{HTL}} + \frac{\epsilon_{\mathrm{r,Pero}}}{\epsilon_{\mathrm{r,ETL}}} d_{\mathrm{ETL}} \big) \tag{6.14}$$

We can rearrange this expression for the electric field in the perovskite:

$$E_{\mathrm{Pero}} = V_{\mathrm{bi}} \big(d_{\mathrm{Pero}} + \frac{\epsilon_{\mathrm{r,Pero}}}{\epsilon_{\mathrm{r,HTL}}} d_{\mathrm{HTL}} + \frac{\epsilon_{\mathrm{r,Pero}}}{\epsilon_{\mathrm{r,ETL}}} d_{\mathrm{ETL}} \big)^{-1} \tag{6.15}$$

With Equation 6.11, we can approximate the potential drop in the perovskite:

$$\Delta V_{\mathrm{Pero}} = d_{\mathrm{Pero}} V_{\mathrm{bi}} \big(d_{\mathrm{Pero}} + \frac{\epsilon_{\mathrm{r,Pero}}}{\epsilon_{\mathrm{r,HTL}}} d_{\mathrm{HTL}} + \frac{\epsilon_{\mathrm{r,Pero}}}{\epsilon_{\mathrm{r,ETL}}} d_{\mathrm{ETL}} \big)^{-1} \tag{6.16}$$

We define the correction factor b as the fraction of the built-in potential that drops within the perovskite:

$$b = \frac{\Delta V_{\mathrm{Pero}}}{V_{\mathrm{bi}}}$$

$$= \big(1 + \frac{\epsilon_{\mathrm{r,Pero}} d_{\mathrm{HTL}}}{\epsilon_{\mathrm{r,HTL}} d_{\mathrm{Pero}}} + \frac{\epsilon_{\mathrm{r,Pero}} d_{\mathrm{ETL}}}{\epsilon_{\mathrm{r,ETL}} d_{\mathrm{Pero}}} \big)^{-1} \tag{6.17}$$

For the cases in Figure 6.C.1(a) and (b) and the device parameters in Table 6.A.1 (without any doping in the ETL) we calculate a correction factor of 0.25 and 0.73, respectively, meaning that the potential drop within the perovskite is approximately 0.25 V and 0.73 V (V_{bi} is 1 V). This is in good agreement with the simulations.

Next to impacting the electric field in the perovskite bulk, potential drops within the CTLs also impact the current that is measured in TAIC and in general current transient measurements. This is illustrated in Figure 6.C.1(c) and (d) for the dielectric constants of $\epsilon_{\mathrm{r,ETL}} = 1$ in and $\epsilon_{\mathrm{r,ETL}} = 10$ for the ETL. The total extracted current in both cases consists of the ionic current and a displacement current in the perovskite, which are opposite in sign. For a lower dielectric constant of $\epsilon_{\mathrm{r,ETL}} = 1$ the displacement

current makes up a significant part of the total current J_{tot}, and the total current is only a fraction of the ionic current J_{ion}. This occurs due to the higher potential drop and, consequently, the higher electric field in the ETL. Ions that accumulate at the interface lead to a change of the electric field and consequently a displacement current. For a higher electric field in the ETL, the relative change of the electric field due to accumulated ionic carriers becomes lower, limiting the displacement current in the ETL. This also leads to a displacement current in the perovskite bulk because the current has to be constant throughout the device.

When integrating the total current, the ion density is significantly underestimated. Here, it would lead to an estimated ion density of $1.8 \cdot 10^{15}$ cm^{-3}, significantly lower than the actual value of $1.0 \cdot 10^{16}$ cm^{-3}. We can, however, account for underestimation due to the displacement current with the correction factor in Equation 6.2, resulting in a more accurate ion density of $7.2 \cdot 10^{15}$ cm^{-3}.

With Equation 6.17 and the parameters in Table 6.C.1, we can estimate the correction factor for the $MAPbI_3$ and the triple-cation device to be 0.76 and 0.66, respectively.

Table 6.C.1: Parameter values used to calculate the correction factor of the $MAPbI_3$ and the triple-cation device.

Parameter	$MAPbI_3$	Triple-cation	Comment
Thickness HTL (nm)	2	2	Estimate
Thickness perovskite (nm)	470.0	550.0	Measured with profilometer
Thickness ETL (nm)	20.0	30.0	Estimate
Dielectric constant HTL	4.0	4.0	Estimate
Dielectric constant perovskite	33.0	43.0	From C-f measurements
Dielectric constant ETL	5.0	5.0	Estimate

6.D Additional Information

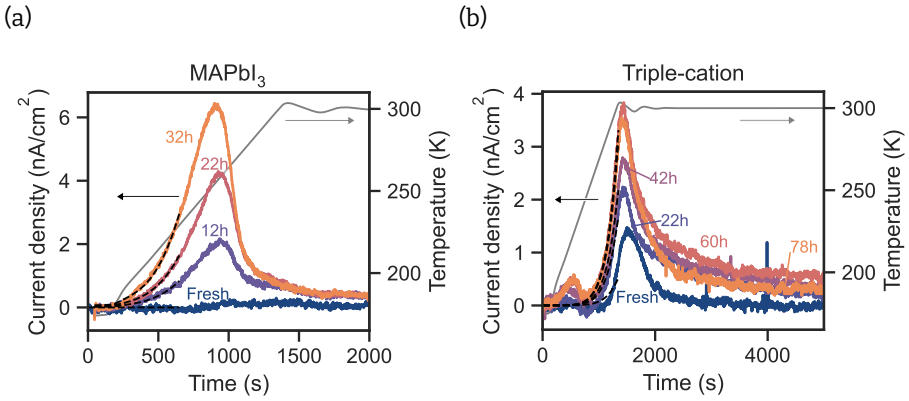

Figure 6.D.1: Thermally activated ion current measurements of a second (a) $MAPbI_3$ and (b) triple-cation perovskite solar cell for different stressing durations. The black dashed lines represent fits. The gray line represents an exemplary temperature sweep. The extracted ion parameters are shown in Table 6.D.1.

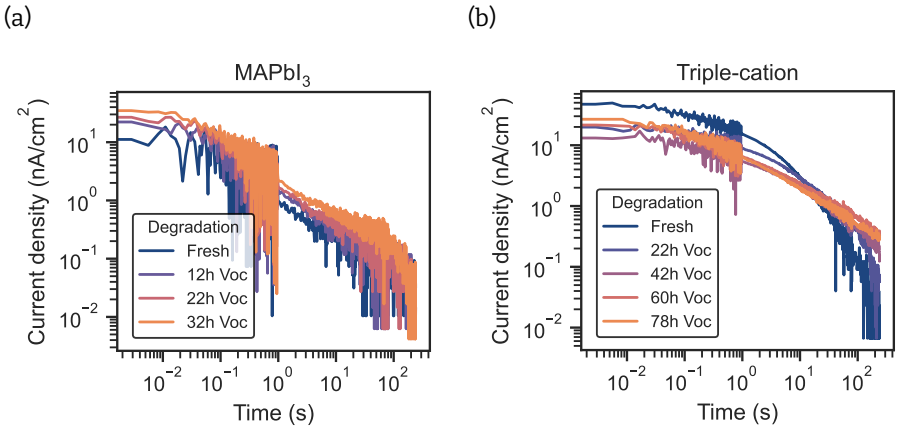

Figure 6.D.2: Current transient measurements after switching off the applied bias after cooling the devices down to 175 K in a TAIC measurement of (a) a $MAPbI_3$ device and (b) a triple-cation device. The noise changes around 1 s because the integration time of the source-measure unit changes.

Table 6.D.1: Estimated values of the activation energy E_{a}, ionic conductivity at 300 K $\sigma_{\mathrm{ion,300K}}$, ion density N_{ion}, and diffusion coefficient at 300 K $D_{\mathrm{ion,300K}}$ for the second $MAPbI_3$ and the triple-cation devices in Figure 6.D.1. The values were extracted from the low-temperature fit and the integral of the TAIC measurements. The error of N_{ion} is estimated from the minimum detectable ion density based on the noise of the current and the diffusion coefficient at the temperature of the current peaks. The errors of the $\sigma_{\mathrm{ion,300K}}$ correspond to the fitting error. The error of $D_{\mathrm{ion,300K}}$ is propagated based on the errors of N_{ion} and $\sigma_{\mathrm{ion,300K}}$. For the fresh $MAPbI_3$ device, we could not extract any values because the current is below the noise.

Device	Stressing	E_{a} (eV)	$\sigma_{\mathrm{ion,300K}}$ (S/cm)	N_{ion} (cm^{-3})	$D_{\mathrm{ion,300K}}$ (cm^2/s)
$MAPbI_3$	Fresh	0.25	-	-	-
	12h		$9.0\pm0.7\cdot10^{-13}$	$5.8\pm0.2\cdot10^{17}$	$2.5\pm0.2\cdot10^{-13}$
	22h		$1.8\pm0.1\cdot10^{-12}$	$9.3\pm0.2\cdot10^{17}$	$3.1\pm0.2\cdot10^{-13}$
	32h		$3.2\pm0.2\cdot10^{-12}$	$12.1\pm0.1\cdot10^{17}$	$4.2\pm0.3\cdot10^{-13}$
Triple-cation	Fresh	0.42	$5.7\pm0.8\cdot10^{-14}$	$2.9\pm0.3\cdot10^{17}$	$3.1\pm0.5\cdot10^{-14}$
	22h		$1.8\pm0.2\cdot10^{-13}$	$13.1\pm0.4\cdot10^{17}$	$2.2\pm0.3\cdot10^{-14}$
	42h		$2.4\pm0.3\cdot10^{-13}$	$19.1\pm0.5\cdot10^{17}$	$2.0\pm0.3\cdot10^{-14}$
	60h		$3.6\pm0.5\cdot10^{-13}$	$27.1\pm0.5\cdot10^{17}$	$2.1\pm0.3\cdot10^{-14}$
	78h		$3.4\pm0.4\cdot10^{-13}$	$24.2\pm0.5\cdot10^{17}$	$2.2\pm0.3\cdot10^{-14}$

Table 6.D.2: Fitting value of the product of ion density and diffusion coefficient prefactor $N_{\mathrm{ion}}D_{0,\mathrm{ion}}$ extracted from the low temperature fits in Figure 6.3. The errors correspond to the fitting error.

Device	Stressing	$N_{\mathrm{ion}}D_{0,\mathrm{ion}}$ $(cm\,s)^{-1}$
$MAPbI_3$	Fresh	$2.7\pm0.2\cdot10^{9}$
	12h	$1.8\pm0.1\cdot10^{10}$
	22h	$2.7\pm0.2\cdot10^{10}$
	32h	$3.5\pm0.2\cdot10^{10}$
Triple-cation	Fresh	$1.5\pm0.1\cdot10^{9}$
	22h	$1.4\pm0.1\cdot10^{10}$
	42h	$2.0\pm0.1\cdot10^{10}$
	60h	$4.5\pm0.1\cdot10^{10}$
	78h	$8.0\pm0.3\cdot10^{10}$

Table 6.D.3: Values for the activation energy E_a, ion density N_{ion}, and mobility $\mu_{0,ion}$ extracted from the drift-diffusion simulations in Figure 6.4. The values were extracted by fitting the low-temperature current and integrating the total current of the TAIC measurements. Because the ion density is significantly underestimated in the field-limited case, we do not determine the ionic mobility.

	Set E_a (eV)	Fit E_a (eV)	Set $\sigma_{0,ion}$ (S/cm)	Fit $\sigma_{0,ion}$ (S/cm)	Set N_{ion} (1/cm^3)	Approx. N_{ion} (1/cm^3)	Set $\mu_{0,ion}$ (cm^2/Vs)	Approx. $\mu_{0,ion}$ (cm^2/Vs)
Ion-limited	0.3	0.29	$1.1 \cdot 10^{-9}$	$7.3 \cdot 10^{-10}$	10^{15}	$1.2 \cdot 10^{15}$	$7 \cdot 10^{-6}$	$3.9 \cdot 10^{-6}$
			$2.4 \cdot 10^{-9}$	$1.6 \cdot 10^{-9}$	$2.2 \cdot 10^{15}$	$2.5 \cdot 10^{15}$		$4.1 \cdot 10^{-6}$
			$5.2 \cdot 10^{-9}$	$3.6 \cdot 10^{-9}$	$4.6 \cdot 10^{15}$	$5.2 \cdot 10^{15}$		$4.4 \cdot 10^{-6}$
			$1.1 \cdot 10^{-8}$	$7.8 \cdot 10^{-9}$	10^{16}	$1.0 \cdot 10^{16}$		$4.8 \cdot 10^{-6}$
	0.6	0.61	$4.8 \cdot 10^{-6}$	$6.5 \cdot 10^{-6}$	10^{15}	$1.2 \cdot 10^{15}$	$3.0 \cdot 10^{-2}$	$3.4 \cdot 10^{-2}$
			$1.0 \cdot 10^{-5}$	$1.6 \cdot 10^{-5}$	$2.2 \cdot 10^{15}$	$2.5 \cdot 10^{15}$		$4.1 \cdot 10^{-2}$
			$2.2 \cdot 10^{-5}$	$3.8 \cdot 10^{-5}$	$4.6 \cdot 10^{15}$	$5.2 \cdot 10^{15}$		$4.5 \cdot 10^{-2}$
			$4.8 \cdot 10^{-5}$	$8.3 \cdot 10^{-5}$	10^{16}	$1.0 \cdot 10^{16}$		$5.1 \cdot 10^{-2}$
Field-limited	0.3	0.28	$1.1 \cdot 10^{-8}$	$4.9 \cdot 10^{-9}$	10^{17}	$2.6 \cdot 10^{16}$	$7.0 \cdot 10^{-7}$	-
			$2.4 \cdot 10^{-8}$	$1.0 \cdot 10^{-8}$	$2.2 \cdot 10^{17}$	$3.4 \cdot 10^{16}$		-
			$5.2 \cdot 10^{-8}$	$2.1 \cdot 10^{-8}$	$4.6 \cdot 10^{17}$	$3.8 \cdot 10^{16}$		-
			$1.1 \cdot 10^{-7}$	$4.4 \cdot 10^{-8}$	10^{18}	$4.0 \cdot 10^{16}$		-
	0.6	0.56	$4.8 \cdot 10^{-5}$	$1.1 \cdot 10^{-5}$	10^{17}	$3.1 \cdot 10^{16}$	$3.0 \cdot 10^{-3}$	-
			$1.0 \cdot 10^{-4}$	$2.5 \cdot 10^{-5}$	$2.2 \cdot 10^{17}$	$3.5 \cdot 10^{16}$		-
			$2.2 \cdot 10^{-4}$	$5.3 \cdot 10^{-5}$	$4.6 \cdot 10^{17}$	$3.8 \cdot 10^{16}$		-
			$4.8 \cdot 10^{-4}$	$1.1 \cdot 10^{-4}$	10^{18}	$4.0 \cdot 10^{16}$		-

Table 6.D.4: Ion density estimated from current transient measurements measured at 175 K in Figure 6.D.2.

Device	Stressing	N_{ion} (cm^{-3})
$MAPbI_3$	Fresh	$9.8 \cdot 10^{15}$
	12h	$1.2 \cdot 10^{16}$
	22h	$1.3 \cdot 10^{16}$
	32h	$1.8 \cdot 10^{16}$
Triple-cation	Fresh	$4.8 \cdot 10^{16}$
	22h	$5.5 \cdot 10^{16}$
	42h	$5.1 \cdot 10^{16}$
	60h	$6.8 \cdot 10^{16}$
	78h	$5.7 \cdot 10^{16}$

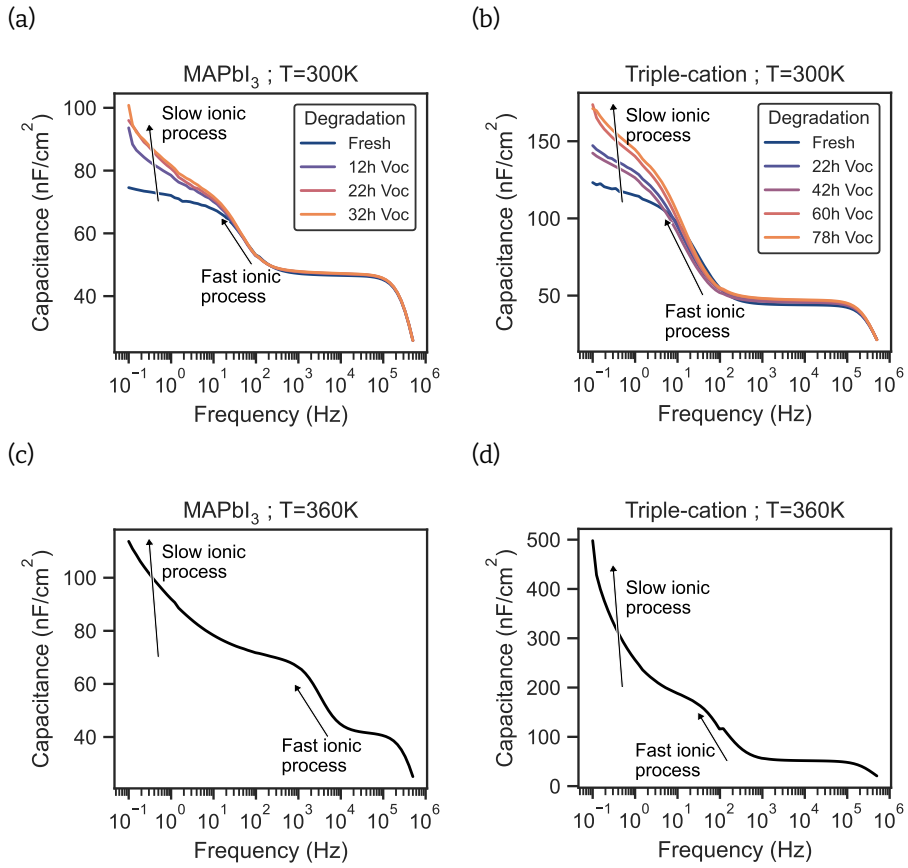

Figure 6.D.3: Capacitance frequency measurements of (a) a $MAPbI_3$ device at 300 K after different stressing durations at V_{oc}, (b) a triple-cation device at 300 K after different stressing durations at V_{oc}, (c) a $MAPbI_3$ device at 360 K and (d) a triple-cation device at 360 K.

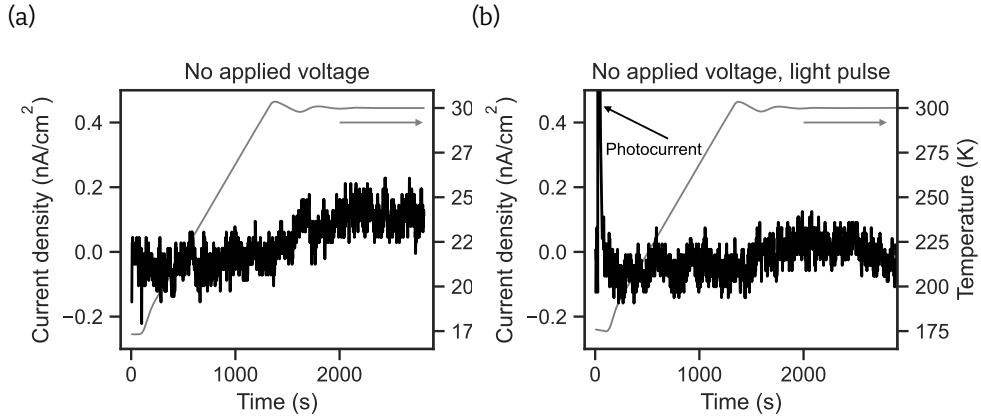

Figure 6.D.4: TAIC measurement of a triple-cation device (a) without any applied voltage during the cool-down and (b) without any applied voltage during the cool-down and briefly illuminated at 175 K.

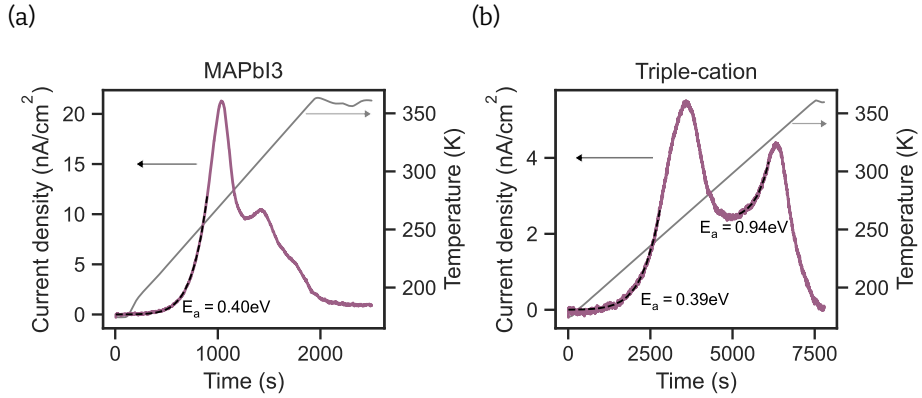

Figure 6.D.5: TAIC measurements starting and ending at 360 K of (a) a $MAPbI_3$ and (b) a triple-cation device. The temperature sweep speed for the $MAPbI_3$ device is 0.1 K/s and for the triple-cation device 0.025 K/s. Dashed lines indicate fits.

Bibliography

[1] J. Thiesbrummel *et al.*, "Ion-Induced Field Screening as a Dominant Factor in Perovskite Solar Cell Operational Stability", *Nature Energy*, vol. 9, no. 6, pp. 664–676, 2024.

[2] J. Thiesbrummel *et al.*, "Universal Current Losses in Perovskite Solar Cells Due to Mobile Ions", *Advanced Energy Materials*, vol. 11, no. 34, p. 2 101 447, 2021.

[3] L. J. F. Hart *et al.*, "More is Different: Mobile Ions Improve the Design Tolerances of Perovskite Solar Cells", *Energy & Environmental Science*, vol. 17, no. 19, pp. 7107–7118, 2024.

[4] M. Diethelm *et al.*, "Probing Ionic Conductivity and Electric Field Screening in Perovskite Solar Cells: a Novel Exploration Through Ion Drift Currents", *Energy & Environmental Science*, vol. 18, no. 3, pp. 1385–1397, 2025.

[5] J. Diekmann *et al.*, "Determination of Mobile Ion Densities in Halide Perovskites via Low-Frequency Capacitance and Charge Extraction Techniques", *The Journal of Physical Chemistry Letters*, vol. 14, no. 18, pp. 4200–4210, 2023.

[6] M. C. Schmidt, E. Gutierrez-Partida, M. Stolterfoht, and B. Ehrler, "Impact of Mobile Ions on Transient Capacitance Measurements of Perovskite Solar Cells", *PRX Energy*, vol. 2, no. 4, p. 043 011, 2023.

[7] S. Wang, P. Kaienburg, B. Klingebiel, D. Schillings, and T. Kirchartz, "Understanding Thermal Admittance Spectroscopy in Low-Mobility Semiconductors", *The Journal of Physical Chemistry C*, vol. 122, no. 18, pp. 9795–9803, 2018.

[8] D. V. Lang, "Deep-Level Transient Spectroscopy: A New Method to Characterize Traps in Semiconductors", *Journal of Applied Physics*, vol. 45, no. 7, pp. 3023–3032, 1974.

[9] R. A. Awni *et al.*, "Influence of Charge Transport Layers on Capacitance Measured in Halide Perovskite Solar Cells", *Joule*, vol. 4, no. 3, pp. 644–657, 2020.

[10] S. Reichert, Q. An, Y.-W. Woo, A. Walsh, Y. Vaynzof, and C. Deibel, "Probing the Ionic Defect Landscape in Halide Perovskite Solar Cells", *Nature Communications*, vol. 11, no. 1, p. 6098, 2020.

[11] M. H. Futscher, M. K. Gangishetty, D. N. Congreve, and B. Ehrler, "Quantifying Mobile Ions and Electronic Defects in Perovskite-Based Devices with Temperature-Dependent Capacitance Measurements: Frequency vs Time Domain", *The Journal of Chemical Physics*, vol. 152, no. 4, p. 044 202, 2020.

[12] L. McGovern, I. Koschany, G. Grimaldi, L. A. Muscarella, and B. Ehrler, "Grain Size Influences Activation Energy and Migration Pathways in MAPbBr $_3$ Perovskite Solar Cells", *The Journal of Physical Chemistry Letters*, vol. 12, no. 9, pp. 2423–2428, 2021.

[13] M. C. Schmidt and B. Ehrler, "How Many Mobile Ions Can Electrical Measurements Detect in Perovskite Solar Cells?", *ACS Energy Letters*, vol. 10, no. 5, pp. 2457–2460, 2025.

[14] A. Baumann, S. Väth, P. Rieder, M. C. Heiber, K. Tvingstedt, and V. Dyakonov, "Identification of Trap States in Perovskite Solar Cells", *The Journal of Physical Chemistry Letters*, vol. 6, no. 12, pp. 2350–2354, 2015.

[15] M. R. Khan, J. A. Schwenzer, J. Lehr, U. W. Paetzold, and U. Lemmer, "Emergence of Deep Traps in Long-Term Thermally Stressed CH_3 NH_3 PbI_3 Perovskite Revealed by Thermally Stimulated Currents", *The Journal of Physical Chemistry Letters*, vol. 13, no. 2, pp. 552–558, 2022.

[16] G. Gordillo, C. A. Otálora, and M. A. Reinoso, "Trap Center Study in Hybrid Organic-Inorganic Perovskite Using Thermally Stimulated Current (TSC) Analysis", *Journal of Applied Physics*, vol. 122, no. 7, p. 075 304, 2017.

[17] Z. Xu, L. Wang, Q. Han, Y. Kamata, and T. Ma, "Suppression of Iodide Ion Migration via Sb_2 S_3 Interfacial Modification for Stable Inorganic Perovskite Solar Cells", *ACS Applied Materials & Interfaces*, vol. 12, no. 11, pp. 12 867–12 873, 2020.

[18] M. Leoncini *et al.*, "Electronic Transport, Ionic Activation Energy and Trapping Phenomena in a Polymer-Hybrid Halide Perovskite Composite", *Journal of Science: Advanced Materials and Devices*, vol. 6, no. 4, pp. 543–550, 2021.

[19] S. Moghadamzadeh *et al.*, "Spontaneous Enhancement of the Stable Power Conversion Efficiency in Perovskite Solar Cells", *Journal of Materials Chemistry A*, vol. 8, no. 2, pp. 670–682, 2020.

[20] A. Ciavatti *et al.*, "Radiation Hardness and Defects Activity in PEA_2 $PbBr_4$ Single Crystals", *Advanced Functional Materials*, vol. 34, no. 46, p. 2 405 291, 2024.

[21] B. Kim, J. Kim, and N. Park, "First-Principles Identification of the Charge-Shifting Mechanism and Ferroelectricity in Hybrid Halide Perovskites", *Scientific Reports*, vol. 10, no. 1, p. 19 635, 2020.

[22] P. S. Whitfield *et al.*, "Structures, Phase Transitions and Tricritical Behavior of the Hybrid Perovskite Methyl Ammonium Lead Iodide", *Scientific Reports*, vol. 6, no. 1, p. 35 685, 2016.

[23] M. H. Futscher and J. V. Milić, "Mixed Conductivity of Hybrid Halide Perovskites: Emerging Opportunities and Challenges", *Frontiers in Energy Research*, vol. 9, p. 629 074, 2021.

[24] S. Shah *et al.*, "Impact of Ion Migration on the Performance and Stability of Perovskite-Based Tandem Solar Cells", *Advanced Energy Materials*, vol. 14, no. 48, p. 2 400 720, 2024.

[25] D. A. Jacobs *et al.*, "The Two Faces of Capacitance: New Interpretations for Electrical Impedance Measurements of Perovskite Solar Cells and Their Relation to Hysteresis", *Journal of Applied Physics*, vol. 124, no. 22, p. 225 702, 2018.

[26] S. T. Birkhold, J. T. Precht, R. Giridharagopal, G. E. Eperon, L. Schmidt-Mende, and D. S. Ginger, "Direct Observation and Quantitative Analysis of Mobile Frenkel Defects in Metal Halide Perovskites Using Scanning Kelvin Probe Microscopy", *The Journal of Physical Chemistry C*, vol. 122, no. 24, pp. 12 633–12 639, 2018.

[27] D. A. Jacobs, C. M. Wolff, X.-Y. Chin, K. Artuk, C. Ballif, and Q. Jeangros, "Lateral Ion Migration Accelerates Degradation in Halide Perovskite Devices", *Energy & Environmental Science*, vol. 15, no. 12, pp. 5324–5339, 2022.

[28] C. Li, A. Guerrero, S. Huettner, and J. Bisquert, "Unravelling the Role of Vacancies in Lead Halide Perovskite Through Electrical Switching of Photoluminescence", *Nature Communications*, vol. 9, no. 1, p. 5113, 2018.

[29] S. G. McCallum, O. Nicholls, K. O. Jensen, M. V. Cowley, J. E. Lerpinière, and A. B. Walker, "Bayesian Parameter Estimation for Characterising Mobile Ion Vacancies in Perovskite Solar Cells", *Journal of Physics: Energy*, vol. 6, no. 1, p. 015 005, 2024.

[30] M. C. Schmidt, A. O. Alvarez, J. J. De Boer, L. J. Van De Ven, and B. Ehrler, "Consistent Interpretation of Time- and Frequency-Domain Traces of Ion Migration in Perovskite Semiconductors", *ACS Energy Letters*, vol. 9, no. 12, pp. 5850–5858, 2024.

[31] M. H. Futscher *et al.*, "Quantification of Ion Migration in $CH_3NH_3PbI_3$ Perovskite Solar Cells by Transient Capacitance Measurements", *Materials Horizons*, vol. 6, no. 7, pp. 1497–1503, 2019.

[32] C. Eames, J. M. Frost, P. R. F. Barnes, B. C. O'Regan, A. Walsh, and M. S. Islam, "Ionic Transport in Hybrid Lead Iodide Perovskite Solar Cells", *Nature Communications*, vol. 6, no. 1, p. 7497, 2015.

[33] J. Haruyama, K. Sodeyama, L. Han, and Y. Tateyama, "First-Principles Study of Ion Diffusion in Perovskite Solar Cell Sensitizers", *Journal of the American Chemical Society*, vol. 137, no. 32, pp. 10 048–10 051, 2015.

[34] U.-G. Jong *et al.*, "Influence of Water Intercalation and Hydration on Chemical Decomposition and Ion Transport in Methylammonium Lead Halide Perovskites", *Journal of Materials Chemistry A*, vol. 6, no. 3, pp. 1067–1074, 2018.

[35] Y. Shao *et al.*, "Grain Boundary Dominated Ion Migration in Polycrystalline Organic–Inorganic Halide Perovskite Films", *Energy & Environmental Science*, vol. 9, no. 5, pp. 1752–1759, 2016.

[36] M. Ghasemi *et al.*, "A Multiscale Ion Diffusion Framework Sheds Light on the Diffusion–Stability–Hysteresis Nexus in Metal Halide Perovskites", *Nature Materials*, vol. 22, no. 3, pp. 329–337, 2023.

[37] D. Yang, W. Ming, H. Shi, L. Zhang, and M.-H. Du, "Fast Diffusion of Native Defects and Impurities in Perovskite Solar Cell Material CH_3 NH_3 PbI_3", *Chemistry of Materials*, vol. 28, no. 12, pp. 4349–4357, 2016.

[38] L. Bertoluzzi *et al.*, "Mobile Ion Concentration Measurement and Open-Access Band Diagram Simulation Platform for Halide Perovskite Solar Cells", *Joule*, vol. 4, no. 1, pp. 109–127, 2020.

[39] A. O. Alvarez *et al.*, "Ion Migration and Space-Charge Zones in Metal Halide Perovskites Through Short-Circuit Transient Current and Numerical Simulations", *Advanced Electronic Materials*, vol. 10, no. 11, p. 2 400 241, 2024.

[40] L. McGovern *et al.*, "Reduced Barrier for Ion Migration in Mixed-Halide Perovskites", *ACS Applied Energy Materials*, vol. 4, no. 12, pp. 13 431–13 437, 2021.

[41] B. A. Seid *et al.*, "Understanding and Mitigating Atomic Oxygen-Induced Degradation of Perovskite Solar Cells for Near-Earth Space Applications", *Small*, vol. 20, no. 30, p. 2 311 097, 2024.

Summary

Perovskite solar cells have shown impressive efficiency gains over the last years. However, their limited stability is still hindering their commercialization. Mobile ions that migrate within the perovskite layer have been linked to various loss mechanisms, decreasing the short-circuit current density, open-circuit voltage, and fill factor. Therefore, accurately quantifying mobile ions in perovskite solar cells is an essential step to decrease losses that are linked to ion migration. In this thesis, we focus on understanding and applying various electrical measurement techniques to quantify mobile ions in perovskite solar cells. By combining electrical measurements with drift-diffusion simulations, we connect the migration of mobile ions to observables like the capacitance and electric current in measurements of the time-dependent capacitance and current, as well as the frequency-dependent capacitance. The combination of these techniques, together with simulations, results in a comprehensive understanding of the impact of mobile ions, allowing for the quantification of mobile ionic defects.

In **Chapter 1**, we introduce metal halide perovskites, including their crystal structure, advantageous properties like their tunable bandgap, strong absorption, and long diffusion lengths of electronic carriers. Furthermore, we discuss the different ionic defects, i.e., Frenkel and Schottky defects, and the migration of vacancies and interstitials. We showcase the electrostatic effect that mobile ions can have on the energy band distribution of a perovskite solar cell. After discussing measurement techniques used for qualitatively characterizing mobile ions in perovskite solar cells, we introduce the three main measurement techniques used to quantify mobile ions throughout this thesis: capacitance frequency, capacitance transient, and current transient measurements. Finally, we discuss the fundamentals of drift-diffusion simulations, one of the main tools used in this thesis to explain the impact of mobile ions on the different electrical measurement techniques.

In **Chapter 2** we focus on the origin of the transient direction in capacitance transient measurements. Contrary to the model originally proposed in the literature, we show with drift-diffusion simulations that the transient direction is not caused by the po-

larity of the migrating ionic defect. Instead, we demonstrate that the direction of the transients depends on which capacitance is modulated when mobile ions redistribute. In case of high electronic carrier densities, mobile ions modulate the depletion layer in the perovskite, resulting in an increase in the transient, independent of the polarity of the ions. In case of low electronic carrier densities, i.e., intrinsic perovskites, the capacitance of the transport layers is modulated, resulting in decreasing transients. We verify these results by changing the electronic carrier density via photo excitation, allowing us to switch between decreasing and mainly increasing transients.

Charge transport layers are usually not accounted for when characterizing mobile ions in complete perovskite solar cells, even though they can significantly impact the measurements. Therefore, we characterize a simple device consisting of only electrodes and a $MAPbI_3$ perovskite in **Chapter 3**. This way, we do not have to account for the impact of charge transport layers on the measurement response. We characterize the perovskite device with capacitance transient, current transient, and capacitance frequency measurements in the dark and under illumination. By reproducing the measurements with drift-diffusion simulations, we can link the different observed signatures to mobile ions. We find that the measurements in the dark directly probe the ionic process. In contrast, under illumination, we measure the modulation of recombination processes due to mobile ions. Because of the good agreement of experimental results and simulations, we can estimate the ionic properties, namely the density, diffusion coefficient, and activation energy of the mobile ions of the $MAPbI_3$ perovskite.

If the density of mobile ions in perovskite solar cells is high enough to screen the built-in field, electrical measurements no longer allow for an estimation of the ion density, which we illustrate in **Chapter 4**. The studied techniques include capacitance transient, current transient, capacitance frequency, and low-frequency Mott-Schottky measurements. Using drift-diffusion simulations, we show that if the ion density is high enough to screen the built-in potential, only a fraction of the mobile ions is probed, resulting in a saturation of the capacitance or current. Then, the ion density cannot be determined accurately anymore.

In **Chapter 5** we develop a computationally inexpensive, yet accurate approximation of drift-diffusion simulations. By expressing the ionic accumulation and depletion layer in the perovskite and the depletion layers in the charge transport layers as step functions, we approximate the net-charge density and potential distribution within perovskite solar cells. Accounting for the drift of mobile ions after removing an applied bias and computing the frequency-dependent small-signal solution of the perovskite device allows for the approximation of capacitance transient, capacitance frequency, and current transient measurements. We validate the model by extracting

the ionic conductivity, and for lower ion densities, also the density and diffusion coefficient from drift-diffusion simulations. Finally, we apply the model to quantify the ionic conductivity and activation energy by fitting experimental capacitance transients, capacitance frequency measurements, and current transients of triple cation perovskite solar cells.

To simplify the characterization of mobile ions in perovskite solar cells, we introduce a new electrical measurement technique, thermally activated ion current (TAIC) in **Chapter 6**. The technique is based on measuring the ionic current during a temperature sweep. At low temperatures, mobile ions hardly migrate due to their low diffusion coefficient. Increasing the temperature results in an exponential increase in the current due to the temperature-activated diffusion coefficient of the mobile ions. Once the perovskite becomes depleted of mobile ions, the current decreases. We can express the current in the TAIC measurement with a simple equation accounting for the ion density, diffusion coefficient, and activation energy. Using TAIC, we quantify a $MAPbI_3$ and a triple-cation perovskite, finding a higher activation energy and lower diffusion coefficient in the triple-cation device. Because of its simplicity and intuitive nature, TAIC measurements are a promising technique to quantify mobile ions in perovskite solar cells.

Samenvatting

Perovskiet zonnecellen hebben de afgelopen jaren indrukwekkende efficiëntieverbeteringen laten zien. Toch wordt hun commercialisering nog steeds belemmerd door hun beperkte stabiliteit. Mobiele ionen die migreren binnen de perovskietlaag zijn gekoppeld aan verschillende verliesmechanismen, waardoor de kortsluitstroomdichtheid, nullastspanning en vulfactor afnemen. Daarom is het nauwkeurig kwantificeren van mobiele ionen in perovskiet zonnecellen een essentiële stap om verliezen die gekoppeld zijn aan ionenmigratie te verminderen. In dit proefschrift richten we ons op het begrijpen en toepassen van verschillende elektrische meettechnieken om mobiele ionen in perovskiet zonnecellen te kwantificeren. Door elektrische metingen te combineren met drift-diffusie simulaties verbinden we de migratie van mobiele ionen met observeerbare grootheden, zoals de capaciteit en elektrische stroom in metingen van de tijdsafhankelijke capaciteit en stroom, evenals de frequentie-afhankelijke capaciteit. De combinatie van deze technieken, samen met simulaties, resulteert in een uitgebreid begrip van de impact van mobiele ionen, wat de kwantificering van mobiele ionische defecten mogelijk maakt.

In **Hoofdstuk 1** introduceren we metaalhalogenide perovskieten, inclusief hun kristalstructuur, gunstige eigenschappen zoals hun afstembare bandkloof, sterke absorptie en lange diffusielengtes van elektronische ladingdragers. Verder bespreken we de verschillende ionische defecten, te weten Frenkel- en Schottky-defecten, en de migratie van vacatures en interstitiëlen. We tonen het elektrostatische effect dat mobiele ionen kunnen hebben op de energiebandverdeling van een perovskiet zonnecel. Na het bespreken van meettechnieken die worden gebruikt voor het kwalitatief karakteriseren van mobiele ionen in perovskiet zonnecellen, introduceren we de drie belangrijkste meettechnieken die in dit proefschrift worden gebruikt om mobiele ionen te kwantificeren: capaciteit-frequentie-, capaciteit-transiënt- en stroom-transiëntmetingen. Ten slotte bespreken we de grondbeginselen van drift-diffusie simulaties, een van de belangrijkste hulpmiddelen die in dit proefschrift wordt gebruikt om de impact van mobiele ionen op de verschillende elektrische meettechnieken te verklaren.

In **Hoofdstuk 2** richten we ons op de oorsprong van de transiënte richting in capaciteit-transiëntmetingen. In tegenstelling tot het model dat oorspronkelijk in de literatuur werd voorgesteld, tonen we met drift-diffusie simulaties aan dat de transiënte richting niet wordt veroorzaakt door de polariteit van het migrerende ionische defect. We laten zien dat de richting van de transiënten in plaats daarvan afhangt van welke capaciteit wordt gemoduleerd wanneer mobiele ionen zich herverdelen. In het geval van hoge elektronische ladingdragerdichtheden moduleren mobiele ionen de depletielaag in de perovskiet, wat resulteert in een toename van de transiënt, onafhankelijk van de polariteit van de ionen. In het geval van lage elektronische ladingdragerdichtheden, oftewel intrinsieke perovskieten, wordt de capaciteit van de transportlagen gemoduleerd, wat resulteert in afnemende transiënten. We verifiëren deze resultaten door de elektronische ladingdragerdichtheid te veranderen via foto-excitatie, waardoor we kunnen schakelen tussen afnemende en voornamelijk toenemende transiënten.

Ladingtransportlagen worden meestal niet meegenomen bij het karakteriseren van mobiele ionen in complete perovskiet zonnecellen, hoewel ze de metingen significant kunnen beïnvloeden. Daarom karakteriseren we in **Hoofdstuk 3** een eenvoudig apparaat dat alleen bestaat uit elektroden en een $MAPbI_3$ perovskiet. Op deze manier hoeven we geen rekening te houden met de impact van ladingstransportlagen op de meetrespons. We karakteriseren het perovskietapparaat met capaciteit-transiënt-, stroom-transiënt- en capaciteit-frequentiemetingen in het donker en onder belichting. Door de metingen te reproduceren met drift-diffusie simulaties, kunnen we de verschillende waargenomen signalen koppelen aan mobiele ionen. We stellen vast dat de metingen in het donker direct het ionische proces peilen. Onder belichting meten we daarentegen de modulatie van recombinatieprocessen als gevolg van mobiele ionen. Vanwege de goede overeenkomst tussen experimentele resultaten en simulaties, kunnen we de ionische eigenschappen inschatten, namelijk de dichtheid, diffusiecoëfficiënt en activeringsenergie van de mobiele ionen van de $MAPbI_3$ perovskiet.

Als de dichtheid van mobiele ionen in perovskiet zonnecellen hoog genoeg is om het ingebouwde veld af te schermen, is het niet langer mogelijk een inschatting te maken van de ionendichtheid met elektrische metingen, wat we in **Hoofdstuk 4** illustreren. De bestudeerde technieken omvatten capaciteit-transiënt, stroom-transiënt, capaciteit-frequentie, en laagfrequentie Mott-Schottky-metingen. Met behulp van drift-diffusie simulaties laten we zien dat als de ionendichtheid hoog genoeg is om de ingebouwde potentiaal af te schermen, slechts een fractie van de mobiele ionen wordt gemeten, wat resulteert in een verzadiging van de capaciteit of stroom. In dat geval kan de ionendichtheid niet langer nauwkeurig worden bepaald.

In **Hoofdstuk 5** ontwikkelen we een computationeel efficiënt maar nauwkeurige benadering van drift-diffusie simulaties. Door de ionische accumulatie- en depletielaag in de perovskiet en de depletielagen in de ladingstransportlagen uit te drukken als stapfuncties, benaderen we de netto-ladingsdichtheid en potentiaalverdeling binnen perovskiet zonnecellen. Door rekening te houden met de drift van mobiele ionen na het verwijderen van een aangelegde spanning, en door de frequentie-afhankelijke klein-signaaloplossing van perovskiet zonnecellen te berekenen, wordt het mogelijk om capaciteitstransiënten, capaciteit-frequentiemetingen en stroomtransiënten te benaderen. We valideren het model door de ionische geleidbaarheid, en voor lagere ionendichtheden ook de dichtheid en de diffusiecoëfficiënt, uit drift-diffusie simulaties te extraheren. Ten slotte passen we het model toe om de ionische geleidbaarheid en activeringsenergie te kwantificeren door experimentele capaciteitstransiënten, capaciteit-frequentiemetingen en stroomtransiënten van drievoudig-kation perovskiet zonnecellen te fitten.

Om de karakterisering van mobiele ionen in perovskiet zonnecellen te vereenvoudigen, introduceren we in **Hoofdstuk 6** een nieuwe elektrische meettechniek, thermisch geactiveerde ionenstroom (TAIC). De techniek is gebaseerd op het meten van de ionenstroom tijdens een temperatuurscan. Bij lage temperaturen migreren mobiele ionen nauwelijks vanwege hun lage diffusiecoëfficiënt. Het verhogen van de temperatuur resulteert in een exponentiële toename van de stroom als gevolg van de temperatuur-geactiveerde diffusiecoëfficiënt van de mobiele ionen. Zodra de perovskiet is uitgeput van mobiele ionen, neemt de stroom af. We kunnen de stroom in de TAIC-meting uitdrukken met een eenvoudige vergelijking die rekening houdt met de ionendichtheid, diffusiecoëfficiënt en activeringsenergie. Met behulp van TAIC kwantificeren we een $MAPbI_3$ en een drievoudig-kation perovskiet, waarbij we een hogere activeringsenergie en lagere diffusiecoëfficiënt vinden in de drievoudig-kation perovskiet zonnecel. Vanwege de eenvoud en intuïtieve aard zijn TAIC-metingen een veelbelovende techniek om mobiele ionen in perovskiet zonnecellen te kwantificeren.

List of Publications

1. Moritz C. Schmidt, Emilio Gutierrez-Partida, Martin Stolterfoht, and Bruno Ehrler, "Impact of Mobile Ions on Transient Capacitance Measurements of Perovskite Solar Cells," *PRX Energy*, vol. 2, no. 4, p. 043011(01-10), 2023. (**Chapter 2**)

   Author contributions: M.C.S. conceived the work, carried out the simulations and experiments, performed the analysis, interpreted the results, and wrote the manuscript. E.G.P. fabricated the devices, and M.S. interpreted the transient capacitance results and edited the manuscript. B.E. conceived and supervised the work, interpreted the results, and edited the manuscript.

2. Moritz C. Schmidt, Agustin O. Alvarez, Jeroen J. de Boer, Larissa J.M. van de Ven, and Bruno Ehrler, "Consistent Interpretation of Time- and Frequency-Domain Traces of Ion Migration in Perovskite Semiconductors," *ACS Energy Letters*, vol. 9, no. 12, pp. 5850–5858, 2024. (**Chapter 3**)

   Author contributions: M.C.S. conceived the work, carried out the simulations and measurements, performed the analysis, interpreted the results, and wrote the manuscript. A.O.A. helped with discussions and commented on the manuscript. J.J.d.B. fabricated the devices and commented on the manuscript. L.J.M.v.d.V. carried out the X-ray diffraction and scanning electron microscopy measurements. B.E. conceived and supervised the work, interpreted the results, and commented on the manuscript.

3. Moritz C. Schmidt and Bruno Ehrler, "How Many Mobile Ions Can Electrical Measurements Detect in Perovskite Solar Cells?," *ACS Energy Letters*, vol. 10, no. 5, pp. 2457–2460, 2025. (**Chapter 4**)

   Author contributions: M.C.S. conceived the work, carried out the simulations, performed the analysis, interpreted the results, and wrote the manuscript. B.E. conceived and supervised the work, interpreted the results, and commented on the manuscript.

4. Moritz C. Schmidt, Agustin O. Alvarez, Biruk A. Seid, Felix Lang, and Bruno Ehrler, "Characterization of mobile ions in perovskite solar cells with capacitance and current measurements by approximating drift-diffusion simulations," accepted in PRX Energy, 2025. (**Chapter 5**)

   Author contributions: M.C.S conceived the work, derived the step model, carried out the simulations and electrical measurements, performed the analysis, interpreted the results, and wrote the manuscript. A.O.A. helped with the derivation and commented on the manuscript. B.A.S. fabricated the perovskite solar cells and commented on the manuscript. F.L. commented on the manuscript and supervised B.A.S. B.E conceived and supervised the work, interpreted the results, and edited the manuscript.

5. Moritz C. Schmidt, Agustin O. Alvarez, Riccardo Pallotta, Biruk A. Seid, Jeroen J. de Boer, Jarla Thiesbrummel, Felix Lang, Giulia Grancini, and Bruno Ehrler, "Quantification of mobile ions in perovskite solar cells with thermally activated ion current measurements," submitted, 2025. (**Chapter 6**)

   Author contributions: M.C.S. conceived the work, carried out the simulations and measurements, performed the analysis, interpreted the results, and wrote the manuscript. A.O.A. helped with discussions and commented on the manuscript. R.P. fabricated the $MAPbI_3$ devices and commented on the manuscript. B.A.S fabricated the triple-cation devices and commented on the manuscript. J.J.dB. carried out thickness measurements and commented on the manuscript. J.T. helped with discussions. F.L. supervised the work of B.A.S and commented on the manuscript. G.G. supervised the work of R.P. and commented on the manuscript. B.E. conceived and supervised the work, interpreted the results, and commented on the manuscript.

Other publications by the author:

6. Riccardo Pallotta, Fabiola Faini, Francesco Toniolo, Valentina Larini, Moritz C. Schmidt, Sergio Marras, Giovanni Pica, Silvia Cavalli, Samuele Mattioni, Luis E. Hueso, Matteo Degani, Beatriz Martín-García, Bruno Ehrler, Giulia Grancini, "Reducing the $MAPbI_3$ microstrain by fast crystallization," *Joule*, p. 101964, 2025.

7. Parnian Ferdowsi, Gianluca Bravetti, Moritz C. Schmidt, Efrain Ochoa-Martinez, Shanti Bijani, Aurora Rizzo, Silvia Colella, Ullrich Steiner, Bruno Ehrler, Dominik J. Kubicki, Jovana V. Milić, "Host–Guest Complexation in Wide Bandgap Perovskite Solar Cells," *Solar RRL* vol. 8, no. 1, p. 2300655, 2023.

8. Lucie McGovern, Gianluca Grimaldi, Moritz H. Futscher, Eline M. Hutter, Loreta A. Muscarella, Moritz C. Schmidt, and Bruno Ehrler, "Reduced Barrier for Ion Migration in Mixed-Halide Perovskites," *ACS Applied Energy Materials* vol. 4, no. 12, pp. 13431–13437, 2021.

9. Saba Gharibzadeh, Paul Fassl, Ihteaz M Hossain, Pascal Rohrbeck, Markus Frericks, Moritz C. Schmidt, Motiur Rahman Khan, Tobias Abzieher, Bahram Abdollahi Nejand, Fabian Schackmar, Osbel Almora, Thomas Feeney, Roja Singh, Dirk Fuchs, Uli Lemmer, Jan P. Hofmann, Stefan A.L. Weber, Ulrich W. Paetzold, "Two birds with one stone: dual grain-boundary and interface passivation enables >22% efficient inverted methylammonium-free perovskite solar cells," *Energy & Environmental Science* vol. 14, pp. 5875-5893, 2021.

Acknowledgements

A PhD is rarely straightforward. Research projects often do not go as planned and divert into unexpected directions. Equipment breaks down, or methods turn out to be more complex than anticipated. Equally, research can be rewarding when it does work out, when theories can be confirmed, or new approaches are unexpectedly discovered. In both the ups and downs, the most important thing is to have people around to share them with. I was fortunate to be surrounded by incredible people throughout all the ups and downs of the last few years, and I am very grateful for this.

I want to start by thanking my supervisor, **Bruno**, for giving me the opportunity to work in your group almost 5 years ago. I admire you for always having a view on the big picture and your drive to push the energy transition in the Netherlands. It always gave me extra motivation to know that we are working towards the same goal and share the same motivation. Of course, I also want to thank you for your supervision over the last years. I do not know how many times I dropped by your office, asking, 'Do you have a second?' and you always made time. Thank you for all the scientific discussions and your positive view when things did not work out as planned. Also, thank you for building such an incredible and special group. Many people joined in the last years, and the atmosphere was always welcoming, warm, and positive.

Next, I want to thank **Albert** for leading the LMPV-Team during the majority of my time at Amolf, creating a great atmosphere. I am also grateful for the numerous times you helped me during difficult times in my PhD, with your positive and calming perspective on projects, progress, and the future. **Erik**, thank you for co-supervising my work and your helpful input during discussions over the last years. **Esther**, I always appreciated your enthusiasm and the scientific input during poster sessions and presentations. Thank you for that! Thanks also to **Wiebke** for your optimism during the bus ride back from Veldhoven and your input during poster sessions. I also want to remember **Tae-Youl** for all his scientific input during the time he was at Amolf and his contributions to the perovskite field in general.

I would also like to thank **Thomas Kirchartz**, **Clara Aranda Alonso**, **Shuxia Tao**, **Jan-Anton Koster**, and **Maria Loi** for taking the time to read my thesis and being part of my PhD committee.

Next, I want to thank the Hybrid Solar Cells group. During the four years, the group steadily changed with new people joining and others leaving. Every single one made the group special in their own way, and it was a great pleasure to get to know every single one. I want to start by thanking the two people with whom I spent my entire time at Amolf: Imme and Jeroen. **Imme**, you were so incredibly welcoming when I first joined Amolf, giving me a tour of Amsterdam in my first week and showing me the best falafel in town. I really enjoyed all the scientific discussions, literature clubs, climbing sessions, and, of course, the filming sessions we shared. You are one of the most rigorous and enthusiastic scientists I have met, and I am grateful that we became friends. **Jeroen**, you were the best office mate and PhD partner I could have hoped for. We spent the entire PhD together and shared many memorable experiences at Amolf and at conferences. You have such a calming and positive presence, especially compared to Hades, and I was always glad to have you just opposite of me. **Daphne**, I will never forget our time together at the conference in Barcelona. We should do that again. You are so incredibly kind and empathetic. Thank you for being part of my time and Amolf, and for trying to teach me Dutch during our coffee breaks. **Larissa**, you are so contagiously positive and fun, and I am grateful that you joined the group. I always enjoyed your stories about your vacations and cheering for the Netherlands with you. **Agustin**, you are such an incredibly kind and positive person. Thank you for all your curiosity and input in my research projects. I really enjoyed our long, in-depth discussions and am very grateful that you were part of my time at Amolf. Thank you, **Lars**, for all the fun and positivity you brought into our group. And also for showing me what a *gabber* looks like - in my opinion, it was one of the best costumes at the Christmas lunch. **Jarla**, I always enjoyed hearing your impressive stories about Spitsbergen. Thank you for sharing all your knowledge and your input on ion migration. Thank you **Francesco** for bringing some much-needed positivity and distraction into our office in the last few months, and for your interest in continuing my research. Thank you, **Marc**, for all your fantastic help during the last four years, all the times you brought the gloveboxes back to life or added some feature to the setups. You always had an answer to every question, and our lab would not survive without you. **Gianluca**, you guided me through the first two years of my PhD. Your kindness and knowledge in all kinds of different areas helped me a lot during the first years. **Lucie**, thank you for the warm welcome to Amolf, for helping me through the first year of the PhD, and for bringing so much positivity and kindness to our group. Thanks also to **Loreta** and **Christian** for the warm welcome to the group and the input during the first months. I also had the pleasure to (co)supervise students during my time at Amolf and who taught me a lot. **Menke**, **Roman**, and **Sebastian**, it was a pleasure having you in our group. I also want to thank **Max**, **Filip**, **Oscar**, **Maria**,

Silvia, **Rens**, **Toon**, **Dimitris**, **Thomas**, **Jeong-Ju Paul**, **David**, **Floris**, **Jakub**, **Federico**, **Fiona**, and **Georg** for making the Hybrid Solar Cells so special in the last years.

I am grateful to have crossed paths with so many great people at Amolf over the years. First, I want to thank the best roommate: **Rohit**, your relentless enthusiasm and energy is truly contagious. We had a lot of fun together over the last years and I am very grateful that we became friends. Thank you, **Manuel**, for your kindness and optimism, and for the numerous climbing adventures we went on. I hope many more will follow. **Roel**, thank you for all the fun we had going climbing and for your positivity and help in my third year. Thank you, **Francesca**, for all the time we spent together playing games, having barbecues, or celebrating. Our trip to Marseille was definitely a highlight in the last years. Also, thank you, **Cedric** and **Anna**, for joining Amolf as guests. I deeply enjoyed our climbing sessions in Amsterdam, Spain, and France. **Ethan**, I always enjoyed your humor and all our bouldering sessions. Thank you for that. **Sarah**, thanks for the competitiveness and kindness you brought to LMPV. I always enjoyed our scientific discussion. Thanks also to **Linde**, **Omolara**, and **Fanny** for bringing so much life into our lab. **Davide**, thank you for being incredibly helpful when I lost my bag in Barcelona and all the fun we had at the conference afterwards. I also spent time in the personeelsvereniging, organizing events at Amolf. Thanks to **Mees**, **Imme**, **Evelijn**, **Francesca**, **Manuel**, **Yvonne**, **Yorick**, **Mels**, **Igor**, **Sofija**, **Timo**, and **Jente** for this experience and all the great events we organized. **Susan**, **Magda**, **Deba**, **Hongyu**, **Daan**, **Nikolai**, **Jerome**, **Marcel**, **Jyoti**, **Elaina**, **Loriane**, **Daphne A.**, **Alex**, **Antony**, **Jaime**, **Robin**, **Tom**, **Saskia**, **Nika**, **Stefan**, **Sergio**, **Hollie**, and anybody I might forget, thank you for making Amolf a truly wonderful place to work at during the last years.

My thanks also go to the support staff at Amolf, including **Bas**, **Ricardo**, **Pepijn**, **Ruud**, **Ivo**, **Wouter**, **Menno**, and **Floortje** for all your expertise and help over the last years. I especially want to thank **Max P.**, **Henk-Jan**, **Bob**, and **Wessel** for their constant support, contributions, and modifications to the setups I worked with.

During my PhD, I was fortunate to collaborate not only with people at Amolf but also with many people in other research organizations. First, I want to thank **Martin**. Your critical questions in a meeting in the first months of my PhD led us to rethink capacitance transient measurements, resulting in our exciting collaboration. Thanks also to **Emilio** for being part of this effort and all the good times we had at conferences. I also want to thank **Biruk** and **Felix** for your contributions and input in two of our projects. It was a pleasure to work with you. **Riccardo** and **Giulia**, thank you for involving me in your work and your contributions to my last project. I deeply enjoyed working with you. **Jovana**, your positivity and kindness made it a real pleasure to collaborate with you and **Parnian**. Thank you! I would also like to thank **Carsten**, **Moritz F.**, and **Sand-**

hya for the numerous impedance discussions we had over the last years, which were always deeply interesting and stimulated many ideas. Thanks also to the two people who introduced me to the magic of thin-film solar cells: **Christian** and **Alexander**. I still enjoy thinking back to my time in your group and my first experiences in research. I also want to thank **Saba** and **Uli** for the time in your supervision during my master's thesis, and for bringing me in touch with perovskites.

Außerdem möchte ich meinen guten Freunden **Maik**, **Basti** und **Robert** für all die schönen Unterhaltungen, Urlaube, Fahrradtouren, Wanderungen und Boulder-Sessions danken. Natürlich möchte ich auch meiner wunderbaren Familie danken. Danke, **Mama** und **Papa**, für all die Unterstützung in den letzten Jahren und dafür, dass ihr Pioniere der Photovoltaik wart. Ohne euch wäre ich jetzt nicht da, wo ich bin. Danke auch an **Annika** und **Felix**. Es fällt mir schwer, die richtigen Worte zu finden, um auszudrücken, wie glücklich ich bin, dass ich euch habe. Danke für all eure Unterstützung und all die Momente in den letzten Jahren, in denen wir zusammen gelacht haben. Vielen Dank auch an **Roman** und **Sheila** für all die schönen Momente, die wir in den letzten Jahren gemeinsam erlebt haben. Tot slot, lieve **Margot**, dank je wel voor je onvoorwaardelijke steun en liefde. Jou te ontmoeten tijdens mijn promotie is het mooiste wat me is overkomen, en ik verheug me op onze toekomst samen.

About the Author

Moritz C. Schmidt was born in Bielefeld, Germany, on April 9, 1995. He pursued his bachelor's and master's studies in Electrical Engineering and Information Technology from 2014 to 2021 at the Karlsruhe Institute of Technology in Karlsruhe, Germany.
Intending to contribute to the energy transition, he focused on solar and battery research during his studies. In his bachelor's thesis, he researched organic solar cells in the group of Prof. Alexander Colsmann, which led to a research internship on organic solar cells at Merck in Southampton, United Kingdom. During his master's, he specialized in micro-, nano-, and optoelectronics. After an exchange semester in Trondheim, Norway, he conducted his master's thesis under the supervision of Prof. Ulrich Paetzold, researching interface passivation of perovskite solar cells.
In 2021, he started his PhD at AMOLF in Amsterdam in the group of Prof. Bruno Ehrler, where he focused on the characterization of mobile ions in perovskite solar cells with electrical measurement techniques. The results of his research are presented in this thesis.
In addition to his interest in the energy transition, Moritz enjoys climbing, reading, cycling, and photography.